

“Design, Development and Control of Voltage Source Converters for Grid Integration of Solar PV”

**A Thesis Submitted
In partial fulfillment of the requirements for the award of degree of**

DOCTOR OF PHILOSOPHY

By

**Amarendra Pandey
(2K18/PHD/EE/503)**

Department of Electrical Engineering

**Under the Supervision of
Dr. Alka Singh
Professor, Electrical Engineering Department,
Delhi Technological University**



DEPARTMENT OF ELECTRICAL ENGINEERING

DELHI TECHNOLOGICAL UNIVERSITY

(Formerly Delhi College of Engineering)

Bawana Road, Delhi-110042

JUL 2024

©Delhi Technological University – 2024

All rights reserved

DECLARATION

I hereby certify that the work which is presented in this thesis “**Design, Development and Control of Voltage Source Converters for Grid Integration of Solar PV**” submitted in partial fulfillment of the requirements for the award of the degree of Doctor of Philosophy in the Department of Electrical Engineering, Delhi Technological University, Delhi. This is an authentic record of my own work carried out under the supervision of Dr. Alka Singh. The matter presented in this thesis has not been submitted elsewhere for the award of a degree.

Amarendra Pandey
(2K18/PhD/EE/503)

Place: Delhi

Date: __/__/____

CERTIFICATE

This is to certify that the thesis entitled “**Design, Development and Control of Voltage Source Converters for Grid Integration of Solar PV**” being submitted by **Mr. Amarendra Pandey** for the award of degree of Doctor of Philosophy in the Department of Electrical Engineering, Delhi Technological University, Delhi, is the record of students own work carried out by him under our supervision. The contents of this research work have not been submitted in part or fully to any other institute or University for the award of any degree.

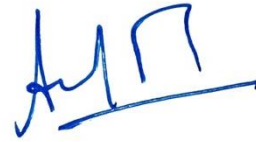
Date:

Prof. Alka Singh
Department of Electrical Engineering
Delhi Technological University, Delhi
Shahbad Daultapur, Delhi-110042, India

ACKNOWLEDGEMENTS

I would like to express my deep and sincere gratitude to my supervisors **Prof. Alka Singh** for their valuable guidance and continuous monitoring of my research work. It was great honor for me to pursue my research work under their supervisions. Prof. Alka Singh has been the main motivating and inspiring factor behind my research work. It's her vigor and hunger to perform in adverse situation, which has inspired me to thrive for excellence and nothing less. Continuous monitoring by her, valuable guidance and input has always been a driving force to complete my research work. It is a life time experience to work under of my supervisor. I would also like to convey my sincere gratitude to **Prof. J.N Rai**, Assistant Professor, DTU, who has taught me the relevant course work. I would like to thank the SRC members mainly **Prof. Uma Nagia**, who have given me valuable guidance and advice to improve quality of my research work. I am extremely grateful to **Dr. Prakash Chittora** and **Dr. Praveen Bansal**, for their valuable assistance and support. I am extremely thankful to staff members of Power System Lab **Ajendra Singh** and **Komal Singh** for providing me immense facility and assistance to carry out my research work. I would like to thank other office staff, Central library and Computer Centre staff, for their valuable co-operation and support. I would like my sincere thanks to **Shudhansu Mittal**, who helped me to develop hardware at initial level of research work. I am extremely grateful to my research group and friends **Saket Gupta**, **Allu Bhargav**, **Akash Seth**, **Kanchan Bala Rai**, **Hemant Saxena**, **Suryakant Shukla**, **Ajishek Raj** for their valuable assistance, co-operation and great source of learning. If I get any success today for my research work, the entire credit should go to my father **Mr. Shiv Shanker Pandey** mother. **Munni Pandey**, wife **Shalija**

Pandey, my younger brother **Shivanshu Pandey**. I would like to thank other family members supporting me directly or indirectly to carry out my research work. I thank to almighty, the father of all for his blessing to accomplish my research work successfully.



Date:

Place: Delhi

Amarendra Pandey

(2k18/PhD/EE/503)

ABSTRACT

The PV based generation is recognized as one of the most promising RES technology and large scale implementation projects in various countries demonstrate this trend. Due to such large scale PV integration, power systems are growing in size and getting complex. Moreover, the use of other renewable energy sources such as wind has also seen an upswing and further trends also show significant increase in power electronic based loads thereby affecting the nature and performance of power systems. Moreover, today's power distribution system face greater challenges like power quality (PQ), efficiency and reliability to maintain grid stability and reliability because of high penetration of PV. It is a major challenge to supply reliable and good quality power round the clock. Voltage fluctuations, voltage imbalance, voltage sag, harmonics and transients are all well-known PQ issues that impair power system performance even in the wake of contemporary technological advancements.

Traditional cost effective solutions include passive filters; however fast and accurate control within 1-2 cycles and transition from lagging to leading vars is possible only using shunt compensators. Voltage source converter (VSC) can be used as shunt compensators to enhance the system's power quality and minimize issues including harmonics, reactive power burden, low power factor, and load unbalancing. New grid code requirements stipulate that the DG system including PV, vehicle to grid and wind turbine system shall contribute to grid stability and services as well as deliver active power to grid.

The proposed work's objective is to develop and design techniques for improving the quality of power supplied to non-linear loads by single-phase and three-phase systems during normal and abnormal grid conditions including low voltage ride through operation. To achieve these objectives, several control algorithms have been developed for improving power quality and LVRT operation. The control methods require the feed forward term, DC-link voltage controllers, synchronization techniques, estimation of the basic component of load current and reference active and reactive power based on magnitude of voltage sag during LVRT operation. Extensive simulation and experimental investigations have been conducted to assess the effectiveness of the system and the

control algorithms. Conventional control techniques viz Synchronous Reference frame Theory (SRFT) and Second Order generalized Integrator (SOGI) have been initially tested on the prototype system developed in the laboratory.

Two new control algorithms for single phase and three phase single stage grid connected PV system which includes self-adaptive Batmen Polynomial (BP) and Radial Basis Function Neural Network (RBFNN) algorithm for active power injection and reactive power compensation. The H-bridge inverters are employed as a SAPF to mitigate many power quality issues and achieve load compensation in single-phase and three-phase systems feeding a range of linear and non-linear loads. Detailed simulation results are recorded and verification of these results on the experimental setup is performed. Simulation has been performed in MATLAB/SIMULINK environment.

PQ problems in three phase distribution system under distorted grid condition have been studied. The control algorithms developed for this system are Levenberg Marquardt (LM) trained SOGI filter with unit template synchronization method and conductance-based control algorithm with D-SOGI based synchronization method. Detailed simulation results are recorded and verification of these results on the experimental setup is performed. Simulation has been performed in MATLAB/SIMULINK environment.

Next, the operation and grid requirement of single phase system during LVRT mode of operation. The designed controllers include adaptive Laguerre polynomial (LP) and Sliding Window Recursive Discrete Fourier Transform (SWRDFT) based controller. The experimental setup has been controlled using dSPACE 1104. Experimental results of all techniques have been analyzed in details.

The operation and grid requirement of three-phase system during LVRT mode of operation includes the design and development of a (Gegenbuer Polynomial) GP function-based and Load power based controller for LVRT and UPF mode of operation. The developed controllers have been equipped with enhanced LVRT capabilities and respond quickly and correctly to changing system conditions. Simulation and experimental results of all techniques have been analyzed in details.

TABLE OF CONTENTS

<i>Declaration</i>	<i>i</i>
<i>Certificate</i>	<i>ii</i>
<i>Acknowledgements</i>	<i>iii-iv</i>
<i>Abstract</i>	<i>v-vi</i>
<i>Table of Contents</i>	<i>vii-xiii</i>
<i>List of Figures</i>	<i>xiv-xxiv</i>
<i>List of Tables</i>	<i>xxv</i>
<i>List of Abbreviations</i>	<i>xxvi-xxvii</i>

Chapter-1: Introduction

1.1 General	1
1.2 Relevance of PQ in Modern Distribution System	3
1.3 Power Quality Issues	4-6
1.3.1 Voltage Sag and Swell	
1.3.2 Short Voltage Interruption	
1.3.3 Large Voltage Interruption	
1.3.4 Voltage Flicker	
1.3.5 Voltage Spikes	
1.3.6 Harmonics Distortion in Voltage and Current	
1.3.7 Poor Power Factor	
1.3.8 Unbalanced Voltage and Currents	
1.3.9 Voltage Fluctuation	
1.4 State of The Art Techniques in PQ	6
1.5 Objective of Proposed Work	7-9
1.5.1 Design of Single-Phase and Three-Phase System	
1.5.2 Mitigation of PQ issues in Single-Phase and Three-Phase Grid	

Connected PV System	
1.5.3 PQ Issues During Distorted Grid Condition	
1.5.4 LVRT and FRT Capability of System	
1.6 Outline of Thesis	10-11
Chapter-2: Literature Survey	
2.1. General Introduction	12
2.2. Survey on Various Power Quality (PQ) issues	12-14
2.3. Survey on Adaptive Control Algorithms for VSC	14-16
2.4. Survey on Grid Connected PV System	16-17
2.5. Survey on Control Techniques for LVRT Capability	17-21
2.6. Research Gap	21
2.7. Research Objective	22
2.8. Conclusion	22
Chapter-3: Design and Development of Three-Phase and Single-Phase Shunt Active Power Filter (SAPF) Grid Connected PV System	
3.1.Introduction	23
3.2.Design and Development of Proposed Single-Phase VSC System	23-35
3.2.1. Calculation of DC Link Reference Voltage	
3.2.2. Design of DC Link Capacitor	
3.2.3. Design of Interfacing Inductor	
3.2.4. Design of Hysteresis Current Controller (HCC)	
3.2.5. Modeling and Stability Analysis of Single Phase Converter	
3.2.6. Modeling of PV Array	
3.2.7. Design of DC-DC Boost Converter	
3.3 Design and Development of Three-Phase VSC System	36-40
3.3.1 Calculation of DC-Link Voltage	
3.3.2 Design of DC-Link Capacitor	
3.3.3 Design of Interfacing Inductor	
3.4 Design and Development of Sensor Circuit	40-43
3.4.1 Current Sensor Circuit	
3.4.2 Voltage Sensor Circuit	

3.5 Design of Level Shifter for IGBT Driver	43-44
3.6 Single Phase Experimental Setup	45
3.7 Three-Phase Experimental Setup	45
3.8 Conclusion	46
Chapter-4: Power Quality Improvement Techniques in Single and Three Phase Grid Connected PV System	
4.1 Introduction	47
4.2 Basic Compensation Principle of Active Filter	47-48
4.3 Conventional Techniques for Extraction of Fundamental load Component in Single-Phase and Three-Phase System	48-53
4.3.1 Synchronous Reference Frame (SRF) Techniques	
4.3.2 Second Order Generalized Integrator(SOGI) Filter	
4.4 Techniques for Extraction of Fundamental load Component in Single-Phase and Three-Phase System	54-59
4.1.1 RBFNN Controller	
4.1.2 Bateman Polynomial based Controller	
4.5 PV Curves and Maximum Power Point Tracking (MPPT) Operation	59-62
4.6 Feed-Forward Current Estimation	62-63
4.7 Loss Component Estimation	63
4.8 Generation of Switching Pulses	63-64
4.9 Performance Analysis of Single-Phase and Three-Phase System	65-86
4.9.1 Simulation Performance of Single Phase System	65-76
4.9.1.1 Simulation Performance with SRF Technique of Single Phase System	
4.9.1.2 Simulation Performance with SOGI Algorithm for Single Phase System	
4.9.1.3 Simulation Performance with BP Controller of Single Phase System	
4.9.1.4 Simulation Performance with RBFNN Controller of Single Phase System	
4.9.2 Simulation Performance of Three Phase System	76-86

4.9.2.1	Simulation Performance with SRF Technique of Three Phase System	
4.9.2.2	Simulation Performance with SOGI Algorithm for Three-Phase System	
4.9.2.3	Simulation Performance with BP Controller of Three-Phase System	
4.9.2.4	Simulation Performance with RBFNN Controller of Three-Phase System	
4.10	Comparison	87-88
4.11	Experimental Performance	88-111
4.11.1	Single Phase Performance	89-100
4.11.1.1	Experimental Performance with SRF Technique of Single Phase System	
4.11.1.2	Experimental Performance with SOGI Algorithm for Single Phase System	
4.11.1.3	Experimental Performance with BP Controller of Single Phase System	
4.11.1.4	Experimental Performance with RBFNN Controller of Single Phase System	
4.11.2	Three Phase performance	100-111
4.11.2.1	Experimental Performance with SRF Technique of Three Phase System	
4.11.2.2	Experimental Performance with SOGI Algorithm for Three-Phase System	
4.11.2.3	Experimental Performance with BP Controller of Three-Phase System	
4.11.2.4	Experimental Performance with RBFNN Controller of Three- Phase System	
4.12	Conclusions	112

Chapter-5: SAPF Operation Under Polluted Grid Condition of Three-Phase System

5.1.	Introduction	113
5.2.	Unit Template Calculation from Polluted Grid in Three Phase System	113-119
5.2.1	Unit Template for Three-Phase System	113-116
5.2.1.1	Simulation Performance of Unit Template Method	
5.2.2	D-SOGI for three phase	116-119
5.2.2.1	Simulation Performance of D-SOGI Filter	
5.3.	VSC Operation of Three-Phase System Under Polluted Grid Condition	119-125
5.3.1.	Three-Phase Levenberg Marquardt(LM) trained SOGI Filter	120-123
5.3.2.	Conductance based Control Algorithm	123-125
5.4.	Performance Analysis of Three Phase System under Normal and Distorted Grid Condition	125-138
5.4.1.	Simulation Performance	125-130
5.4.1.1.	Simulation Performance of LM Trained SOGI	
5.4.1.2.	Simulation Performance of Conductance Based Algorithm	
5.4.2.	Experimental Performance	130-138
5.4.2.1.	Experimental Performance of LM Trained SOGI	
5.4.2.2.	Experimental Performance of Conductance Based Algorithm	
5.5.	Comparison	138-139
5.6.	Conclusion	139-140

Chapter-6: LVRT Operation of Single-Phase System

6.1.	Introduction	141
6.2.	Grid Codes for Single Phase System for Low Voltage Ride Through Operation (LVRT)	142-143
6.3.	Low Voltage Ride Through Operation in Single-Phase System	143-144
6.4.	Reference Current Generation Control Techniques	144-161
6.4.1.	Laguerre Polynomial(LP) based Controller	144-152
6.4.1.1.	Mathematical Formulation of LP Control Techniq	

6.4.1.2.	Unit Template Calculation	
6.4.1.3.	Estimation of Reference Current in Normal Mode	
6.4.1.4.	Estimation of Reference Current in LVRT Mode	
6.4.1.5.	Switching Pulse Generation	
6.4.2.	SWRDFT Control Technique	152-158
6.4.2.1.	Mathematical Design of SWRDFT controller	
6.4.2.2.	Estimation of Reference Current	
6.4.2.3.	Active Power Component	
6.4.2.4.	Reactive Power Component	
6.4.3.	SOGI based Controller	158-161
6.4.3.1.	Reference Current Generation	
6.5.	Simulation Performance Analysis	161-169
6.5.1.	Simulation Performance of Laugerre Polynomial Based Control Technique	161-164
6.5.2.	Simulation Performance of SWRDFT Control Technique	164-166
6.5.3.	Comparison of Proposed LP and SWRDFT control Technique	166-169
6.6.	Comparison	169-170
6.7.	Experimental Performance	171-177
6.7.1.	Operation in Normal Mode Without PV Integration	171-173
6.7.2.	Operation in Normal Mode condition with Integrated PV	173-175
6.7.3.	Operation under Abnormal grid Condition	176-177
6.8.	Conclusion	177

Chapter-7: LVRT Operation of Three-Phase System

7.1.	Introduction	178
7.2.	System Description of Three-Phase System	178-179
7.3.	Reference Current generation control Techniques	179-190
7.3.1.	Gagenbuer Polynomial based Controller	180-182
7.3.2.	Load Power based Adaptive Controller	182-185
7.3.3.	SOGI based Controller	185-186
7.3.4.	Switching Loss Component Extraction	187

7.3.5.	Operation during Voltage Sa	187-188
7.3.6.	Reference Current Generation	188-190
7.3.6.1.	Active Power Component	
7.3.6.2.	Reactive Power Component	
7.4.	Simulation Result and Discussion	190-198
7.4.1.	Simulation Result with GP Controller	190-193
7.4.2.	Simulation Result of Load Power Based Controller	193-195
7.4.3.	Simulation Performance of SOGI based Controller	195-198
7.4.4.	Comparison of proposed GP and Load Power based Control Technique	198-199
7.5.	Experimental Performance	198-204
7.6.	Conclusion	204-205
Chapter-8: Conclusion and Future Scope		
8.1.	Conclusion	206-209
8.2.	Future Scope	209
References		
APPENDIX		

LIST OF FIGURES

Fig.1.1	Abnormal condition in the grid voltage
Fig.2.1	LVRT Curves as per grid codes of different countries
Fig.3.1(a)	Single phase VSC controlled as a compensator
Fig.3.1(b)	Matlab based simulation model of single phase system
Fig.3.2	Single phase VSC with single-stage grid connected PV system
Fig.3.3	Single phase VSC with double-stage grid connected PV system
Fig.3.4	Operation of fixed band HCC loop
Fig.3.5	Working of hysteresis current controller
Fig.3.6	Representation of Active Filter Model
Fig. 3.7	Step response of the system corresponding to different gain parameters
Fig.3.8	Bode plot of voltage control loop with different values of gain
Fig.3.9	Single Diode model of PV array
Fig. 3.10	DC-DC boost converter
Fig.3.11(a)	Configuration of three phase grid VSC system
Fig.3.11(b)	Matlab model of three phase system
Fig. 3.12	Three-phase VSC with single-stage grid connected PV system
Fig.3.13	Three-phase VSC with double-stage grid connected PV system
Fig.3.14	Connection diagram of current sensor
Fig.3.15(a)	Schematic diagram of current sensing circuit
Fig. 3.15(b)	Experimental circuit of current sensor circuit
Fig.3.16	Connection diagram of voltage sensor
Fig.3.17(a)	Schematic diagram of voltage sensor circuit
Fig.3.17(b)	Experimental Circuit of voltage sensor circuit
Fig. 3.18(a)	Schematic diagram of gate driving circuit
Fig. 3.18(b)	Practical Implementation of amplification circuit driver circuit
Fig.3.19	Experimental setup of single phase single-stage grid connected PV system
Fig.3.20	Experimental setup of three phase VSC system
Fig.4.1	Basic diagram of shunt active filter (SAPF) for current harmonic compensation
Fig.4.2(a)	SRFT Control technique for single phase system
Fig.4.2(b)	SRFT control technique for three phase system
Fig.4.3(a)	SRFT simulation model for single phase system
Fig.4.3(b)	SRFT simulation model for three phase system

- Fig.4.4(a)** Design of SOGI filter with gain constant ‘k’
- Fig.4.4(b)** Matlab based SOGI model
- Fig.4.5** Root locus of SOGI filter
- Fig.4.6** Bode diagram of SOGI filter using Eq.4.3 different values of ‘k’
- Fig.4.7** Step response of SOGI filter for different values of gain ‘k’
- Fig. 4.8(a)** Block diagram of General RFNN Model
- Fig.4.8(b)** Block diagram of proposed RFNN single neuron based model
- Fi g.4.8(c)** Simulation model of RBFNN controller
- Fig.4.9(a)** Proposed BP polynomial based adaptive controller
- Fig.4.9(b)** Simulation model of adaptive BP controller
- Fig.4.10(a)** IV and PV curves for different values of irradiance at temperature 25⁰C
- Fig4.10(b)** IV and PV curve on different value of temperature at 1000W/m²
- Fig. 4.11** Flowchart of P & O MPPT algorithm[167]
- Fig.4.12** Switching Pulse Generation
- Fig.4.13** Intermediate performance of SRF technique (a) load current (i_L), (b) load current d- component (i_{Ld}), (c) load current quadrature q-component (i_{Lq}) (d) output fundamental weight
- Fig.4.14** Layout of VSC controlled using SRF technique for single phase system
- Fig.4.15** Simulation performance of single phase VSC controlled by SRF showing (a) source voltage, V_s (b) source current, I_s (c) load current, I_L (d) converter current, I_C (e) dc link voltage, V_{DC} (f) irradiance(W/m²)
- Fig.4.16** THD performance of SRF in single phase system (a) source voltage v_s (b) source current i_s (c) load current i_L
- Fig.4.17** Intermediate performance of SOGI filter (a) load current (i_L), (b) in-phase component of load current (i_{Ld}), (c) quadrature phase component (i_{Lq}) (d) output weight.

- Fig.4.18** Layout of VSC controlled using SOGI technique for single phase system
- Fig.4.19** Simulation performance of SOGI in single phase system showing (a) source voltage, V_s (b) source current, I_s (c) load current, I_L (d) converter current, I_C (e) dc link voltage, V_{DC} (f) irradiance(W/m^2)
- Fig.4.20** THD performance of SOGI controller in single phase system (a) source voltage v_s (b) source current i_s (c) load current i_L
- Fig.4.21** Intermediate performance of BP controller (a) load current (i_L), (b) direct axis component of load current (i_{Ld}), (c) quadrature axis component (i_{Lq}) (d) output weight.
- Fig.4.22** Layout of VSC controlled using adaptive BP technique for single phase system
- Fig.4.23** Simulation performance of adaptive BP in single phase system showing (a) source voltage, V_s (b) source current, I_s (c) load current, I_L (d) converter current, I_C (e) dc link voltage, V_{DC} (f) irradiance(W/m^2)
- Fig.4.24** THD performance of adaptive BP controller in single phase system (a) source voltage v_s (b) source current i_s (c) load current i_L
- Fig.4.25** Intermediate performance of proposed RBFNN controller (a) load current (b) desired weight (c) output weight (d) error function
- Fig.4.26** Layout of VSC controlled using adaptive RBFNN technique for single phase system
- Fig.4.27** Performance of controller showing (a) source voltage, V_s (b) source current, I_s (c) load current, I_L (d) converter current, I_C (e) DC link voltage, V_{DC} (f) fundamental weight, FW
- Fig.4.28** THD performance of SOGI controller in single phase system (a) source voltage v_s (b) load current i_L (c) source current i_s
- Fig.4.29** Three phase SRF control structure
- Fig.4.30(a)** Simulation performance of three phase SAPF controlled by SRF showing (a) source voltage, V_{Sabc} (b) source current, I_{Sabc} (c) load current, I_{Labc} (d) converter current, I_{Cabc} (e) dc link voltage, V_{DC}

- Fig.4.30(b)** Simulation performance of three phase SAPF controlled by SRF showing (a) source voltage, V_{Sabc} (b) source current, I_{Sabc} (c) load current, I_{Labc} (d) converter current, I_{Cabc} (e) dc link voltage, V_{DC} (f) irradiance (W/m^2)
- Fig.4.31** THD performance of SRF in three phase system (a) source voltage v_s (b) source current i_s (c) load current i_L
- Fig.4.32** Three phase SOGI control structure
- Fig.4.33(a)** Simulation performance of three phase system controlled by SOGI filter showing (a) source voltage, V_{Sabc} (b) source current, I_{Sabc} (c) load current, I_{Labc} (d) converter current, I_{Cabc} (e) dc link voltage, V_{DC}
- Fig.4.33(b)** Simulation performance of three phase system controlled by SOGI filter showing (a) source voltage, V_{Sabc} (b) source current, I_{Sabc} (c) load current, I_{Labc} (d) converter current, I_{Cabc} (e) dc link voltage, V_{DC} (f) irradiance (W/m^2)
- Fig.4.34** THD performance of SOGI controller in three phase system (a) source voltage v_s (b) source current i_s (c) load current i_L
- Fig.4.35** Three phase adaptive BP control structure
- Fig.4.36(a)** Simulation performance of adaptive BP controller for three phase system showing (a) source voltage, V_{Sabc} (b) source current, I_{Sabc} (c) load current, I_{Labc} (d) converter current, I_{Cabc} (e) dc link voltage, V_{DC}
- Fig.4.36(b)** Simulation performance of adaptive BP controller for three phase system showing (a) source voltage, V_{Sabc} (b) source current, I_{Sabc} (c) load current, I_{Labc} (d) converter current, I_{Cabc} (e) dc link voltage, V_{DC} (f) irradiance (W/m^2)
- Fig.4.37** THD performance of adaptive BP controller in three phase system (a) source voltage v_s (b) source current i_s (c) load current i_L
- Fig.4.38** Structure of proposed RBFNN controlled three phase VSC
- Fig.4.39** Simulation performance of three phase system controlled by proposed RBFNN showing (a) source voltage, V_{Sabc} (b) source current, I_{Sabc} (c) load current, I_{Labc} (d) converter current, I_{Cabc} (e) dc link voltage, V_{DC}
- Fig.4.40** Simulation performance of three phase system controlled by proposed RBFNN showing (a) source voltage, V_{Sabc} (b) source current, I_{Sabc} (c) load current, I_{Labc} (d) converter current, I_{Cabc} (e) dc link voltage, V_{DC} (f)

irradiance(W/m²)

- Fig.4.41** THD performance of proposed RBFNN in three phase system
- Fig.4.42** Comparison of fundamental weights using (a) SRF (b) SOGI (c) BP and (d) RBFNN
- Fig.4.43** Intermediate performance of SRF control technique showing (a) load current (i_L) (b) direct axis component (I_{Ld}) (c) quadrature axis component (I_{Lq}) (c) output weight
- Fig.4.44** Steady state waveforms of single phase system showing (a) source voltage (v_S) and load current (i_L) (b) source voltage (v_S) and source current (i_S) (c) THD of v_S (2.04%) and i_L (33.61%)(d) THD of v_S (2.07%) and i_S (4.99%)
- Fig.4.45** Dynamic performance of SRFT without PV for single phase system showing (a) ($v_S, i_S, output\ weight, V_{dc}$) (b) (v_S, i_S, i_L, i_c)
- Fig.4.46** Dynamic performance of SRFT with PV for single phase system showing (a) (v_S, i_S, i_L, i_c) (b) (v_S, i_S, I_{pv}, V_{dc})
- Fig.4.47** Intermediate performance of SOGI filter showing (a) load current (i_L), (b) in-phase component of load current ($i_{L\alpha}$), (c) quadrature phase component of load current ($i_{L\beta}$) (d) output weight
- Fig.4.48** Steady state waveforms of single phase system showing (a) Source Voltage (v_S) and load current (i_L) (b) Source Voltage (v_S) and source current (i_S) (c) THD of v_S (1.81%) and i_L (33.64%) (d) THD of v_S (1.75%) and i_S (4.71%)
- Fig.4.49** Dynamic performance of SOGI without PV for single phase system showing (a) ($v_S, i_S, output\ weight, V_{dc}$) (b) (v_S, i_S, i_L, i_c)
- Fig.4.50** Dynamic performance of SOGI with PV for single phase system showing (a) (v_S, i_S, i_L, i_c) (b) (v_S, i_S, I_{pv}, V_{dc})
- Fig.4.51** Intermediate performance of BP controller showing (a) load current (i_L), (b) desired fundamental weight of load current, (c) output fundamental weight of load current(d) output error.
- Fig.4.52** Steady state waveforms of single phase system showing (a) source voltage (v_S) and load current (i_L) (b) source voltage (v_S) and source current (i_S) (c) THD of v_S (2.50%) and i_L (29.08%) (d) THD of v_S (1.65%) and i_S (4.65%)

- Fig.4.53** Dynamic performance of BP controller without PV for single phase system showing (a) $(v_s, i_s, \text{output weight}, V_{dc})$ (b) (v_s, i_s, i_L, i_c)
- Fig.4.54** Dynamic performance of BP controller with PV for single phase system showing (a) (v_s, i_s, i_L, i_c) (b) $(v_s, i_s, I_{pv}, V_{dc})$
- Fig.4.55** Intermediate performance of proposed RBFNN controller
- Fig.4.56** Steady state waveforms of single phase system showing (a) source voltage (v_s) and load current (i_L) (b) source voltage (v_s) and source current (i_s) (c) THD of v_s (1.97%) and i_L (33.54%) (d) THD of v_s (1.88%) and i_s (4.58%)
- Fig.4.57** Dynamic performance of proposed RBFNN controller without PV for single phase system showing (a) $(v_s, i_s, \text{output weight}, V_{dc})$ (b) (v_s, i_s, i_L, i_c)
- Fig.4.58** Dynamic performance of proposed RBFNN controller with PV for single phase system showing (a) (v_s, i_s, i_L, i_c) (b) $(v_s, i_s, I_{pv}, V_{dc})$
- Fig.4.59** Steady state waveforms of three phase system showing (a) source voltage (v_{Sabc}) and load current (i_{Labc}) (b) source voltage (v_{Sabc}) and source current (i_{Sabc}) (c) THD of v_{Sabc} (2.11%) and i_{Labc} (22.78%) (d) THD of v_{Sabc} (1.19%) and i_{Sabc} (6.59%)
- Fig.4.60** Dynamic performance of SRFT without PV for three phase system showing (a) $(v_{sa}, i_{sa}, \text{output weight}, V_{dc})$ (b) $(V_{dc}, i_{sa}, i_{La}, i_{Ca})$ (c) $(v_{sa}, i_{La}, i_{Lb}, i_{Lc})$ (d) $(v_{sa}, i_{sa}, i_{sb}, i_{sc})$
- Fig.4.61** Dynamic performance of SRFT with PV for three phase system showing (a) $(v_{sa}, i_{sa}, i_{La}, i_{Ca})$ (b) $(v_{sa}, i_{sa}, I_{pv}, V_{dc})$
- Fig.4.62** Steady state waveforms of three phase system showing (a) source voltage (v_{Sabc}) and load current (i_{Labc}) (b) source voltage (v_{Sabc}) and source current (i_{Sabc}) (c) THD of v_{Sabc} (1.41%) and i_{Labc} (24.03%) (d) THD of v_{Sabc} (1.07%) and i_{Sabc} (3.25%)
- Fig.4.63** Dynamic performance of SOGI controller without PV for three phase system showing (a) $(v_{sa}, i_{sa}, \text{output weight}, V_{dc})$ (b) $(V_{dc}, i_{sa}, i_{La}, i_{Ca})$ (c) $(v_{sa}, i_{La}, i_{Lb}, i_{Lc})$ (d) $(v_{sa}, i_{sa}, i_{sb}, i_{sc})$
- Fig.4.64** Dynamic performance of SOGI controller with PV for three-phase system

showing (a) $(v_{sa}, i_{sa}, i_{La}, i_{ca})$ showing (b) $(v_{sa}, i_{sa}, I_{pv}, V_{dc})$

- Fig.4.65** Steady state waveforms of three phase system showing (a) source voltage (v_{Sabc}) and load current (i_{Labc}) (b) source voltage (v_s) and source current (i_{Sabc}) (c) THD of v_{Sabc} (2.07%) and i_{Labc} (22.40%)(d) THD of v_{Sabc} (1.31%) and i_{Labc} (3.87%)
- Fig.4.66** Dynamic performance of SRFT without PV for three phase system showing (a) $(v_{sa}, i_{sa}, output\ weight, V_{dc})$ (b) $(V_{dc}, i_{sa}, i_{La}, i_{ca})$ (c) $(v_{sa}, i_{La}, i_{Lb}, i_{Lc})$ (d) $(v_{sa}, i_{sa}, i_{sb}, i_{sc})$
- Fig.4.67** Dynamic performance of SRFT with PV for three phase system showing (a) $(v_{sa}, i_{sa}, i_{La}, i_{ca})$ (b) $(v_{sa}, i_{sa}, I_{pv}, V_{dc})$
- Fig.4.68** Steady state waveforms of three phase system showing (a) source voltage (v_{Sabc}) and load current (i_{Labc}) (b) source voltage (v_{Sabc}) and source current (i_{Sabc}) (c) THD of v_{Sabc} (2.30%) and i_{Labc} (23.77%)(d) THD of v_{Sabc} (1.47%) and i_{Sabc} (2.63%)
- Fig.4.69** Dynamic performance of proposed RBFNN controller without PV for three phase system showing (a) $(v_{sa}, i_{sa}, output\ weight, V_{dc})$ (b) $(V_{dc}, i_{sa}, i_{La}, i_{ca})$ (c) $(v_{sa}, i_{La}, i_{Lb}, i_{Lc})$ (d) $(v_{sa}, i_{sa}, i_{sb}, i_{sc})$
- Fig.4.70** Dynamic performance of proposed RBFNN controller with PV for three phase system showing (a) $(v_{sa}, i_{sa}, i_{La}, i_{ca})$ (b) $(v_{sa}, i_{sa}, I_{pv}, V_{dc})$
- Fig.5.1(a)** Structure of SOGI based unit template technique for three-phase system
- Fig.5.1(b)** Simulation model of SOGI based unit template technique for three-phase system
- Fig.5.2(a)** Simulation performance of conventional unit template method for three phase system
- Fig.5.2(b)** Simulation performance of SOGI based unit template method for three phase system
- Fig.5.3(a)** D-SOGI structure for three-phase system to extract positive and negative voltage components
- Fig.5.3(b)** Simulation model of D-SOGI structure for three-phase system to extract positive and negative voltage components

- Fig.5.4** Simulation performance of D-SOGI for three phase system
- Fig.5.5** Three Phase System Representation
- Fig.5.6(a)** Proposed LM Trained SOGI Control Scheme
- Fig.5.6(b)** Simulation model of LM trained SOGI control scheme for phase-‘a’
- Fig.5.7** Design of LM trained adaptive SOGI for phase-‘a’
- Fig.5.8(a)** Conductance Based Control Algorithm with DSOGI block for distorted grid condition
- Fig.5.8(b)** Simulation model of conductance based control algorithm with DSOGI block for distorted grid condition
- Fig.5.9** Intermediate performance of LM SOGI
- Fig.5.10(a)** Simulation performance of LM SOGI showing (a) source voltage, v_{Sabc} (b) reference current, i_{Rabc} (c) source current, i_{Sabc} (d) load current, I_{Labc} (e) converter current, i_{Cabc} (f) output weight (g) DC link voltage, V_{DC}
- Fig.5.10(b)** Simulation performance of LM SOGI showing (a) source voltage, v_{Sabc} (b) reference current, i_{Rabc} (c) source current, i_{Sabc} (d) load current, I_{Labc} (e) converter current, i_{Cabc} (f) output weight (g) DC link voltage, V_{DC}
- Fig.5.11** THD performance of LM SOGI (a) source voltage v_s (b) load current i_L (c) source current i_s
- Fig.5.12(a)** Simulation performance of conductance based controller showing (a) source voltage, v_{Sabc} (b) reference current, i_{Rabc} (c) source current, i_{Sabc} (d) load current, I_{Labc} (e) converter current, i_{Cabc} (f) load conductance (g) DC link voltage, V_{DC}
- Fig.5.12(b)** Simulation performance of conductance based controller showing (a) source voltage, v_{Sabc} (b) reference current, i_{Rabc} (c) source current, i_{Sabc} (d) load current, i_{Labc} (e) converter current, i_{Cabc} (f) load conductance (g) DC link voltage, V_{DC}
- Fig.5.13** THD performance of conductance based controller (a) source voltage v_s (b) load current i_L (c) source current i_s
- Fig.5.14** Experimental intermediate performance of LM SOGI showing (a) load current (i_L), (b) in-phase component of load current ($i_{L\alpha}$), (c) error (e(t)) and (d) output weight
- Fig.5.15** Steady state waveforms under normal grid system showing (a) source voltage (v_{Sabc}) and load current (i_{Labc}) (b) THD of v_{Sabc} and i_{Labc} (c) source voltage (v_{Sabc}) and source current (i_{Sabc}) (d) THD of v_{Sabc} and i_{Sabc}
- Fig.5.16** Steady state waveforms under distorted grid system showing (a) source voltage (v_{Sabc}) and load current (i_{Labc}) (b) THD of v_{Sabc} and i_L (c) source voltage (v_{Sabc}) and source current (i_{Sabc}) (d) THD of v_{Sabc} and i_{Sabc}
- Fig.5.17** Dynamic performance of LM trained SOGI for three phase system showing

- (a) $(v_{sa}, i_{Ra}, i_{sa}, i_{La}, \text{output weight}, V_{dc})$ (b) $(v_{sa}, i_{sa}, i_{sb}, i_{sc})$ (c) $(v_{sa}, i_{sa}, \text{output weight}, V_{dc})$
- Fig.5.18** Intermediate performance conductance based controller showing (a) distorted source voltage (v_{sa}), (b) load current (i_L), (c) load conductance and (d) total load power
- Fig.5.19** Steady state waveforms normal grid system showing (a) source voltage (V_S) and load current (I_L) (b) THD of V_S and I_L (c) source voltage (V_S) and source current (I_S) (d) THD of V_S and I_S
- Fig.5.20** Steady state waveforms distorted grid system showing (a) source voltage (V_S) and load current (I_L) (b) THD of V_S and I_L (c) source voltage (V_S) and source current (I_S) (d) THD of V_S and I_S
- Fig.5.21** Dynamic performance of conductance based controller for three phase system showing (a) $(v_{sa}, i_{Ra}, i_{sa}, i_{La})$ (b) $(v_{sa}, i_{sa}, i_{sb}, i_{sc})$ (c) $(v_{sa}, i_{sa}, \text{load conductance}, V_{dc})$
- Fig.6.1(a)** LVRT Curves as per grid codes of different countries
- Fig.6.1(b)** Proposed single phase system description
- Fig.6.2(a)** Block diagram representation of the proposed LP controller
- Fig.6.2(b)** Simulation model of LP controller
- Fig.6.3** Diagram indicating switchover between the modes of operation
- Fig.6.4** Flowchart showing the selection of reference powers for designed controller
- Fig.6.5(a)** Control layout based on SWRDFT controller
- Fig.6.5(b)** Simulation Model of SWRDFT controller
- Fig.6.6** SWRDFT controller showing (a) filter interpretation of STFT (b) block diagram of SWRDFT technique (c) equivalent structure of SWRDFT (d) block diagram of SWRDFT based technique
- Fig.6.7** Flowchart showing the selection for reference powers for the designed controller
- Fig.6.8(a)** Design of Adaptive SOGI filter
- Fig.6.8(b)** Simulation Model of SOGI based Controller
- Fig.6.8(c)** Switching Pulse generator Based on SOGI Controller
- Fig.6.9(a)** Intermediate Performance of LP based controller
- Fig.6.9(b)** Simulation performance of LP controller during normal mode operation showing (a) source voltage (v_s), (b) source current (i_s), (c) source reactive power (Q_s) (d) generated PV power P_{PV}
- Fig.6.9(c)** Simulation performance of LP controller during LVRT operation showing (a) source voltage v_s , (b) source current i_s , (c) per unit voltage V_{PU} , (d) inverter active power P_{inv} , (e) inverter reactive power Q_{inv} (f) DC link voltage V_{DC}
- Fig.6.10(a)** Intermediate performance of SWRDFT based controller

- Fig.6.10(b)** Simulation performance of system using SWRDFT control during normal operation showing (a) source voltage (v_s) , (b) source current (i_s), (c) source reactive power (Q_s) (d) generated PV power P_{PV}
- Fig.6.10(c)** Simulation performance of SWRDFT during LVRT operation showing (a) source voltage v_s , (b) source current i_s , (c) per unit voltage V_{PU} , (d) inverter active power P_{inv} , (e) inverter reactive power Q_{inv} (f) DC link voltage V_{DC}
- Fig.6.11(a)** Intermediate performance of SOGI based controller
- Fig.6.11(b)** Simulation performance of system using SOGI control during normal operation showing (a) source voltage (v_s) , (b) source current (i_s), (c) source reactive power (Q_s) (d) generated PV power P_{PV}
- Fig.6.11(c)** Simulation performance of SWRDFT during LVRT operation showing (a) source voltage v_s , (b) source current i_s , (c) per unit voltage V_{PU} , (d) inverter active power P_{inv} , (e) inverter reactive power Q_{inv} (f) DC link voltage V_{DC}
- Fig.6.12** Comparison of Fundamental Weight with different controllers
- Fig.6.13** Intermediate performance of LP controller
- Fig.6.14** Waveforms showing (a) source voltage (v_s) and grid current (i_s) (b) source voltage(v_s) and load current (i_L) (c) THD of v_s (1.87%) and i_L (27.54%)(d) THD of v (1.87%) and i_s (3.94%) for harmonic reduction
- Fig.6.15** Dynamic response during load increase using LP controlled VSC showing $v_s, i_s, i_L, i_{ref}, i_{L(rms)}, \mu_{Load}, V_{DC}$
- Fig.6.16** Waveforms showing (a) source voltage (v_s) and load current (i_L) (b) load power demand (P_L, Q_L) (c) Source Voltage (v_s)and grid current (i_s) (d) power supplied to the grid
- Fig.6.17(a)** Response of LP controlled SAPF integrated with PV
- Fig.6.17(b)** IV and PV curves for PV module indicating MPPT operation point in normal mode of operation
- Fig.6.18** Response of LP controlled VSC in LVRT mode
- Fig.7.1** System Description of Three Phase System
- Fig.7.2(a)** Proposed GP polynomial based adaptive control system
- Fig.7.2(b)** Simulation model of GP polynomial based adaptive controller
- Fig.7.3** Proposed load power based controller
- Fig.7.4** Matlab model of Load power based controller
- Fig.7.4** Switching loss component
- Fig.7.5(a)** Design of SOGI based controller for three phase system

Fig.7.5(b)	Simulation model of SOGI based controller
Fig.7.6	Switching loss component
Fig.7.7	Flowchart for control action under voltage sag conditions
Fig.7.8	Layout of reference current and gating pulse generation
Fig.7.9(a)	Intermediate performance of GP controller
Fig.7.9(b)	Simulation performance of GP controller under UPF mode
Fig.7.9(c)	Simulation performance of GP controller during LVRT mode
Fig.7.10(a)	Intermediate Performance of Load Power Based Controller
Fig.7.10(b)	Simulation Performance of Load Power Based controller under UPF mode
Fig.7.10(c)	Active Power and Reactive Power Demand during LVRT Mode
Fig.7.11(a)	Intermediate performance of SOGI based controller
Fig.7.11(b)	Simulation performance of SOGI based controller under UPF mode
Fig.7.11(c)	Active power and reactive power demand during LVRT mode
Fig.7.12	Comparison of Output Fundamental Weight
Fig.7.13	Intermediate Performance of GP Controller showing (a) load current of phase-a (i_{La}), (b) desired fundamental weight, (c) output fundamental weight (d) error of phase-a
Fig.7.14	Dynamics performance of phase-a during load increase ($i_{sa}, i_{La}, I_{La(rms)}, \mu_{La}$)
Fig.7.15(a)	Waveforms of source voltage (v_{Sabc}) and voltage in per unit (V_{pu})
Fig.7.15(b)	Estimation of pu voltage (V_{pu}) from three-phase source voltages (v_{Sabc}) under different sag conditions.
Fig.7.16(a)	Dynamic performance during sag (V_{pu}, P_S, Q_S, V_{DC})
Fig.7.16(b)	Performance of phase-a during transition from no-sag to sag introduction (v_{sa}, i_{sa}, Q_S)

LIST OF TABLES

Table-1.1: Recent and estimated capacity (GWp)

Table-3.1: Values of Different Parameters

Table-3.2: Choice of PI gain parameters

Table-3.3: User-defined parameters of PV array module

Table-3.4: DC-DC converter parameter selected

Table-3.5: Three-Phase VSC parameter selected

Table 4.1: Comparative Performance of different techniques

Table 4.2 Experimental Performances

Table 5.1: Comparative Performance of different techniques

Table 6.1: Comparative performance of different techniques

Table 7.1: Comparative performance of different techniques

LIST OF ABBREVIATIONS

SAPF: Shunt Active Power Filter

VCO: Voltage Controlled Oscillator

FFT: Fast Fourier Transform

PCC: Point of Common Coupling

SRFT: Synchronous Reference Frame Theory

PV: Photovoltaic

MPPT: Maximum Power Point Technique

PLL: Phase-Locked Loop

SOGI: Second-Order Generalized Integrator

VSC: Voltage Source Converter

CSI: Current Source Converter

IGBT: Insulated-Gate Bipolar Transistor

HCC: Hysteresis Current Controller

PWM: Pulse Width Modulation

THD: Total Harmonic Distortion

UPQC: Unified Power Quality Conditioner

LVRT: Low Voltage Ride Through

LP: Laguerre polynomial

LM: Levenberg Marquardt

GP: Gegenbuer Polynomial

SWRDFT: Sliding Window Recursive Discrete Fourier Transform

RBFNN: Radial Basis Function Neural Network

BP: Batmen Polynomial

FRT: Fault ride Through

Chapter-1: Introduction

1.1. General

Power demand is increasing day by day so it is imperative to increase energy sources also. Integrating renewable energy source (RES) sources into utility grid is a growing opportunity as well as a challenge [1]. The adoption of RES not only meets the energy shortfall but also reduces environmental pollution to a great extent. However, the uncertainty and intermittency of renewable energy sources need to be looked into carefully. The stability and safety of power grid (with RES energy sources) especially in case of faults need detailed studies.

Photovoltaic (PV) based power generation has been thoroughly explored and widely utilized worldwide. The PV technology has seen exponential growth from 1992 till date [1-2]. The PV based generation is recognized as one of the most promising RES technology and large scale implementation projects in various countries demonstrate this trend [2]. Medium to small scale consumers have received several incentives and government grants for adopting PV technology.

Table-1.1 shows the recent and estimated capacity of PV capacity (in GW) worldwide along with the cumulative growth in percentage points [3].

TABLE-1.1 Recent and estimated capacity (GWp)[3-4]

Year-end	2016	2017	2018	2019	2020	2021	2022	2023
Cumulative (GW)	306.5	403.3	512	633	~770	~950	~1150	~1450
Annual New(GW)	76.8	99	109	121	121-154	160-200	191	345.5
Cumulative growth(%)	32%	32%	27%	24%	24%	27%	21%	30%

Due to such large scale PV integration, power systems are growing in size and getting complex. Moreover, the use of other renewable energy sources such as wind has also seen an upswing and further trends also show significant increase in power electronic based loads thereby affecting the nature and performance of power systems [1].

PV panels show poor conversion efficiency while operating normally, and their output is non-linear and dependent on temperature and weather conditions. Thus, the maximum power point tracking (MPPT) approach is utilized to harvest maximum power with maximum efficiency from PV panels [5]. Several MPPT approaches have been proposed in the literature [5]. Perturb & Observe (P & O) MPPT method is applied in this research work because of its simplicity, strong tracking ability, accuracy and ease of implementation.

Moreover, today's power distribution system face greater challenges like power quality (PQ), efficiency and reliability to maintain grid stability and reliability because of high penetration of PV. Hence various grid codes have been proposed to regulate seamless integration of PV system with distributed grid[6]. It is a major challenge to supply reliable and good quality power round the clock. Voltage fluctuations, voltage imbalance, voltage sag, harmonics and transients are all well-known PQ issues that impair power system performance even in the wake of contemporary technological advancements. Harmonic distortion is one of the most significant concerns among these PQ issues [7-8]. Studies indicate that the degree of harmonic distortion in a system rises as the system's technology advances and consumer loads become predominantly non-linear. Such PQ problems deteriorate the supply at the consumer side as well as at the point of common coupling (PCC) for a number of reasons. Sometimes sensitive instruments in hospitals and medical equipment may malfunction because such PQ issues[9].The severity of PQ issues and the resulting economic losses has motivated engineers to search for new, improved and effective solutions for conventional PQ problems such as reactive power compensation, load unbalancing, poor power-factor and voltage regulation[10-11]. Traditional cost effective solutions include passive filters; however fast and accurate control within 1-2 cycles and transition from lagging to leading vars is possible only using shunt compensators. Voltage source converter (VSC) can be used as shunt compensators to enhance the system's power quality and minimize issues including harmonics, reactive power burden, low power factor, and load unbalancing [11].

However, a power system operator finds challenges in the operation of distributed grid due to bidirectional power flow, operation during faulty conditions and maintaining good power quality standards. Thus, more studies need to be carried on control techniques of

grid connected power converter under normal as well as faulty conditions [12]. New grid code requirements stipulate that the DG system including PV, vehicle to grid and wind turbine system shall contribute to grid stability and services as well as deliver active power to grid [13].

In case of grid malfunctioning, there may be severe impacts in the form of flickers, low voltage and poor power quality (PQ) resulting in increased losses. A voltage sag in grid connected system is a transient caused due to lightning strikes, power line short circuits, and other mishaps [14]. The islanding protection may be activated and a power outage may result if the momentary drop in grid voltage amplitude exceeds the normal voltage threshold. The stability of the grid connected PV is also affected to a certain level. Thus, the designed control strategies for power converters should be equipped to detect the fault and most importantly to react quickly to mitigate the potential adverse effect of fault to the grid side [15].

1.2. Relevance of PQ in Modern Distribution System:

The term "electric power quality" (PQ) is used to analyze and maintain the desired quality of the power [6,16]. Problems with the AC supply system can have a variety of causes, including both natural ones like lightning, flashovers, equipment failure, and faults as well as man-made ones such voltage distortions and notches. Due to their non-sinusoidal current requirement and non-linear load behavior, a number of the customer loads products also contaminate the supply system. Hence, the supply system's voltage, current, or frequency deviations—which might lead to equipment failure—are used to measure power quality [17]. The voltage at the point of common coupling (PCC), where many loads are connected, frequently shows harmonics, surges, spikes, notches, sag/dip, glitches, flickers, outages, swell, imbalance, fluctuations etc. These problems emerge in the supply system especially in the presence of nonlinear loads like furnaces, uninterruptible power supplies, and variable speed drives. Nevertheless, power quality concerns related to the current drawn from the AC mains include poor power factor, harmonic currents, reactive power load, and unbalanced currents, and harmonic currents caused by some nonlinear loads. Several methods have been developed to address these problems in either already-in-use systems or soon-to-be-constructed equipment [18]. The activities of design and

development engineers engaged in research and development (R&D) in the fields of power electronics, power systems, electric drives, digital signal processing, and sensors have changed as a result. The bulk of equipment that use power converters at the front end must properly designed in light of these recently identified demands. Depending on the nature of the loads, such as voltage-fed loads, current-fed loads, or a combination of both, a series of power filters of various types, such as passive, active, and hybrid in shunt, series, or a combination of both configurations, are used externally to mitigate power quality issues. PQ issues such as poor power factor, harmonic currents, unbalanced currents, and excessive neutral current can be solved due to these methods. Custom power devices like Distribution Static Compensators (DSTATCOMs), Dynamic Voltage Restorers (DVRs), and Unified Power Quality Conditioners (UPQCs) [19] are often used to mitigate current, voltage, or both types of power quality issues.

1.3. Power Quality Issue[6,7,20-21]:

The power distribution networks face several PQ issues. The transient and steady state categories that might be used to characterize various PQ issues are detailed in this section.

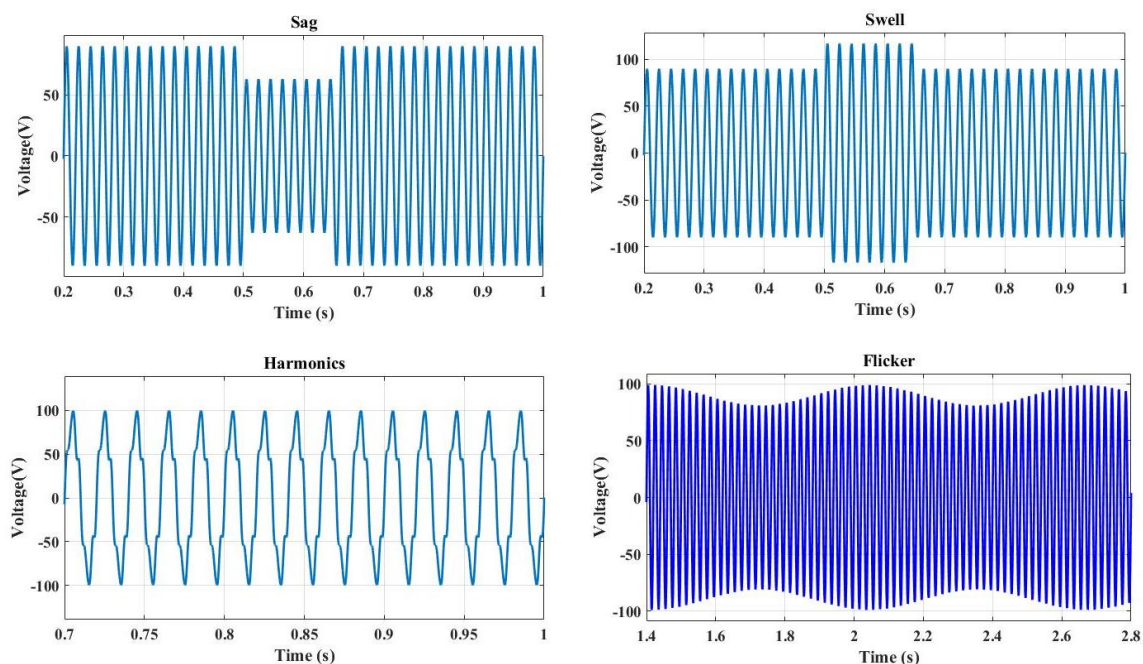


Fig.1.1 Abnormal conditions in the grid voltage

1.3.1. Voltage Sag and Swell:

Voltage sag is defined as a decrease in the root mean square (rms) value of voltage lying between 0.1 and 0.9 pu, whereas voltage swell is defined as an increase in rms value of

voltage between 1.1 and 1.8 pu at the power frequency level. Voltage rise and fall times range from 0.5 cycles to 1 minute.

1.3.2. Short Voltage Interruption:

In an electrical power system, the loss of voltage for a short time is called a voltage interruption ($\text{rms} < 0.1 \text{ pu}$). This pause can last anywhere from a half cycle to three seconds.

1.3.3. Large Voltage Interruption:

When there is no electricity for more than a minute, a "long voltage interruption" results.

1.3.4. Voltage Flicker:

A consistent voltage fluctuation that occurs at a frequency lower than the power frequency is known as voltage flicker. Voltage flicker may be caused due to load variation, short circuit faults, grid switching etc.

1.3.5. Voltage Spikes:

Voltage spikes are fast, significant fluctuations in voltage magnitude. The duration of spikes might range from a few microseconds to a few milliseconds and are usually caused by lightning strikes, grid interaction, load switching, capacitor switching, electromagnetic interference etc.

1.3.6. Harmonic Distortion in Voltage and Current:

Harmonics are integer multiples of the fundamental frequency, which for the Indian power system is 50 Hz, several nonlinear load cause harmonic such as distortion comprise integral multiple of voltage and current. In a power system, harmonic signals alter the voltage and current waveform thereby distorting them from the ideal sinusoidal waveform. Harmonic distortion is measured using the Total Harmonic Distortion (THD).

1.3.7. Poor Power Factor:

In a power distribution system, a low PF on the supply side increases the load on the supply system. This is in contrast to a situation with a Unity Power Factor (UPF) which is always preferred.

1.3.8. Unbalanced Voltage and Currents:

Unbalanced voltage or current is measured by how much the negative or zero sequence components differ from the positive sequence component. Unbalanced operation of three-

phase system is caused by voltages that are not equal. Unbalanced currents cause too much current in the system's neutral wire, which could cause equipment to malfunction.

1.3.9. Voltage Fluctuation:

The term "voltage fluctuation" refers to transient fluctuations in voltage level. Typically, this fluctuation is smaller than 0.1 pu.

1.4. State of the Art Techniques in PQ:

The control of single-phase and three-phase grid-connected PV systems with the ability to improve power quality under normal and distorted grid conditions feeding non-linear loads and assessing low voltage ride through capability under faulty grid conditions has been thoroughly discussed in the literature. PV systems have their own inherent non-linearity, it is vital to employ maximum power point tracking techniques. The researchers have proposed a few different methodologies, some of which are referred to as "Perturb and Observe" (P&O), "incremental conductance," "fuzzy-based," and "neural network-based." Due to the fact that the P&O approach is both the simplest and most successful of the bunch, it is applied in the thesis work.

The research contained in this thesis focuses on the development of appropriate controllers designed to mitigate a number of power quality concerns and provide ride-through capabilities during grid faults. The control algorithms must be capable of completing multiple tasks, including the estimation of the fundamental component, the estimation of the synchronizing signal, the estimation of the DC-link voltage controller, the estimation of the feed-forward current, and reactive power support during faulty grid conditions.

Several control-techniques have been developed to estimate the fundamental component of the load current in single-phase and three-phase systems under varying grid conditions. While developing these control algorithms, rapid response and minimum oscillations under steady-state and dynamic conditions under varied scenarios were taken into account. In both single-phase and three-phase grid connected PV systems, several techniques have been implemented to improve power quality and fault-riding capabilities in abnormal grid situations. Conventional techniques such as Synchronous reference frame theory (SRFT) and Second Order Generalized Integrator (SOGI) have been implemented. New controllers have been proposed such as adaptive Bateman Polynomial (PB) and Radial

basis function neural network (RBFNN) based on Gaussian distribution function are described in the literature. SOGI controllers and its various variants have been implemented in both single-phase and three-phase systems.

Different control strategies have been considered for the fundamental component extraction of load current under polluted grid conditions, including the Double Second Order Generalized Integrator (D-SOGI) and unit template based control strategy for three-phase systems. Maintaining the quality of the power in a polluted grid is a priority while developing and designing the controller. Levenberg Marquardt (LM) trained SOGI filter and Conductance based control approach are two of the controllers employed in this work. Similar to this, a single phase system uses SOGI based controller, Laguerre Polynomial(LP) and Fast Fourier transform-based sliding window recursive discrete Fourier(SWRDFT) transform-based approach, and in case of three-phase system uses SOGI based controller, Gagenbuer polynomial(GP) based controller and Load power-based control technique is used for PQ improvement and LVRT mode operation.

1.5. Objectives of the Proposed Work:

Based on a complete literature review of the design and development of the shunt compensator and its control methods for single-phase and three-phase systems, it has been concluded that the development of control algorithms must address a large number of considerable challenges. This result was obtained after investigating the shunt compensator's design and development. Concerns like these include things like reaction time, convergence, computing load, complexity, static error, robustness, and stable operation under both steady-state and dynamic situations.

The primary objectives of the proposed research are to design and develop single-phase and three-phase control techniques for VSC with advanced features. These VSCs are realized as shunt compensator. Moreover, the thesis investigates some of the applications VSC in grid integration of renewable energy sources such as solar photovoltaic (PV) systems under normal and abnormal grid conditions. These objectives have been accomplished by designing and developing single-phase and three-phase shunt compensators. Extensive testing of these compensators has been carried out under various loading by implementing some new control algorithms. Testing under abnormal condition

such as low voltage ride through (LVRT) has also been attempted. The work can be broadly categorized under the following section.

1.5.1.Design of Single-Phase and Three-Phase System:

Conventional H bridge configuration for single-phase and 3-leg configuration for three-phase system has been designed simulated and developed experimentally. Power components for the single-phase VSC include a DC-link capacitor and respective H-bridges. Moreover, interface inductors, a single/three-phase programmable supply, linear and non-linear loads, and a voltage source converter are used. A 3 leg VSC configuration having six IGBT has been realized for a three phase system. A three-phase AC programmable supply has been used into a system that operates on three-phase power. Voltage and current sensors are used in the hardware configuration of a single-phase or three-phase grid-connected photovoltaic (PV) system to measure the different voltage and current parameters of the system. Both the grid voltage parameters and the PV arrangement were taken into consideration throughout for the design of PV array.

1.5.2. Mitigation of PQ issues in Single-Phase and Three-Phase Grid Connected PV System:

The power distribution system faces PQ issues such voltage sag and swells, harmonics distortion, poor power factor (PF), and load unbalancing because of the inductive and non-linear nature of loads. According to IEEE standards, it's important to maintain sinusoidal supply currents while also reducing harmonics in the supply current. Designing and creating innovative control techniques for VSC control in single-phase and three-phase prototype power systems has become a prominent area of study in the last ten years. The goal of this thesis was to design and develop new control algorithms for control of VSCs for single and three phase system. Literature review discusses a number of the conventional control algorithms such as Synchronous Reference Frame Theory, SOGI filter-based, and two new control techniques such as adaptive Bateman polynomial (BP) controller and Radial basis function neural network (RBFNN)-based Gaussian distribution function recommended for VSC in SAPF control methods. Moreover, the Perturb and Observe (P & O) a maximum power point tracking (MPPT) method is applied in order to

extract the most possible power from PV while maintaining highest possible efficiency. The comprehensive simulation studies and VSC hardware implementation are performed for linear and non-linear loads in single-phase and three-phase grid connected PV systems. In-depth details are provided on the dynamic performance of VSC and the effectiveness of the recommended control strategies in reducing PQ issues under steady-state and dynamic load scenarios. The PQ problem studies in single phase system focus on 1) PF correction 2) harmonic reduction 3) load reactive power compensation and in three phase on 1) PF correction 2) harmonic reduction 3) load reactive power compensation and 4) load balancing.

1.5.3. PQ Issues During Distorted Grid Condition:

This study presents different control schemes for improving the behavior of distribution system under distorted grid conditions. Under unbalanced supply and harmonics in the grid voltage, normal compensation algorithms fail to give desired results. Regulation of balanced and sinusoidal grid currents as several IEEE/ IET standards and grid codes becomes a major challenge. This work discusses the design of two control techniques for control of the grid connected converter namely conductance based controller and Levenberg Marquardt (LM) trained SOGI control technique realized for compensation in three phase system. The designed algorithm consists of calculating of reference current under highly unbalanced and distorted supply condition. The experimental and simulation results are validated and discussed in this thesis for single phase and three phase system.

1.5.4. LVRT and FRT Capability of System:

Voltage control and power quality (PQ) management are crucial aspects for the control of grid connected voltage source converters (VSC). Flickers, low voltage, and poor power quality (PQ) caused by grid malfunctions can increase losses. Lightning strikes, power line short circuits, and other events create grid-connected voltage sags. If the temporary drop in grid voltage amplitude exceeds the usual voltage threshold, islanding protection may trigger and cause a power loss. Stability of grid-connected PV may be compromised. Consequently, power converter control techniques should identify faults and act fast to minimize grid side damage. In this study control techniques have been developed

to improve PQ and LVRT capability. The new control techniques applied to solar photovoltaic (PV) tied single-phase grid include a Sliding Window Recursive Discrete Fourier Transform (SWRDFT) based algorithm and adaptive Laguerre polynomial (LP) controller, similarly for three-phase system the development of new algorithm based on adaptive Gegenbuer polynomial (GP) and load power based controller have been discussed. The major goal is to operate the VSC as per the standard grid codes and ensure quality power is delivered to the grid even under abnormal grid conditions. The system is designed to work at unity power factor during normal mode of operation. Reactive power injection is mandated as per a country's grid code and helps to regulate the voltage profile and low voltage ride through (LVRT) during grid voltage fluctuations. Additionally control features have been added to maintain satisfactory response under low voltage condition also.

1.6. Thesis Outline:

The thesis has chapters.

Chapter 1: Introduction: This chapter provides a brief introduction to the power quality issues that are present in the distribution system, as well as other challenges that are present in the distribution system, such as PV integration and faulty grid condition, as well as the control methods that can be used to deal with these challenges.

Chapter 2: Literature Review: In this chapter, the literature review on power quality problem/challenges and remedies is given. This chapter includes a comprehensive literature overview of shunt compensator setups and control techniques. At the conclusion of this chapter, research gaps are identified based on a comprehensive literature review.

Chapter 3: Design and Development of Single-Phase and Three-Phase Voltage Source Converter (VSC) Grid Connected PV System: This chapter discusses the design and development of single and three-phase VSC-based systems connected in shunt configuration for simulation and experimental studies. Focus is laid on voltage and current sensor circuits, and level converter circuits for gate driving for experimental testing. Stability analysis of single-phase and three-phase systems with various PI controller gain setting values is also addressed. In addition, the modeling of PV systems and integration into the grid are discussed in this chapter.

Chapter 4: Power Quality Improvement Techniques in Single and Three Phase Grid Connected PV System:

This chapter examines the incorporation of PV at the DC link of VSC. Also, this chapter covers PQ concerns mitigation control strategies like as SOGI, SRF, adaptive BP controller and adaptive RBFNN based on the Gaussian distribution function for control of VSC.

Chapter 5: VSC Operation under Polluted Grid Condition: This chapter examines the PQ enhancement strategies such as conductance based algorithms and LM trained SOGI filters for three phase systems that are operating under distorted grid conditions. In this chapter, a variety of traditional approaches such as unit template method based on SOGI filter and D-SOGI control techniques are explored for the purpose of unit template extraction methods under distorted grid conditions.

Chapter 6: LVRT Operation of Single-Phase System: In this chapter, the low voltage ride through operation for a single phase grid tied PV system is discussed. Normal operation mode as well as operation when the grid undergoes fault is observed. Sliding window recursive discrete Fourier transform (SWRDFT) and adaptive Laguerre Polynomial (LP) based controller are the two control methods developed and discussed in this chapter. Both of these methods are used for control of H-bridge VSC which is capable of LVRT operation.

Chapter 7: LVRT Operation of Three-Phase System: In this chapter, the low voltage ride through operation for a three-phase grid tide PV system is discussed in case of faulty grid operation mode. Load power and GP function based algorithm are the two three-phase control methods that are discussed in this chapter. Both of these methods have been designed for control of three legs VSC capable of normal as well as LVRT operation.

Chapter 8: Conclusion: The various control methods and the integration of PV into the grid in single-phase and three-phase systems is summarized in this chapter. In the conclusion part, the future direction of research in this field also discussed.

Chapter-2: Literature Survey

2.1. General Introduction

This chapter discusses into great detail on the necessity for a compensator in compliance with different IEEE standards, numerous PQ difficulties, mitigation strategies, and LVRT operation. Voltage source converters (VSC) based on photovoltaic (PV) technology deliver active power transmission to the grid and load. Grid current balancing, harmonic reduction, reactive power balancing, and supply side power factor improvement to unity are important features to be controlled. The PV source can be directly linked to the VSC at its DC connection using a single-stage design. This chapter contains a thorough analysis of the literature on identifying adaptive control techniques for estimating the main load current component and producing reference currents. Also, a variety of control mechanisms have been tested in order to make the system resilient. A variety of configurations for single-phase and three-phase grid-connected systems have been analyzed and put into practice for the proposed system's successful implementation on the basis of an exhaustive literature review.

2.2. Survey on Various Power Quality (PQ) issues:

Power electronics loads are employed in many industrial, commercial, and residential loads, which have led to a variety of PQ issues at the distribution level. The major sources of PQ issues include switching between loads, variable speed drives (VSDs), arc furnaces, various rectification circuits on the load and grid sides, and non-linear loads [22-23]. These loads may be broadly divided into two groups: current harmonic sources and voltage harmonic sources. Reactive power demand, feeder losses caused by warming of conductors, poor power factor, voltage sag and rise, and poor voltage regulation increase as the fraction of this type of load increases, which affect the grid system [24]. Transformers and other nearby equipment are negatively impacted by this [25]. As a result, this chapter examines and investigates a thorough assessment of the many PQ challenges, solutions, and worldwide standards.

Due to the high demand of reactive power needed by nonlinear load, the system will experience high levels of voltage and current harmonics. Due to this, the power factor on the grid side is also reduced, and the source current's sinusoidal form is altered. Grid

current and voltage must have a low THD percentage, according to standards from the International Electrochemical Commission (IEC) and the Institute of Electrical and Electronics Engineers (IEEE) [26-27]. IEEE 1159:2009 describes what you should do to monitor the characteristics of both single-phase and three-phase systems [28]. These standards are necessary so that manufacturers, researchers, and software developers can demonstrate them and calculate the power consumption of a system [29]. The guidelines for suggested practices and the management of harmonics in electrical power systems are outlined in IEEE 519:1992 [30]. The IEEE 1547:2018 standard, a revision of IEEE 1547:2003 [31], outlines the requirements and guidelines for integrating distributed energy sources into electric power systems (EPSs) and other interfaces [32].

Passive filters, active power line conditioners, and hybrid filters are just a few of the methods that have been considered in literature and put to use to minimize harmonics [33-39]. Active power line conditioner is a suitable technique for harmonic compensation since switching technology has been developed recently and there are less expensive ways to implement it, using DSP/field-programmable-gate-array(FPGA) based systems. Harmonics in the current are frequently eliminated by the use of active power filters (APFs) of the shunt type. In order to address voltage issues including voltage sag, voltage swell, flickers, voltage changes, voltage imbalance, and voltage harmonics, a series active compensator is connected in series at the load end. Series active power filters include DVRs and Solid State Static Series Compensators (SSSCs) [40]. The distribution system makes extensive use of shunt active power filters, a sort of DSTATCOM [41- 43]. With a shunt connection, it may be utilized as a VSC or Current Source Inverter (CSI) to the PCC. The active filter has been utilized to address current quality issues such voltage control, load balancing, and reactive power compensation. Several individuals now employ this compensator to address PQ issues as switching devices have improved [44,45]. When two active power filters are used in tandem, it is referred to as a "hybrid active power filter." An example of a hybrid active power filter is the UPQC [46-48]. Both voltage and current PQ issues can be improved, but it is difficult to regulate and requires additional switches, leading to higher cost.

2.3. Survey on Adaptive Control Algorithms for VSC:

The precision with which the control algorithm extracts the reference current and accounts for harmonics produced by the load determines the efficacy of SAPF. In published studies [49-57], several temporal and frequency domain control approaches have been proposed. Conventional methods that are well-known and productive include Synchronous Reference Frame Theory (SRFT), Instantaneous Reactive Power Theory, Symmetrical Component Based Theory, and algorithms based on the cancellation of double frequency components. Many unique algorithms have been developed, including the Composite and Model observer-based technique [54-55] and the Kernel incremental learning algorithm [55-56]. These algorithms work well, but they need estimation of various parameters, extensive arithmetic operations, and extra filters. Moreover, a variety of frequency-domain algorithms, such as Fourier transform and the Kalman filter, have been used to control the VSC used as an active filter.

Adaptive signal processing techniques have grown used in a number of areas in recent decades, including active noise cancellation, signal amplification, noise filtering, and echo cancellation. Least mean square (LMS) is the most often used adaptive algorithm due to its fundamental structure [58]. The step size defines how well the algorithm works in terms of weight convergence, and changing it directly affects its performance. The normalized least mean square (NLMS) technique was designed to solve the inadequacies of the LMS approach [59]. It is well known that, the step size parameter plays significant impact on the performance of LMS and NLMS. When determining the ideal step size, there is a trade-off between steady-state error and convergence. As a result, numerous focused study on this topic.

The variable step size (VSS)-based adaptive approach is an alternative to the fixed step size. The approach must have a very low constant error and a high convergence rate in order for the adaptation to be successful[60], this study describes a simple VSS-LMS approach with adjustable step size and Mean Square Error reduction (MSE). The VSS-LMS approach, on the other hand, is dependent on the initialization of the input weight vector and necessitates the adjustment of the step-size during sudden input signal fluctuations. The authors of [61-62] developed two conventional adaptive algorithm approaches, the Least Mean Fourth (LMF) and the Least Mean Absolute Third (LMAT).

The LMF and LMAT techniques outperform the usual LMS algorithm in terms of MSE, convergence speed, and steady-state error.

Many adaptive algorithms[62] based on adaptive-linear-element (ADALINE) have recently been employed to identify the fundamental frequency component of load current. Qasim et al. [63] proposed three adaptive algorithms, two for predicting frequency and voltage and one for calculating load current. Particle Swarm Optimization (PSO) is utilized to increase each ADALINE's dynamic effectiveness. Chilipi et al. [64] developed a LMMN (least mixed norm) method. This approach captures all dynamic harmonics from the load current while simultaneously reducing the error created by the LMMN filter, hence improving dynamic performance. Badoni et al. [65] extracted the load current components and minimized the MSE using a discrete-time Weiner filter. B. Subudhi et al.[66] estimates the positive sequence current using a Kalman-based H filter. Furthermore, despite considerable swings in grid and load disturbances, the dc-link voltage is managed by the adaptive principles of the Kalman algorithm. In the literature[67-69], several writers have suggested compensation systems based on Artificial Neural Networks (ANN). Many ANN topologies have been published, such as the adaptive euro Fuzzy inference system (ANFIS), the radial functional neural network (RFNN), the feed-forward ANN, and the adaptive linear neural network (ADALINE). One of the most well-known and often utilized of these networks is the feed forward ANN [70] investigated control methods based on ANFIS-LMS as a technique of decreasing PQ difficulties.

The MMCF-SOGI multiple complex coefficient filter-based control algorithm is described in [71]. Manoj et al. created the Adaptive zero attraction least-squares-mean approach (ZA-LMS)[72]. Recent papers have examined the adaptive neural network-based approach [73], Wiener filter [74], Gauss Newton-based controller [75], the Affine projection algorithm [76], the combination (ATC-DLMS) diffusion estimation [77], and the Z2-proportional diffusion algorithm [78].

Alhaj Hussain et al. [79] investigated other adaptive filtering approaches, including the combination LMS-LMF algorithm, which outperforms all others. Modi et al. [80] described an improved Widrow-Hoff technique for optimizing grid current by extracting the basic load current. In [81] describes adaptive weighted zero attracting (RZA) control methods. Pavitra et al. [82] investigated optimum DSTATCOM impedance management. Pinaki

Mitra et al. [83] described a DSTATCOM artificial immune adaptive control method. M.Qasimet et al. suggest a implementation of ANN for SAPF [84], Neural network-based conductance estimate [85], and ANN-based predictive and adaptive control [86].

2.4. Survey on Grid Connected PV System:

Renewable energy sources including wind and photovoltaic (PV) power during the past ten years [87-88]. It is a crucial responsibility for those in charge to maintain the system's dependability and stability as well as the quality of the power. Each country has its own grid protocol that specifies how to link renewable energy sources to the electric system [89-92].

PV systems can be scaled up, are clean, don't use fuel, and need no maintenance[93]. On the other hand, PV energy production is constrained by high installation costs, poor efficiency, and energy generation that is reliant on the weather [94-97]. The average solar system efficiency varies between 9% and 17% when different types of weather are taken into consideration [98]. Solar energy is a volatile type of energy since it depends on the weather. Using the proper control mechanisms is essential for ensuring the efficient and secure operation of photovoltaic (PV) systems. Several tracking algorithms [99-101] for maximizing the output of a solar PV array have been discussed in the literature. Due to their simplicity, traditional MPPT methods, including as those that use Fractional short-circuit current (FSCC), Fractional open-circuit voltage (FOCV), Hill Climbing and Perturb and Observe, are often employed in a variety of circumstances [102-103].

Grid-connected PV systems are becoming more prevalent due to the availability of sunlight and advancements in power electronics. Voltage, frequency, phase angle, and amplitude are the most crucial parameters to track and regulate for grid-connected applications, according to control studies. Yet, synchronization is a major issue for inverters linked to the grid. According to Aisyah et al. [104], Murillo-Yarce et al. [105], PV systems may operate in both islanding/standalone mode and grid-integrated mode, depending on how they are configured and operated.

There are single-phase and three-phase distribution systems, and different kinds of loads have been connected based on customer requirements [106, 107]. Both single-phase H-bridge VSC and three-phase VSC can integrate PV into the distribution grid [108,109]. In

[110,111], the authors proposed a single-phase, multilayer photovoltaic (PV) inverter architecture with a special pulse width modulation (PWM) control method for grid-connected PV systems. In the literature, PV systems have been connected to distribution grids in single-stage [112–116] and double-stage configurations for the capacity of active power injection [117] as well as the improvement of power quality. The most crucial factor in the integration of solar PV for efficient power injection is the design of the PV array [118, 129]. Battery storage systems have also been used as power backup during power outages and to reduce the unpredictable nature of solar PV [120, 121]. Tsai-Fu et al. [122] compared the power losses of single-stage and two-stage grid-connected photovoltaic systems. The overall power loss in a single-stage grid-connected PV system is comparable to that of a two-stage grid-connected PV system, according to loss analysis, and the single-stage system can save a boost converter stage. PV integration enables for active power injection into the grid if the load requirement is less than the power generation for power. A DC-DC converter is not utilized in a single-stage configuration, but a DC-DC converter is used in a double-stage format. MPPT techniques have been applied and published in the literature in both versions. In single-stage configuration, MPPT provides the reference DC-link voltage to regulate the DC-link voltage at maximum power point [123, 124], but in double-stage setup, MPPT is used to create the duty-cycle of the DC-DC.

2.5. Survey on Control Techniques for LVRT Capability:

In recent years, the penetration of renewable energy sources (RES) into the electrical grid has risen significantly thereby reducing the negative consequences of fossil fuel-based power plants. As a result of reduced module pricing, photovoltaic (PV) technology has become popular among other renewable energy sources [125-126]. This is needed to meet the ever increasing energy demand of industrial consumers and household consumers. This widespread use of single-phase and three-phase grid-connected PV systems and the emergence of large-scale distributed generation (DG) systems have raised concerns about grid reliability, quality and availability. Several grid standards and regulating criteria have been issued by power system operators (PSOs) or international groups (e.g. IEC and IEEE) to govern the interaction of DGs with the utility grid [127-129]. The regulations for wind power system or DGs connected to a medium or high-level grid account for majority of

grid requirements. Only a few grid codes and papers [130-131] explain the regulations pertaining to single phase PV systems. Grid-connected PV systems are often utilized on a modest scale at residential level and are designed to disconnect from the grid in the event of a malfunction within a few cycles [32]. However, due to the increasing penetration of PV in large-scale grid-connected systems, disconnection may produce undesirable conditions and also leads to detrimental influence on the distributed grid's dependability, stability and availability [132-134]. In the event of a voltage malfunction, it may result in flickers, low voltage and poor PQ problems resulting in decreased energy output and higher transmission and distribution losses [127]. Thus, focus on large scale PV integration needs to be studied from different perspectives.

Alternatively, if a grid-connected PV system can offer ancillary services such as reactive power support and low voltage ride through (LVRT) capabilities [135], the end user will not experience flicker or poor power quality and PSOs will not have to restrict PV electrical grid integration. Such PV-grid systems will be smarter and more actively controlled in the coming years; thereby making the system more reliable. Low voltage ride through operation of the PV integrated system involves providing additional reactive power support based on the VSC rating. Depending on the amount of voltage sag at the point of common coupling (PCC), the much needed reactive power is injected into the grid as per grid standards [127].

With a high penetration of PV power into the utility grid, both short term and long term disturbances are more likely to happen. These manifest in the form of voltage and frequency disturbances, unbalances in three phase voltage and flickers. They can be further classified into long term disturbances and short term disturbances like as sag and swell in voltage, voltage spike and power outage [108]. Short term disturbances are more likely to happen [136-137]. Therefore, advance control strategies for the grid connected PV inverter need to ensure stable and reliable operation under these abnormal conditions.

Therefore, grid codes and standards are required for the grid connected PV system for having capability of ride through the transient voltage sag [138]. Many countries have updated their own grid codes according to the grid requirements in order to ensure safety and seamless transfer of electrical energy to the grid. Many international bodies have also

developed their own standards such as IEEE in US, Germany, IEC in DKE and Switzerland [139].

Here a few grid codes for different countries are specified for single phase system [138,139]

1. Germany: The German grid code, also known as "VDE-AR-N 4105," addresses the technical criteria for grid connection of decentralized energy generation systems, including single-phase systems. The ranges of voltage and frequency, response periods, and other pertinent factors are specified in the regulations for LVRT functioning [139].

2. Spain: The "RD 1699/2011" grid code specifies the technical requirements for connecting low voltage, single-phase generation units to the grid. The specifications cover the necessary LVRT capabilities, voltage and frequency ranges, reaction times, and safety precautions are listed in [139].

3. UK: The National Grid Electricity System Operator (ESO), which is in charge of managing the UK grid code, lays out the technical specifications for integrating and running generation systems, including single-phase systems. In accordance with the grid code, LVRT operation, voltage and frequency restrictions, and other relevant parameters have been detailed in [139].

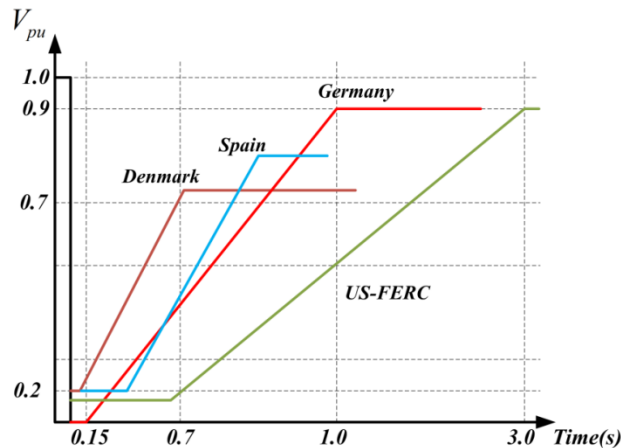


Fig.2.1 LVRT Curves as per grid codes of different countries

Fig.2.1 depicts multiple LVRT curves for specific countries. The German grid code requires generating systems to be capable of riding through a 0.15s voltage failure when the grid voltage amplitude drops to 0 V and inject some reactive current I_q into the grid, as

shown in Fig.2.1. On the same lines, other countries have set their benchmarks for reactive power injection.

The major challenges for single phase grid connected PV systems are in designing appropriate controllers. The control methods presented should function properly for unity power factor mode operation (UPF) in steady state and inject computed reactive power in faulty or abnormal grid conditions. Some suitable methods for LVRT operation for single phase grid connected PV systems are mentioned in the literature [139] which mentioned different methods for compute appropriate reference current to handle ride through failures. Several control techniques for LVRT operation of two stage and single stage PV linked systems have been presented in the past [15, 127, 131, 140-144]. The operating principle of a single-phase grid-connected PV system in LVRT mode is discussed in this paper [127], which is based on single-phase PQ theory and a proportional resonant current control scheme. Paper [131] discusses an LVRT scheme for a transformer less single phase grid connected inverter (6sw-Cuk derived transformer-less inverter) based on single-phase instantaneous p-q theory. In paper [140], discusses LVRT operation based on synchronizing techniques (Second order general integral (SOGI) phase locked loop (PLL), T/4 delay PLL and Enhanced PLL). Paper [141] discusses three different configurations of transformer-less PV inverters in a single phase system such as full-bridge inverters with bipolar modulation (FB-BP), full-bridge inverters with DC bypass topology and the highly efficient and reliable inverter concept (HERIC) inverters are used for LVRT operation. Their control strategy based on two cascade loops viz. an inner loop for PQ issues and outer loop for current reference generation for inner loop. Braking chopper based LVRT scheme for single stage PV plant is discussed in [15] and an analytical approach for LVRT operation enhancement for single stage PV plant based on positive and negative sequence component in [142], a Z-source inverter based PV with LVRT capability is discussed in [143] and a new swarm algorithm (SSA) based controller for LVRT operation of grid connected PV is discussed in [144]. However, the majority of single phase LVRT capable systems utilize multiple PI regulators, which adds to the complexity of the system.

For three-phase system, several issues under faulty grid condition are quite likely to take place in three-phase distribution systems. These are non-sinusoidal current injection [128,145], oscillation in active and reactive power demand [146] and over-tripping.

Therefore, different control methods are presented and some of the control methods are mentioned in literature[128, 147-152]. Paper [147] discusses a LVRT control strategy for two-stage three-phase PV-system which is based on computation of symmetrical components of voltage and current under faults. Paper [128] discusses a LVRT scheme based on interweaved generalized integrator (IGI) filter. Paper [148] presents a LVRT technique for a three-phase grid connected inverter based on non-linear phase-locked loop (PLL). In paper [149] the LVRT performance is analyzed using wavelet fuzzy neural network for weak grid condition while a positive sequence(PS) and negative sequence(NS) current controller for LVRT control has been discussed in[150]. An instantaneous active power control (ISPC) [151] and average active-reactive control (AARC) in [152] have been proposed for unbalanced grid condition. It is found that most of the proposed control strategies suffer from oscillation in active power and DC link voltage under abnormal grid condition.

2.6. Research Gap

Based on the extensive literature review, following research gaps are identified:-

1. Fast and adaptive control techniques should be exploited to extract the harmonics from distorted grid and to generate reference current
2. Advanced control techniques for single-phase and three-phase grid connected PV system for improvement in power quality are required. Some advanced techniques have been studied for shunt compensators
3. It is imperative to study how these controllers can be modified in the presence of PV source.
4. Non-PLL and PLL based fast and efficient synchronization techniques based on different types of adaptive filters etc. need to be designed and tested
5. Synchronization techniques considering polluted grid, weak grid and different loading conditions should be addressed.
6. Work on LVRT and FRT studies is very limited
- 7.

2.7. Research Objectives

1. Design and implementation of modern control algorithms for PQ improvement under different loading conditions.
2. Design and performance Investigation of controllers under voltage sag, swell, harmonics, noise etc. and unbalanced grid conditions.
3. Integration of PV under normal and abnormal grid conditions.
4. Implementation of grid code which include LVRT and FRT capabilities of voltage source converters.

2.8. Conclusion:

In this chapter, a comprehensive literature review was conducted on single-phase and three-phase PV systems that are grid-connected, focusing on PV modeling, MPPT approaches, control algorithms, installation, and power management. Based on the literature review and the justifications for employing PV, a research gap and a list of study objectives have been established.

Chapter-3: Design and Development of Three-Phase and Single-Phase Shunt Active Power Filter (SAPF) Grid Connected PV System

3.1 Introduction

In this chapter, design and modeling of a VSC as compensator for single and three-phase with and without PV integration are discussed in detail. This chapter also discusses design of PV array and modeling of single stage and double stage PV system. VSC based system are designed and controlled to assure the successful implementation of new control approaches and their performance is examined on a prototype system under various system conditions. Grid supply, current and voltage sensors, a DSP, a VSC, and linear-nonlinear loads make up the majority of the built system. The design of each part is thoroughly discussed below.

3.2. Design and Development of Single-Phase VSC System:

Fig. 3.1(a) depicts the layout of a single phase SAPF system that is both effective and efficient when utilized with and without a grid-connected PV system.

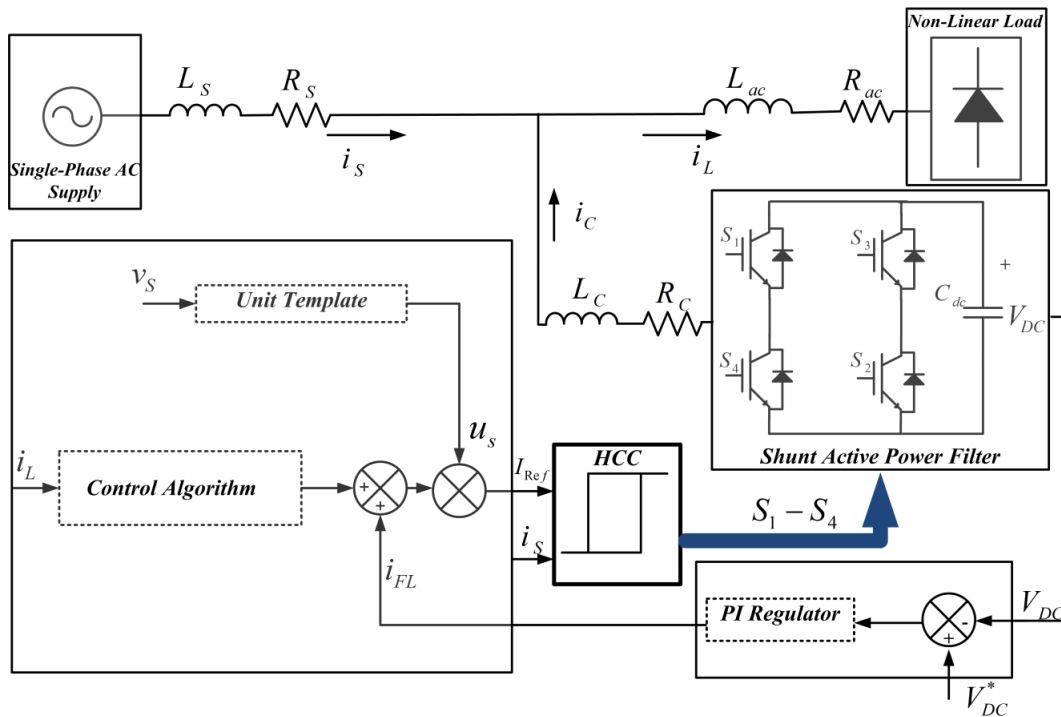


Fig.3.1(a) Single phase VSC controlled as a compensator

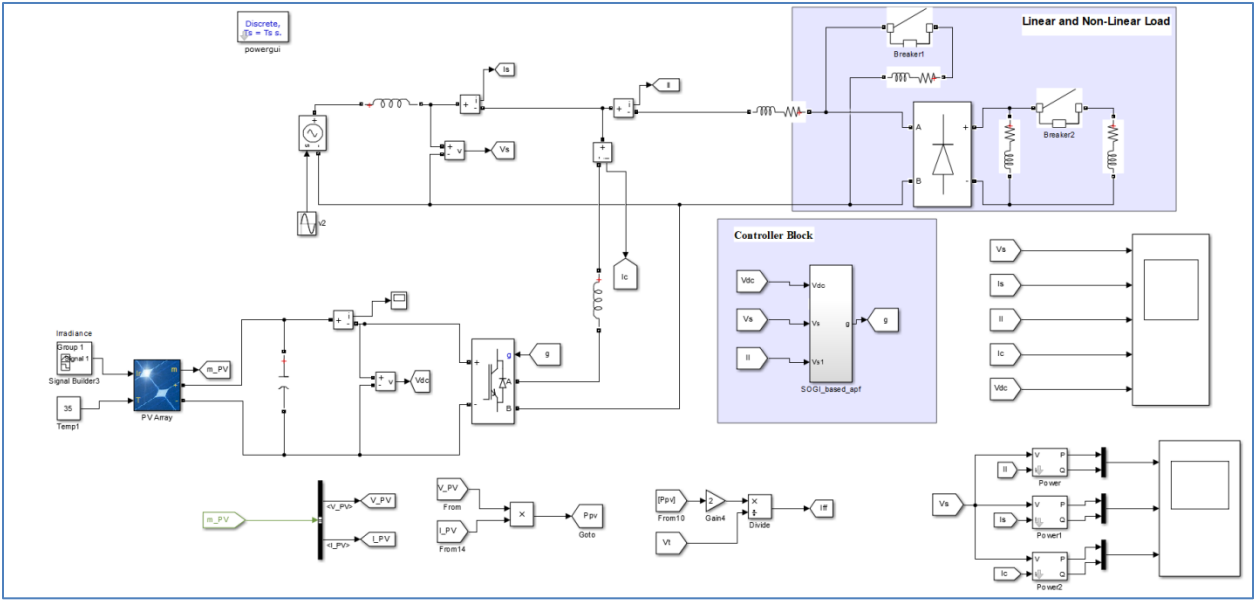


Fig.3.1(b) Matlab based simulation model of single phase system

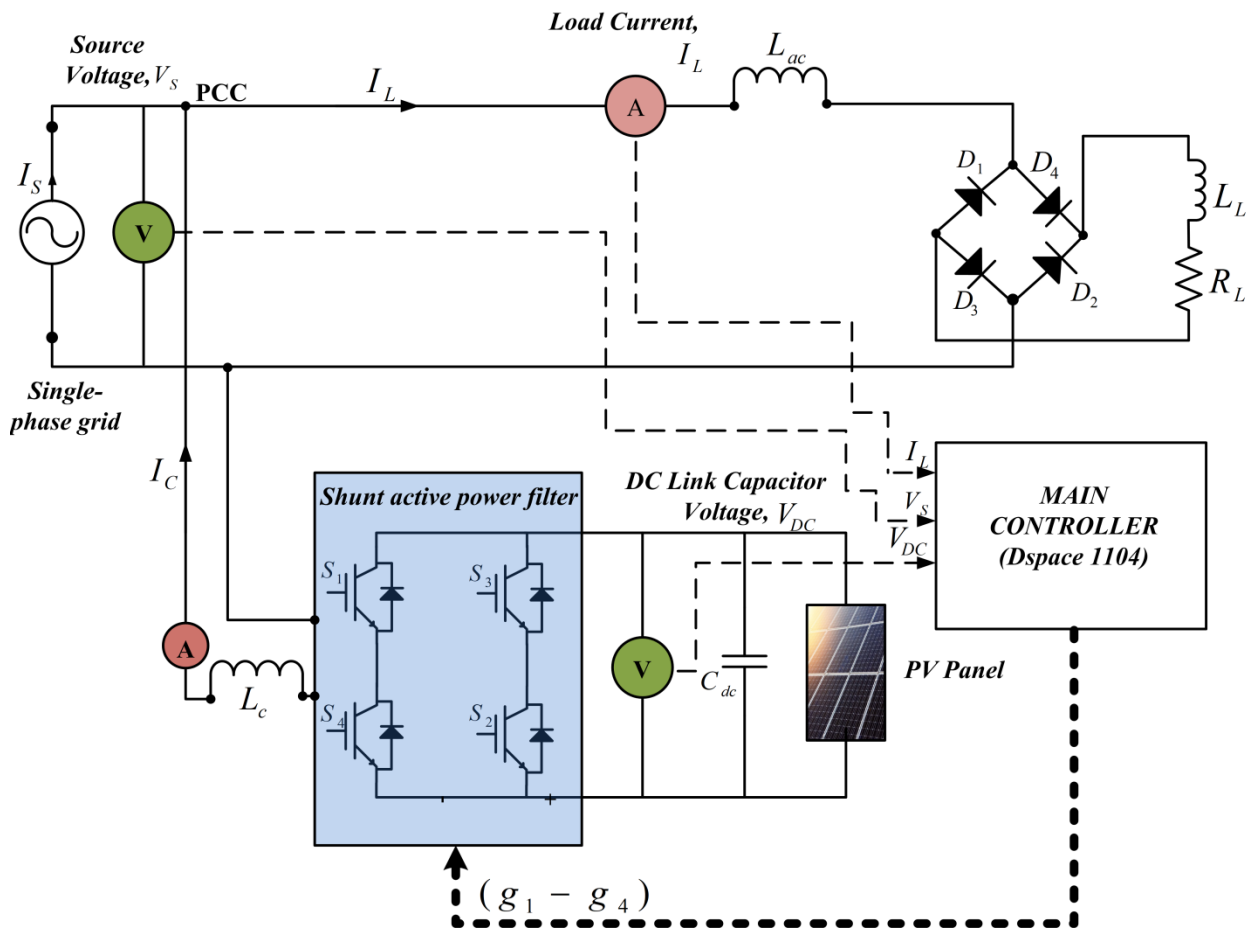


Fig.3.2 Single phase VSC with single-stage grid connected PV system

The designed system is realized to mitigate harmonics due to the non-linear load in the present system, perform reactive power compensation due to the inductive nature of the load, operate at low voltage under faulty grid conditions, and also improve power quality under distorted grid conditions. There are two ways to link the PV array to the grid: single stage and double stage systems. Fig.3.2 shows single phase VSC single stage grid connected PV system.

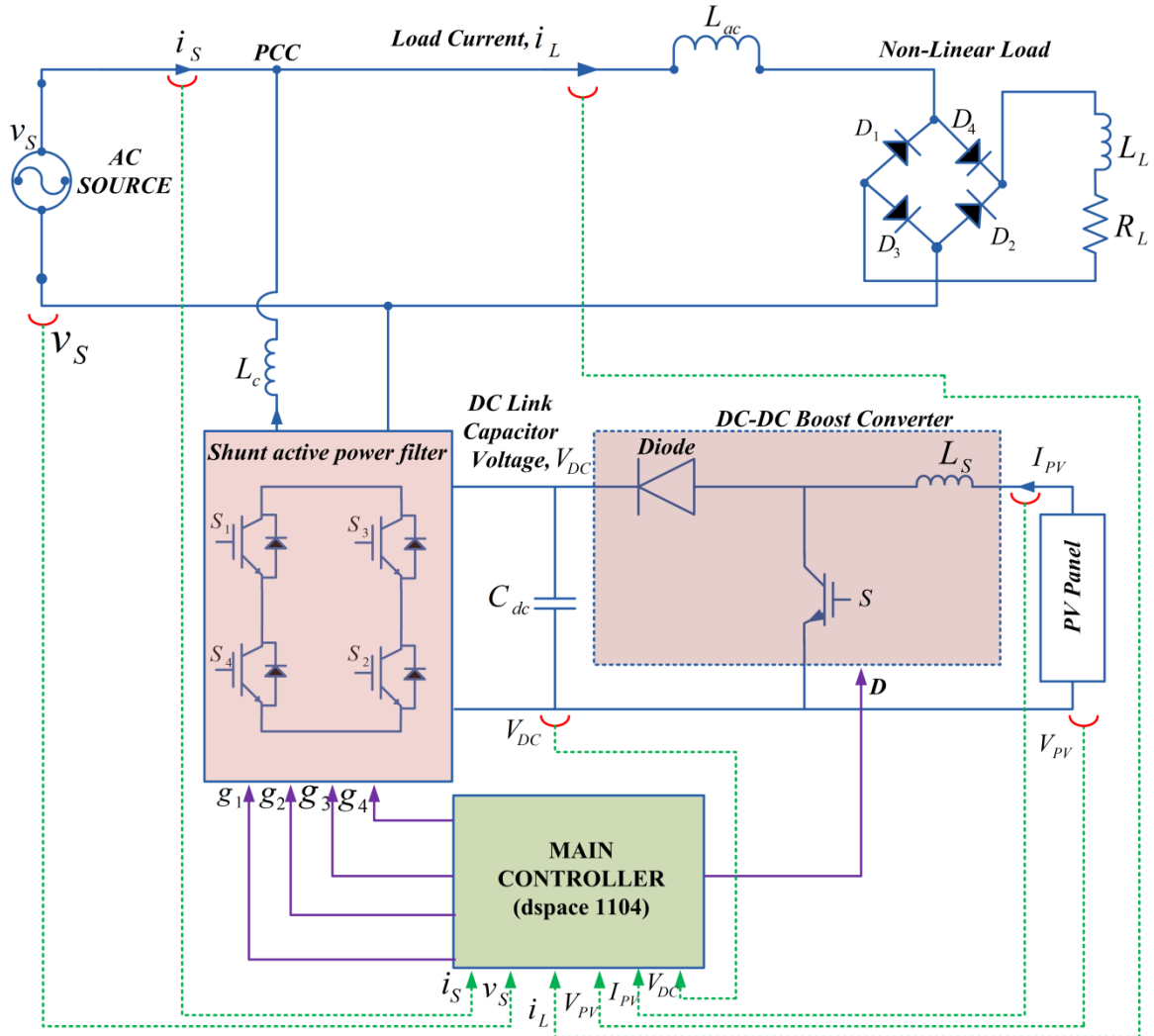


Fig.3.3 Single phase VSC with double-stage grid connected PV system

The PV array has been linked directly to the VSC's DC-link in this setup. In this setup, no DC-DC converter has been employed hence a single-phase grid connected PV system is considered. The DC-link voltage's reference voltage, which is the maximum power point voltage, is achieved using the MPPT approach. Active power injection into the grid is

facilitated by this design. Fig. 3.3 depicts a single phase double-stage PV system that is connected to the grid. In this case, the PV system has been connected to the VCS using a DC-DC converter as illustrated in Fig. 3.3. The double stage system is advantageous to the single stage system when it comes to the robustness of the system, controllability, and the ability to employ PV arrays with lower ratings.

The design of different components of a single-phase grid connected without or with solar energy integration is now discussed. The following design quantities have been considered [44]

1. DC link capacitors
2. Interfacing inductors
3. DC reference value
4. DC-DC converter
5. Current and Voltage sensors
6. PV array configuration
7. Amplification Circuits

3.2.1. Calculation of DC link reference voltage:

The DC link reference voltage of the system is depends on supply voltage of the system, for proper PWM control in a single-phase system, the system's DC link voltage must be greater than the peak supply voltage [44]. The peak value of the single phase system calculated as

$$A_m = \sqrt{2}v_s \quad (3.1)$$

where, A_m is the peak amplitude of AC phase voltage, v_s is the source voltage of single phase system. The rating of single phase system is 110V, 50Hz for simulation performance and 40V, 50Hz for the experimental system. The calculation of DC-link voltage can be given as:

$$V_{dc_{ref}} > A_m = \sqrt{2}v_s \quad (3.2)$$

The dc reference value is calculated as 56.56V for experimental setup and set at 80V, for simulation the dc link reference voltage value is 155V and it is set as 200V for the SAPF operation.

3.2.2. Design of DC-link capacitor:

DC-link voltage of the VSC is very sensitive to input grid voltage and the load current. The value of DC-link capacitance should be large enough to sustain DC-link voltage during dynamics[44]. The DC-link capacitance can be calculated using Eq.(3.3).

$$C_{dc} = \frac{v_{gh} i_c \tau g}{\frac{1}{2}(V_{dcref}^2 - V_{dcm}^2)} \quad (3.3)$$

Here, $h(1.2)$ is the overloading factor, $i_c(10A)$ is the compensator or VSC current, τ (0.02s) is time-constant, $g(0.3)$ is gain constant, V_{dcref} (200V) is the reference DC-link voltage and $V_{dcm}(155.56V)$ is minimum DC-link voltage. Applying these values in Eq.(3.3), gives

$$C_{dc} \approx 1000\mu F \quad (3.4)$$

A value of DC-link capacitor higher than the calculated value has been chosen for simulation. Selected value of $C_{dc} = 1500\mu F$. Similarly, for the experimental system, i_c is 10A, V_{dcref} is 40V and V_{dcm} is 55.56V and the calculated value of DC-link capacitor by Eq.(3.4) is 1706 μF . Higher value of DC-link capacitance for the experimental setup is selected and it is chosen as 2200 μF as per the availability in the laboratory.

3.2.3. Design of Interfacing Inductor:

Interfacing inductor is used to filter out the ripples in the current. Higher value of inductor provides better filtering but at the same time power loss is higher[44]. Hence, proper design of interfacing or filter inductor (L_f) is very necessary and is calculated by Eq.(3.5).

$$L_f = \frac{\sqrt{3}mV_{dcref}}{12hf_s\Delta i} \quad (3.5)$$

Here, m is the modulation index ($m = 1$), V_{dcref} is DC-link reference voltage, h is the overloading factor, f_s is the switching frequency and Δi is the ripple content in the current and it is considered as 5% of maximum current. For simulation purpose its value is calculated to be

$$L_f \approx 3.20mH \quad (3.6)$$

For experimental purpose its value is selected as

$$L_f \approx 2.0mH \quad (3.7)$$

Based on the availability and the calculated values, interfacing inductors of 3.5mH are selected for the simulation and experimental system.

Table-3.1 Values of Different Parameters

S.No	Parameter	Simulation Value	Experimental Value
1	Supply voltage	110V, 50Hz	110V, 50Hz
2	DC-link reference voltage	200V	200V
3	DC-link capacitance	1500uF	2200uF
4	Interfacing Inductor	3.20mH	2.0mH

3.2.4. Design of Hysteresis Current Controller (HCC):

Hysteresis current control is utilized to generate switching pulses. HCC is the most widely used current control technology due to its simple implementation, remarkable stability, absence of tracking error, very fast transient response, inherent limiting maximum current, and inherent resilience against load parameter variations. A survey of used current control approaches for PWM converters demonstrates, as shown in [153, 154], that HCC is superior for active power filter applications. HCC provides superior suppression of low-order harmonics than PWM control, which is the primary objective of the active power filter. It is easy to accomplish with great precision and rapid response. However, its switching frequency is variable which is a drawback.

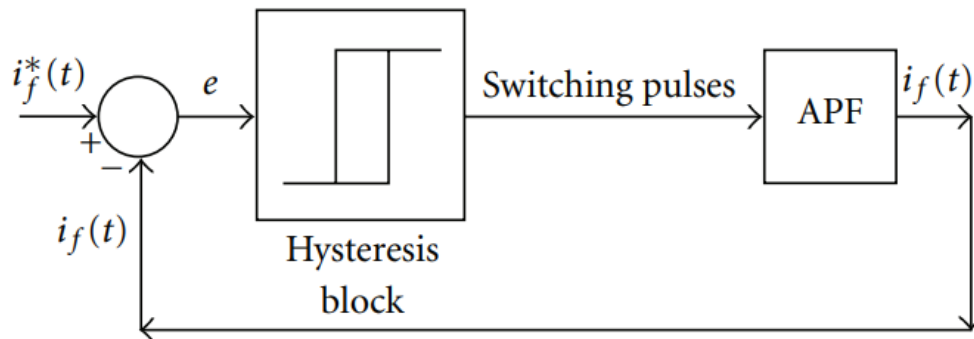


Fig.3.4 Operation of fixed band HCC loop

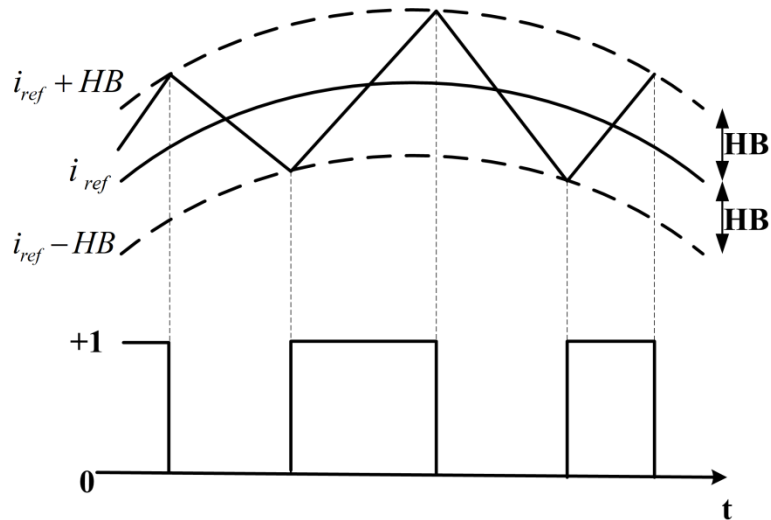


Fig.3.5 Working of hysteresis current controller

The error function is constrained by the HCC approach inside a predetermined hysteresis band. As shown in Fig.3.4, when the error exceeds either the upper or lower hysteresis limit, the hysteretic controller switches in order to keep the error within the predetermined range and feeds these pulses to VSI in order to provide the reference current. This technique is used for controlling a voltage source inverter so that the output current follows the a reference current waveform.

Fig.3.5 shows the outputs of the hysteresis blocks are directly sent to VSI switches as firing pulses. HCC produces four pulses in a single-phase system and six pulses in a three-phase system[155]. The hysteresis bandwidth (HB) in fixed-band HCC has been treated as a constant, and in this study it has been taken as 2% of main current shown in Fig.3.5.

3.2.5. Modeling and Stability Analysis of Single Phase Converter:

In this section, the mathematical modeling of single phase VSC is carried out. The proposed SAPF model shown in Fig.3.6 incorporates a PI regulator block (G_{PI}), current control block and voltage source converter represented as $K_{con}(s)$. Thus, the VSC model is realized using an outer voltage control loop and an inner current control loop. The outer loop is designed to regulate the DC link voltage of the VSC (V_{dc}) to reference DC voltage (V_{dc}^*). The actual grid current I_s is regulated to reference grid current (I_s^*)and

appropriate pulses are developed using the hysteresis current controller (HCC). $K_{con}(s)$ represents the transfer function of VSC which can be determined with the help of small signal analysis. The VSC based system is assumed to be under steady state condition for finding out the transfer function. The relationship between the converter input connected towards grid side (AC side) and converter output side (DC link) is depicted. The real and reactive power flow between the source, load and VSC are depicted in Eq.(3.8).

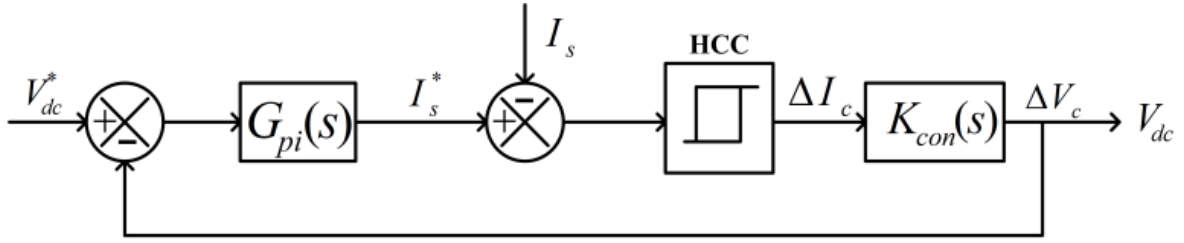


Fig. 3.6 Representation of Active Filter Model

$$P_{cap} = P_{conv} - P_{loss} - P_{ind} \quad (3.8)$$

Here P_{cap} denotes the rate of energy stored in the capacitor, P_{conv} is the power input to converter, P_{loss} is active power loss in SAPF and P_{ind} is power absorbed in interfacing inductor.

$$P_{cap} = \frac{d}{dt} \left(\frac{1}{2} C_{dc} V_{dc}^2 \right) \quad (3.9)$$

$$P_{conv} = v_s i_c \quad (3.10)$$

$$P_{ind} = \frac{d}{dt} \left(\frac{1}{2} L_c i_c^2 \right) \quad (3.11)$$

$$P_{loss} = i_c^2 R_c \quad (3.12)$$

Using Eq. (3.8) to Eq. (3.12)

$$C_{dc} V_{dc} \frac{dV_{dc}}{dt} = \left[v_s i_c - L_c i_c \frac{di_c}{dt} - i_c^2 R_c \right] \quad (3.13)$$

Substituting i_c and V_{dc} with appropriate terms including incremental changes Δi_c and ΔV_{dc} respectively in Eq. (3.13)

$$i_c = i_{co} + \Delta i_c$$

$$V_{dc} = V_{dco} + \Delta V_{dc}$$

where i_{co} and V_{dco} denote steady state operating points, neglecting the higher order terms is obtained as

$$C_{dc}V_{dco} \frac{d\Delta V_{dc}}{dt} = \left[V_s i_{co} + V_s \Delta i_c - L_c i_{co} \frac{d\Delta i_c}{dt} - i_{co}^2 R_c - 2i_{co} \Delta i_c R_c \right] \quad (3.14)$$

Under steady state condition Eq. (3.13) can be written as

$$0 = [V_s i_{co} - i_{co}^2 R_c] \quad (3.15)$$

Now on subtracting Eq.(3.14) and Eq.(3.15) we get

$$C_{dc}V_{dco} \frac{d\Delta V_{dc}}{dt} = \begin{bmatrix} V_s \Delta i_c - L_c i_{co} \frac{d\Delta i_c}{dt} \\ -2i_{co} \Delta i_c R_c \end{bmatrix} \quad (3.16)$$

The transfer function of converter $K_{con} = \frac{\Delta V_{dc}}{\Delta I_c}$ is obtained as

$$K_{con} = \frac{[V_s - L_c i_{co} s - 2i_{co} R_c]}{C_{dc} V_{dco} s} \quad (3.17)$$

In the voltage control loop, the HCC block is employed to provide necessary gate pulses to VSC. The output of PI is supplied to HCC and utilized to generate reference current.

For the modeling of PI controller, in Fig.3.6 the block $G_{pi}(s)$ represents PI regulator which consists of one proportional and one integral controller to regulate DC link voltage at reference value. The PI controller is used to regulate the DC link voltage to its reference value such that the steady state error estimated in V_{dc} reduces to zero. The control scheme is designed so that the grid compensates the converter losses. The PI controller depicted as $G_{pi}(s)$ block is represented as

$$G_{pi}(s) = K_p + \frac{K_i}{s} \quad (3.18)$$

where K_p is proportional gain and K_i is integral gain of the given system. Now using Fig.3.6 the transfer function of voltage control loop can be written as

$$T(s) = \frac{G_{pi}(s)K_{con}(s)}{1+G_{pi}(s)k_{con}(s)} \quad (3.19)$$

Substituting Eq. (3.17) and (3.18) and values of parameters mentioned in the Appendix, T(s) expression comes out to be

$$T(s) = \frac{110K_i + 110K_p s}{0.3s^2 + 110K_p s + 110K_i} \quad (3.20)$$

Appropriate values for PI gains need to be selected for proper control of the system. Accordingly, the step response and bode plot of the system are shown in Fig.3.7 and Fig.3.98 respectively. Table-3.2 shows the different combinations of K_p and K_i and the corresponding rise time, settling time and overshoot for step response, phase margin of the system evaluated from bode plot. From Table-3.2, K_p and K_i values are selected to be

0.55 and 15 respectively for which the response of the system is better and stability is ensured. The plots highlight fast settling time and good convergence achieved at moderate overshoot and satisfactory PM of 82.366° .

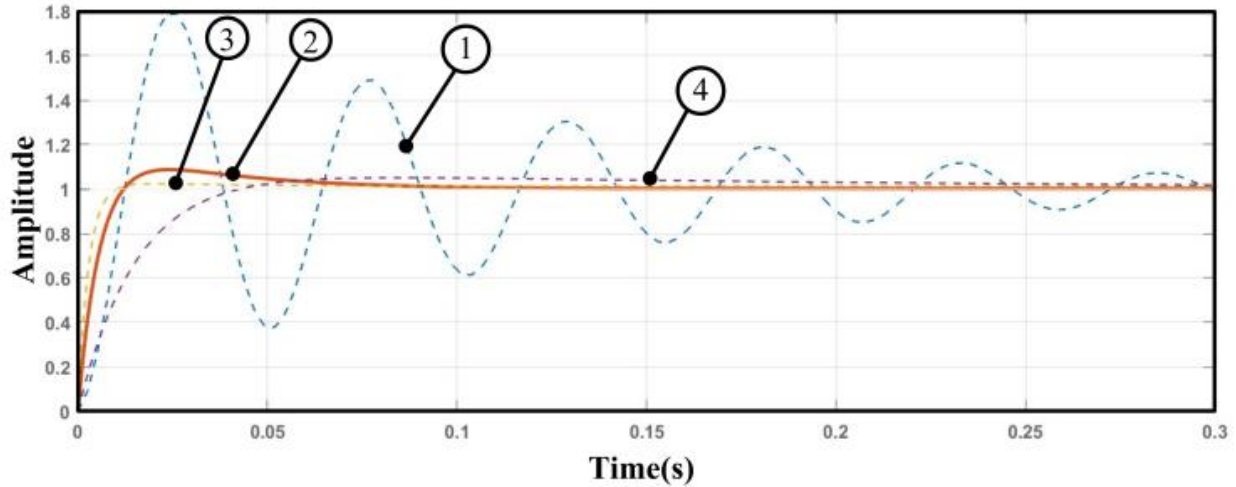


Fig.3.7 Step response of the system corresponding to different gain parameters

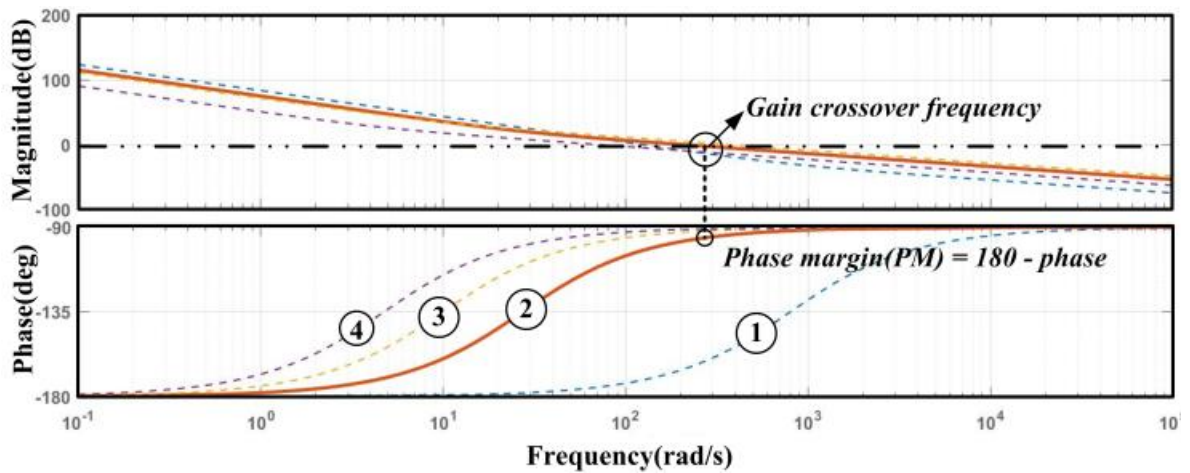


Fig.3.8 Bode plot of voltage control loop with different values of gains

Table 3.2. Choice of PI gain parameters

S.No.	K_p	K_i	PM(Phase margin($^\circ$))	Ts (Settling time(s))	Tr (Rise time(s))	% Overshoot
1	0.05	40	8.6572	0.4186	0.0088	78.88
2	0.55	15	82.366	0.0762	0.0083	8.768
3	1	10	88.438	0.1855	0.0056	2.338
4	0.19	0.9	86.119	0.2853	0.268	5.1195

3.2.6. Modeling of PV Array:

A solar cell can be modeled in several ways, taking various factors into account. The single-diode model with series resistance and parallel resistance is thought to be simpler to model and to be closer to the practical diode [22,81]. Fig. 3.9 depicts the single-diode model with series and shunt resistance.

By using KCL the equation of output current (I_c) is calculated as

$$I_c = I_{ph} - I_d - I_p \quad (3.20)$$

$$I_c = I_{ph} - I_o \left[\exp\left(\frac{V_c + IR_s}{a}\right) - 1 \right] - \frac{V_c + IR_s}{R_p} \quad (3.21)$$

where, I_{ph} is Photo Current, I_d is diode current, I_p is leakage current in parallel resistors and a is ideality factor can be defined as

$$a = \frac{N_s A k T_c}{q} \quad (3.22)$$

where, k = Boltzmann constant $=1.381 \times 10^{-23}$; $q=1.602 \times 10^{-19}$; A = diode ideality factor, whose value is considered to be 1.4 for silicon polycrystalline array module; N_s = no. of cells in series of PV array; T_c = temperature. In the MATLAB/Simulink the PV panel considered parameters are tabulated in Table 3.3

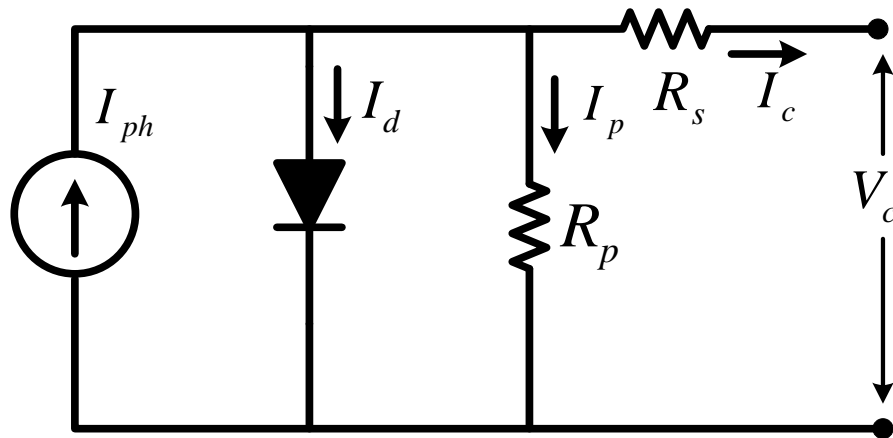


Fig. 3.9 Single Diode model of PV array

Table 3.3: User-defined parameters of PV array module

Parameters	Ratings
Maximum power	146.65W
Cells per module (N_{cell})	72
Open Circuit Voltage (V_{oc})	49.7V
Short Circuit Current (I_{sc})	4A
Voltage at maximum power V_{mp}	41.9V
Current at maximum power I_{mp}	3.5A
Shunt Resistance R_{sh}	116.32 Ω
Series Resistance R_{se}	0.569 Ω
Temperature coefficient of V_{oc} (%/deg.C)	-0.27
Temperature coefficient of I_{sc} (%/deg.C)	0.05

In this study, for the simulation performance the array is considered with number of series cells N_s as 5 and number of parallel cells N_p as 4 for 2.7kW of PV power output.

3.2.7. Design of DC-DC boost converter[156]:

A DC-DC converter is power electronics based circuit, which can step-up or step-down the level of the DC voltage. Boost DC-DC converter is used for stepping up the DC voltage shown in Fig.3.10. The output voltage of the boost converter can be written as

$$V_0 = \frac{V_{in}}{1-D} \quad (3.23)$$

where, V_0 is output voltage of the converter, V_{in} is the input voltage of the converter and D is the duty cycle of the converter which can be written as

$$D = \frac{T_{on}}{T} \quad (3.24)$$

where, T_{on} is the on time of the switch and T is the time period.

The performance of the boost converter will be determined by the values of the inductor and capacitor employed in the converter. With the volt-sec balance technique, the value of the inductor is determined for boost operation. This value determines the system's

ripple current as well as the mode of operation, such as continuous or discontinuous conduction mode. The inductor's value ought to be

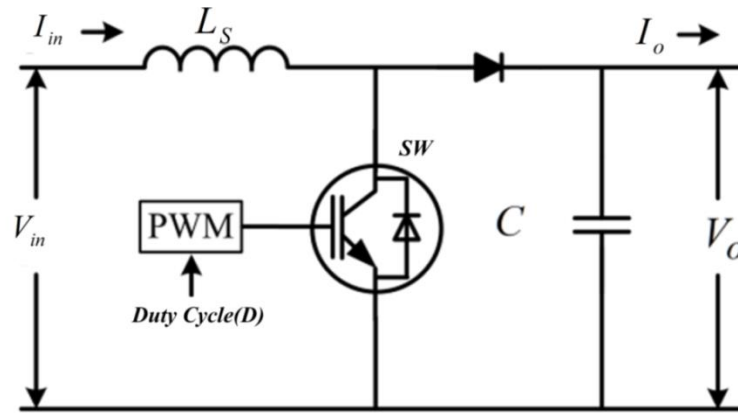


Fig.3.10 Layout of DC-DC boost converter

$$L_s \geq \frac{V_{in}D}{f_s \Delta I_0} \quad (3.25)$$

where, L_s is the source inductance of the boost converter, f_s is the switching frequency of the converter and ΔI_0 is the ripple in output current. For single phase VSC application $f_s = 5kHz$ and $\Delta I_0 = 30\%$ is considered.

The capacitance value can be calculated by using current-sec balance theory and it can be written as

$$C = \frac{DI_{0(max)}}{f_s \Delta V_0} \quad (3.26)$$

where, ΔV_0 is ripple in output voltage, for this application 2% ripple is considered.

Table.3.4 DC-DC converter parameter selected

S.no.	Parameter	Values
1	Switching Frequency	5kHz
2	Capacitor	~10uF
3	Inductor	2.5mH

3.3. Design and Development of Three-Phase VSC System:

Fig. 3.11(a) depicts a three-phase VSC configuration implemented as shunt compensator in three-phase three wire system. This arrangement has been evaluated under both normal and distorted grid voltage conditions. It is utilized for meeting reactive power demand of load and provides harmonic mitigation under non-linear or linear load conditions. The same configuration is also capable of handling low voltage ride through operation.

Fig. 3.12 depicts the system configuration for a grid-connected, three-phase, three-wire, single-stage PV system. A PV string or array is connected to the DC-link voltage of a three-phase VSC. A DC-DC converter is not required in this configuration. The MPPT method is used to generate the reference DC-link voltage (V_{dcref}). This technique can be used for low voltage ride through, harmonic reduction of grid current under linear and nonlinear load situations and active and reactive power correction.

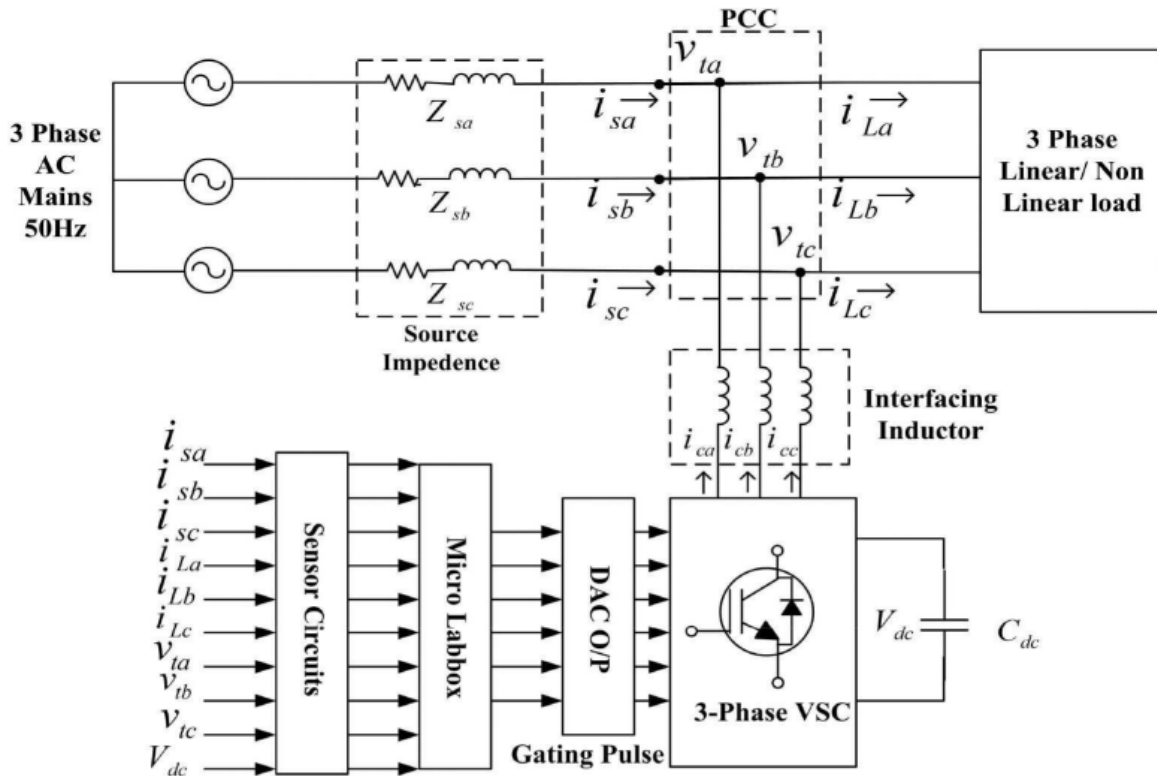


Fig.3.11(a) Configuration of three phase grid VSC system

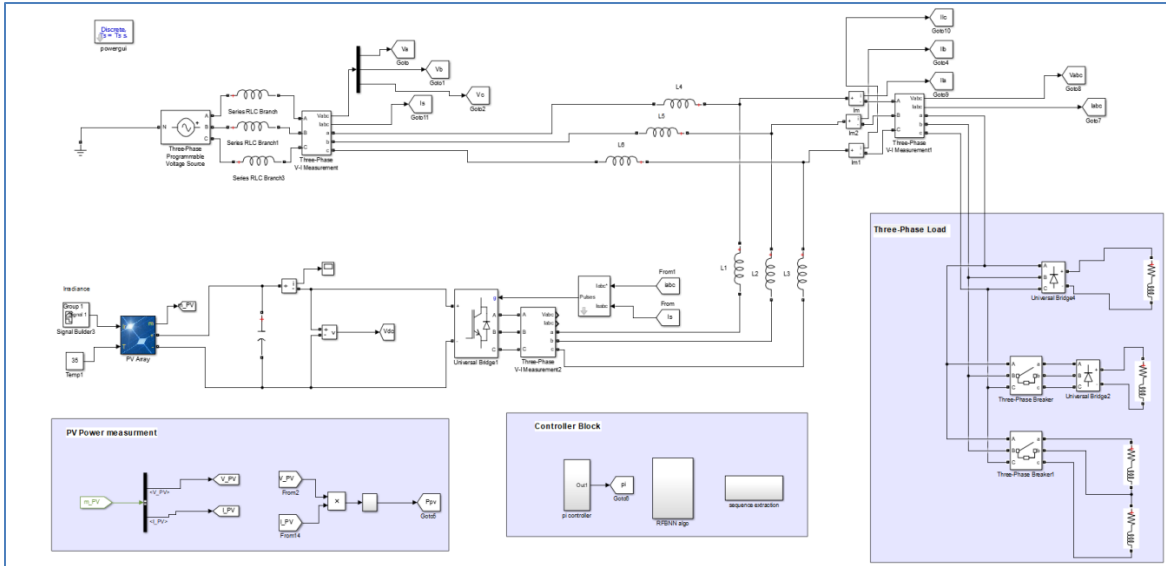


Fig.3.11(b) Matlab model of three phase system

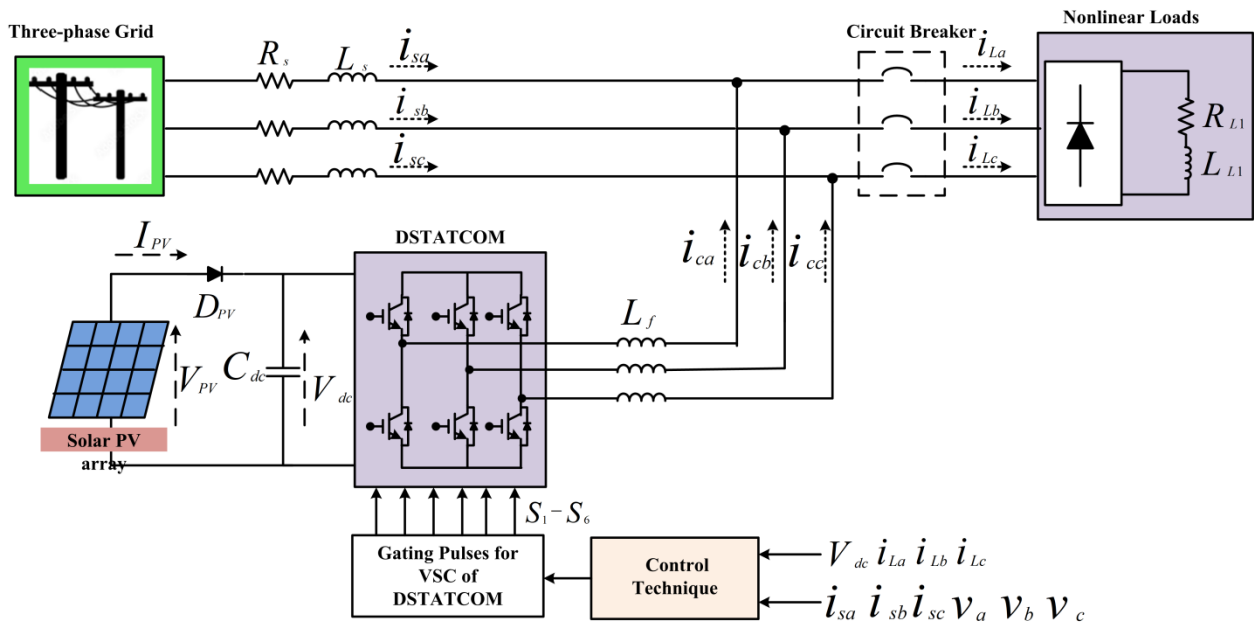


Fig.3.12 Three-phase VSC with single-stage grid connected PV system

Figure 3.13 depicts the system configuration of a grid-tied, triple-phase, double-stage PV system. This design uses a DC-DC boost converter to match the PV output with DC link voltage of VSC. The MPPT method is used to vary the duty cycle which is supplied to the DC-DC boost converter. Less number of PV modules can be used in this configuration compared to a single-stage grid-tied PV system. In addition, the design of

various systems has been discussed. HCC and the sensor component have already been covered. Simulation and experimental results consider different test case viz the normal balanced grid, the distorted grid, and low voltage conditions.

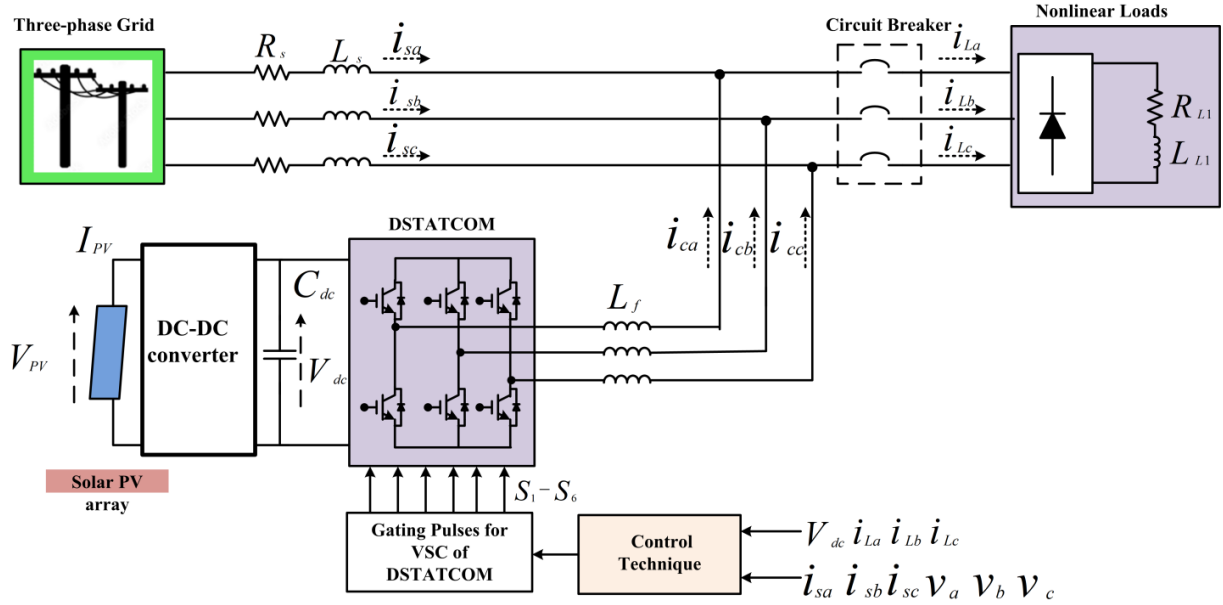


Fig.3.13 Three-phase VSC with double-stage grid connected PV system

3.3.1. Calculation of DC link voltage:

The DC link reference voltage of the system is depends on supply voltage of the system and it is expected that the DC-link voltage will be able to add reactive power to the grid. As a result, the applied grid voltage needs to be a little bit greater than the three-phase VSC's DC-link voltage [157]. The magnitude of the grid voltage can be calculated using the factor Eq. (3.27).

$$A_m = \frac{2\sqrt{2}v_{LL}}{\sqrt{3}} \quad (3.27)$$

where, A_m is the peak amplitude of AC phase voltage and v_{LL} is the line source voltage of three phase system . The rating of three phase system is 70V, 50Hz for the experimental system and 110V, 50Hz for simulation performance. The calculation of DC-link voltage can be given as:

$$V_{dc_{ref}} > A_m = \frac{2\sqrt{2}v_{LL}}{\sqrt{3}} \quad (3.28)$$

The dc reference value is calculated as 114.29V for experimental setup and set at 150V, for simulation the dc link reference voltage value is 155V and it set as 200V for the SAPF operation.

3.3.2. Calculation of DC link Capacitor

The input grid voltage and load current have a significant impact on the DC-link voltage of the VSC. For DC link voltage to be maintained throughout dynamics, the DC-link capacitance value must be high enough [157]. The DC link's capacitance can be calculated using the Eq. (3.29).

$$C_{dc} = \frac{6v_{ph}i_c h \tau g}{\left[V_{dc_{ref}}^2 - V_{dc_m}^2\right]} \quad (3.29)$$

where, v_{ph} is phase voltage of three phase system, i_c is the compensator current ($i_c = 25A$), h is overloading factor considered to be 1.2 for this application, τ is time constant for this application it is equal to 0.02sec, g is gain constant($g=0.04$), V_{dc_m} is the minimum dc link voltage ($V_{dc_m} = 155$) and $V_{dc_{ref}}$ is the DC link reference voltage ($V_{dc_{ref}} = 200V$).

3.3.3. Calculation of interfacing inductor

Current ripples are filtered out using an interface inductor. Better filtering is provided by inductors with greater values, but the loss is also higher [157]. As a result, it is crucial to properly build the interface or filter inductor (I_f), which is done by calculating by Eq.(3.30).

$$L_f = \frac{\sqrt{3}mV_{dc_{ref}}}{12hf_s\Delta i} \quad (3.30)$$

where, m is the modulation index, h is overloading factor, f_s is the switching frequency and Δi is the ripple current and it is considered 5% of the maximum current.

Table.3.5 Three-Phase VSC parameter selected

S.no.	Parameter	Simulation Values	Experimental Value
1	Supply Voltage	110V(L-L)	110V(L-L)

1	DC Link Voltage	200V	200V
2	DC Link Capacitor	1500 μ F	1500 μ F
3	Interface Inductor	3.5mH	3.5mH

3.4. Design and Development of Sensor Circuit:

3.4.1. Current Sensor Circuit:

LEM make LA-25P current sensor is used in the laboratory for sensing the grid and load current. It provides galvanic isolation between electronic and power circuits. According to the application, this transducer connection has been made as shown in Fig.3.14. With a conversion ratio of 1000:1, it provides a nominal value of 25A. A $\pm 15V$ supply is required to operate this sensor, and the output voltage is measured across resistance (R_{io}) and the further signal is fed to the amplification circuit. The experimental representation of current sensor is shown in Figure 3.14 and Fig.3.15(a) shows the schematic circuit diagram of current sensor. Fig.3.15(b) shows experimental circuit of current sensor circuit.

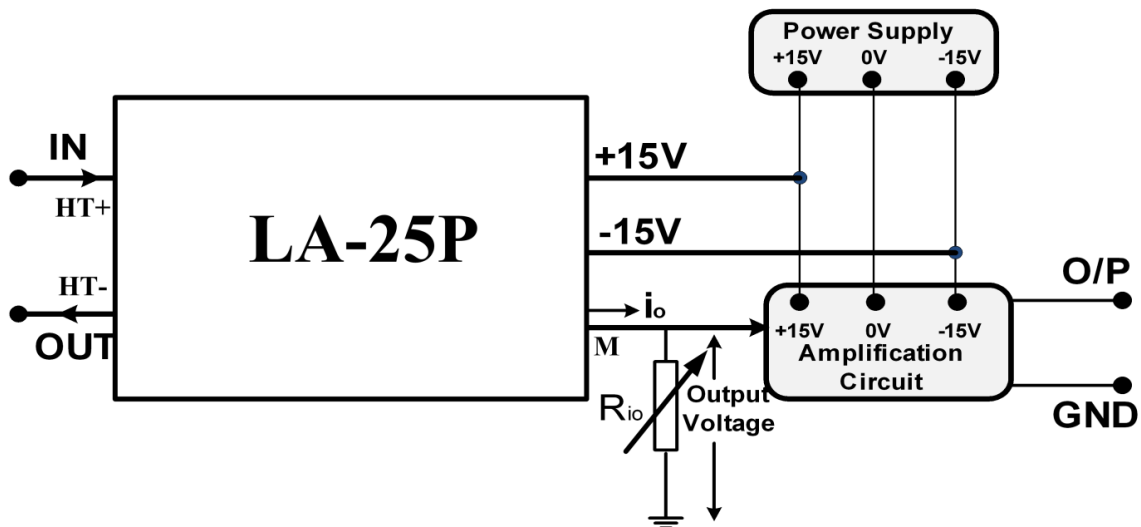


Fig. 3.14 Connection diagram of current sensor

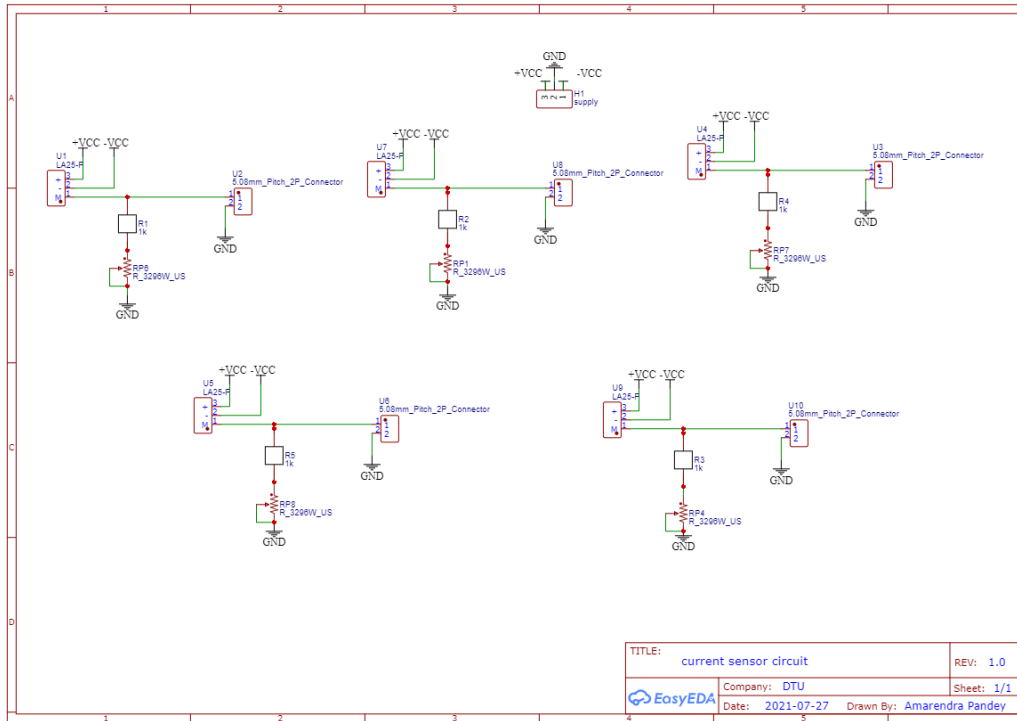


Fig.3.15 (a) Schematic diagram of current sensing circuit using EasyEDA

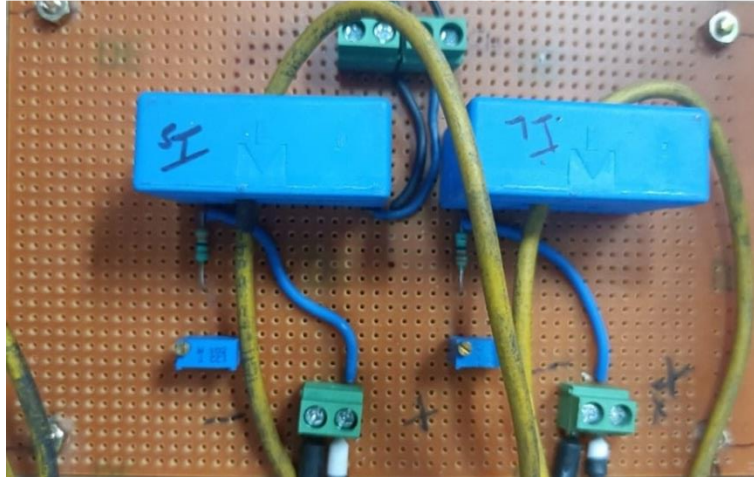


Fig.3.15(b) Experimental circuit of current sensor circuit

3.4.2. Voltage Sensor Circuit:

LEM make LV-25P voltage sensors which are used for sensing the PCC voltage and voltage across DC link capacitors. This sensor has a conversion ratio of 2500:1000; it provides the nominal value of 25V. A $\pm 15V$ supply is required to operate this sensor. The

input voltage signal is fed to +HT and -HT terminals; the output voltage is measured across terminal M across resistance (R_{vo}) and a further signal is provided to the amplification circuit. The experimental representation of voltage sensor is shown in Figure 3.16 and Fig.3.17(a) shows schematic diagram of voltage sensor circuit. Fig.3.17(b) shows experimental circuit of voltage sensor circuit developed in the laboratory.

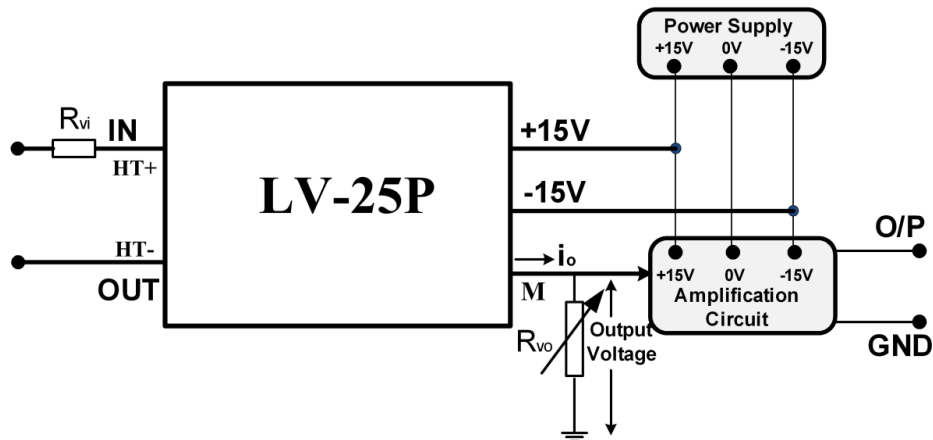


Fig. 3.16 Connection diagram of voltage sensor

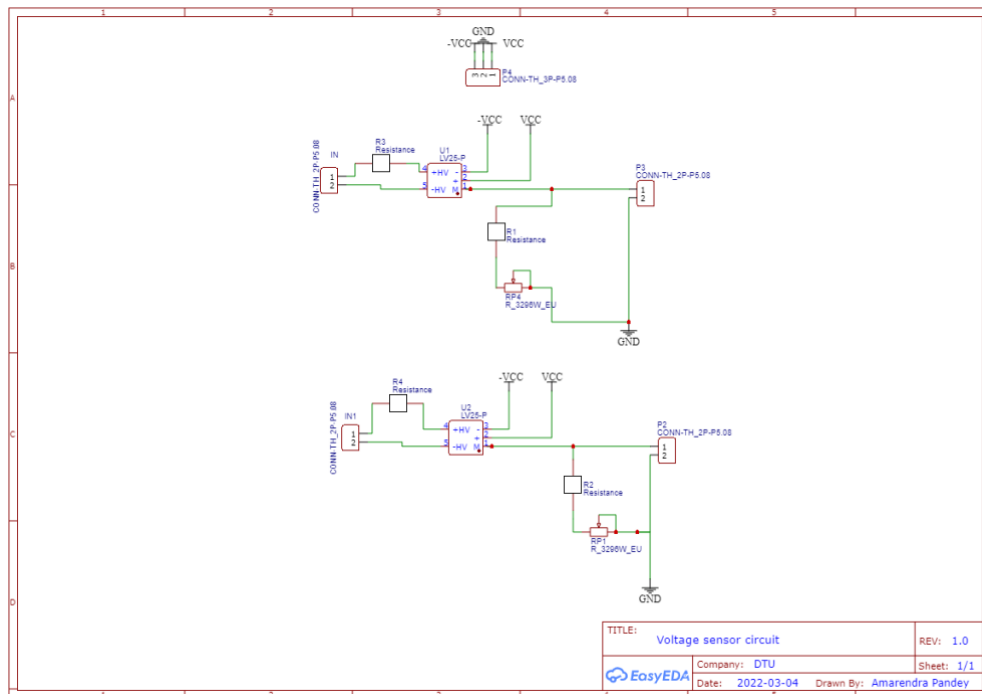


Fig.3.17(a) Schematic diagram of voltage sensor circuit drawn using EasyEDA

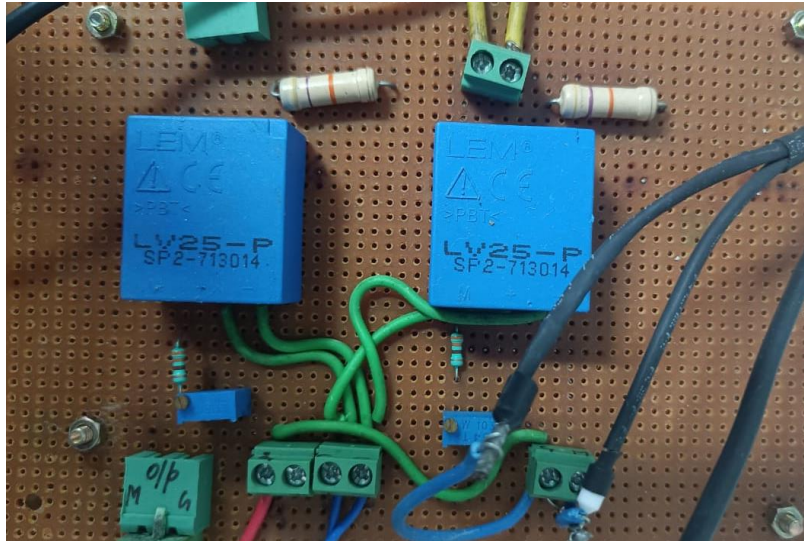
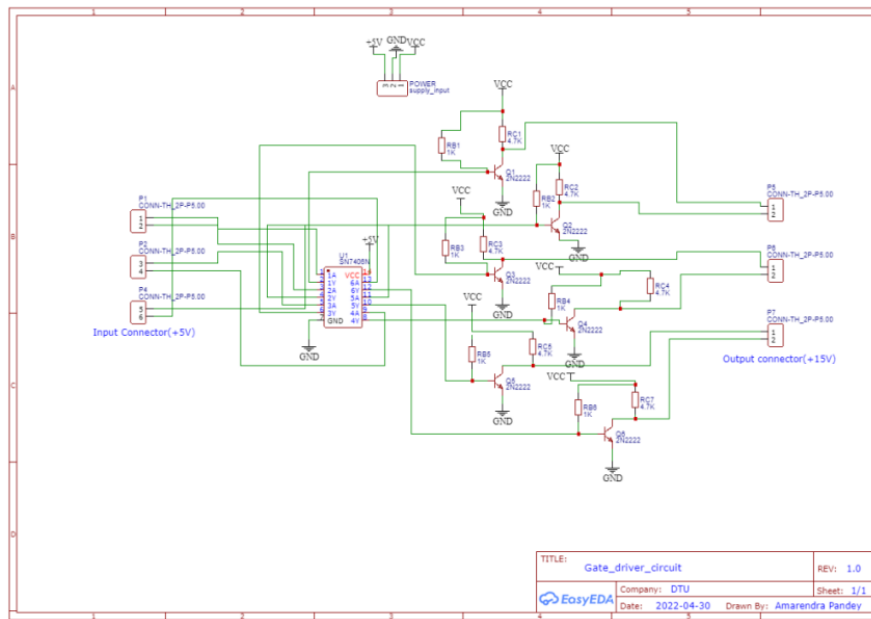


Fig.3.17(b) Experimental Circuit of voltage sensor circuit developed in the labortory



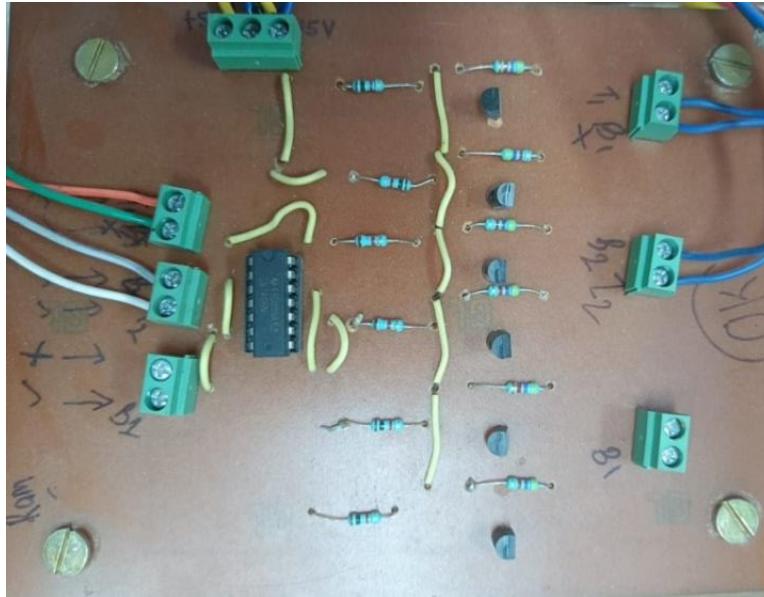
(a)

Fig. 3.18 (a) Schematic diagram of gate driving circuit using EasyEDA

3.5.Design of Level Shifter for IGBT Driver:

The dSPACE-1104/MicroLab box 1202 generates PWM signal of nearly +5V and the voltage to needed to trigger the IGBTs is +15V. Therefore, an amplification circuit has to be connected between the dSPACE-1104/MicroLab box 1202 and driver circuit

(SKYPER-32 pro) as shown in schematic circuit diagram of driver circuit in Fig. 3.18(a). It consists of AND Gate IC-7406 and transistor 2N222. IC required +5V DC supply and NPN transistor needed +15V DC supply to operate. The experimental model is shown in Figure 3.18 (b).



(b)

Fig. 3.18 (b) Practical Implementation of amplification circuit driver circuit

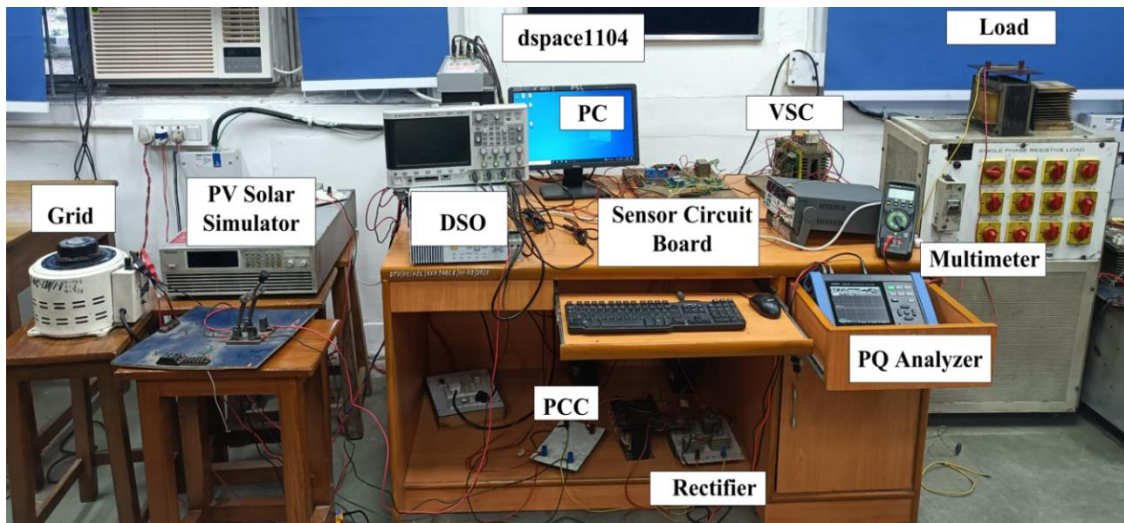


Fig.3.19 Experimental setup of single phase single-stage grid connected PV system

3.6. Single Phase Experimental Setup:

Fig.3.19 shows the experimental setup of single phase VSC controlled as a SAPF in single-stage grid connected PV system. The principle parts required for the setup are listed as follows: personal computer, single-phase programmable supply; dSPACE 1104 board; auxiliary DC supply; voltage and current sensors; H-bridge VSC; DSO; interfacing inductor; resistive load; load side inductor; diode bridge rectifier, programmable AC/DC supply.

Three-Phase Experimental Setup:

Fig.3.20 depicts the experimental setup developed for a three-phase grid-connected PV system.

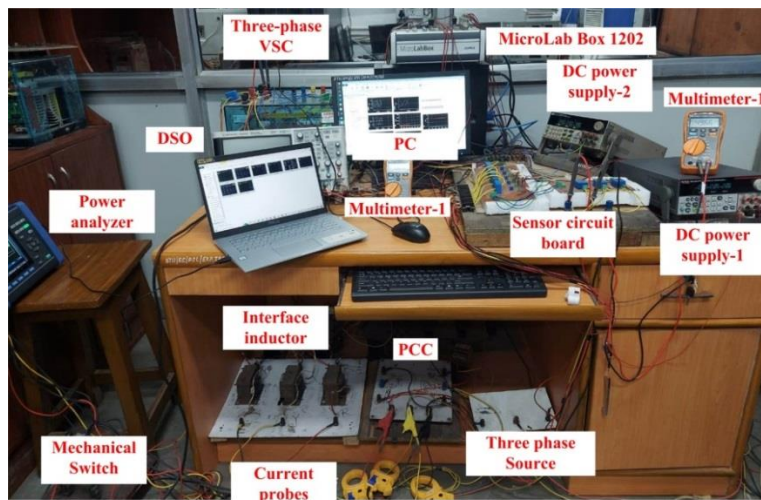


Fig.3.20 Experimental setup of three phase VSC system

The primary components are as follows: (1) PC (2) MicroLAB Box 1202 (3) Bridge rectifier (4) PV simulator (brand) (5) Programmable DC supply (6) Sensors and gating circuit (7) Three-phase VSC (8) Interfacing inductors (9) three-phase variable AC supply (10) Resistive load (11) Inductive load (12) DSO (13) Three phase programmable AC supply (build) (14) Power analyzer (HIKOI).

3.7. Conclusion:

This chapter provides a detailed discussion of the design and development of single-phase and three-phase grid-connected PV systems. Moreover, experimental prototype

setup figures, system configuration, and design equations have been shown. In single-phase and three-phase grid-connected PV systems, PV arrays of required rating can be connected in single-stage and double-stage configurations. It is important to enhance the quality of the power, offer reactive power compensation, inject active power into the grid, and meet the reactive power of the load. Hence these system configurations will be thoroughly tested in simulation as well as experimental prototypes in the upcoming chapters.

Chapter-4: Power Quality Improvement Techniques in Single and Three Phase Grid Connected PV System

4.1 Introduction

This chapter discusses controllers for VSC operating as a filter and it is designed to mitigate PQ problems. The PV panels maybe, integrated to VSC in one of two ways: single stage or double stage. A PV array coupled to a power distribution system has been described and designed in this work. The PV array of 2.7kW is connected to the system at the DC link of an H-bridge converter and is designed to function as an active shunt filter. Thus, studies on active filter connected to utility grid and RES integrated VSC are discussed in detail.

4.2 Basic Compensation Principle of Active Filters:

The fundamental block diagram for a shunt active filter is shown in the Fig.4.1. A shunt active power filter is designed to mitigate the effects of harmonic distortion and reactive power in electrical power systems. It works by injecting a compensating current into the power system to cancel out the harmonics and reactive power.

The basic compensation principle of a shunt active power filter is based on the concept of current control. The filter monitors the current in the power system and compares it to a reference current waveform. If the current contains harmonics or reactive power, the filter injects a compensating current into the system that is out of phase with the harmonic or reactive current. By doing so, the filter cancels out the undesired current components and restores the waveform to its original sinusoidal shape.

The compensation principle of a shunt active power filter involves several steps[158]:

Current sensing: The filter measures the current in the power system using a current transformer or other sensing device.

Current filtering: The filter removes any high-frequency noise or disturbances from the measured current signal.

Current reference generation: The filter generates a reference current waveform that represents the desired sinusoidal current without harmonics or reactive power.

Current comparison: The filter compares the measured current with the reference current waveform to determine the amount of harmonics or reactive power present.

Current injection: The filter injects a compensating current into the power system that is out of phase with the undesired current components. The compensating current is generated by an inverter that is controlled by the filter's control circuitry.

Feedback control: The filter continually adjusts the compensating current to ensure that the current in the power system remains sinusoidal and free from harmonics and reactive power.

By using this compensation principle, shunt active power filters can provide effective harmonic and reactive power mitigation in electrical power systems thereby improving power quality.

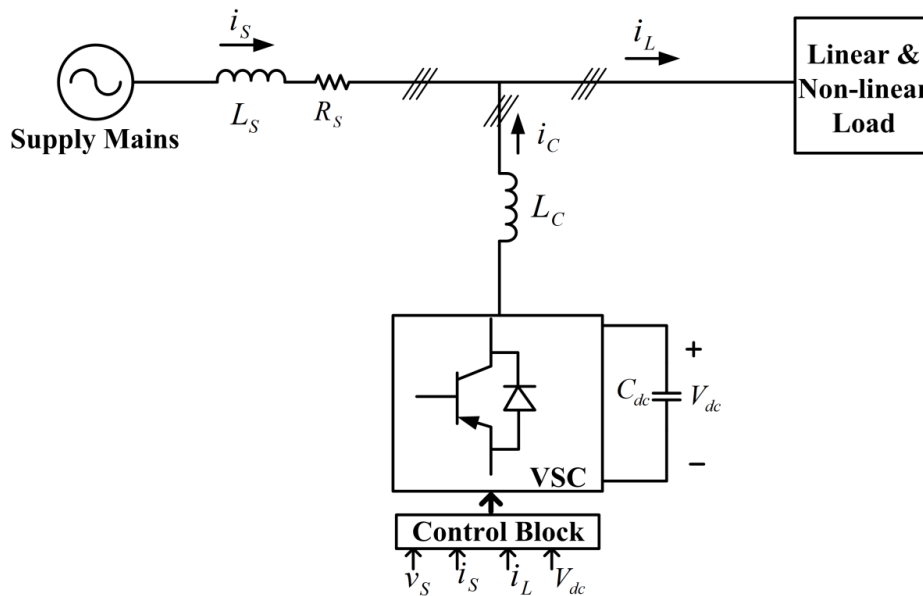


Fig.4.1 Basic diagram of shunt active filter (SAPF) for current harmonic compensation

4.3 Conventional Techniques for Extraction of Fundamental load Component in Single-Phase and Three-Phase System

Control methods required for VSC control are employed to estimate the reference supply currents. The observed PCC voltages, supply currents, load currents, and DC bus voltage of VSC are all inputs to the controller. The basic control algorithm processes these input signals and reference supply currents are estimated. The computed reference supply currents are compared to the detected supply currents in order to operate the hysteresis

current controller, which generates switching pulses for IGBTs of VSC utilized as a SAPF in single and three phase systems. Two conventional control techniques are briefly covered in this subsection. It includes the essential formulas needed and generates reference currents for VSC.

4.3.1 Synchronous Reference Frame (SRF) Technique:

Using the SRFT approach, the basic active power component of the load current is extracted in this section [159]. The SRFT is based on the transformations of load currents by Clarke and Park transformation to produce α , β load current components in three phase systems. The Clark transformation is used to convert three phase quantity into two phase quantity given in Eq.(4.1) and Park transformation is used to convert stationary two phase quantity into rotating two phase quantity given in Eq.(4.2). The two transformations involved are

I. Clark Transformation

$$\begin{bmatrix} i_{L\alpha} \\ i_{L\beta} \end{bmatrix} = \frac{\sqrt{2}}{3} \begin{bmatrix} 1 & -1/2 & -1/2 \\ 0 & \sqrt{3}/2 & -\sqrt{3}/2 \end{bmatrix} \begin{bmatrix} i_{La} \\ i_{Lb} \\ i_{Lc} \end{bmatrix} \quad (4.1)$$

II. Park Transformation

$$\begin{bmatrix} i_{Ld} \\ i_{Lq} \end{bmatrix} = \frac{\sqrt{2}}{\sqrt{3}} \begin{bmatrix} \cos\theta & \sin\theta \\ -\sin\theta & \cos\theta \end{bmatrix} \begin{bmatrix} i_{L\alpha} \\ i_{L\beta} \end{bmatrix} \quad (4.2)$$

where i_{Ld} is rotating axis direct component, i_{Lq} is rotating axis quadrature component, $i_{L\alpha}$ is stationary axis in-phase component, $i_{L\beta}$ is stationary axis out of phase component and i_{La}, i_{Lb}, i_{Lc} and phase load current of phase-a, phase b and phase c respectively.

For Single Phase System

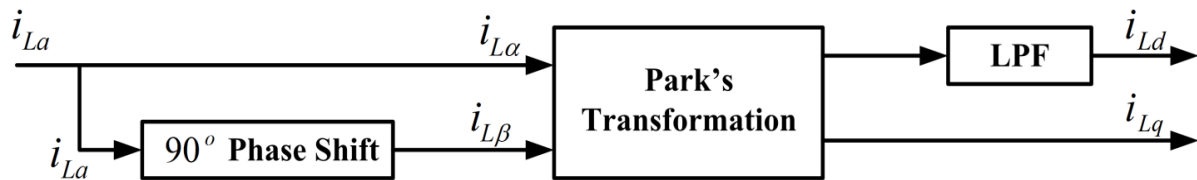


Fig.4.2(a) SRFT Control technique for single phase system

For single phase system the in-phase component and the quadrature-phase component are necessary for fundamental component estimation. The in-phase component $i_{L\alpha}$ is taken as the load current itself while a quadrature-phase component is obtained using 90° phase

shift as shown in Fig.4.2(a). The SRFT technique's estimation of the fundamental load current contains significant ripples and requires filtering; hence a low pass filter (LPF) has been used to remove the ripples.

For Three Phase System

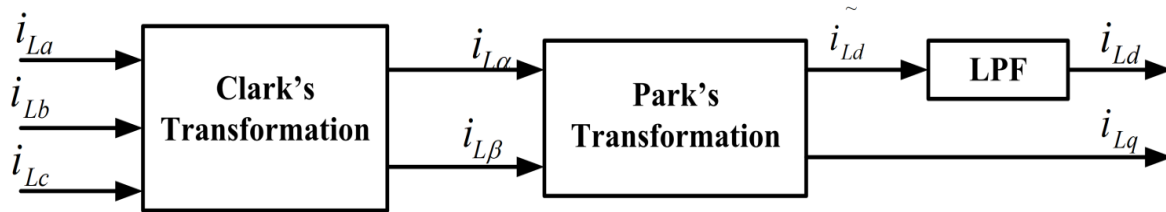


Fig.4.2(b) SRFT control technique for three phase system

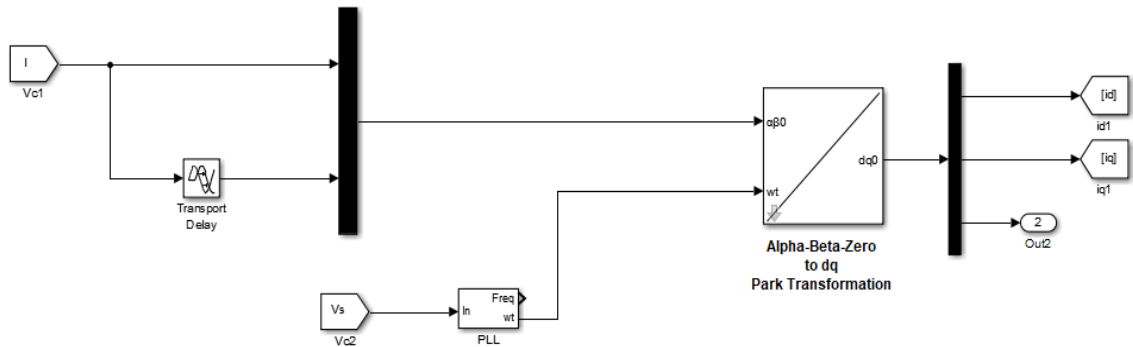


Fig.4.3(a) SRFT simulation model for single phase system

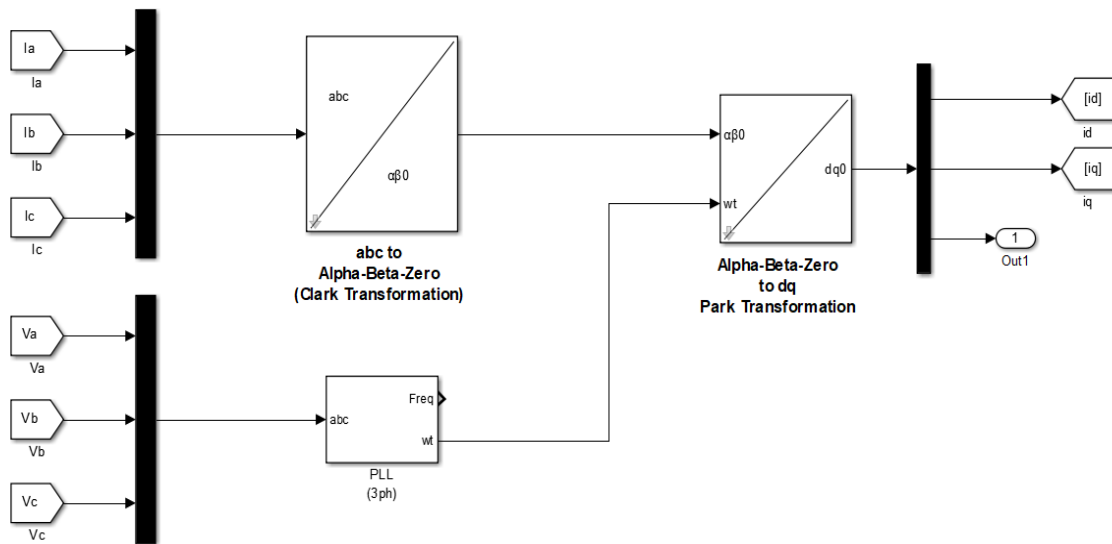


Fig4.3(b) SRFT simulation model for three phase system

4.3.2 Second Order Generalized Integrator(SOGI) Filter:

It is a second order generalized integrator which acts like band-pass filter (BPF) and low pass filter (LPF). The block diagram of SOGI is shown in Fig.4.4(a). SOGI controller produces two orthogonal outputs namely direct axis and quadrature axis at same frequency ω_o and having same amplitude [160]. The direct axis output ($i_{L\alpha}$) is in phase with input and quadrature axis output ($i_{L\beta}$) lags input by 90° . The transfer function shown in Eq.(4.3) and Eq.(4.4) acts like BPF and LPF respectively and gain (K) of SOGI filter decides the bandwidth of filter. The problem with the fixed gain SOGI controller is that it works best only under narrow range of operating conditions. Moreover, once tuned it is not possible to vary these gains.

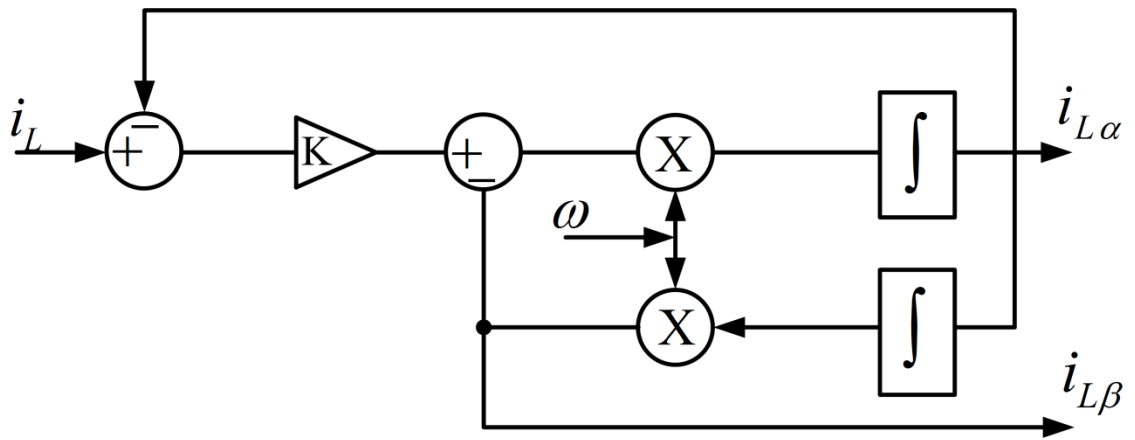


Fig.4.4(a) Design of SOGI filter with gain constant 'k'

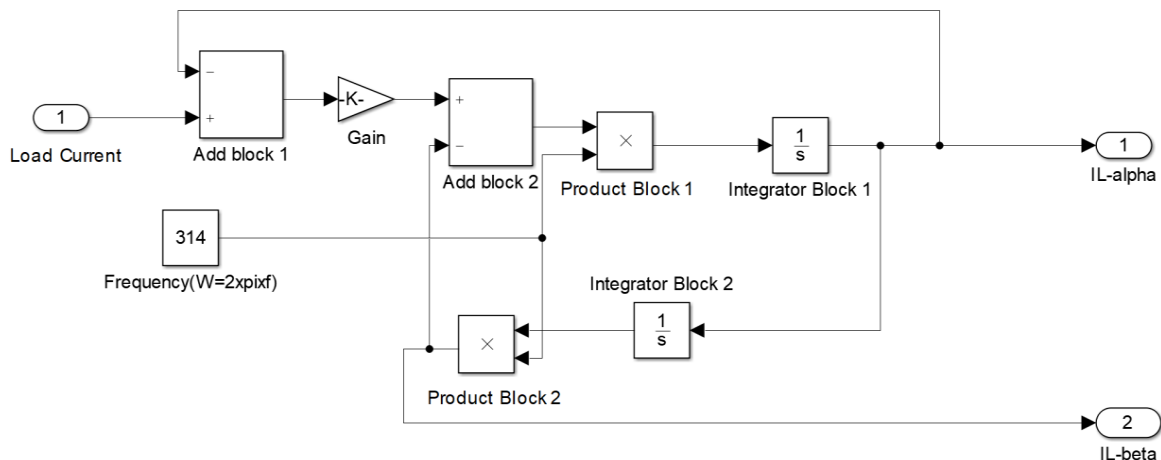


Fig.4.4(b) Matlab based SOGI model

$$\frac{i_{L\alpha}}{i_L} = \frac{K\omega_o S}{S^2 + K\omega_o S + \omega_o^2} \quad (4.3)$$

$$\frac{i_{L\beta}}{i_L} = \frac{K\omega_o^2}{S^2 + K\omega_o S + \omega_o^2} \quad (4.4)$$

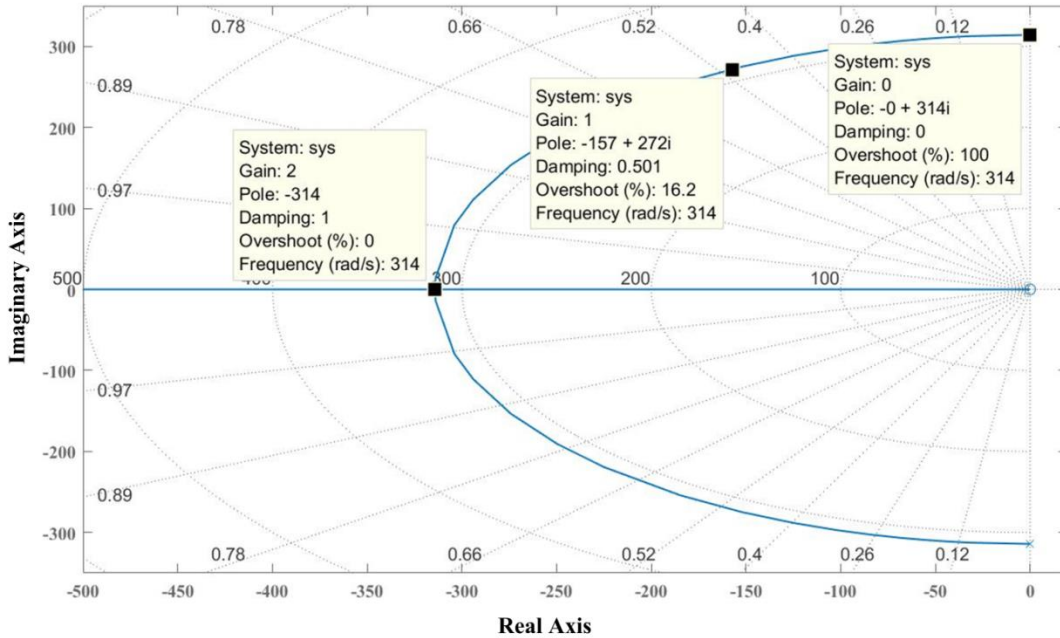


Fig.4.5 Root locus of SOGI filter

For stability analysis of the proposed system, root locus is shown in Fig.4.5 for different values of gain (k). The root locus is also analyzed in Fig.4.5 to check the stability of close loop transfer function. From the plot, it is clear that for $k = 0$ the system behaves like undamped system, for k in between 0 to 2 it behaves like underdamped system and for $k = 2$ it is critically damped system. A further increment in gain k leads the system to overdamped characteristics as shown in Fig.4.5.

The bode plot of BPF shown in Eq.(4.3) is shown in Fig.4.6 for different value of gain (k). It is observed from Fig.4.6 as the k increases; the bandwidth of filter increases and for lower value of k bandwidth decreases and becomes sharper. A sharper filtering action is required for effective BPF. Fig.4.7 shows the step response of Eq.(4.3) which shows a low value of k leads to a sluggish response and settling time is more. Effective filtering and fast response both are desired, and hence the value of k should be judiciously decided.

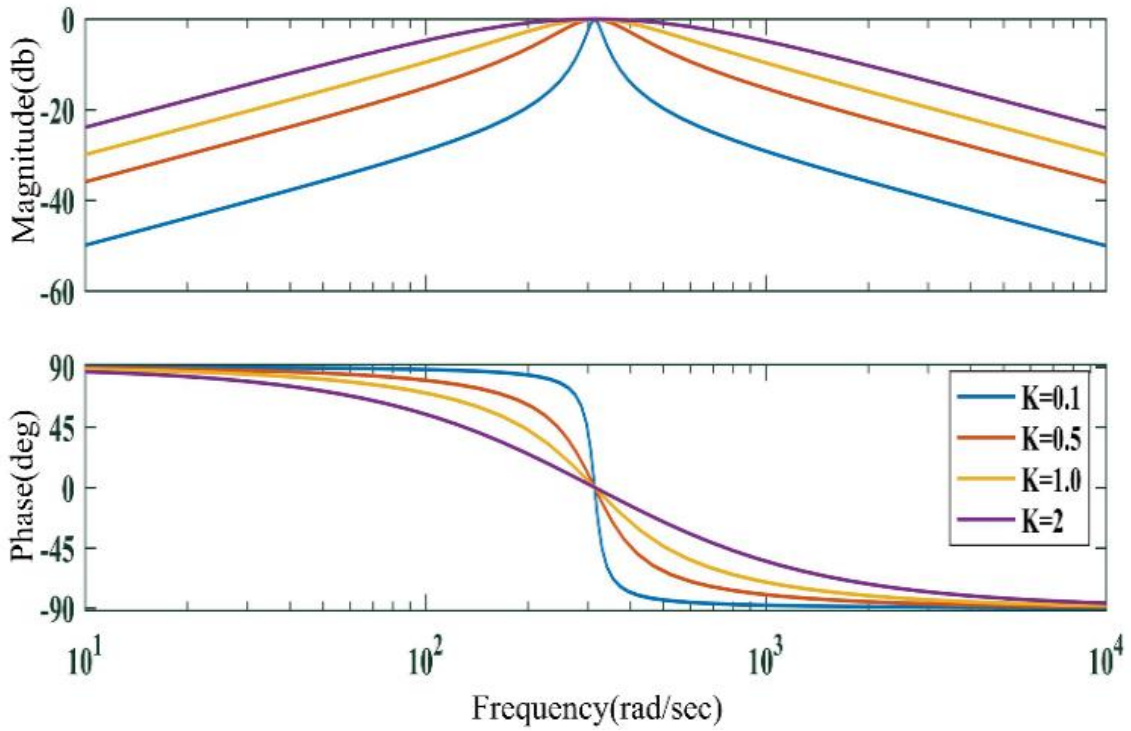


Fig.4.6 Bode diagram of SOGI filter using Eq.(4.3) different values of ' k '

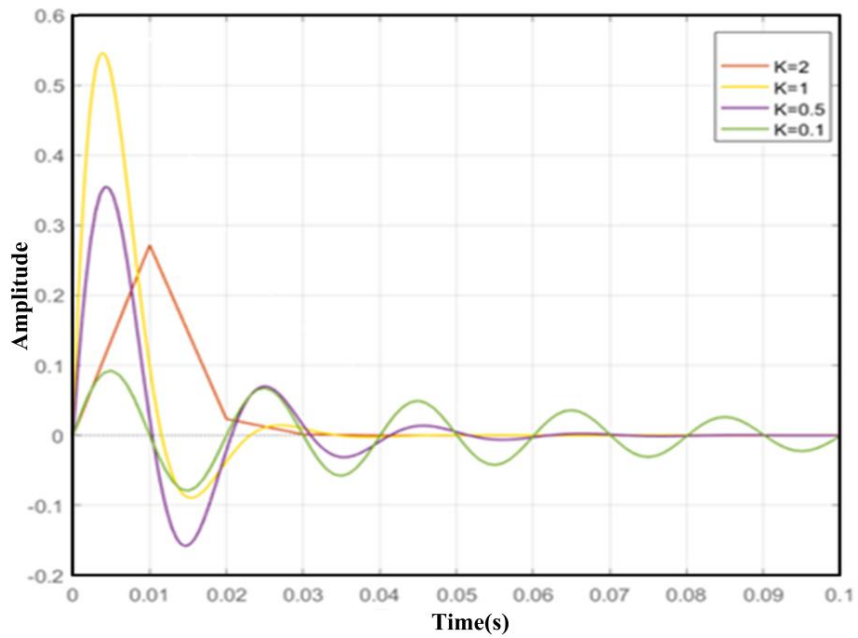


Fig.4.7 Step response of SOGI filter for different values of gain ' k '

The gain k is decided as 0.707 for the simulation purpose to be the most appropriate.

4.4. Techniques for Extraction of Fundamental load Component in Single-Phase and Three-Phase System:

In this section two new controllers have been briefly discussed, it includes the essential formulas needed and generates reference current for VSC.

4.4.1. RBFNN Controller

Fig.4.1 shows the schematic diagram of an H-bridge shunt compensator connected to a system feeding non-linear loads. The shunt compensator comprises four and six switches based on system which are effectively controlled using the RBFNN controller. For Implementation of RBFNN, gather training data and use k-means clustering to set the centers of the radial basis functions. Train the network by calculating activations with Gaussian functions and adjusting weights to minimize prediction error. Finally, evaluate the model's performance using metrics like Least Mean Squared Error (LMS) .The control scheme is designed to correctly track the fundamental component of load current under all load variations. The RBFNN technique is effectively designed to work as an adaptive filter and provide PQ improvement.

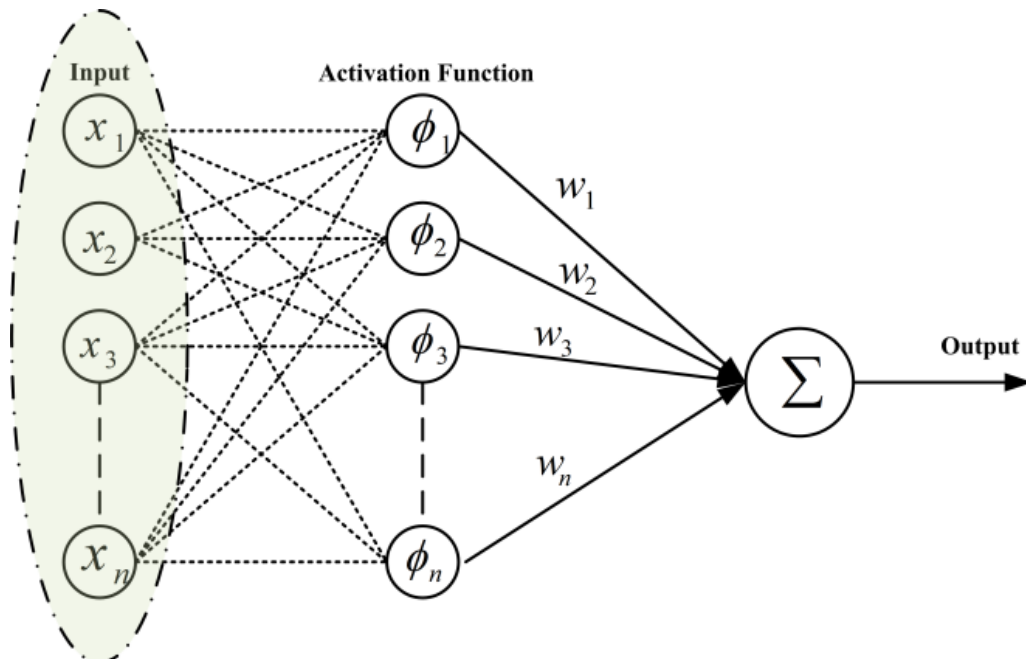


Fig. 4.8(a) Block diagram of General RBFNN Model

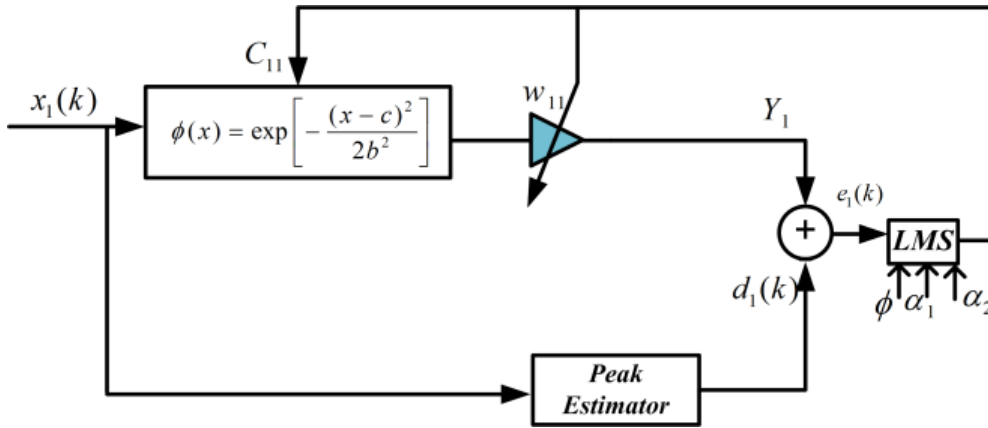


Fig. 4.8(b) Block diagram of proposed RBFNN single neuron based model

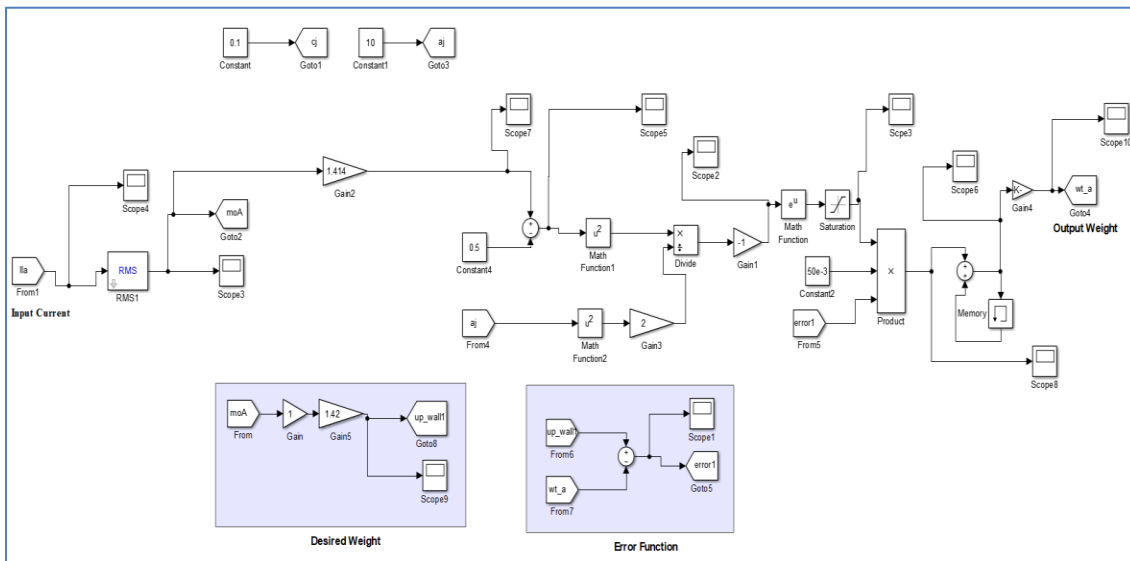


Fig. 4.8(c) Simulation model of RBFNN controller

Fig.4.8(a) shows the configuration of generalized RBFNN model with multiple inputs, multiple neurons in the hidden layer and a single output. This is the conventional method involving multiple weights of associated neurons and is a complex approach. The proposed adaptive RBFNN controller in Fig.4.8(b) shows the proposed configuration with one input (load current), single neuron in hidden layer and output (y_1) corresponding to the extracted weight. This network is trained online using the Least means Square (LMS) technique. Only two parameters viz. weight (w_{11}) and centre (c_{11}) are required to be trained to obtain the fundamental component of load current (Y_1). The

trained network can then be utilized for PQ improvement. The details of the proposed controller including the peak estimated current (d_1), error (e_1) and constants (α_1, α_2) are discussed in the next Section.

4.4.1.1 Mathematical Formulation

This Section discusses the mathematical details of the developed RBFNN controller. In Fig.4.8(a), the activation function (Φ_j) of the j^{th} node in the hidden layer is defined as

$$\Phi_j = \exp\left(-\frac{z_j^2}{2b_j^2}\right) \quad (4.5)$$

where $z_j = \|(X - c_j)\|$ and $X = [x_1, x_2, x_3 \dots \dots x_n]$ denote the input vector for the NN, $c_j = [c_{j1}, c_{j2}, c_{j3} \dots \dots c_{jn}]$ denotes the centre vector for the j^{th} node, b_j is basis width of the j^{th} node. The output of the generalized RFBNN model is computed using Eq.(4.6)

$$y_n(k) = w_1\Phi_1 + w_2\Phi_2 + \dots w_n\Phi_n \quad (4.6)$$

where $w_1, w_2, \dots \dots \dots w_n$ are the weights to be updated.

The conventional RBFNN controller in Fig.4.8(a) computes single output once all the weights have been tuned. In contrast, the proposed configuration in Fig.4.8(b) considers only a single neuron in the hidden layer which is updated using generalized LMS technique as shown in Eq.(4.7)

$$w_{kj}(k+1) = w_{kj}(k) - \alpha_1 \frac{\partial E}{\partial w_{kj}} \quad (4.7)$$

where α_1 is the convergence factor and <1 , the single weight w_{11} is updated as

$$w_{11}(k+1) = w_{11}(k) - \alpha_1 \frac{\partial E}{\partial w_{11}} \quad (4.8)$$

where $E = 0.5 * (d_1 - y_1)^2$ denotes the error and is computed using the desired output (d_1) and actual output (y_1), Substituting

$$\frac{\partial E}{\partial w_{11}} = -(d_1 - y_1)\Phi_1 \quad (4.9)$$

The weight equation is now updated as

$$w_{11}(k+1) = w_{11}(k) + \alpha_1(d_1 - y_1)\Phi_1 \quad (4.10)$$

Similarly, the center c_{ji} can be updated as

$$c_{11}(k+1) = c_{11}(k) - \alpha_2 \frac{\partial E}{\partial c_{11}} \quad (4.11)$$

where α_2 is another convergence factor <1 . Using the chain rule for derivatives,

$$\frac{\partial E}{\partial c_{11}} = \frac{\partial E}{\partial y_1} \frac{\partial y_1}{\partial \Phi_1} \frac{\partial \Phi_1}{\partial z_1} \frac{\partial z_1}{\partial c_{11}} \quad (4.12)$$

These partial derivatives are computed as

$$\frac{\partial E}{\partial y_1} = -(d_1 - y_1), \frac{\partial y_1}{\partial \Phi_1} = w_{11}, \frac{\partial \Phi_1}{\partial z_1} = -\frac{\Phi_1 z_1}{2b_1^2} \frac{\partial z_1}{\partial c_{11}} \text{ and } z_1 \frac{\partial z_1}{\partial c_{11}} = -(x_1 - c_1) \quad (4.13)$$

The updation for center, c_{11} is obtained as

$$c_{11}(k+1) = c_{11}(k) + \alpha_2 (d_1 - y_1) w_{11}(k) \frac{\Phi_1}{2b_1^2} (x_1 - c_1) \quad (4.14)$$

For simplification, b_1^2 is taken as 1.0. The diagram showing the online updation of weight and center for system is shown in Fig.4.8(b).

4.4.2. Bateman Polynomial based Controller:

Bateman polynomial (BP) was proposed by Bateman [161]. These BP polynomials belong to the family of orthogonal polynomials. There are numerous generalization extensions and application of the Bateman polynomials discussed in the literature [161-166]. The BP polynomials can be defined by the relation

$$F_n \left(\frac{d}{dx} \right) \text{sech}(x) = \text{sech}(x) P_n(\tan(x)) \quad (4.15)$$

where P_n is a Legendre polynomials. The BP function $F_n(x)$ satisfies recurrence relation for integer values of 'n'

$$(n+1)^2 F_{n+1}(x) = -(2n+1)x F_n(x) + n^2 F_{n-1}(x) \quad (4.17)$$

where n is integer.

$$F_0(x) = 1 \quad (4.18)$$

$$F_1(x) = -x \quad (4.19)$$

$$F_2(x) = \frac{1}{4} + \frac{3}{4}x^2 \quad (4.20)$$

The fundamental current of a load is estimated in this study using the approximation function $F_n(x)$, which is applicable to any function. In an ANN network, this polynomial function may simply replace the hidden layer. This means that BP-based algorithms can be designed to be faster and less resource-intensive than those based on multi-layer perceptron networks.

Fig.4.9(a) shows the new controller implementation based on adaptive Bateman polynomials. The input is the load current (i_L), and the output is the extracted fundamental weight (μ_L) of the load. The Least Mean Square (LMS) method is used to

train this network remotely. The basic component of load current may be obtained by training with just one parameter weight (w). This network's output is put to use in the order to enhance PQ.

The formula for weight updation using the LMS training approach is

$$w(k) = w(k - 1) + \alpha_1 e(k) F_n(k) \quad (4.21)$$

where α is learning rate and $w(k)$ is updated fundamental weight of respective phase.

Now μ_L

$$\mu_L = w(k) [\sum_{k=0}^n F_k(i_L)] \quad (4.22)$$

where $w(k)$ is weight of the system trained by LMS. Similarly for three phase system phase-a phase-b and phase-c weights are separately trained adaptively.

$$\mu_{La} = w_a(k) [\sum_{k=0}^n G_k(i_{La})] \quad (4.23)$$

$$\mu_{Lb} = w_b(k) [\sum_{k=0}^n G_k(i_{Lb})] \quad (4.24)$$

$$\mu_{Lc} = w_c(k) [\sum_{k=0}^n G_k(i_{Lc})] \quad (4.25)$$

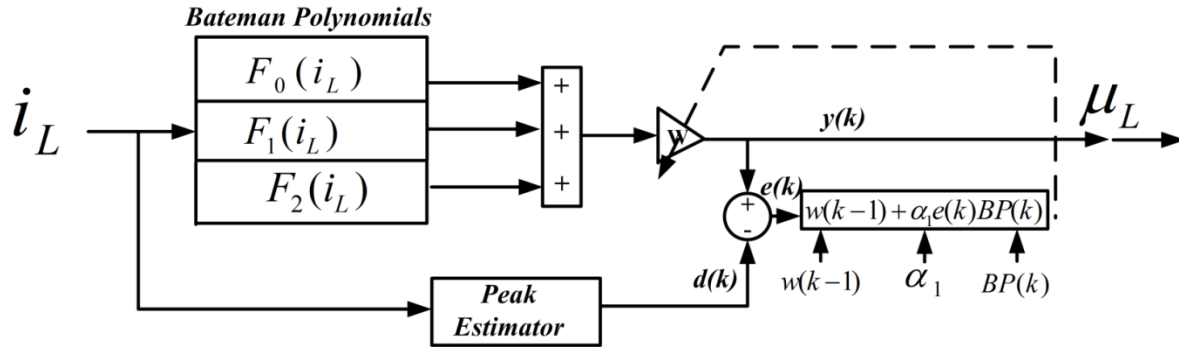


Fig.4.9(a) Proposed BP polynomial based adaptive controller

where $w_a(k)$, $w_b(k)$ and $w_c(k)$ are the respective weights of phase-‘a’, phase-‘b’ and phase- ‘c’ trained by LMS and μ_{La} , μ_{Lb} and μ_{Lc} are fundamental weights extracted for phase-a, phase-b and phase-c. The average weight of three-phase system is given by

$$\mu_{L(av)} = \frac{\mu_{La} + \mu_{Lb} + \mu_{Lc}}{3} \quad (4.26)$$

In this work PV has been integrated to the grid, to ensure maximum power transfer from PV to grid MPPT algorithm has been used and discussed in the following section.

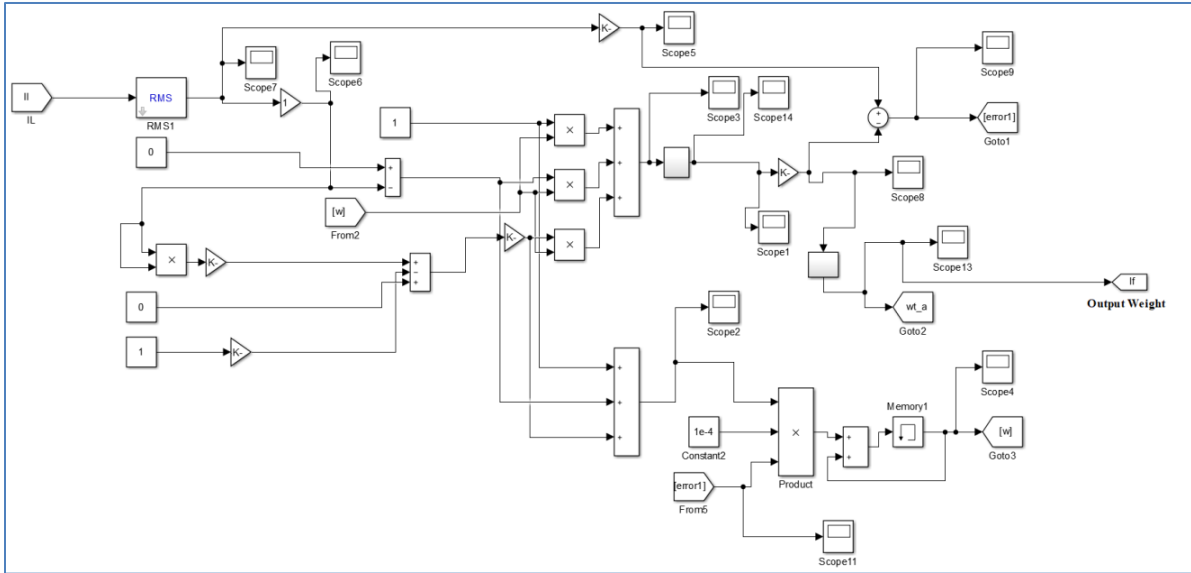


Fig.4.9(b) Simulation model of adaptive BP controller

4.5. PV Curves and MPPT Operation:

The environmental factors, in particular the temperature and irradiance, have a significant impact on the performance of PV. In section 3.1.6 the modeling of PV array has been discussed and for simulation performances a 2.7kW PV array has been used in this study.

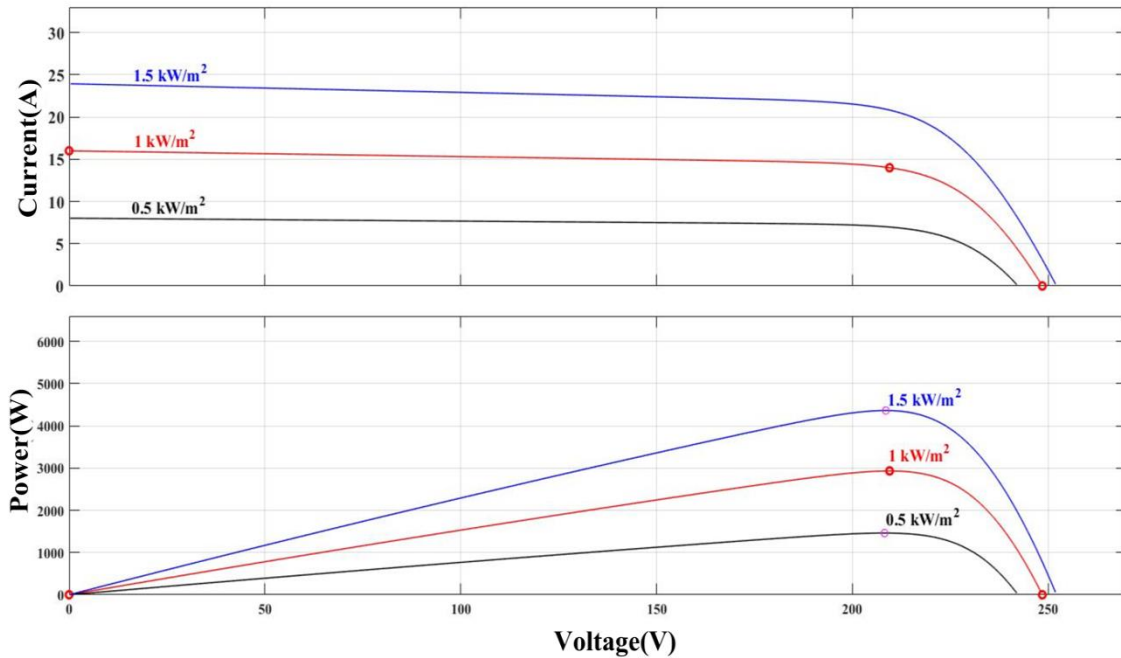


Fig.4.10(a) IV and PV curves for different values of irradiance at temperature 25⁰C

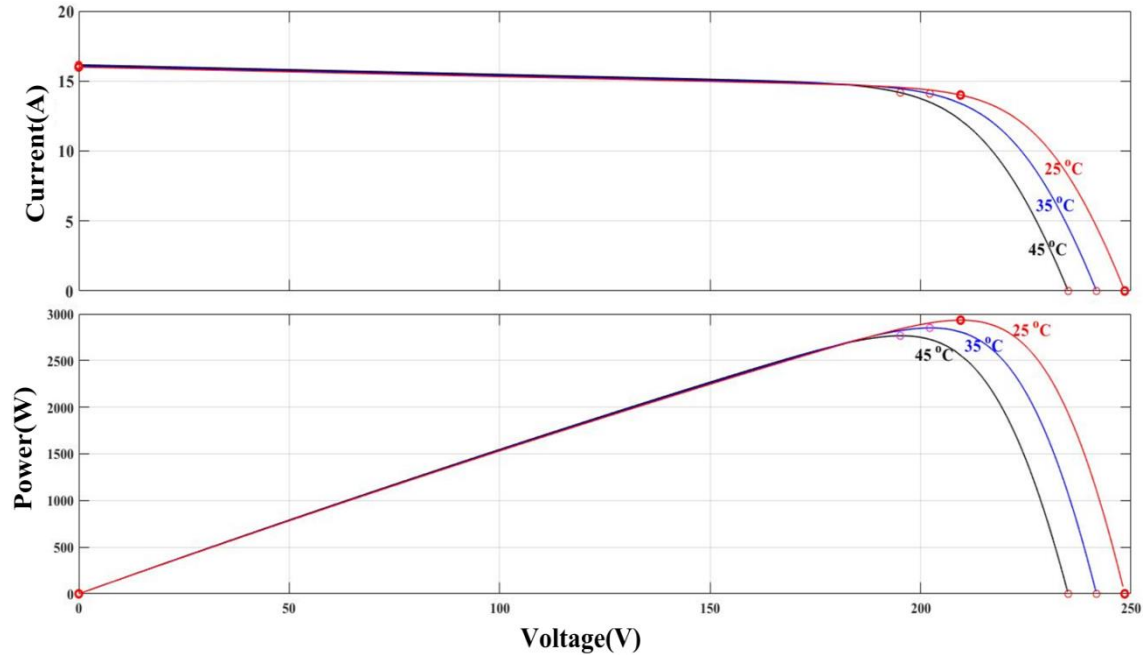


Fig4.10(b) IV and PV curve on different value of temperature at 1000W/m²

Fig.4.10 depicts a module's P-V and I-V curves. According to Fig. 4.10(a), the PV current and power change significantly when the irradiation changes. Fig.4.10(b) shows IV and PV curves on different value of temperature, with change in temperature the operating voltage point for maximum power (P_{mp}) changes considerably. The output power of a PV array is lower at higher temperatures and higher at lower temperature. Maximum power point is referred to as maximum power point (P_{mpp}), maximum power point voltage as maximum power point (V_{mpp}), and maximum power point current as maximum power point (I_{mpp}), respectively. To get the maximum power possible out of the PV module, string, or array, MPPT algorithm is necessary. P&O, Incremental Conductance (INC), and soft computing-based techniques like fuzzy logic and artificial neural network (ANN)-based algorithms are only a few of the MPPT algorithms that have been developed and used in the literature[102-103, 123-124]. P&O is one of the simplest and most straightforward algorithms out of all those addressed in the literature. It also offers good tracking performance. Fig.4.11 depicts the P&O algorithm flow-charts for a single-stage grid-connected PV system. The technique is based on obtaining voltage and current samples at regular intervals, it calculates power using those data, compares it to previously obtained power values, and predicts the maximum power at voltage (V_{mpp}).

Given in Eq.(4.27), the mathematical expression for the P & O algorithm for single-stage grid-connected PV systems yields V_{mpp} and is subsequently used as V_{DCref} .

$$\begin{cases} V_{new} = V_{old} + \Delta V & \Delta P \times \Delta V > 0 \\ V_{new} = V_{old} - \Delta V & \Delta P \times \Delta V < 0 \\ V_{new} = V_{old} & \Delta P \times \Delta V = 0 \end{cases} \quad (4.27)$$

The voltage step size used in Eq.(4.26) to update the reference maximum power voltage at each step is denoted by the symbol ΔV . In Eq.(4.28), the mathematical expression for the P & O algorithm for a double-stage grid-connected PV system with duty-cycle generation and DC-DC boost converter input is provided.

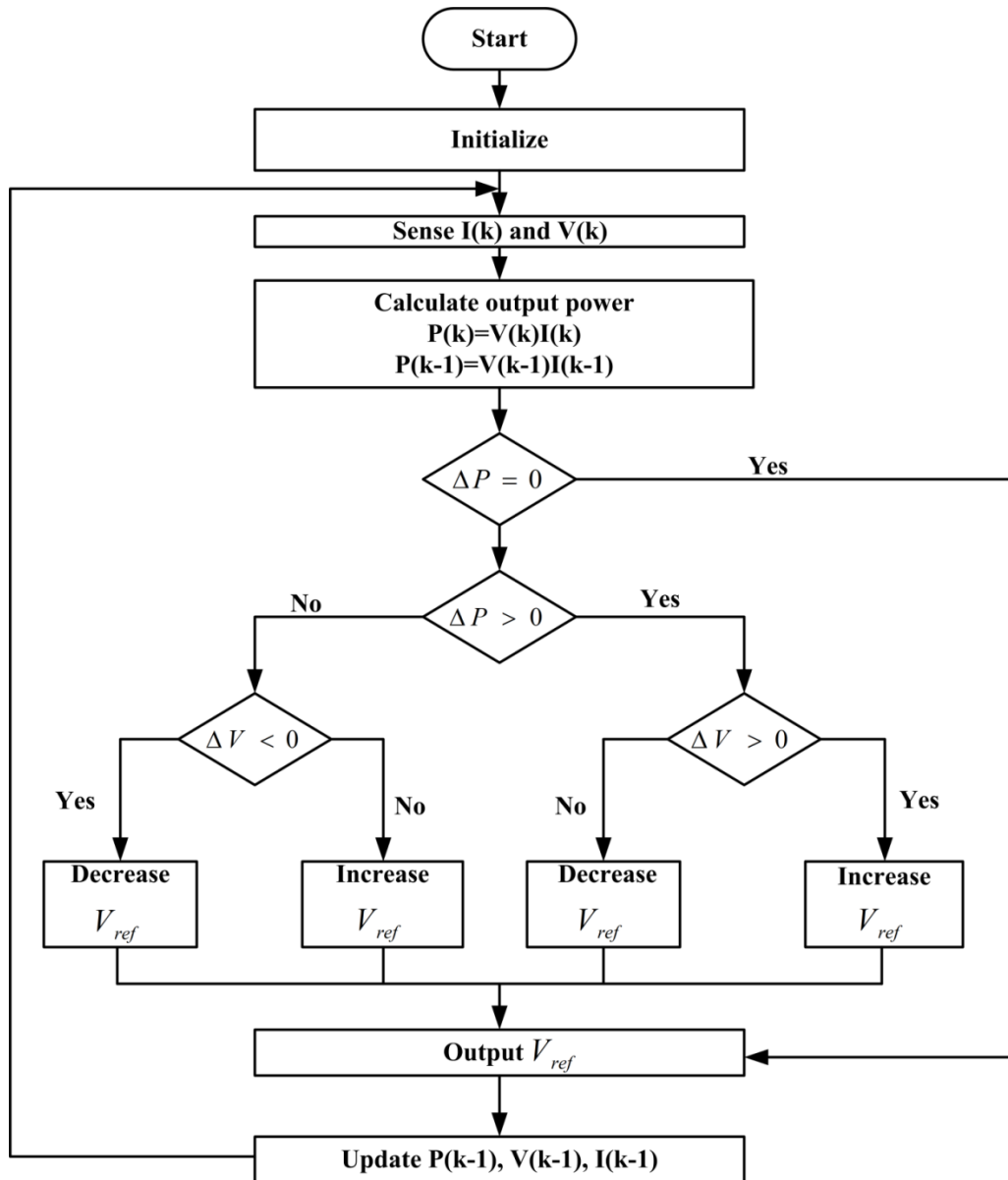


Fig. 4.11 Flowchart of P & O MPPT algorithm[167]

$$\begin{cases} D_{new} = D_{old} + \Delta D & \Delta P \times \Delta V > 0 \\ D_{new} = D_{old} - \Delta D & \Delta P \times \Delta V < 0 \\ D_{new} = D_{old} & \Delta P \times \Delta V = 0 \end{cases} \quad (4.28)$$

Here, D stands for the inverter's duty cycle, and ΔD stands for the step-size to update D 's value. While a bigger step-size results in a quicker reaction, it also causes higher oscillations, which are undesirable because they continuously vary the output voltage. Because of this, an optimal value of $\Delta V = 0.1V$ for a single-stage system and $\Delta D = 0.001$ for a double-stage grid-connected PV system have been chosen.

4.6. Feed-Forward Current Estimation:

With VSC, the PV array transfers active power to the electrical system in accordance with its capacity and rating. In ideal case, the power generated by PV is delivered to the grid in an amount that is equal to the active power measured at the output of VSC ($P_{pv}=P_c$), however there is a small loss in the inverter. In this case, P_{pv} stands for the power produced by the PV, while P_c is the AC side power of the VSC. At a DC link, power is computed as follows:

$$P_{pv} = V_{pv}I_{pv} \quad (4.29)$$

Active power calculated for 'a' phase at ac side of the inverter

$$P_c = V_{rms}I_{rms} = \frac{V_t I_{ff}}{2} \quad (4.30)$$

Here, V_t is the maximum magnitude of the voltage signal for single phase system generated by using second order generalized integrator (SOGI) filter.

$$V_t = \sqrt{v_{sp}^2 + v_{sq}^2}; u_p = \frac{v_{sp}}{v_t} \quad (4.31)$$

where V_t is maximum amplitude of voltage signals and v_{sp} is in-phase and v_{sq} is quadrature components.

For three-phase system V_t is given by

$$V_t = \frac{2}{3} \sqrt{v_a^2 + v_b^2 + v_c^2} \quad (4.32)$$

where v_a, v_b and v_c are the phase voltages of three phase system. I_{ff} is the feed forward current or peak current magnitude of the VSC current which is injected to the grid.

For single phase system:

I_{ff} for single phase system is calculated by using Eq.(4.29), Eq.(4.30) and Eq.(4.31).

Thus I_{ff} is given by Eq.(4.34)

$$P_{pv} = P_C = \frac{V_t I_{ff}}{2} \quad (4.33)$$

$$I_{ff} = \frac{2P_{pv}}{V_t} \quad (4.34)$$

For three-phase system:

I_{ff} for three-phase system is calculated by using Eq.(4.29), Eq.(4.30) and Eq.(4.32). Thus

I_{ff} will be

$$P_{pv} = P_C = 3 \frac{V_t I_{ff}}{2} \quad (4.35)$$

$$I_{ff} = \frac{2P_{pv}}{3V_t} \quad (4.36)$$

4.7. Loss Component Estimation:

In practice, unexpected transients impact the system performance owing to rapid changes in load. Monitoring and regulating the DC link voltage (V_{DC}) is crucial for efficient SAPF compensation service. It is important to regulate DC link voltage and to reduce the error in DC link voltage (V_{DC}), a typical conventional proportional-integral (PI) feedback controller is required and may be easily constructed. The error can be expressed as follows:

$$e_{DC} = V_{DCref} - V_{DC} \quad (4.37)$$

For switching losses requirement, the reference value of DC link (V_{DCref}) is subtracted from real time DC link voltage (V_{DC}), and thus switching loss will be estimated as

$$w_{loss} = k_p e_{DC} + k_i \int e_{DC} dt \quad (4.38)$$

where, k_p and k_i are the PI controller's proportional and integral gains.

4.8. Generation of Switching Pulses:

The overall active power demand of the load is computed by estimating the basic active power component of load current and the loss component determined from dc link voltages (V_{DC}).

$$w_{eff} = w_{loss} + w_p - I_{ff} \quad (4.39)$$

where w_p is output fundamental weight of load current of the system. Furthermore, for the single phase system, the required fundamental reference current (i_s^*) is calculated by multiplying the predicted fundamental active component of the load (w_{eff}) by the unit in-phase component (u_p).

$$i_s^* = w_{eff} \times u_p \quad (4.40)$$

where u_p is unit vector template

$$u_p = \frac{v_{sp}}{v_t} \quad (4.41)$$

Similarly, for the three-phase system, the required fundamental reference currents (i_{sabc}^*) is calculated by multiplying the predicted fundamental active component of the load (w_{eff}) by the unit in-phase component (u_{abc}).

$$i_{sabc}^* = w_{eff} \times u_{abc} \quad (4.42)$$

where u_{abc} denotes unit vector templates for the three respective phases

$$u_a = \frac{v_{sa}}{v_t}; u_b = \frac{v_{sb}}{v_t}; u_c = \frac{v_{sc}}{v_t} \quad (4.43)$$

Hysteresis current controller (HCC) is used for its simplicity and robust working for generation of switching signals. According to Fig.4.12, the hysteresis current controller (HCC) block creates gate pulses by comparing the measured source current (i_s) with the reference current (i_s^*).

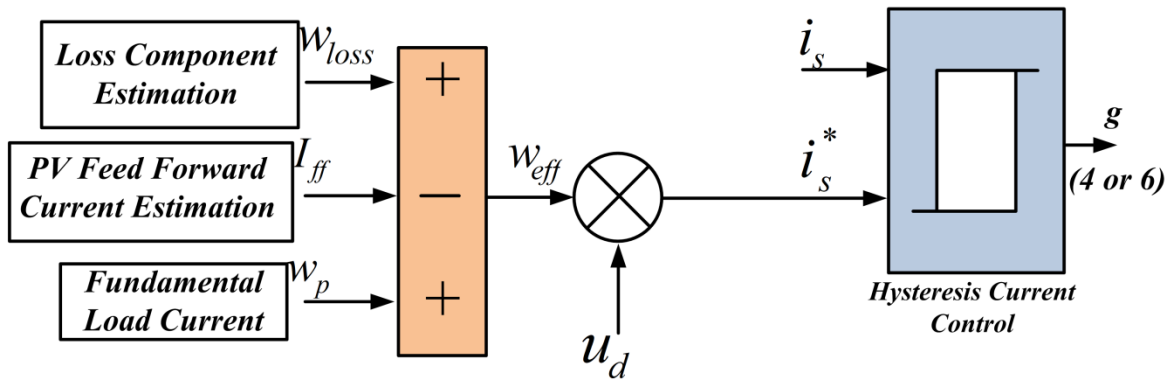


Fig.4.12 Switching Pulse Generation

4.9. Performance Analysis of Single-Phase and Three-Phase System:

The next section provides a detailed study of the given controller's performance for both with and without solar power.

4.9.1. Simulation Performance of Single Phase System:

This Section presents the results with the SRF, SOGI, adaptive BP based controller and adaptive RBFNN technique for a single-phase grid-connected system with/without PV integration. A 2.7kW PV array is integrated to power distribution system feeding non-linear loads and linear loads. The system is simulated and its operation under various conditions is investigated using Simulink/ MATLAB.

4.9.1.1. Simulation Performance with SRF Technique of Single Phase System:

Fig.4.13 shows the simulation results of intermediates parameters of SRF control algorithm on load change. It shows load current (i_L), load current d-component (i_{Ld}), load current quadrature q-component (i_{Lq}) and output fundamental weight.

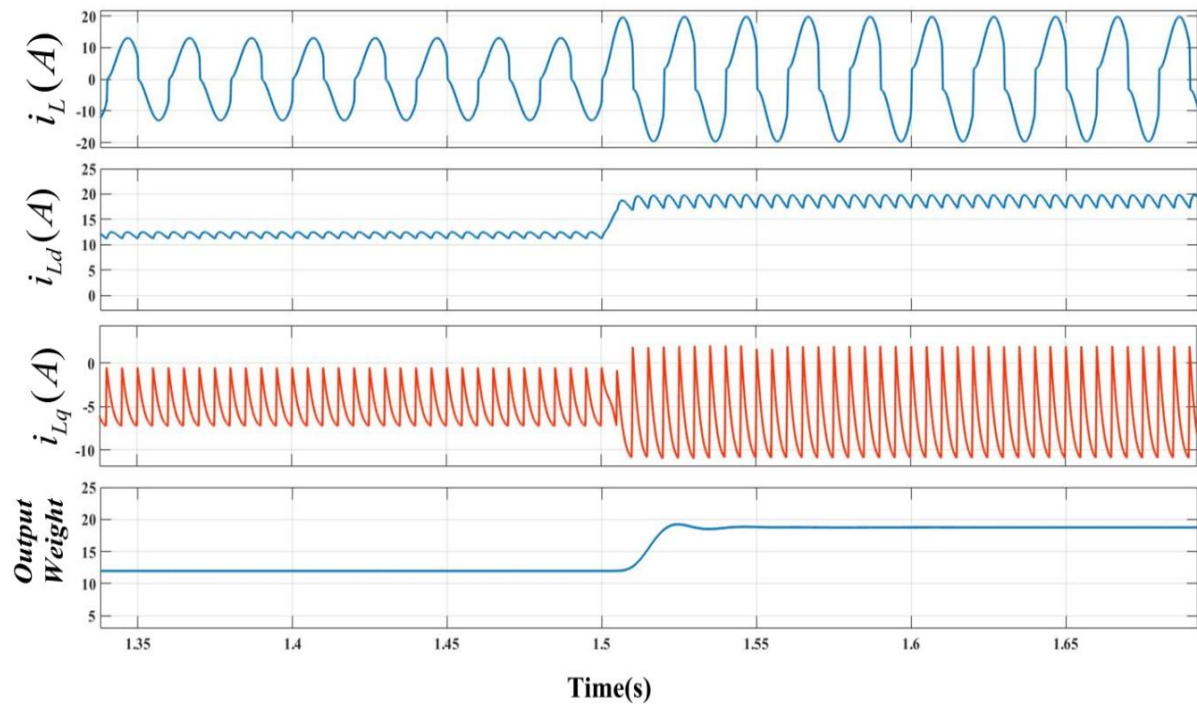


Fig.4.13 Intermediate performance of SRF technique (a) load current (i_L), (b) load current d- component (i_{Ld}), (c) load current quadrature q-component (i_{Lq}) (d) output fundamental weight

Fig.4.14 shows the schematic diagram of single-phase VSC controlled by SRF control technique. Fig.4.15 shows simulation performance of SRF control algorithm during the variation from day time tonight time and linear, non-linear load variation for single phase grid connected 2.7kW of PV system. Fig.4.15 shows the plots for supply voltage(v_s), supply currents (i_s), load currents (i_L), compensator currents (i_c), DC link voltage (V_{dc}) and irradiance (I_{rr}). At starting time day mode is present, the irradiance is assumed to be a constant value 1000W/m^2 . At $t=1.0\text{s}$ linear load is inserted and at $t=1.3\text{s}$ non-linear load is inserted into the system. At $t=1.6\text{s}$ night time is simulated and irradiance level is decreased till 0W/m^2 . Hence, the PV output power becomes zero during this period. During day time of operation the grid receives power from PV and due to this the source voltage and current is out of phase similarly during night mode of operation PV power become zero so the requirement of the load is supplied by source thus during this time source voltage and current in in-phase to each other.

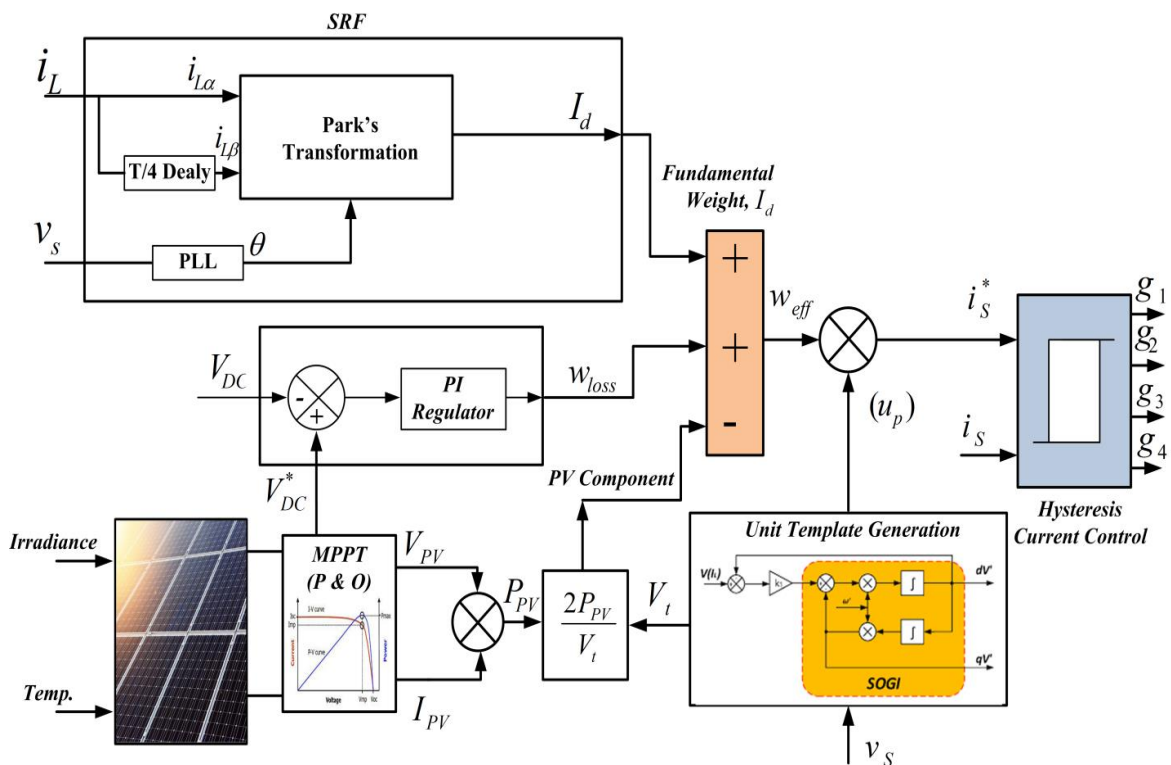


Fig.4.14 Layout of VSC controlled using SRF technique for single phase system

The compensator current also changes and the supply current increases to meet the new load demand. Even in the presence of distorted load currents, the supply current maintains sinusoidal behavior throughout both load change and irradiance change. In a single phase grid linked PV system, the PQ issues are successfully improved by SRF algorithm.

Fig.4.16 shows the total harmonic distortion (THD) in source voltage, source current and load current to be 0.25%, 4.26% and 29.14% respectively during closed loop operation of SAPF. The proposed controller is able to maintain THD level of source current as per IEEE 519 and IEEE 1547 standard.

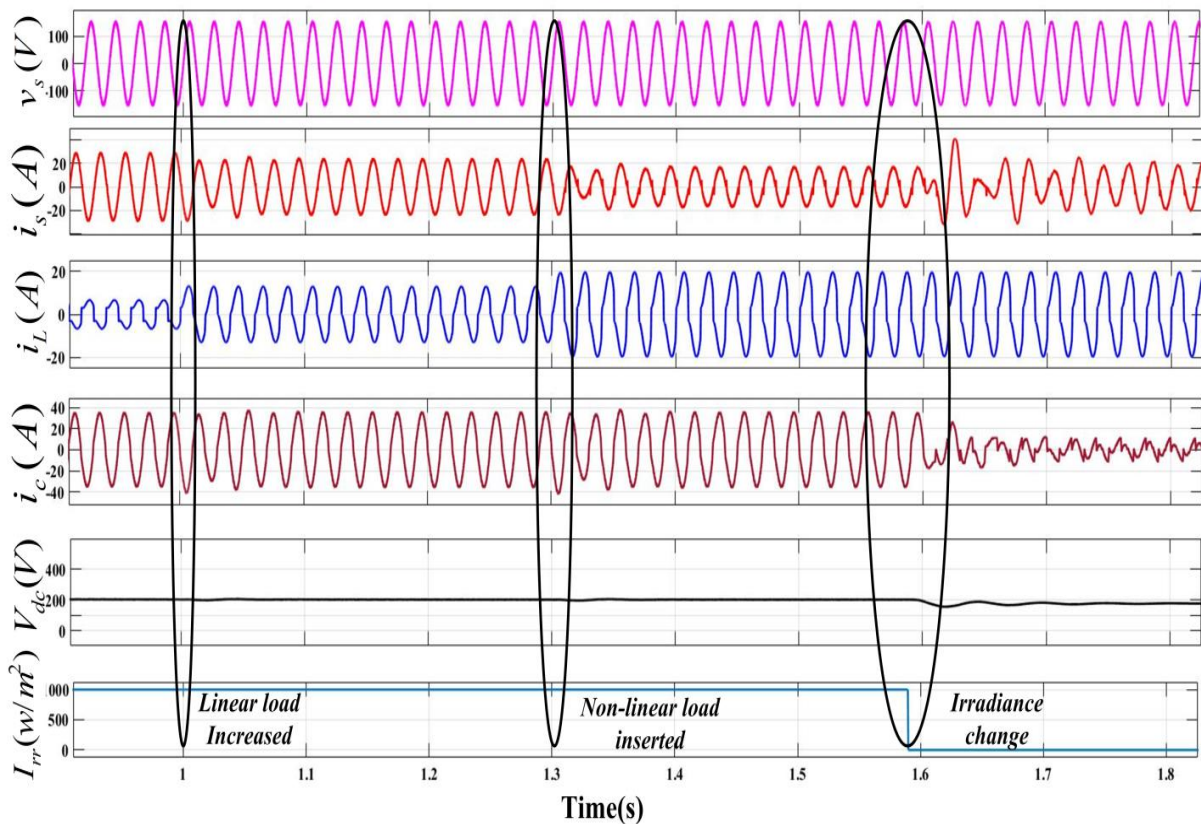


Fig.4.15 Simulation performance of single phase VSC controlled by SRF showing (a) source voltage, v_s (b) source current, i_s (c) load current, i_L (d) converter current, i_c (e) dc link voltage, V_{DC} (f) irradiance (W/m²)

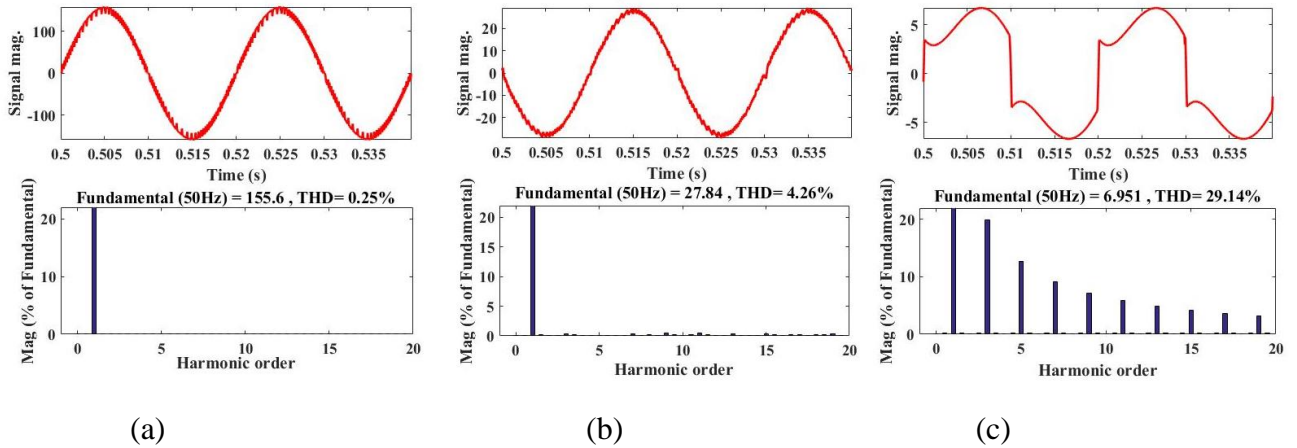


Fig.4.16 THD performance of SRF in single phase system (a) source voltage v_s (b) source current i_s (c) load current i_L

4.9.1.2. Simulation Performance with SOGI Algorithm for Single Phase System:

Fig.4.17 shows intermediate performance of SOGI filter during the load change, shows load current (i_L), in-phase component of load current ($i_{L\alpha}$), quadrature phase component ($i_{L\beta}$) and output weight.

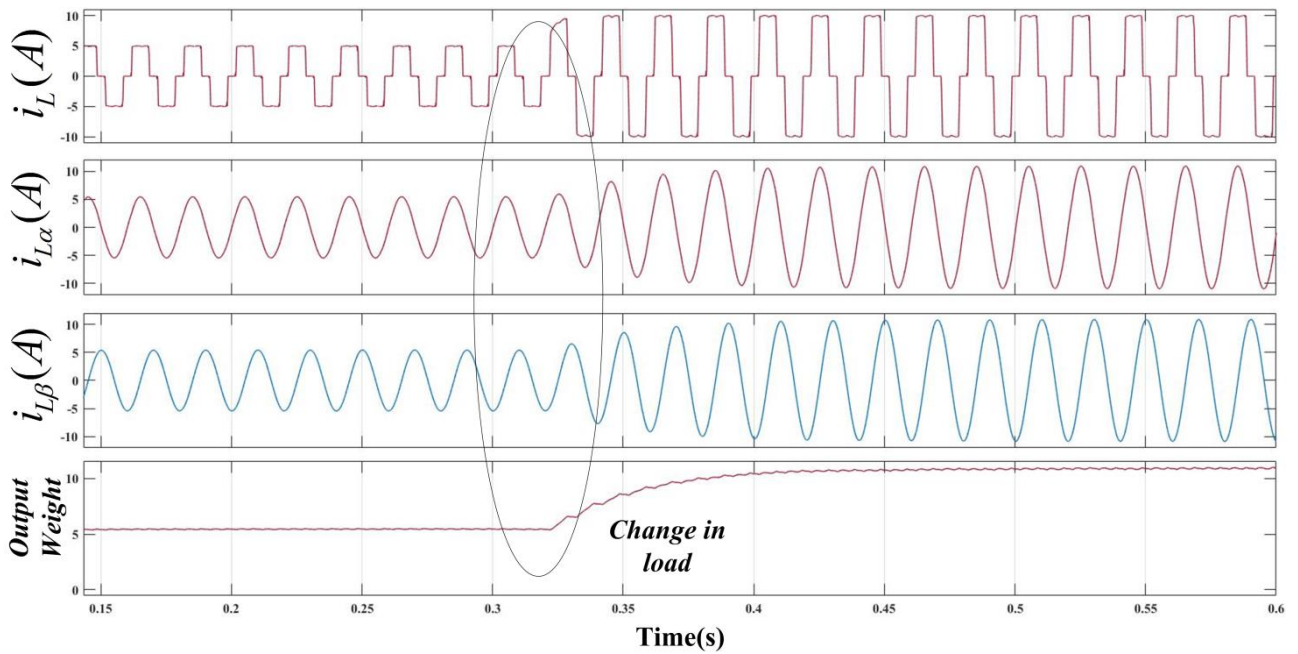


Fig.4.17 Intermediate performance of SOGI filter (a) load current (i_L), (b) in-phase component of load current (i_{Ld}), (c) quadrature phase component (i_{Lq}) (d) output weight.

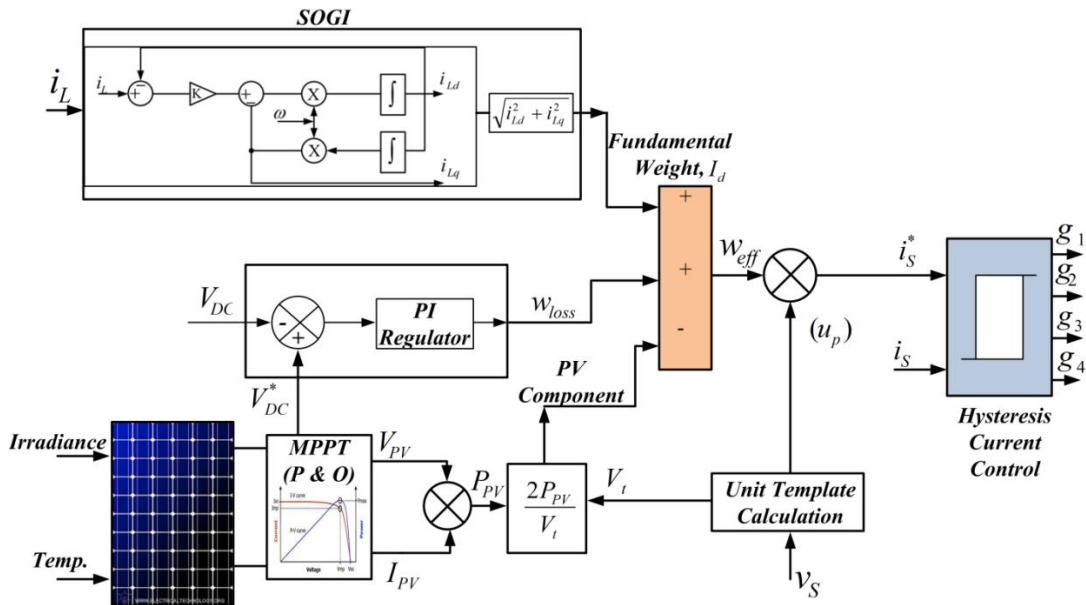


Fig.4.18 Layout of VSC controlled using SOGI technique for single phase system

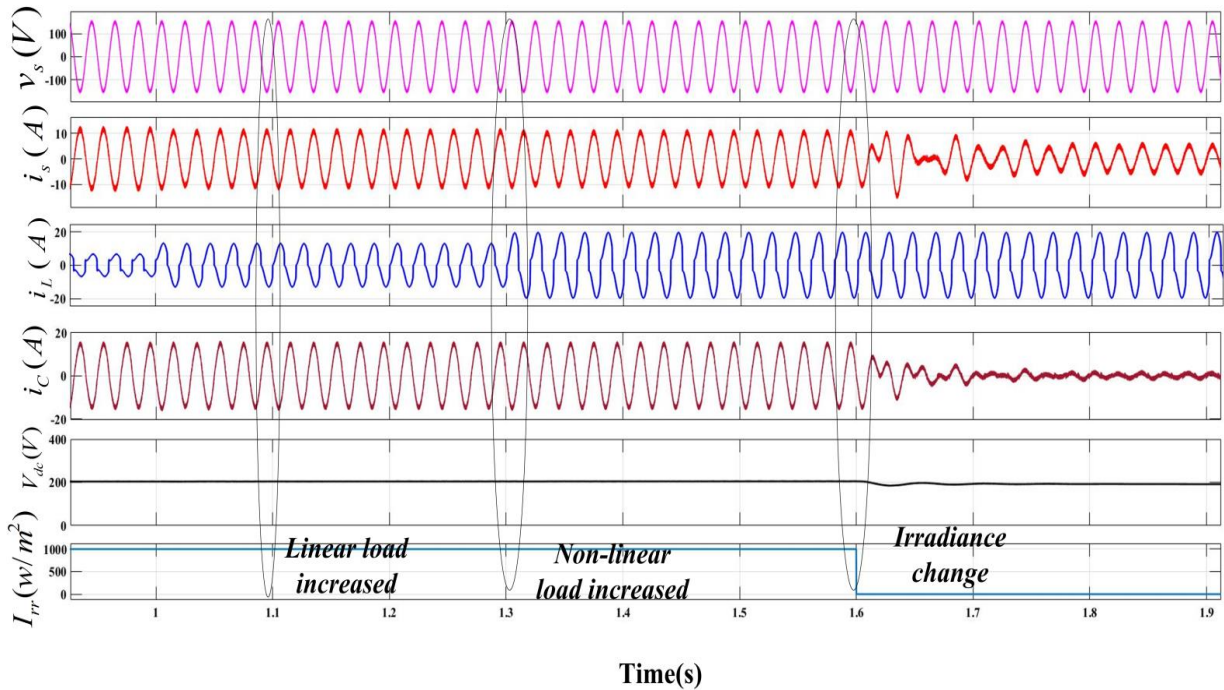


Fig.4.19 Simulation performance of SOGI in single phase system showing (a) source voltage, v_s (b) source current, i_s (c) load current, i_L (d) converter current, i_c (e) dc link voltage, V_{DC} (f) irradiance (W/m²)

Fig.4.18 shows the structure of PV connected single-phase VSC controlled by SOGI filter. Fig.4.19 shows the simulation performance of SOGI control algorithm under the irradiance variation from day time and night time and under linear and non-linear load variation for single phase grid connected PV system.

Fig.4.19 shows the plots for supply voltage (v_s), supply currents (i_s), load currents (i_L), compensator currents (i_c), DC link voltage (V_{dc}) and irradiance (I_{rr}). At starting time day mode is simulated and the irradiance is kept at $1000\text{W}/\text{m}^2$. At $t=1.0\text{s}$ linear load is inserted and at $t=1.3\text{s}$ non-linear load is inserted into the system. At $t=1.6\text{s}$ night time simulated. Hence irradiance level is decreased to $0\text{W}/\text{m}^2$. The PV delivers power to grid and load during the day time, which causes the source voltage and current to be out of phase. As PV power is zero during night time, the load requirements are supplied by the source thus the source voltage and current are in phase. The supply current maintains sinusoidal behavior throughout both load change and irradiance change, even in the presence of distorted load currents. The SOGI algorithm satisfactorily addresses the PQ concerns in a single phase grid connected PV system.

Fig.4.20 shows the total harmonic distortion (THD) in source voltage, source current and load current to be 0.14%, 3.34% and 26.51% respectively during closed loop operation of SAPF. The proposed controller is able maintain THD level of source current as per IEEE 1547 and 519 standard.

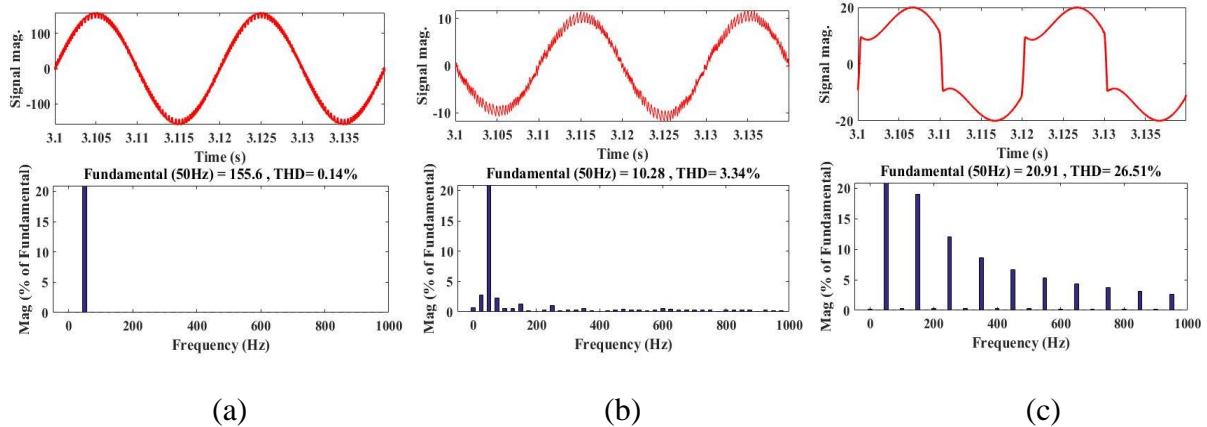


Fig.4.20 THD performance of SOGI controller in single phase system (a) source voltage v_s (b) source current i_s (c) load current i_L

4.9.1.3. Simulation Performance with BP Controller of Single Phase System:

Fig.4.21 shows the intermediate performance of proposed adaptive BP algorithm trained by LMS, shows load current (I_L), desired weight, output fundamental weight and error of the system. As the load changes, the output fundamental weight of the system follows the desired weight and the error between desired weight and output fundamental weight is very less as shown in Fig.4.21.

Fig.4.22 shows the structure of single phase VSC controlled by adaptive BP controller. For single phase system Fig.4.23 shows the plots for supply voltage(v_s), supply currents (i_s), load currents (i_L), compensator currents (i_c), DC link voltage (V_{dc}) and irradiance (W/m^2). A single-phase supply of 110V, 50Hz is system ac input and both linear and non-linear loads are considered. Initially, the connected load comprises linear and non-linear components. Both day time and night time cases are explored. During daytime PV array of 2.7kW with irradiance of $1000 W/m^2$ is simulated upto $t=1.6s$ and beyond $t=1.6s$ PV array irradiance is reduced to $0W/m^2$ (considered as night time). Thus, the results in Fig.4.23 highlight the effect of PV integration till $t=1.6s$ and its subsequent removal thereafter.

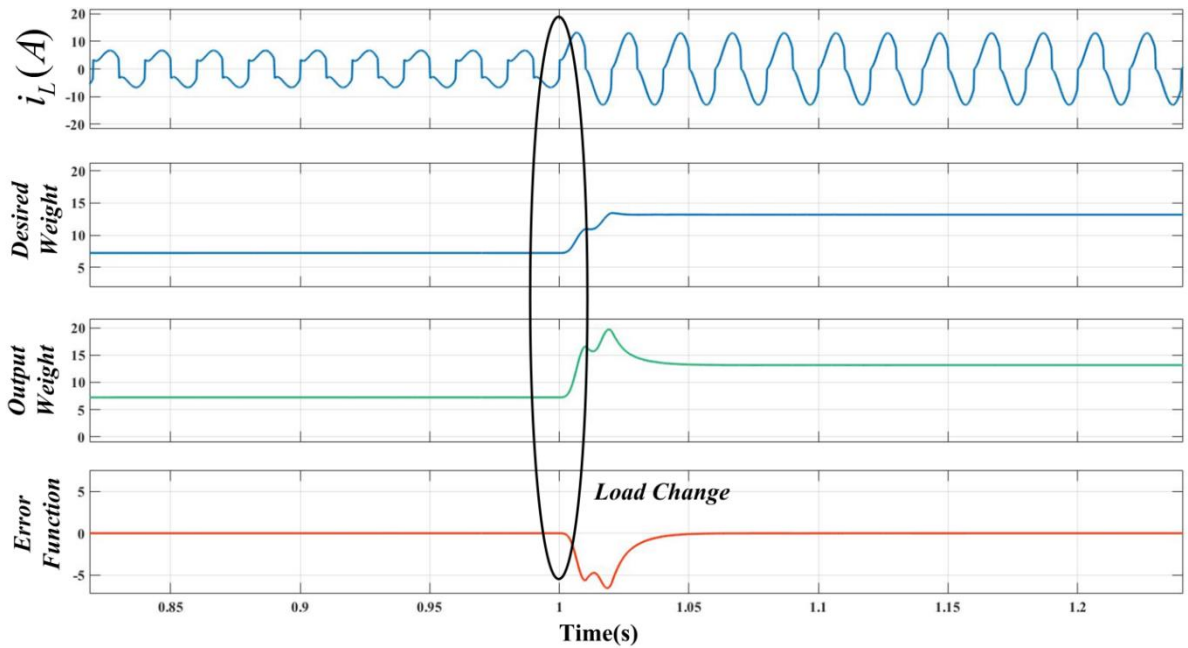


Fig.4.21 Intermediate performance of BP controller (a) load current (i_L), (b) direct axis component of load current (i_{Ld}), (c) quadrature axis component (i_{Lq}) (d) output weight.

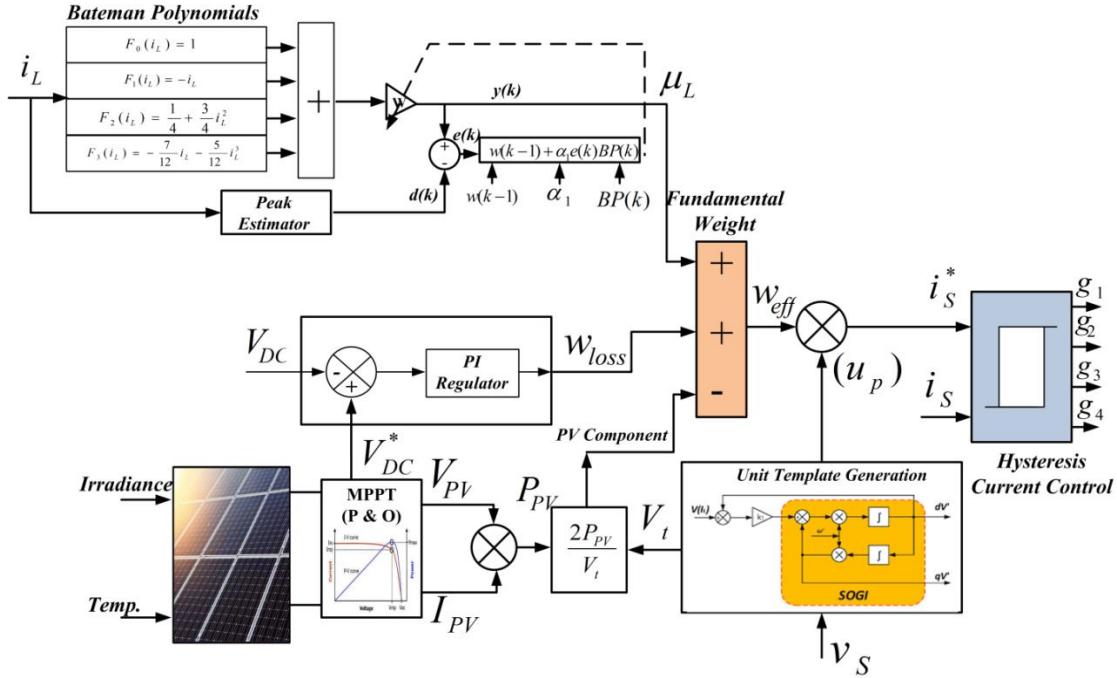


Fig.4.22 Layout of VSC controlled using adaptive BP technique for single phase system

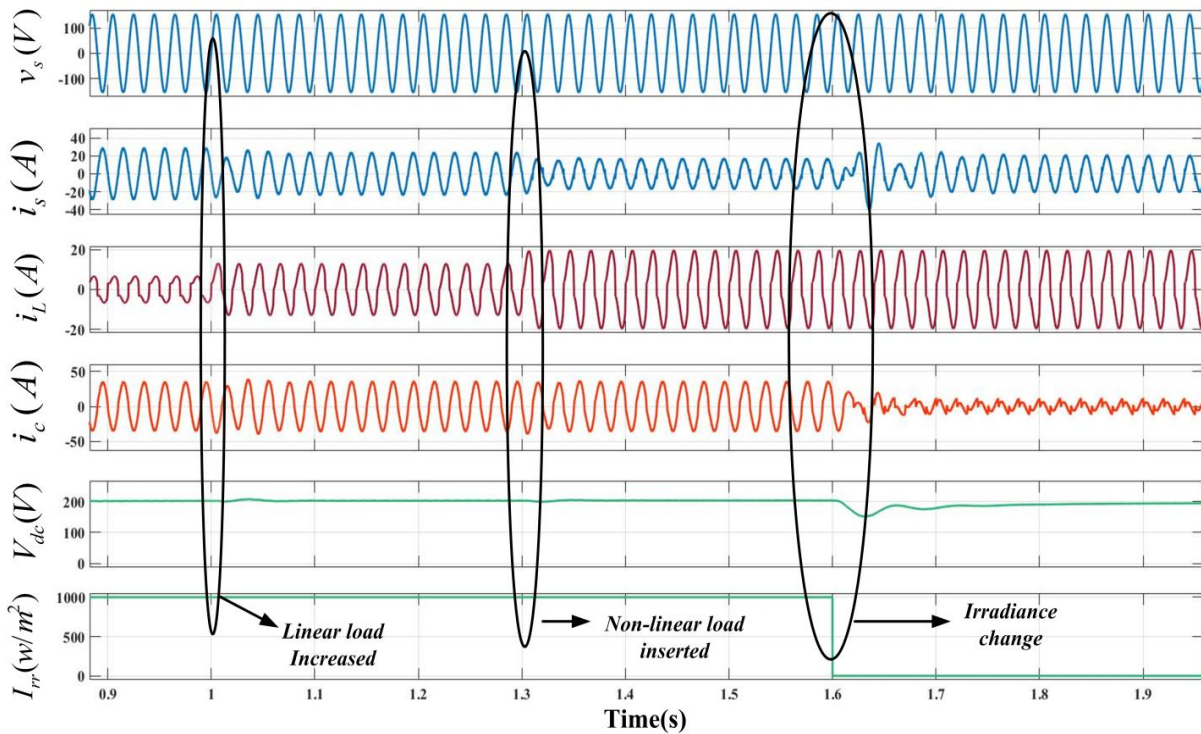


Fig.4.23 Simulation performance of adaptive BP in single phase system showing (a) source voltage, v_s (b) source current, i_s (c) load current, i_L (d) converter current, i_c (e) dc link voltage, V_{DC} (f) irradiance (W/m²)

The night time operation corresponds to SAPF operation without RES integration. The tracked weight is shown in Fig.4.23 and it is observed that the actual weight tracking is fast achieved within 2 cycles even when the linear load inserted at $t=1s$ and a non-linear load increased at $t=1.3s$. Convergence is reached within two cycles irrespective of the load changes. Fig.4.23 shows PQ improvement results and focuses on power factor correction and harmonic mitigation. Severe load variation is introduced at $t=1s$ and $1.3s$. The compensator injects the necessary currents and the grid currents are sinusoidal. Thus, the adaptive BP controller achieves load compensation.

Fig.4.24 shows the total harmonic distortion (THD) in source voltage, source current and load current to be 0.26%, 3.32% and 28.08% respectively during closed loop operation of SAPF. The proposed controller is able maintain THD level of source current as per IEEE 519 and 1547 standard.

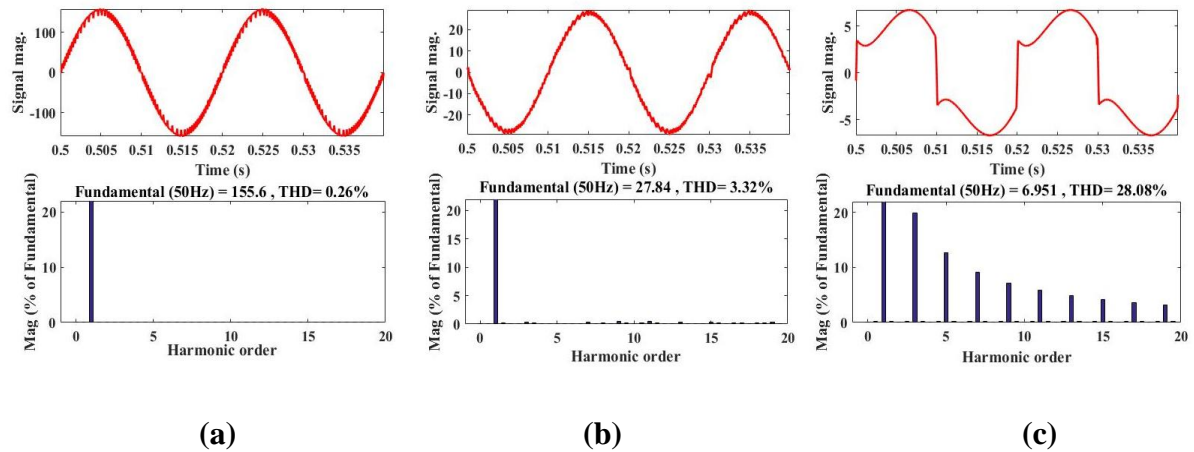


Fig.4.24 THD performance of adaptive BP controller in single phase system (a) source voltage v_s (b) source current i_s (c) load current i_L

4.9.1.4. Simulation Performance with RBFNN Controller of Single Phase System:

Fig.4.25 shows the intermediate performance of proposed RBFNN algorithm, shows load current (I_L), desired weight, output fundamental weight and error of the system. Proposed RBFNN is trained by LMS. As the load changes, the output fundamental weight of the system follows the desired weight and the error between desired weight and output fundamental weight is very less as shown in Fig.4.25.

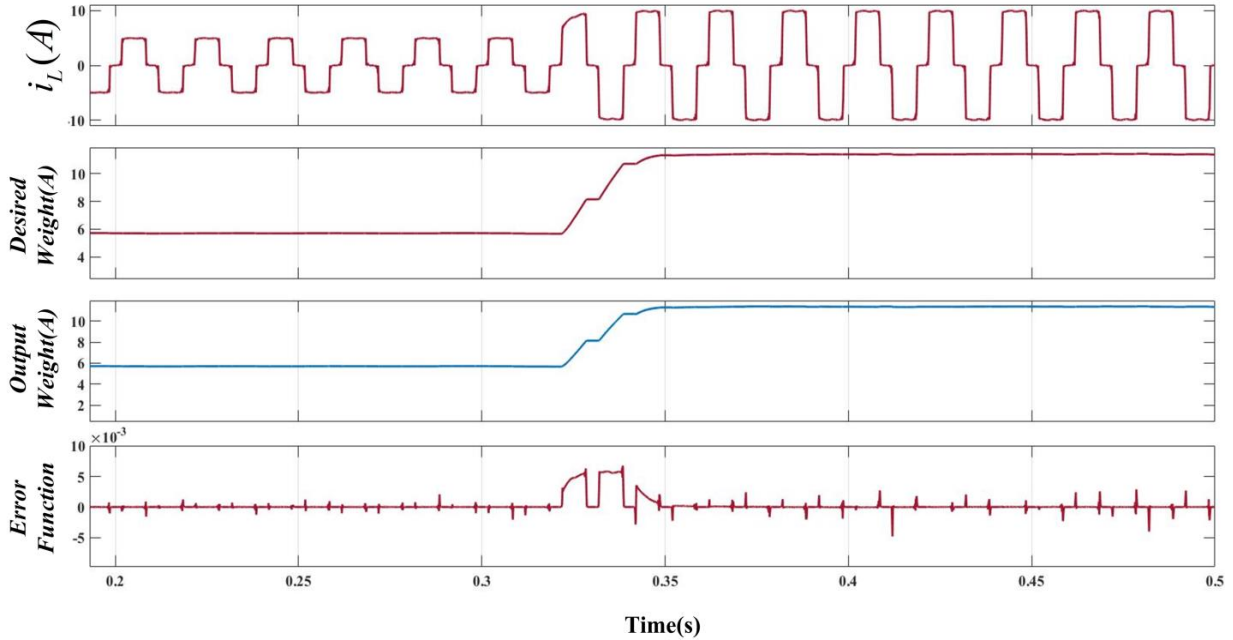


Fig.4.25 Intermediate performance of proposed RBFNN controller (a) load current (b) desired weight (c) output weight (d) error function

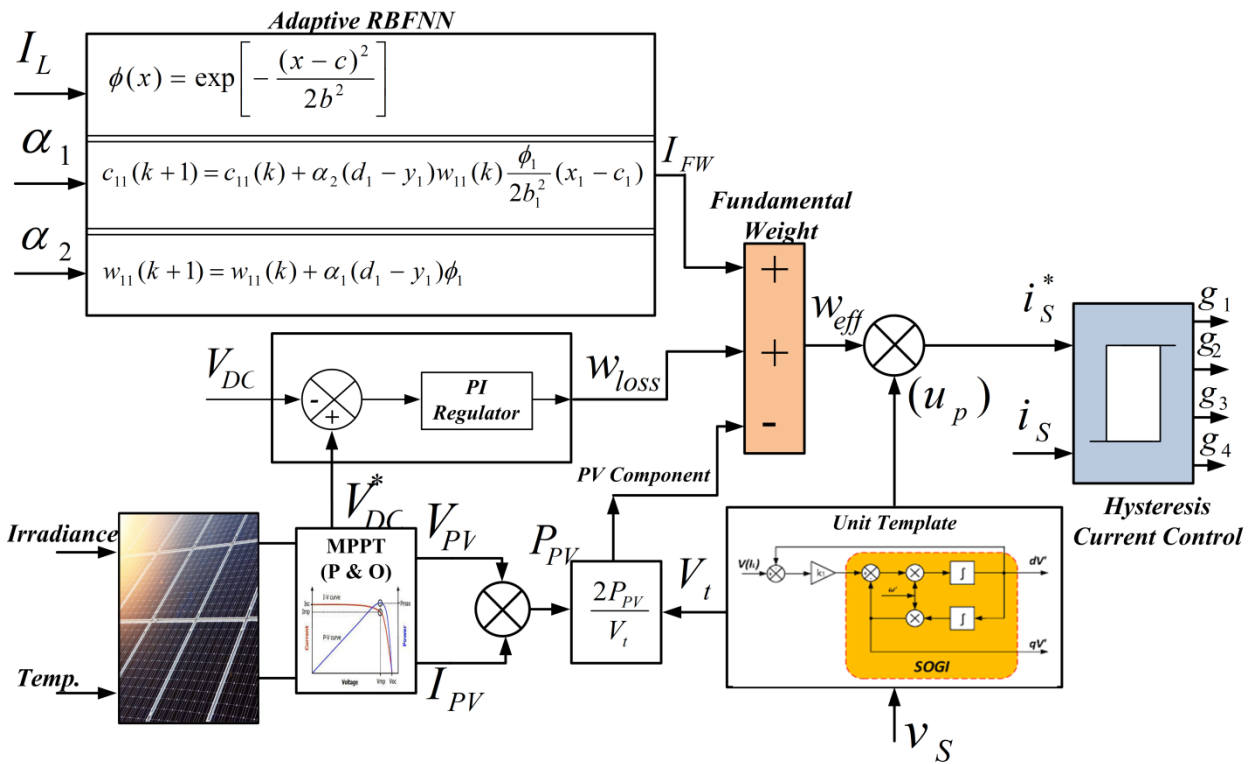


Fig.4.26 Layout of VSC controlled using adaptive RBFNN technique for single phase system

Fig.4.26 shows the structure of single phase VSC controlled by proposed RBFNN control algorithm. For single phase system Fig.4.27 shows the plots for supply voltage(v_s), supply currents (i_s), load currents (i_L), compensator currents (i_c), DC link voltage (V_{dc}) and fundamental weight (FW). A single-phase supply of 110V, 50Hz is system ac input and both linear and non-linear loads are considered. Initially, the connected load comprises linear and non-linear components. Both day time and night time cases are explored. During daytime PV array of 2.7kW with irradiance of 1000 W/m^2 is simulated upto $t=1.6\text{s}$ and beyond $t =1.6\text{s}$ PV array irradiance is reduced to 0W/m^2 (considered as night time). Thus, the results in Fig.4.27 highlight the effect of PV integration till $t=1.6\text{s}$ and its subsequent removal thereafter. The night time operation corresponds to VSC operation without RES integration. Fig.4.27 shows PQ improvement results and focuses on power factor correction and harmonic mitigation. Load variation is introduced at $t=1\text{s}$ and 1.3s . The compensator injects the necessary currents and the grid currents are sinusoidal. Thus, the developed adaptive RBFNN controller achieves load compensation.

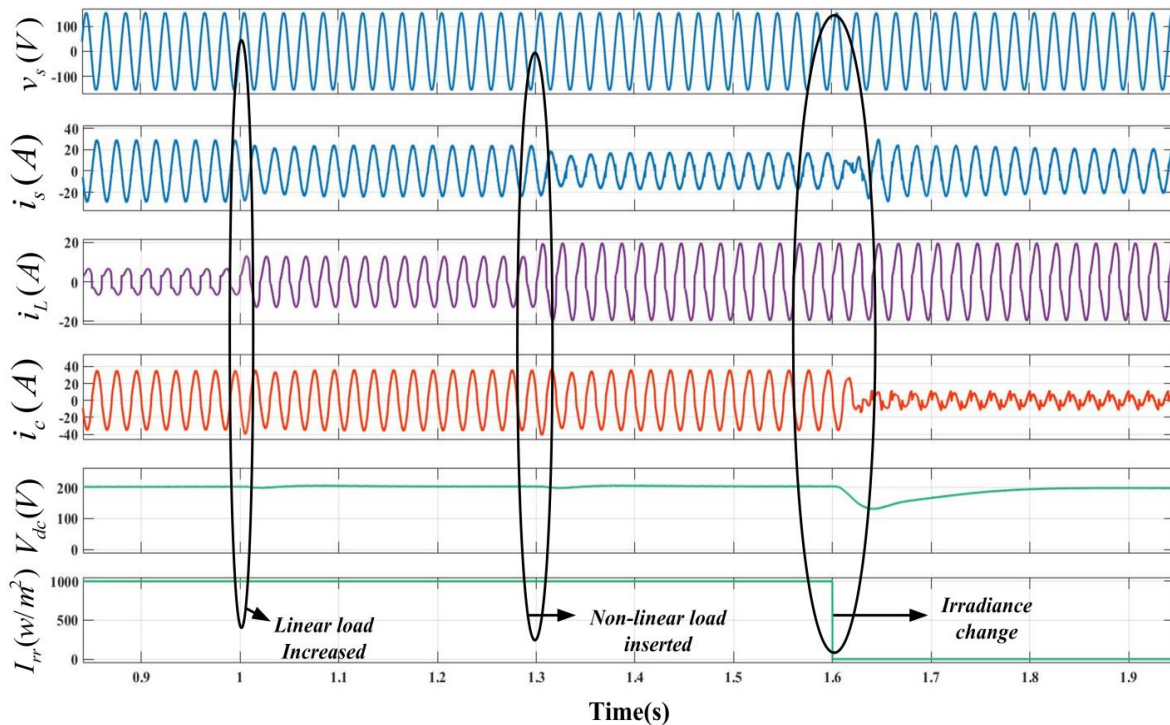


Fig.4.27 Performance of controller showing (a) source voltage, v_s (b) source current, i_s (c) load current, i_L (d) converter current, i_c (e) DC link voltage, V_{DC} (f) fundamental weight, FW

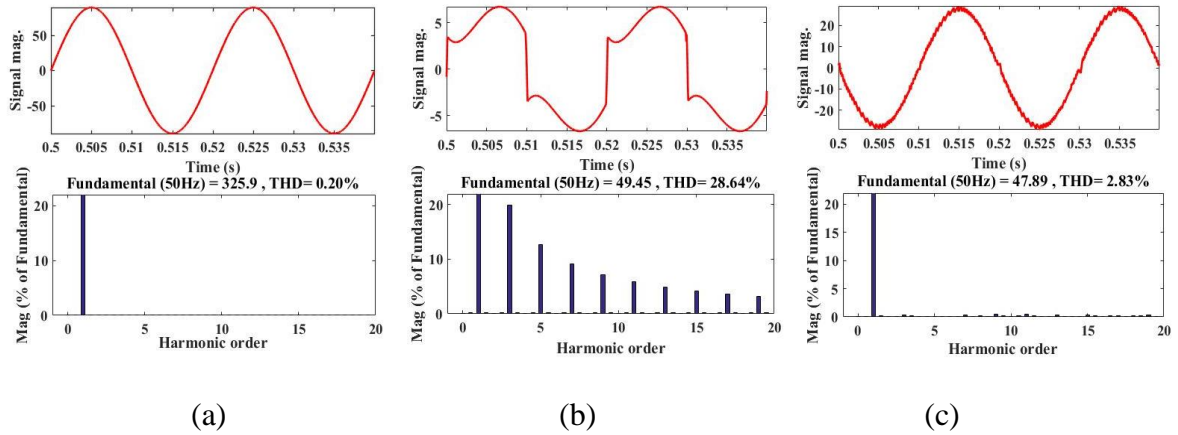


Fig.4.28 THD performance of SOGI controller in single phase system (a) source voltage v_s (b) load current i_L (c) source current i_s

Fig.4.28 shows the total harmonic distortion (THD) in source voltage, source current and load current to be 0.20%, 2.83% and 28.64% respectively during closed loop operation of SAPF. The proposed controller is able maintain THD level of source current as per IEEE 519 and 1547 standard.

4.9.2. Simulation Performance of Three Phase System:

This Section presents the results with the SRF, SOGI, adaptive BP based controller and adaptive RBFNN technique for a three-phase grid-connected system with/without PV integration. A 2.7kW PV array is integrated to power distribution system feeding non-linear loads and linear loads. The system is simulated and its operation under various conditions is investigated using Simulink/ MATLAB.

4.9.2.1. Simulation Performance with SRF Technique for Three Phase System:

Fig.4.29 shows the structure three-phase VSC controlled by SRF control technique. Fig.4.30 shows simulation performance of SRF control algorithm during the variation from day time to night time and linear, non-linear load variation for three phase grid connected PV system of 2.7kW same as single phase system.

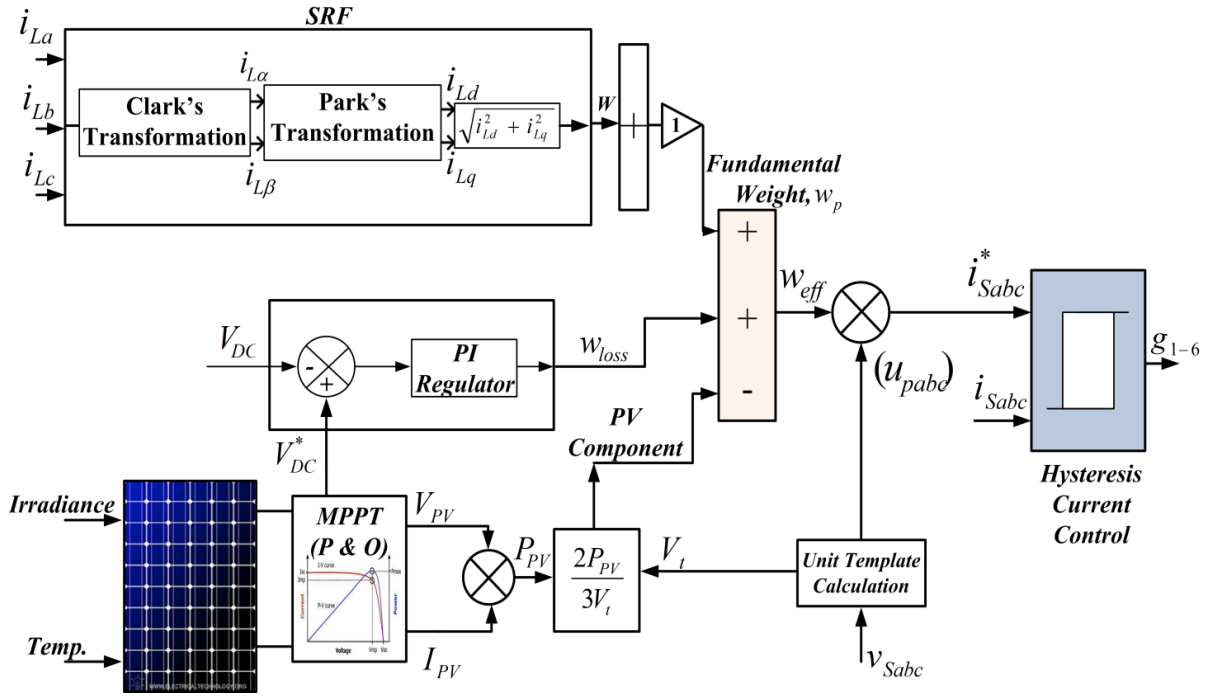


Fig.4.29 Three phase SRF control structure

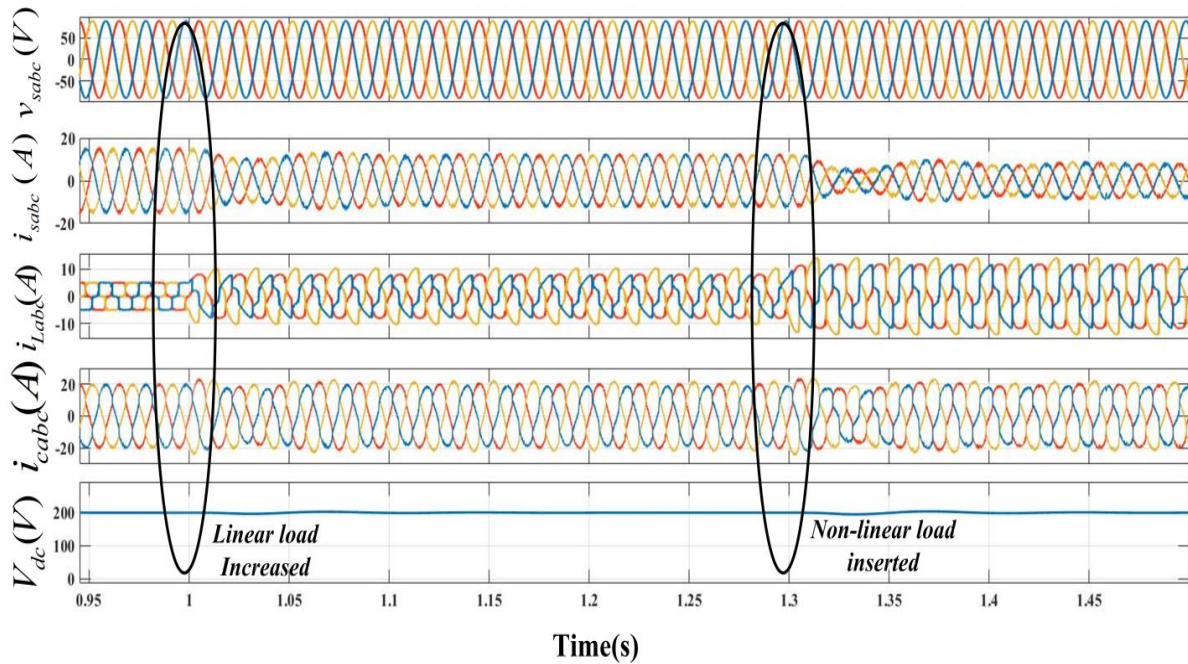


Fig.4.30(a) Simulation performance of three phase SAPF controlled by SRF showing (a) source voltage, v_{Sabc} (b) source current, i_{Sabc} (c) load current, i_{Labc} (d) converter current, i_{Cabc} (e) dc link voltage, V_{DC}

Fig.4.30(a) shows the plots for supply voltage(v_{sabc}), supply currents (i_{sabc}), load currents (i_{Labc}), compensator currents (i_{cabc}) and DC link voltage (V_{dc}). Fig.4.30(b) shows the plots for supply voltage(V_s), supply currents (i_{sabc}), load currents (i_{Labc}), compensator currents (i_{cabc}), DC link voltage (V_{dc}) and irradiance (I_{rr}). At starting time day mode is present, the irradiance is 1000W/m^2 . At $t=1.0\text{s}$ linear load is inserted and at $t=1.3\text{s}$ non-linear load is inserted into the system in Fig.4.30(a). At $t=1.6\text{s}$ night time is simulate. Thus irradiance level decreased to 0W/m^2 and PV output power become zero during this period in Fig.4.30(b).

As a result, the source voltage and current are out of phase when the grid is operating during the day. Similarly, when the grid is operating at night, when PV power is zero and the load is provided by the source then the source voltage and current are in phase. The supply current maintains sinusoidal behavior throughout both load change and irradiance change, even in the presence of distorted load currents.

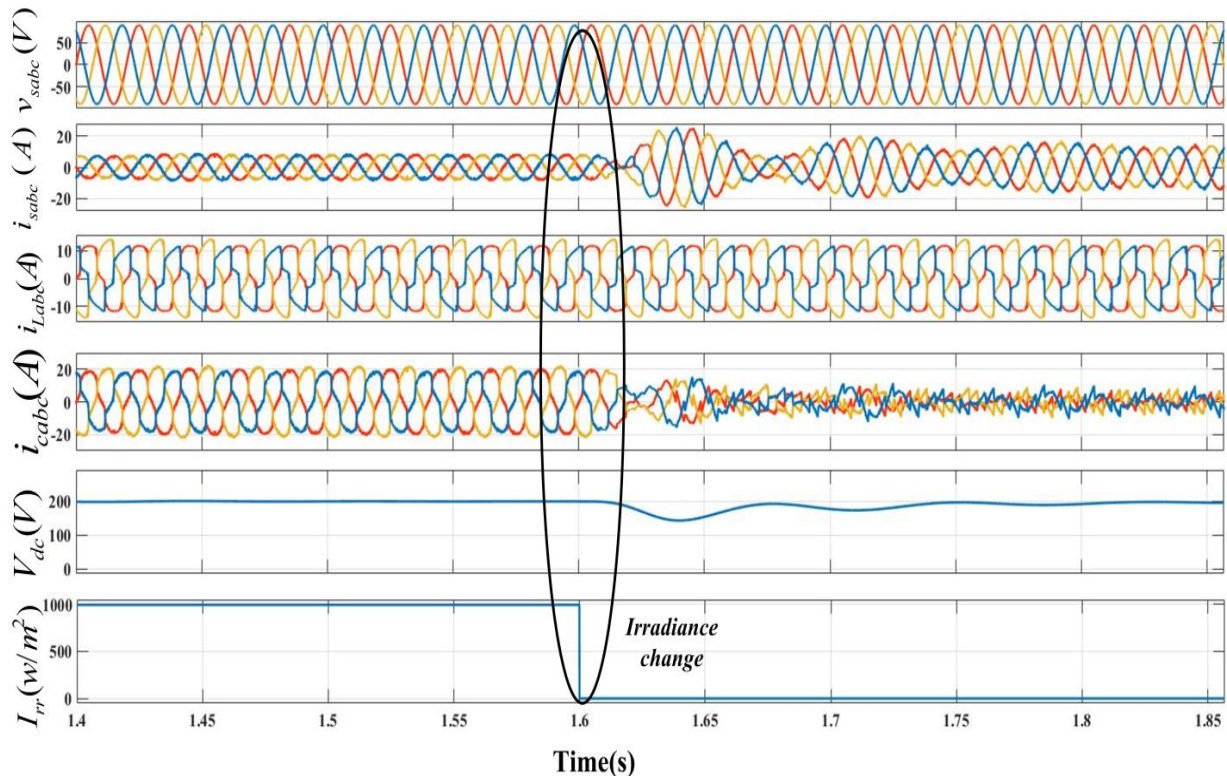


Fig.4.30(b) Simulation performance of three phase SAPF controlled by SRF showing (a) source voltage, v_{sabc} (b) source current, i_{sabc} (c) load current, i_{Labc} (d) converter current, i_{cabc} (e) dc link voltage, V_{DC} (f) irradiance (W/m^2)

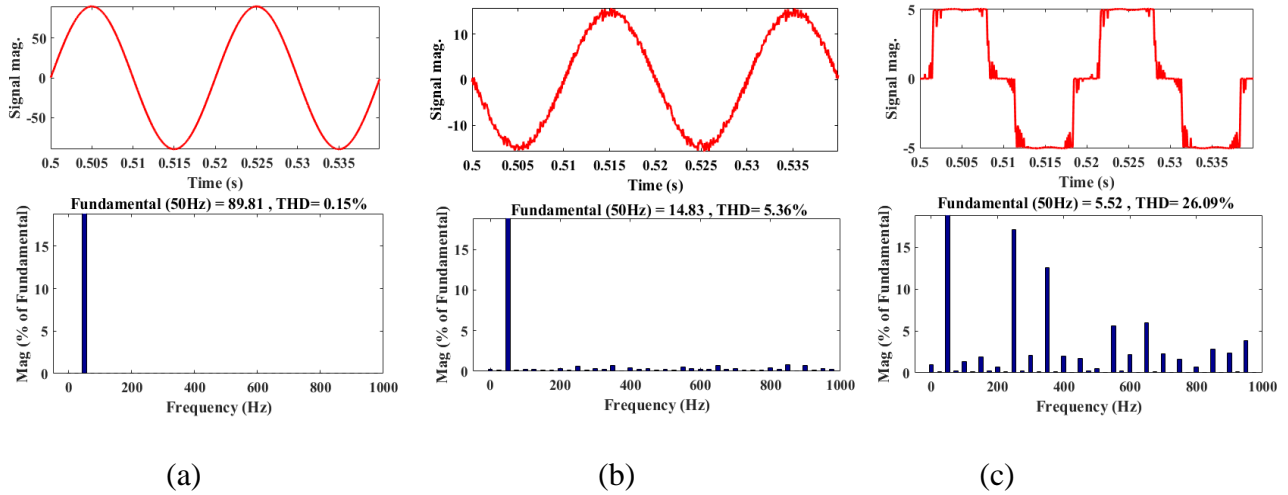


Fig.4.31 THD performance of SRF in three phase system (a) source voltage v_s (b) source current i_s (c) load current i_L

Fig.4.31 shows the total harmonic distortion (THD) in source voltage, source current and load current to be 0.15%, 5.36% and 26.09% respectively during closed loop operation of SAPF. The proposed controller is not able maintain THD level of source current as per IEEE 519 and IEEE 1547 standard.

4.9.2.2. Simulation Performance with SOGI Algorithm for Three-Phase System:

Fig.4.32 shows the structure three-phase VSC controlled by SOGI control technique. Fig.4.33 shows simulation performance of SOGI control algorithm during the variation from day time to night time and linear, non-linear load variation for three phase grid connected PV system same as single phase system.

Fig.4.33(a) shows the plots for supply voltage(v_{sabc}), supply currents (i_{sabc}), load currents (i_{Labc}), compensator currents (i_{cabc}) and DC link voltage (V_{dc}) Fig.4.33(b) shows the plots for supply voltage(V_s), supply currents (i_{sabc}), load currents (i_{Labc}), compensator currents (i_{cabc}), DC link voltage (V_{dc}) and irradiance (I_{rr}). Some disturbances like as linear load, non-linear load and transient from day time to night time at 1sec, 1.3sec in Fig.4.33(a) and 1.6sec in Fig.4.33(b) respectively, during all these disturbance the supply current maintains sinusoidal behavior throughout both load change and irradiance change, even in the presence of distorted load currents.

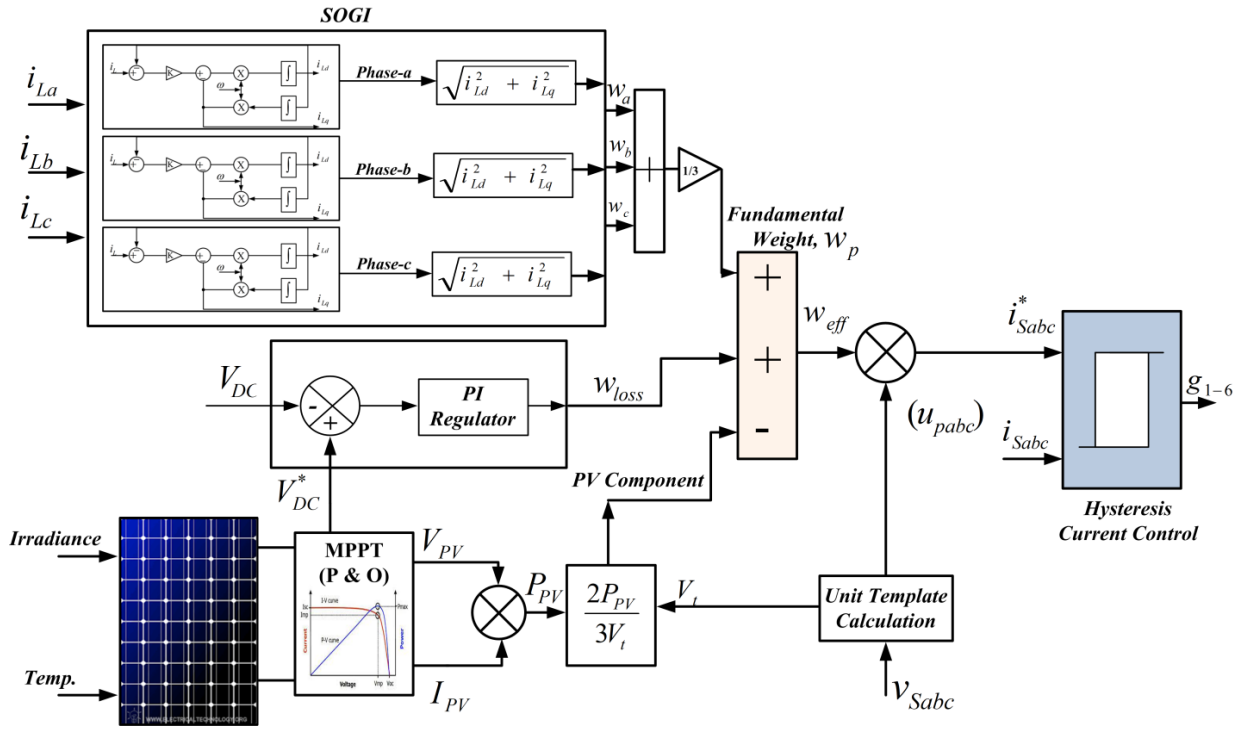


Fig.4.32 Three phase SOGI control structure

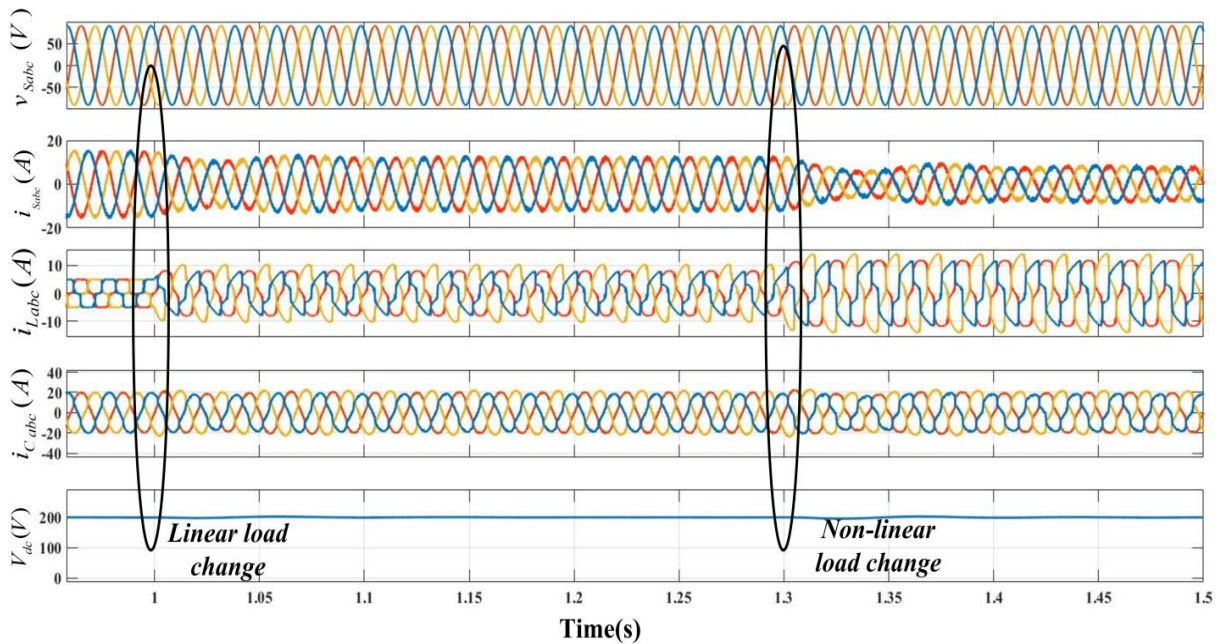


Fig.4.33(a) Simulation performance of three phase system controlled by SOGI filter showing (a) source voltage, v_{Sabc} (b) source current, i_{Sabc} (c) load current, i_{Labc} (d) converter current, i_{Cabc} (e) dc link voltage, V_{DC}

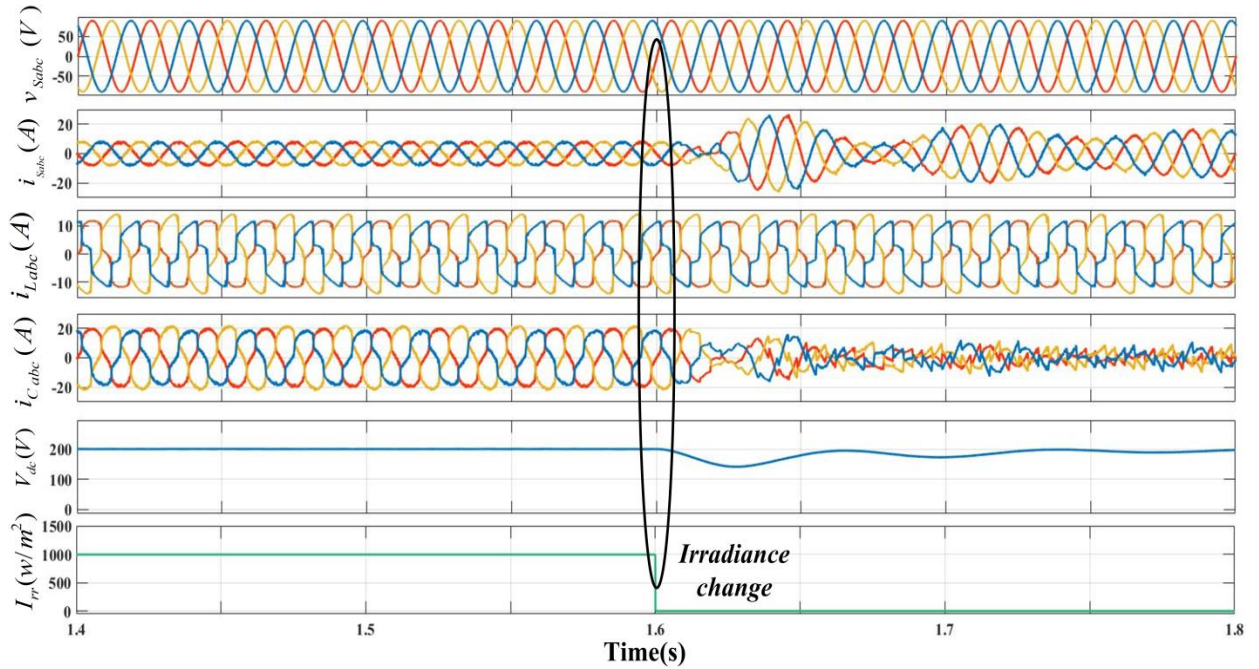


Fig.4.33(b) Simulation performance of three phase system controlled by SOGI filter showing (a) source voltage, v_{Sabc} (b) source current, i_{Sabc} (c) load current, i_{Labc} (d) converter current, i_{Cabc} (e) dc link voltage, V_{DC} (f) irradiance (W/m^2)

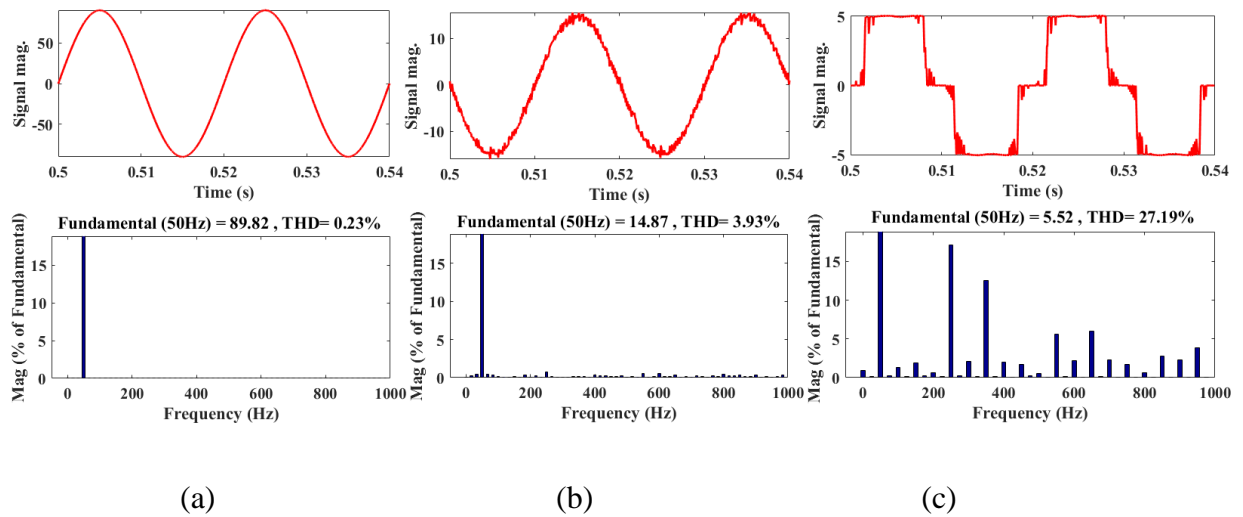


Fig.4.34 THD performance of SOGI controller in three phase system (a) source voltage v_s (b) source current i_s (c) load current i_L

Fig.4.34 shows the total harmonic distortion (THD) in source voltage, source current and load current to be 0.23%, 3.93% and 27.19% respectively during closed loop operation of

SAPF. The proposed controller is able maintain THD level of source current as per IEEE 1547 and 519 standard.

4.9.2.3. Simulation Performance with BP Controller of Three-Phase System:

Fig.4.35 shows the structure three-phase VSC controlled by SOGI control technique. Fig.4.36 shows simulation performance of SOGI control algorithm during the variation from day time to night time and linear, non-linear load variation for three phase grid connected PV system same as single phase system. Fig.4.36(a) shows the plots for supply voltage(v_{sabc}), supply currents (i_{sabc}), load currents (i_{Labc}), compensator currents (i_{cabc}) and DC link voltage (V_{dc}). Fig.4.36(b) shows the plots for supply voltage(v_{sabc}), supply currents (i_{sabc}), load currents (i_{Labc}), compensator currents (i_{cabc}), DC link voltage (V_{dc}) and irradiance (I_{rr}). Some disturbances like as linear load, non-linear load and transient from day time to night time at 1s, 1.3s in Fig.4.36(a) and 1.6s in Fig.4.36(b) respectively, during all these disturbance the supply current maintains sinusoidal behavior throughout both load change and irradiance change, even in the presence of distorted load currents.

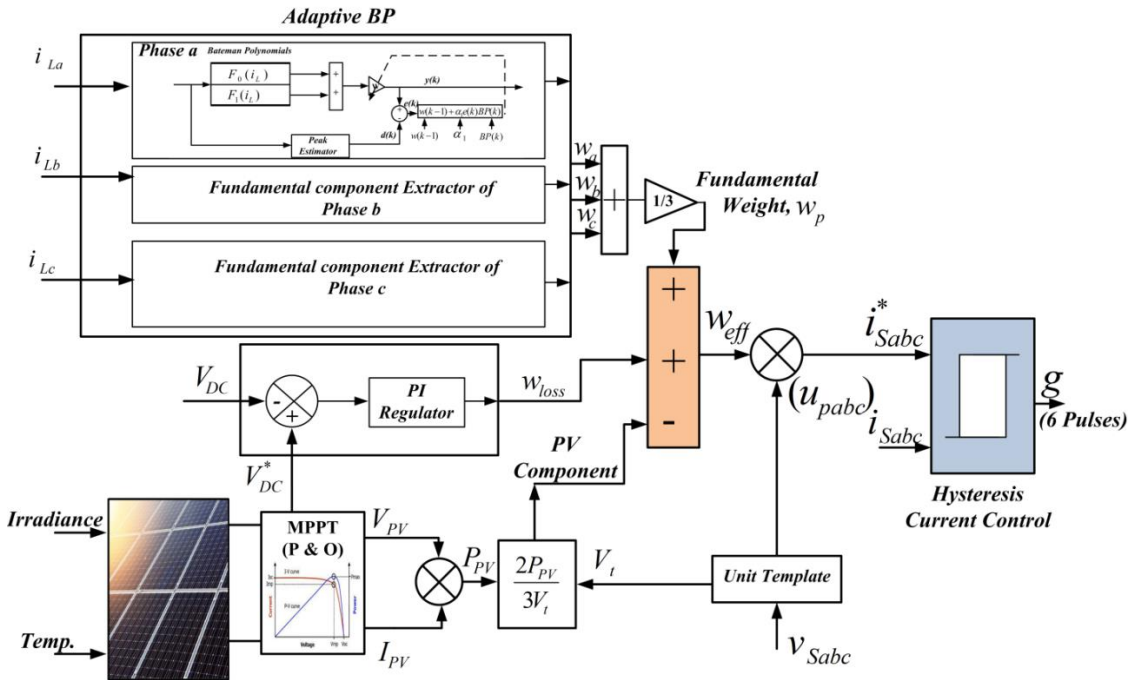


Fig.4.35 Three phase adaptive BP control structure

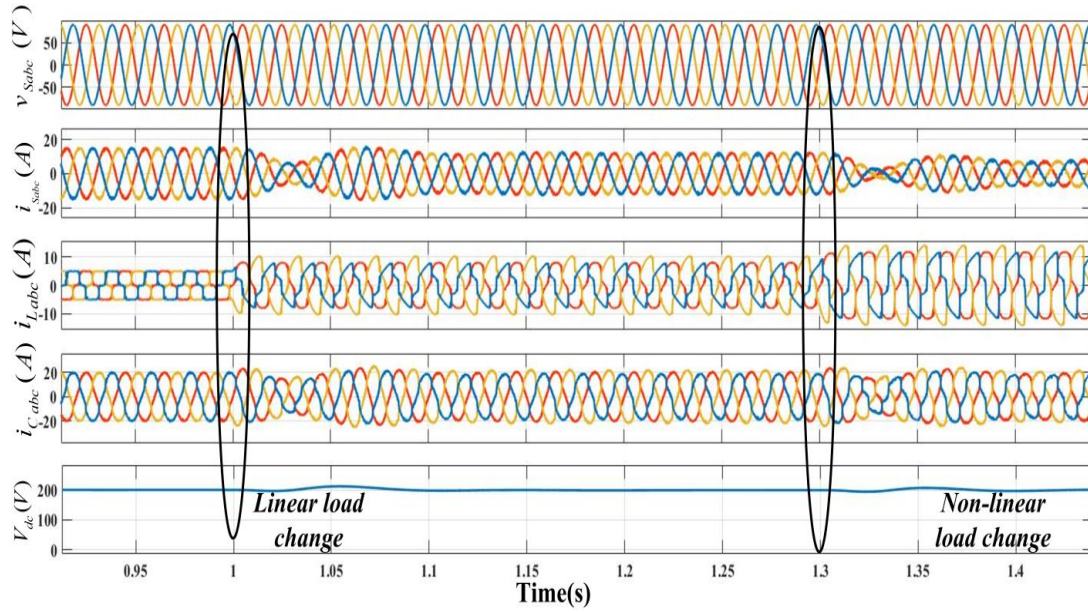


Fig.4.36(a) Simulation performance of adaptive BP controller for three phase system showing (a) source voltage, v_{Sabc} (b) source current, i_{Sabc} (c) load current, i_{Labc} (d) converter current, i_{Cabc} (e) dc link voltage, V_{DC}

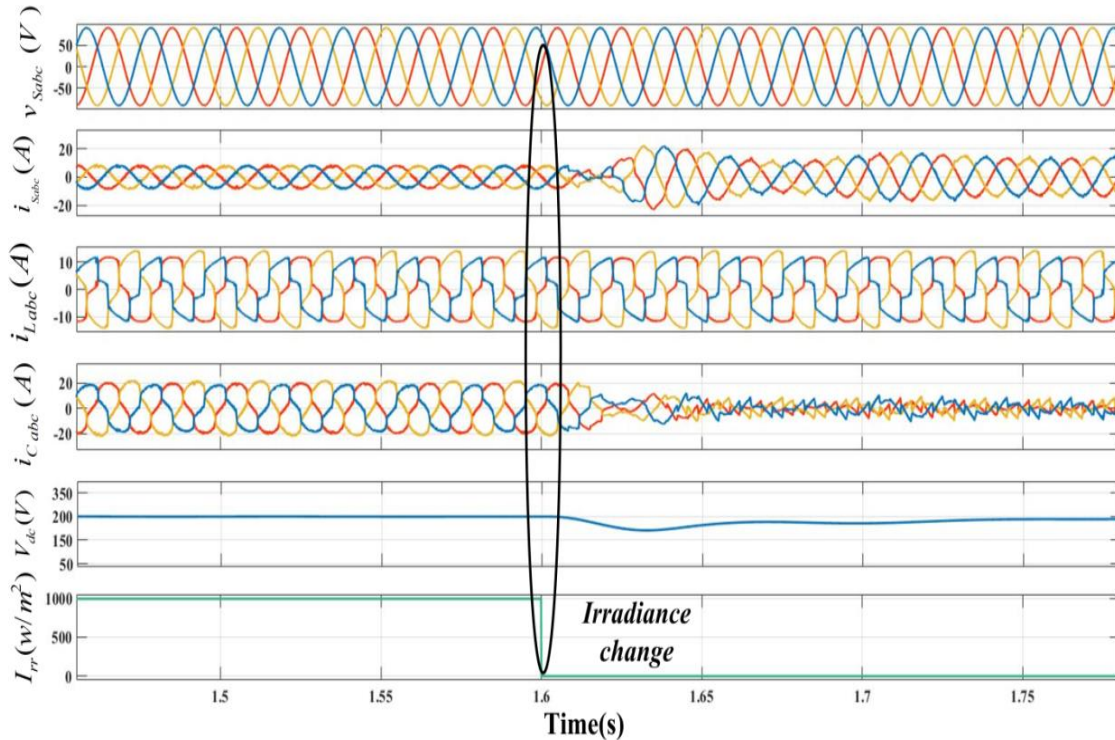


Fig.4.36(b) Simulation performance of adaptive BP controller for three phase system showing (a) source voltage, V_{Sabc} (b) source current, I_{Sabc} (c) load current, I_{Labc} (d) converter current, I_{Cabc} (e) dc link voltage, V_{DC} (f) irradiance (W/m^2)

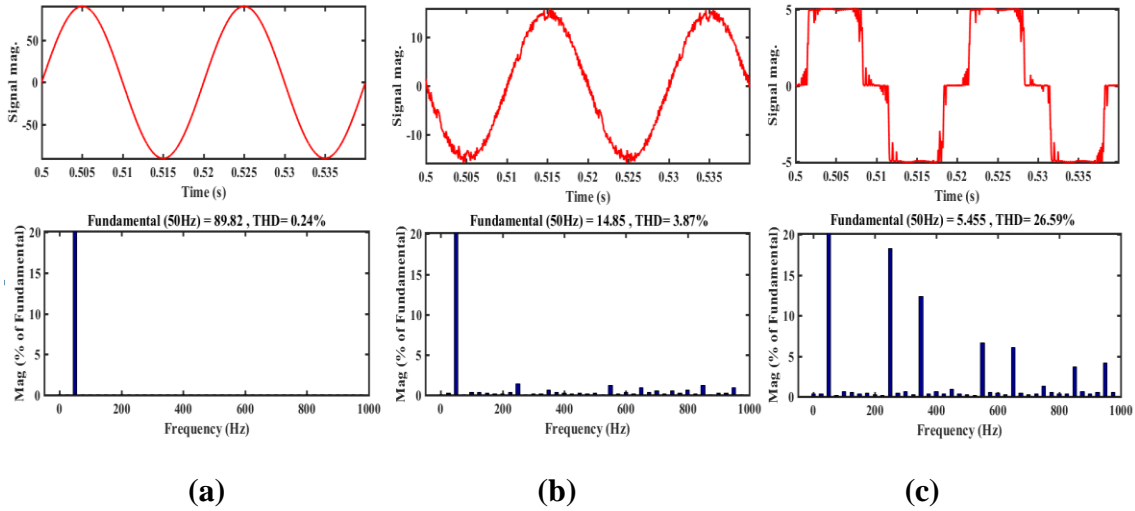


Fig.4.37 THD performance of adaptive BP controller in three phase system (a) source voltage v_s (b) source current i_s (c) load current i_L

Fig.4.37 shows the total harmonic distortion (THD) in source voltage, source current and load current to be 0.24%, 3.87% and 26.59% respectively during closed loop operation of SAPF. The proposed controller is able maintain THD level of source current as per IEEE 519 and 1547 standard.

4.9.2.4. Simulation Performance with RBFNN Controller of Three-Phase System:

Fig.4.38 shows the structure three-phase VSC controlled by SOGI control technique. Fig.4.39 shows simulation performance of SOGI control algorithm during the variation from day time to night time and linear, non-linear load variation for three phase grid connected PV system same as single phase system.

Fig.4.39 shows the plots for supply voltage (v_{sabc}), supply currents (i_{sabc}), load currents (i_{Labc}), compensator currents (i_{cabc}), DC link voltage (V_{dc}) and irradiance (I_{rr}). Some disturbances like as linear load, non-linear load and transient from day time to night time at 1s, 1.3s in Fig.4.39 and 1.6s in Fig.4.40 respectively, during all these disturbance the supply current maintains sinusoidal behavior throughout both load change and irradiance change, even in the presence of distorted load currents.

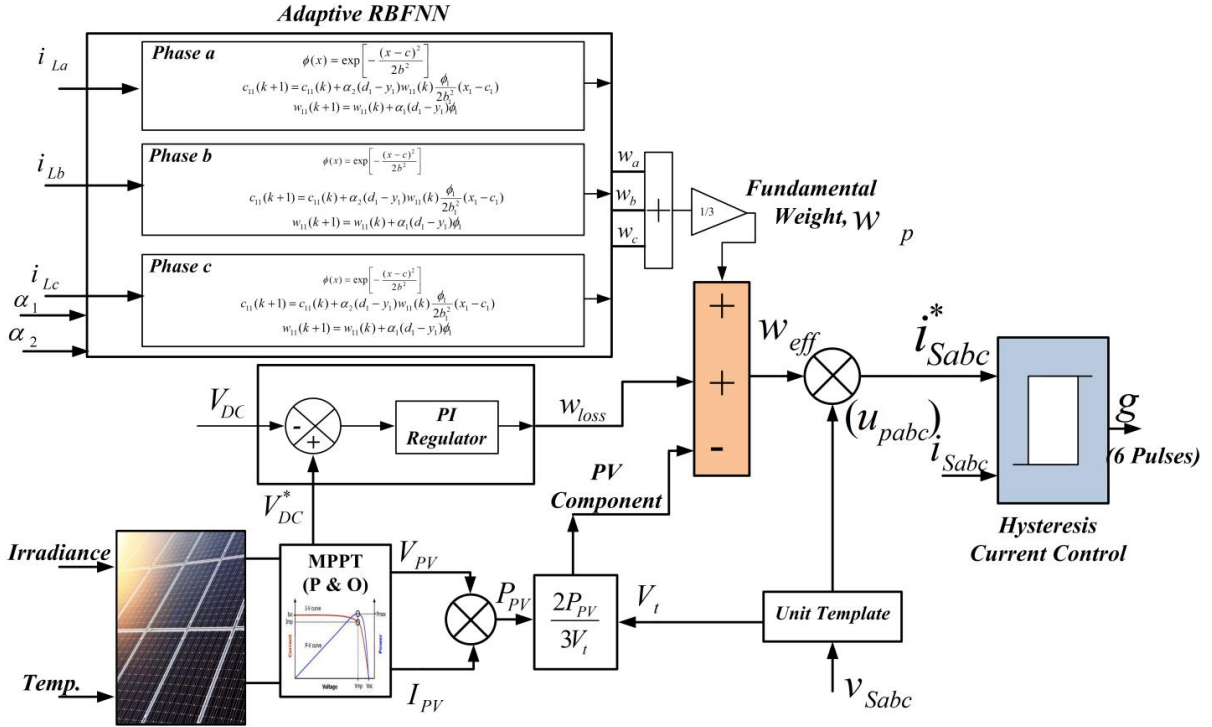


Fig.4.38 Structure of proposed RBFNN controlled three phase VSC

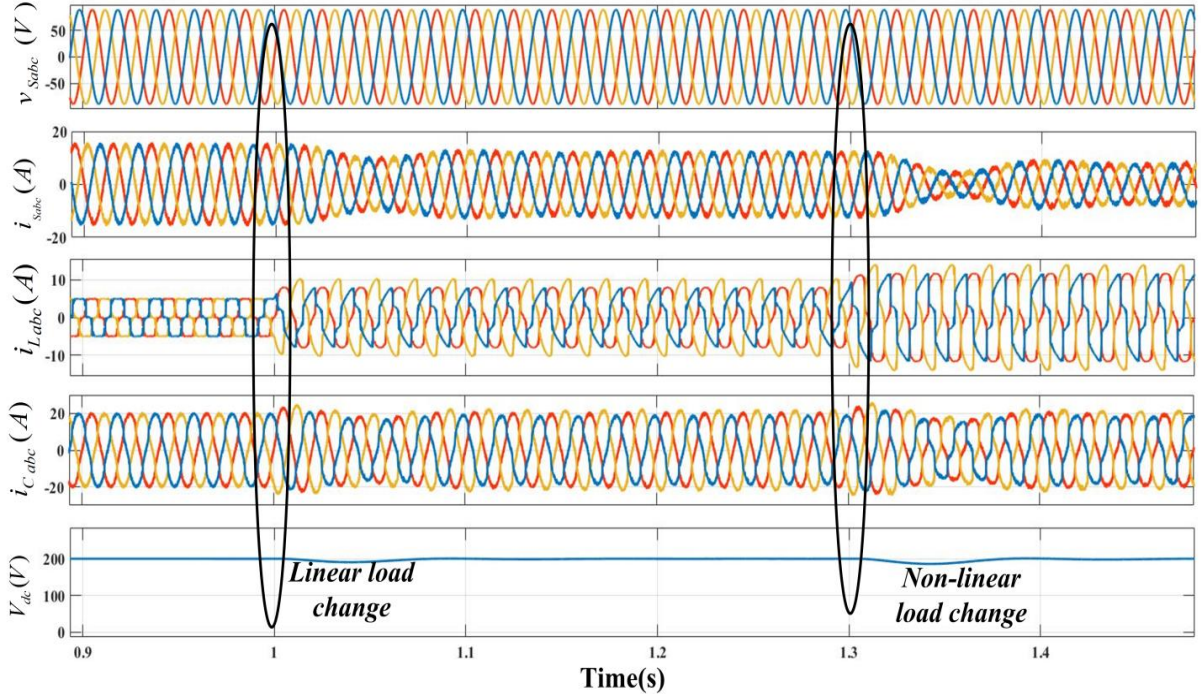


Fig.4.39 Simulation performance of three phase system controlled by proposed RBFNN showing (a) source voltage, V_{Sabc} (b) source current, I_{Sabc} (c) load current, I_{Labc} (d) converter current, I_{Cabc} (e) dc link voltage, V_{DC}

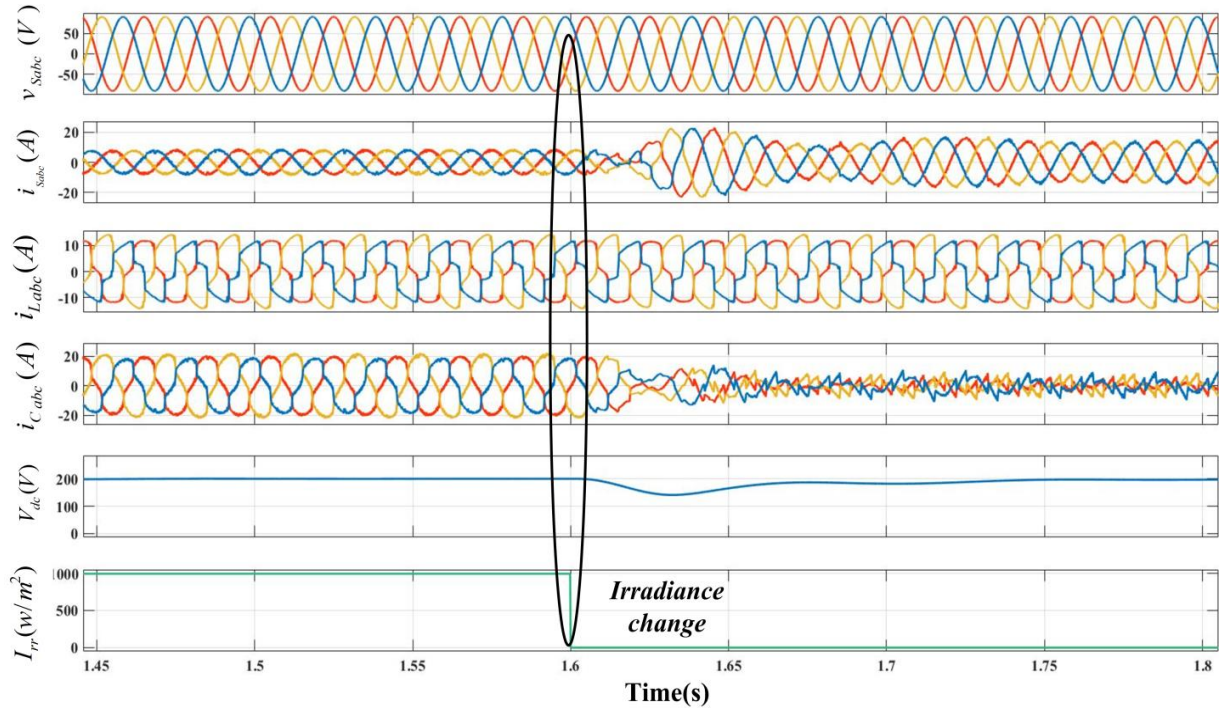


Fig.4.40 Simulation performance of three phase system controlled by proposed RBFNN showing (a) source voltage, v_{Sabc} (b) source current, i_{Sabc} (c) load current, i_{Labc} (d) converter current, i_{Cabc} (e) dc link voltage, V_{DC} (f) irradiance (W/m^2)

Fig.4.41 shows the total harmonic distortion (THD) in source voltage, source current and load current to be 0.26%, 2.23% and 27.59% respectively during closed loop operation of VSC. The proposed controller is able maintain THD level of source current as per IEEE 519 and 1547 standard.

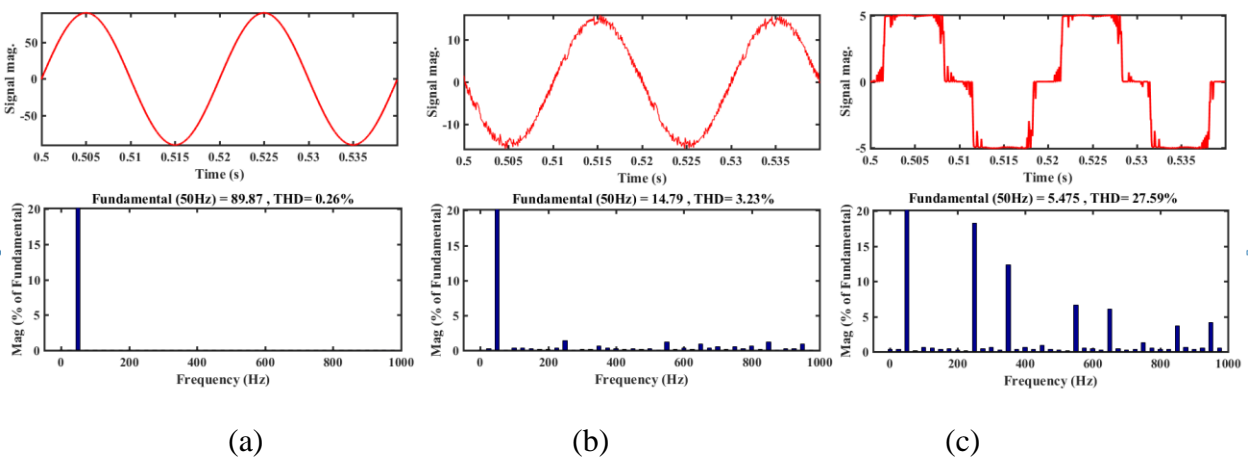


Fig.4.41 THD performance of proposed RBFNN in three phase system

4.10. Comparison:

After the detailed analysis of simulation performance of the proposed controllers, the comparison result with conventional SRF technique and SOGI model are presented in Fig.4.42 and Table-4.1. It shows that SRF technique shows delay in response because it is phase locked-loop (PLL) is dependent and complex in nature and SRFT shows also high steady state error as shown in the Fig.4.42. SOGI show a fast convergence of weight with oscillation compared to other proposed controllers. Both the techniques SRF and SOGI are non-adaptive in nature. Comparatively, both these controllers have fast convergence without any delay in response, almost no oscillation and zero steady state error. The adaptive BP controller has a peak overshoot during the load change. The BP based controller and RBFNN based controller are adaptive in nature. Also, total harmonic distortion (THD) of supply currents of both techniques is much lower with the conventional techniques. The SRF technique and the SOGI need modifications for satisfactory performance. The proposed adaptive BP and RBFNN are simple and give excellent results under load variations. These can be applied to VSC integrated with PV array as well as without PV array.

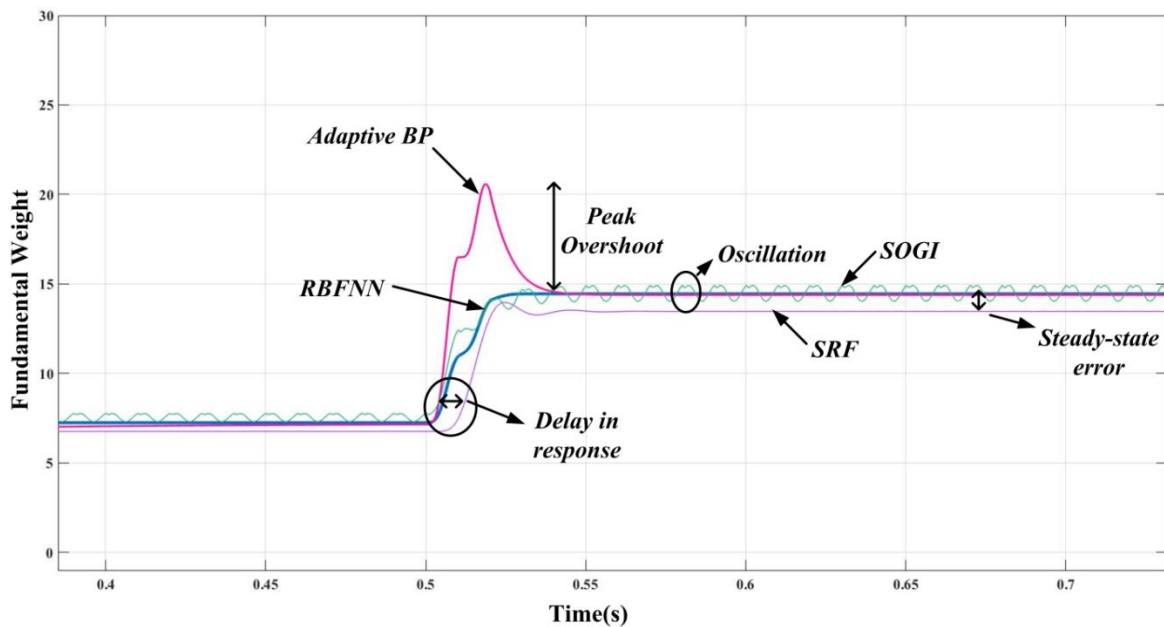


Fig.4.42 Comparison of fundamental weights using (a) SRF (b) SOGI (c) BP and (d) RBFNN

Table 4.1: Comparative Performance of different techniques					
S.No.	Parameter	SRF technique	SOGI	BP	RBFNN
1.	PLL (requirement)	Yes	No	No	No
2.	Technique	Non-adaptive	Non-adaptive	Adaptive	Adaptive
3.	Tracking performance	Moderate	Moderate	Good	Good
4.	Weight Convergence	Moderate(>2 cycles)	Moderate(>3 cycles)	Fast (< 2 cycles)	Fast (< 2 cycles)
5.	Steady state error	Yes	No	No	No
6.	Oscillation	No	Yes	No	No
7.	Dependency on control parameters	Highly dependent	Yes	No, self-adaptive	No, self-adaptive
8.	Complexity	Very high	Medium	Lower	Lower
9.	% Peak Overshoot	NA	NA	Yes	NA
Single phase system					
10.	% THD of v_s	0.25%	0.14%	0.26%	0.20%
11.	% THD of i_L	29.14%	26.51%	28.08%	28.64%
12.	% THD of i_s	4.26%	3.34%	3.23%	2.83%
Three Phase System					
13.	% THD of v_{sabc}	0.15%	0.23%	0.24%	0.26%
14.	% THD of i_{Labc}	26.09%	27.19%	26.59%	27.59%
15.	% THD of i_{sabc}	5.36%	3.96%	3.87%	3.23%

4.11. Experimental Performance:

An experimental setup of a single-phase and three-phase system has been developed to validate the simulation results of the proposed system. The performances of SRF, SOGI, Adaptive BP based controller and adaptive RBFNN are investigated in steady state and dynamic changes under various loading scenarios for both the cases viz. SAPF without and with PV integrated system. The experimental parameters are mentioned in the Appendix.

4.11.1. Single Phase Performance:

The experimental performances of SRF, SOGI, adaptive BP based controller and adaptive RBFNN is investigated in single phase system and the steady state and dynamic response under various loading scenarios for both the cases viz. SAPF without and with PV integrated system is analyzed in following section.

4.11.1.1. Experimental Performance with SRF Technique for Single-Phase System:

The experimental performances of SRF is investigated in single phase system and the steady state and dynamic response under various loading scenarios for both with and without PV integrated system is analyzed. The intermediate performance of SRF control technique is shown in Fig.4.43 which shows load current (i_L), direct axis component of load current (I_{Ld}), quadrature axis component of load current (I_{Lq}) and output weight of SRFT. The output weight of SRFT changes as the load changes but it has some oscillation as shown in Fig.4.43.

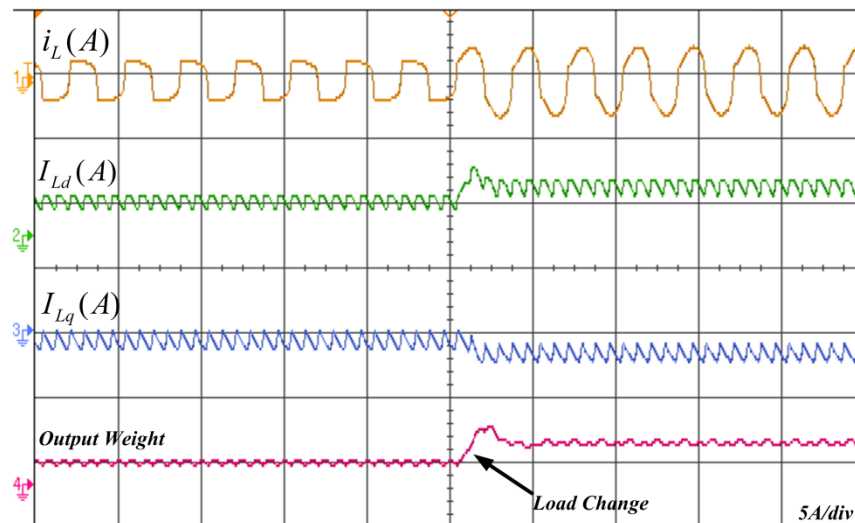


Fig.4.43 Intermediate performance of SRF control technique showing (a) load current (i_L) (b) direct axis component (I_{Ld}) (c) quadrature axis component (I_{Lq}) (c) output weight

The steady state performance of the single phase system is shown in Fig.4.44. Fig.4.44(a) shows waveform of source voltage(V_s) and load current(I_L). Fig.4.44(b) shows the waveform of source voltage (V_s) and source current(I_s). The THD in load current is

33.61% as shown in Fig.4.44(c). The THD in source voltage is 2.07% and THD in source current 4.99% shown in Fig.4.44(d) which as per IEEE 519 standard. The SRF based single phase VSC performs harmonic reduction for supply currents in single system. In addition, the supply voltage and current have an in-phase relationship showing almost unity power factor operation

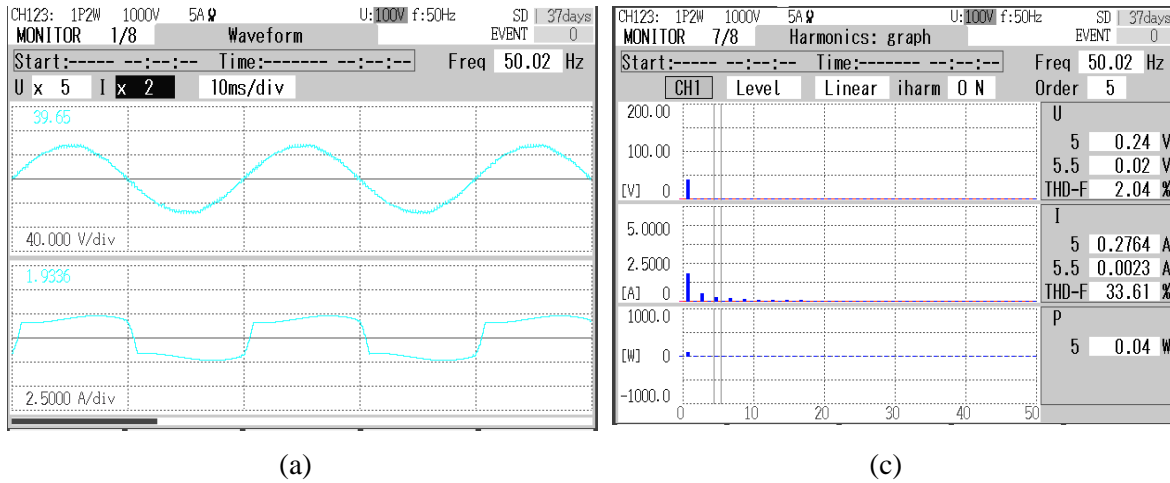


Fig.4.44 Steady state waveforms of single phase system showing (a) source voltage (v_s) and load current (i_L) (b) source voltage (v_s) and source current (i_s)

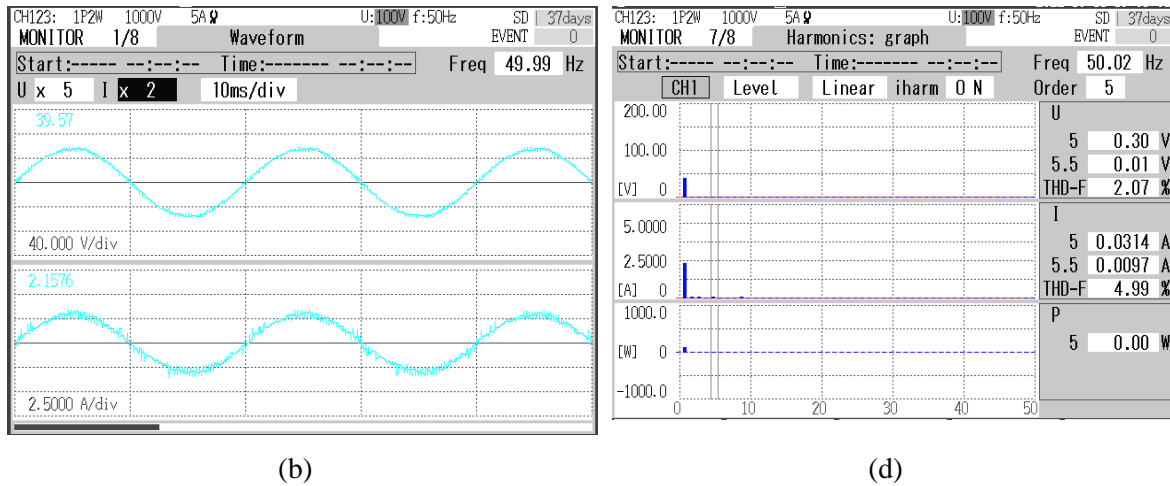


Fig.4.44 Steady state waveforms of single phase system showing (c) THD of v_s (2.04%) and i_L (33.61%) (d) THD of v_s (2.07%) and i_s (4.99%)

The dynamic performance of the single phase system without PV is shown in Fig.4.45 (a-b) in which source voltage (v_s), source current (i_s), load current (i_L), converter current (i_c) DC link voltage (V_{DC}), and output fundamental weight are shown. From Fig.4.45 (a-b)

it is observed that during the change in load, the DC link voltage is stable and the grid current is sinusoidal. The harmonic content in grid current is also maintained as per IEEE 519 standard.

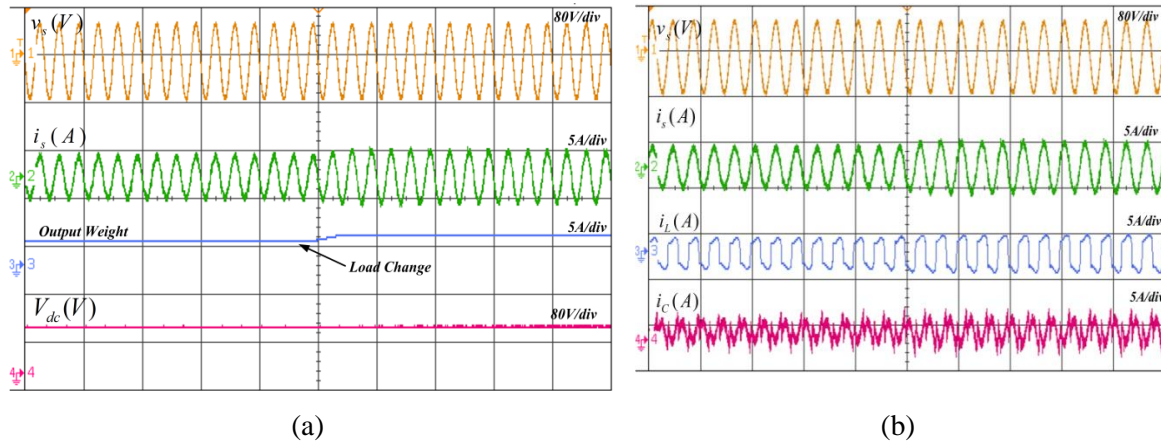


Fig.4.45 Dynamic performance of SRFT without PV for single phase system showing (a) $(v_s, i_s, \text{output weight}, V_{dc})$ (b) (v_s, i_s, i_L, i_C)

Fig.4.46 (a-b) shows dynamic performance of SRF for single phase system with PV integrated at the DC link of the inverter. Fig.4.46(a) shows (v_s, i_s, i_L, i_C) and clearly an out of phase relationship between the source voltage and source current are visible due to PV integration. Fig.4.46(b) shows $(v_s, i_s, I_{pv}, V_{dc})$ in which DC link voltage is stable.

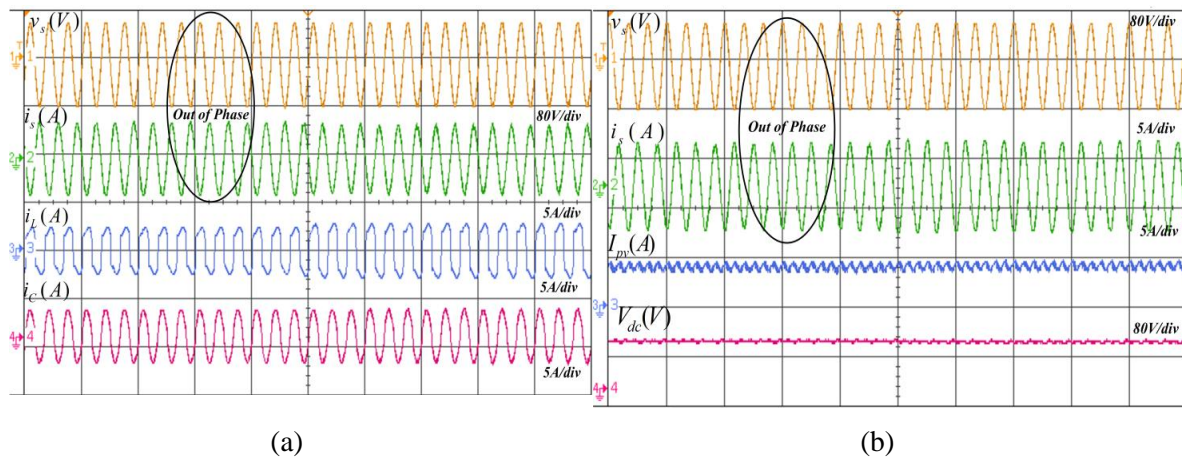


Fig.4.46 Dynamic performance of SRFT with PV for single phase system showing (a) (v_s, i_s, i_L, i_C) (b) $(v_s, i_s, I_{pv}, V_{dc})$

4.11.1.2. Experimental Performance with SOGI Controller for Single-Phase System:

The intermediate performance of SOGI controller is shown in Fig.4.47 which shows load current (i_L), in filtered phase component of load current ($i_{L\alpha}$), filtered quadrature phase component of load current ($i_{L\beta}$) and output weight of SOGI controller. The output weight of SOGI changes as the load changes but it takes two cycles to converge as shown in Fig.4.47.

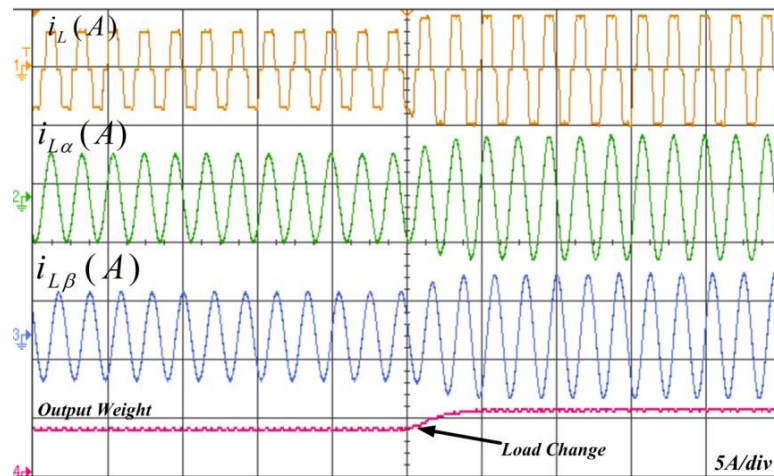
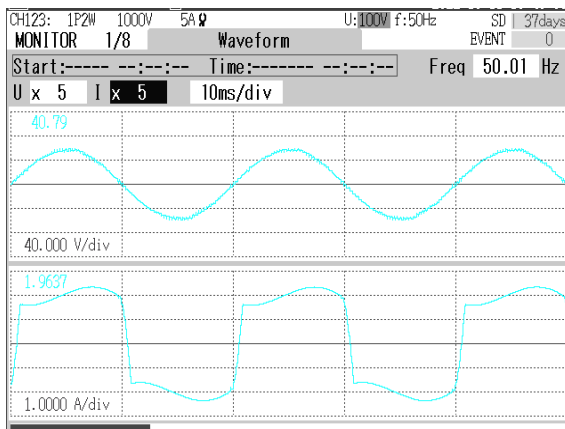
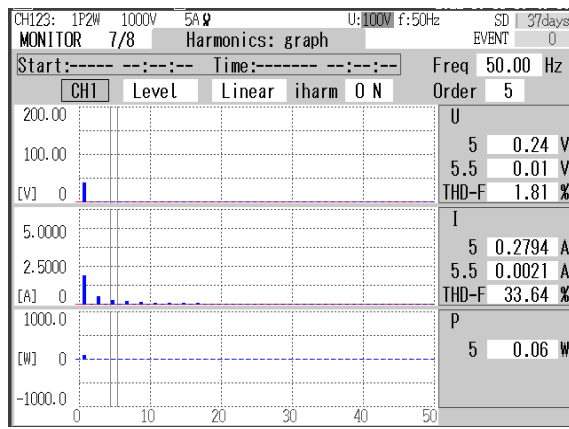


Fig.4.47 Intermediate performance of SOGI filter showing (a) load current (i_L), (b) in-phase component of load current ($i_{L\alpha}$), (c) quadrature phase component of load current ($i_{L\beta}$) (d) output weight.



(a)



(c)

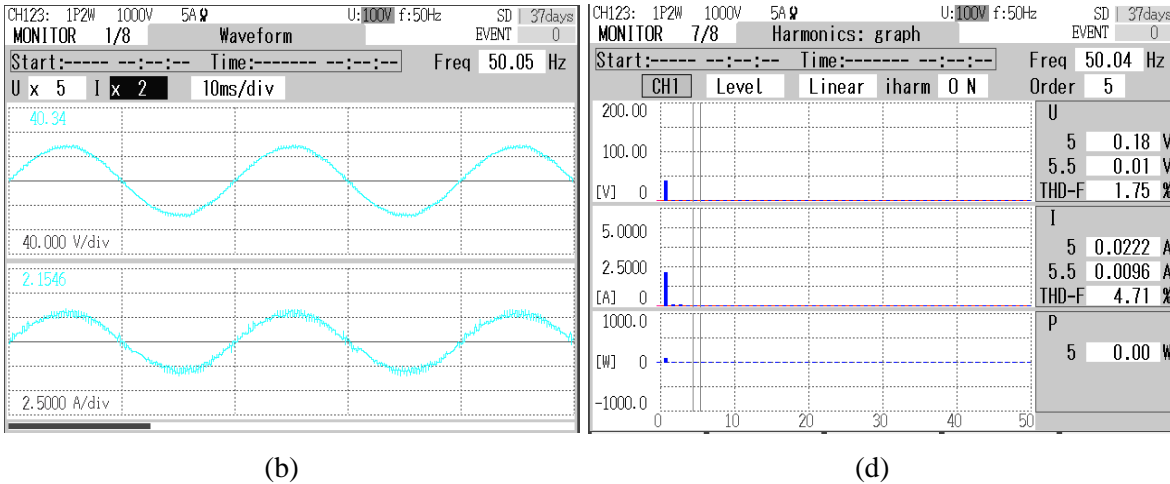


Fig.4.48 Steady state waveforms of single phase system showing (a) Source Voltage (v_s) and load current (i_L) (b) Source Voltage (v_s) and source current (i_s) (c) THD of v_s (1.81%) and i_L (33.64%) (d) THD of v_s (1.75%) and i_s (4.71%)

The steady state performance of the single phase system is shown in Fig.4.48. Fig.4.48(a) shows waveform of source voltage(v_s) and load current(i_L). Fig.4.48(b) shows the waveform of source voltage (v_s) and source current(i_s). The THD in load current is 33.64% as shown in Fig.4.48(c).The THD in source voltage is 1.75% and THD in source current is 4.71% as shown in Fig.4.48(d) which as per IEEE 519 standard.

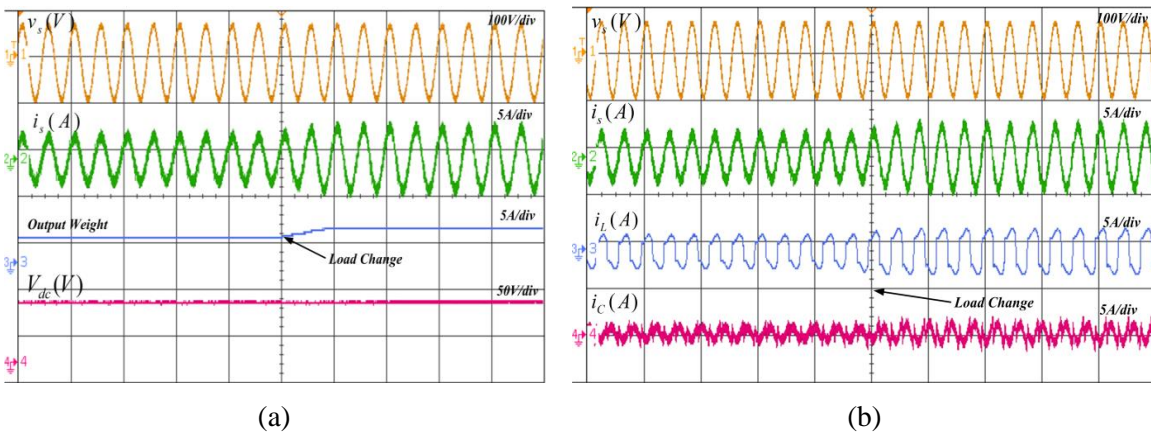


Fig.4.49 Dynamic performance of SOGI without PV for single phase system showing (a) ($v_s, i_s, output\ weight, V_{dc}$) (b) (v_s, i_s, i_L, i_C)

The dynamic performance of the single phase system without PV is shown in Fig.4.49 (a-b) in which source voltage (v_s), source current (i_s), load current (I_L), converter current (i_c), DC link voltage (V_{DC}), and output fundamental weight are shown. From Fig.4.49 (a-b) it can be noticed that the grid current is sinusoidal and the DC link voltage is stable with changes in load. Grid current harmonic content is also upheld in accordance with IEEE 519 standard.

Fig.4.50 (a-b) shows dynamic performance of SOGI for single phase system with PV integrated at the DC link of the inverter. Fig.4.50(a) shows (v_s, i_s, i_L, i_c) and clearly an out of phase relationship between the source voltage and source current are visible due to PV integration. Fig.4.50(b) shows (v_s, i_s, I_{pv}, V_{dc}).

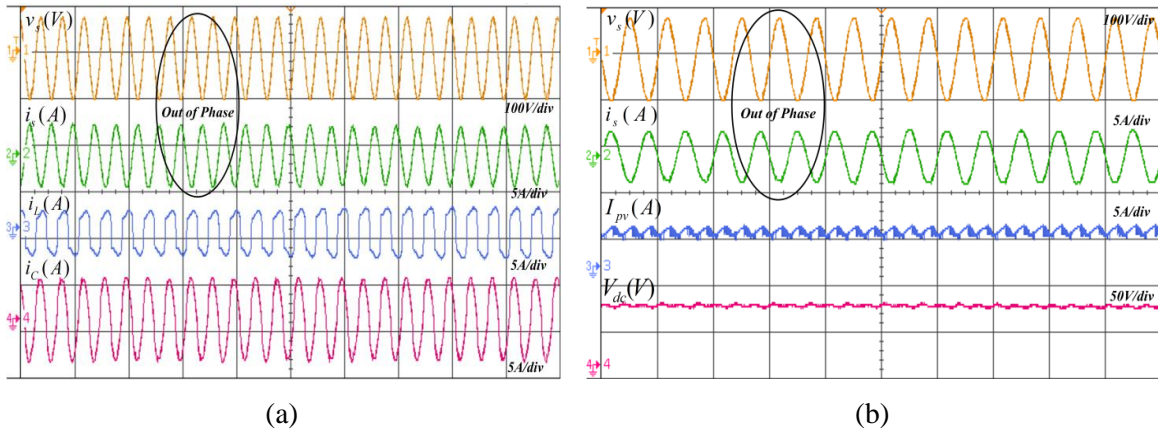


Fig.4.50 Dynamic performance of SOGI with PV for single phase system showing (a) (v_s, i_s, i_L, i_c) (b) (v_s, i_s, I_{pv}, V_{dc})

4.11.1.3. Experimental Performance with Adaptive BP Controller for Single-Phase System:

The intermediate performance of BP controller is shown in Fig.4.51 which shows load current (i_L), desired fundamental weight of load current, output fundamental weight of load current and error output weight of BP controller.

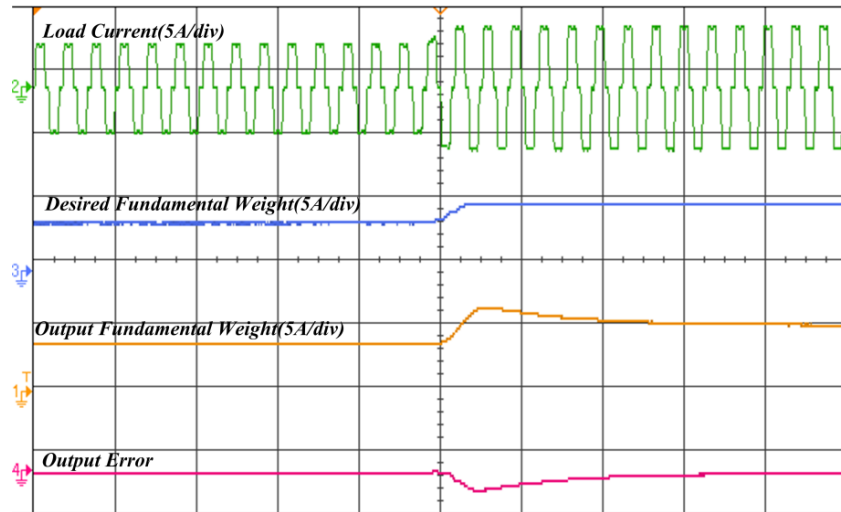
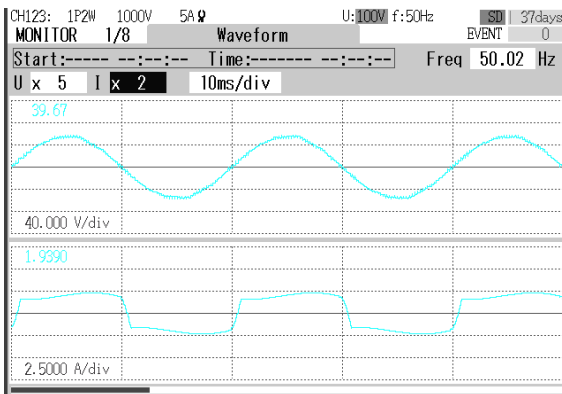
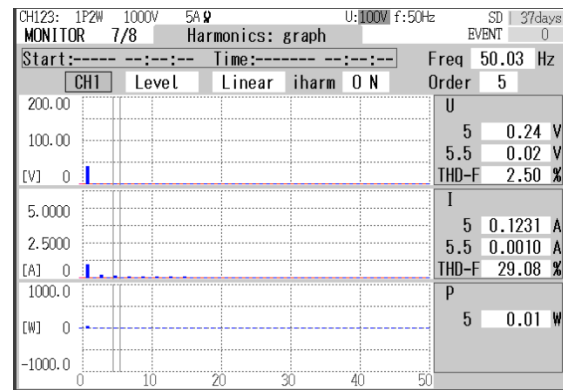


Fig.4.51 Intermediate performance of BP controller showing (a) load current (i_L), (b) desired fundamental weight of load current, (c) output fundamental weight of load current (d) output error.

The steady state performance of the single phase system is shown in Fig.4.52. Fig.4.52(a) shows waveform of source voltage (v_s) and load current (i_L). Fig.4.52(b) shows the waveform of source voltage (v_s) and source current (i_s). The THD in load current is 29.08% as shown in Fig.4.52(c). The THD in source voltage is 1.65% and THD in source current is 4.65% as shown in Fig.4.52(d) which as per IEEE 519 standard.

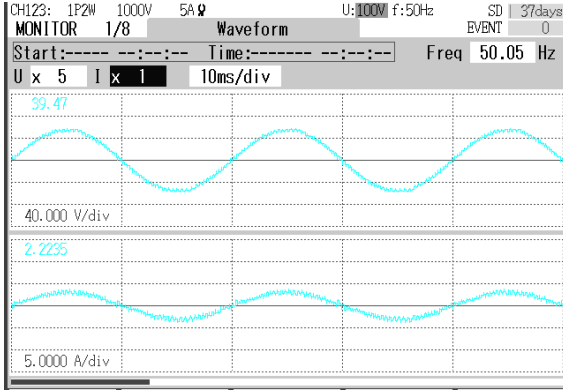


(a)

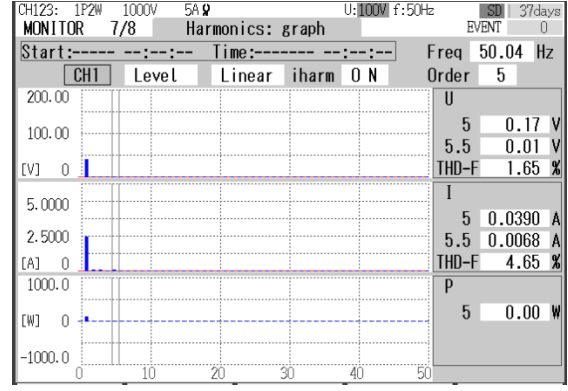


(c)

Fig.4.52 Steady state waveforms of single phase system showing (a) source voltage (v_s) and load current (i_L) (b) source voltage (v_s) and source current (i_s)

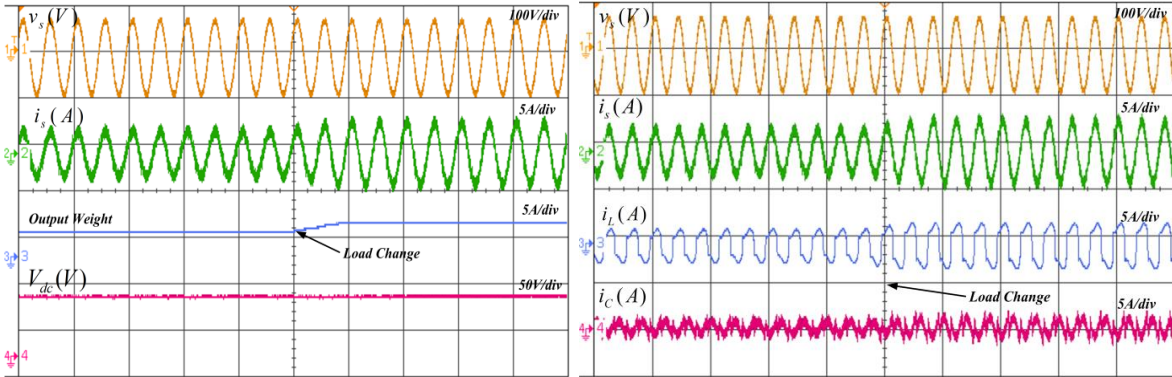


(b)



(d)

Fig.4.52 Steady state waveforms of single phase system showing (c) THD of v_s (2.50%) and i_L (29.08%) (d) THD of v_s (1.65%) and i_s (4.65%)



(a)

(b)

Fig.4.53 Dynamic performance of BP controller without PV for single phase system showing (a) ($v_s, i_s, output\ weight, V_{dc}$) (b) (v_s, i_s, i_L, i_c)

The dynamic performance of the single phase system without PV integration is shown in Fig.4.53 (a-b) in which source voltage (V_s), source current (I_s), load current (I_L), converter current (i_c), DC link voltage (V_{DC}), and output fundamental weight are shown. From Fig.4.53 (a-b) it is noted that the grid current is sinusoidal and the DC link voltage is stable with changes in load. Grid current harmonic content is also upheld in accordance with IEEE 519 standard.

Fig.4.54 (a-b) shows dynamic performance of BP controller for single phase system with PV integrated at the DC link of the inverter. Fig.4.54(a) shows (v_s, i_s, i_L, i_c) and clearly

an out of phase relationship between the source voltage and source current are visible due to PV integration. Fig.4.54(b) shows $(v_s, i_s, I_{pv}, V_{dc})$.

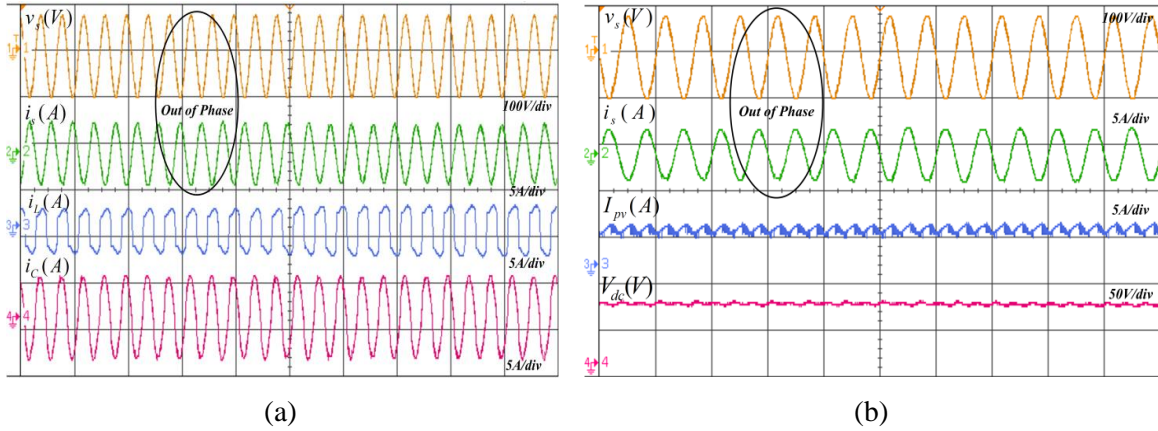


Fig.4.54 Dynamic performance of BP controller with PV for single phase system showing (a) (v_s, i_s, i_L, i_c) (b) $(v_s, i_s, I_{pv}, V_{dc})$

4.11.1.4. Experimental Performance with RBFNN Controller for Single-Phase System:

The experimental performances of RBFNN is investigated in single phase system and the steady state and dynamic response under various loading scenarios for both with and without PV integrated system is analyzed.

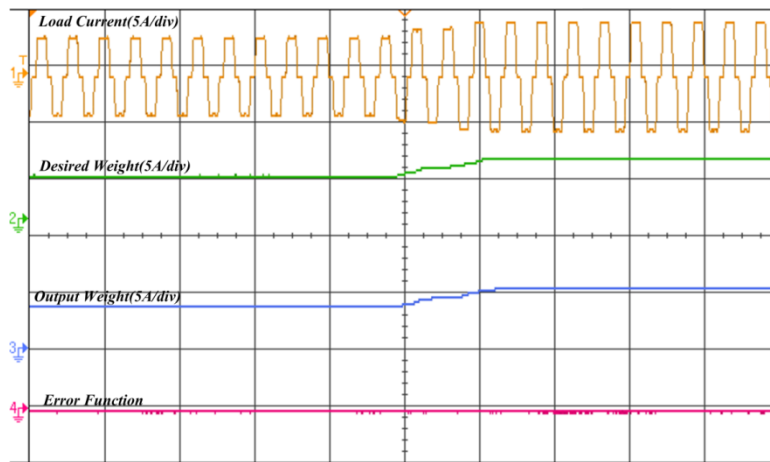
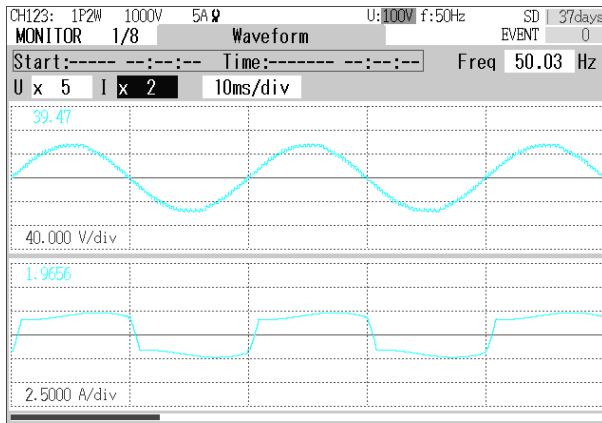
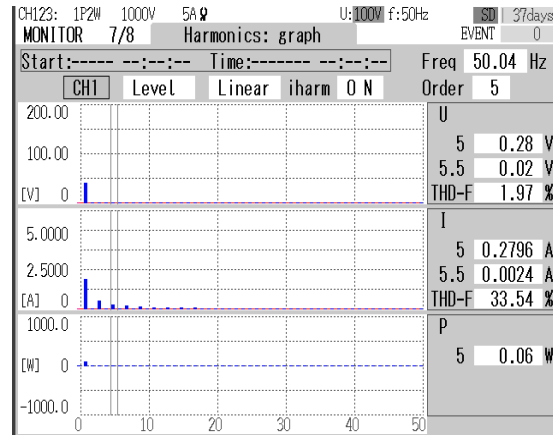


Fig.4.55 Intermediate performance of proposed RBFNN controller

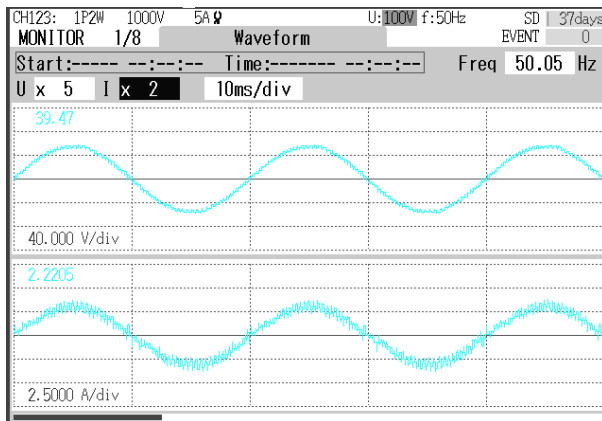
The intermediate performance of proposed RBFNN controller is shown in Fig.4.55 which shows load current (i_L), desired weight of load current, output weight of load current and error between desired weight and output weight of proposed RBFNN controller. The output weight of proposed RBFNN controller changes as the load values and it is shown in Fig.4.55. The steady state performance of the single is shown in Fig.4.56. Fig.4.56(a) shows waveform of source voltage(V_S) and load current(I_L). Fig.4.56(b) shows the waveform of source voltage (V_S) and source current(I_S). The THD in load current is 33.54% as shown in Fig.4.56(c).The THD in source voltage is 1.88% and THD in source current 4.58% shown in Fig.4.56(d) which as per IEEE 519 standard.



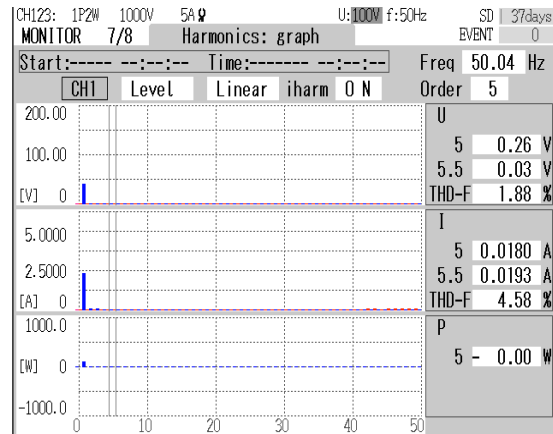
(a)



(c)



(b)



(d)

Fig.4.56 Steady state waveforms of single phase system showing (a) source voltage (v_S) and load current (i_L) (b) source voltage (v_S) and source current (i_S) (c) THD of v_S (1.97%) and i_L (33.54%) (d) THD of v_S (1.88%) and i_S (4.58%)

The dynamic state performance of proposed single-phase system is taken during load disturbances with help of digital storage oscilloscope. The dynamic performance of the system without PV is shown in Fig.4.57 (a-b) in which source voltage (v_s), source current (i_s), load current (i_L), converter current (i_c), DC link voltage (V_{DC}), and output fundamental weight are shown. From Fig.4.57 (a-b) it is observed that during the change in load, the DC link voltage is stable and the grid current is sinusoidal.

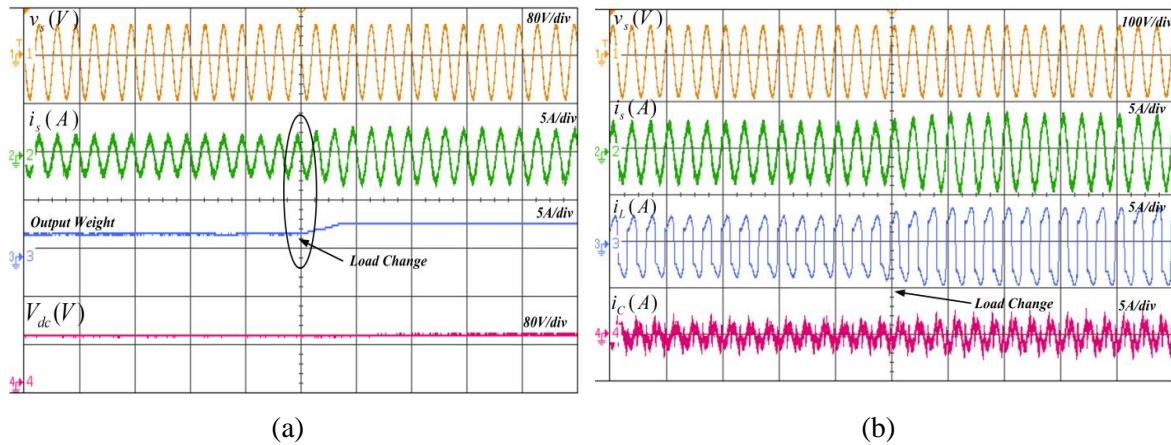


Fig.4.57 Dynamic performance of proposed RBFNN controller without PV for single phase system showing (a) ($v_s, i_s, output\ weight, V_{dc}$) (b) (v_s, i_s, i_L, i_c)

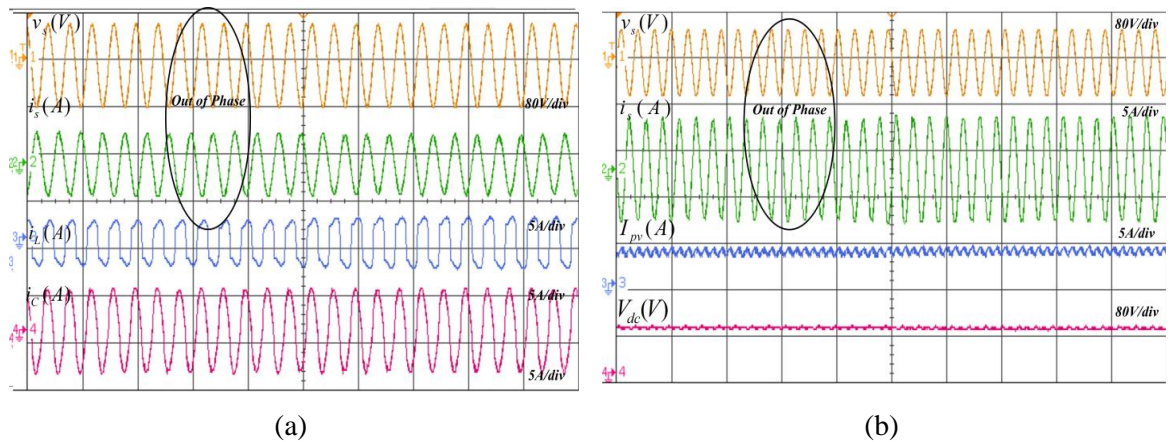


Fig.4.58 Dynamic performance of proposed RBFNN controller with PV for single phase system showing (a) (v_s, i_s, i_L, i_c) (b) (v_s, i_s, I_{pv}, V_{dc})

Fig.4.58(a-b) shows dynamic performance of proposed system with PV integrated at the DC link of the inverter in single phase system. Fig.4.58(a) shows (v_s, i_s, i_L, i_c) and clearly

an out of phase relationship between the source voltage and source current are visible due to PV integration. Fig.4.58(b) shows $(v_s, i_s, I_{pv}, V_{dc})$. The reference current is computed using the proposed RBFNN controller.

4.11.2. Three Phase Performance:

The performances of SRF, SOGI, adaptive BP based controller and adaptive RBFNN is investigated in three-phase system and the steady state and dynamic response under various loading scenarios for both the cases viz. SAPF without and with PV integrated system is analyzed in following section.

4.11.2.1. Experimental Performance with SRF Technique for Three-Phase System:

The experimental performances of RBFNN is investigated in three phase system and the steady state and dynamic response under various loading scenarios for both with and without PV integrated system is analyzed. The steady state performance of the three-phase system is shown in Fig.4.59. Fig.4.59(a) shows waveform of three phase source voltage (V_{Sabc}) and three phase load current (I_{Labc}). Fig.4.59(b) shows the waveform of three phase source voltage (V_{Sabc}) and three phase source current (I_{Sabc}). The THD in load current is 22.78% as shown in Fig.4.59(c). The THD in source voltage is 2.11% and THD in source current 6.59% shown in Fig.4.59(d) which is close to IEEE 519 standard.

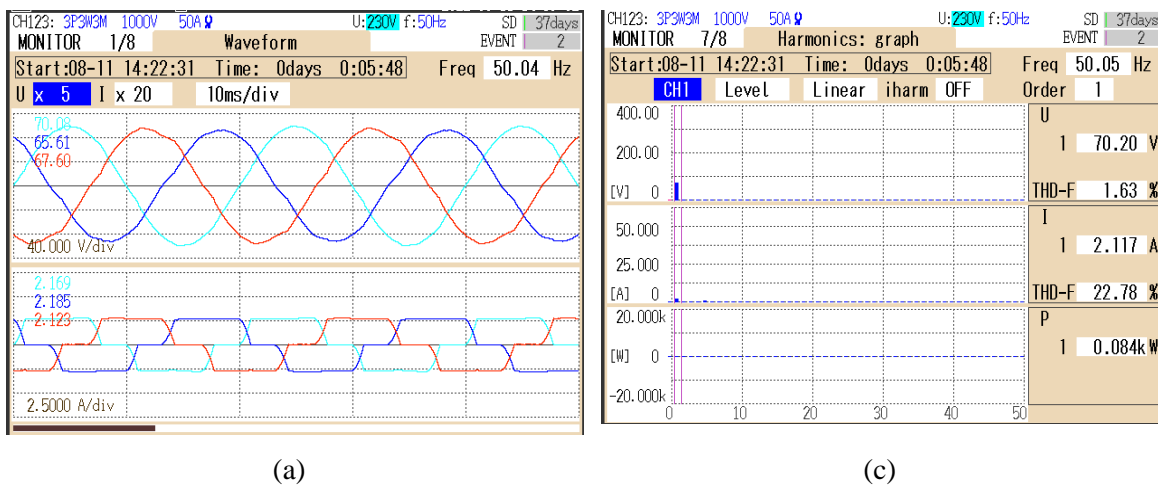
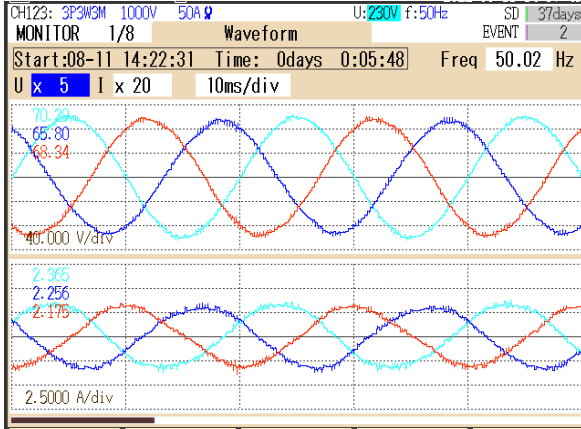
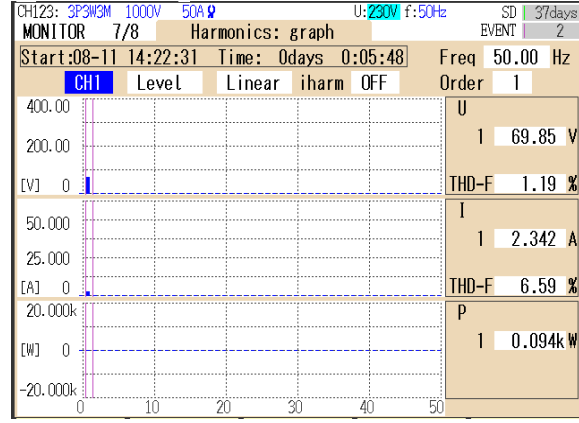


Fig.4.59 Steady state waveforms of three phase system showing (a) source voltage (v_{Sabc}) and load current (i_{Labc}) (b) source voltage (v_{Sabc}) and source current (i_{Sabc})



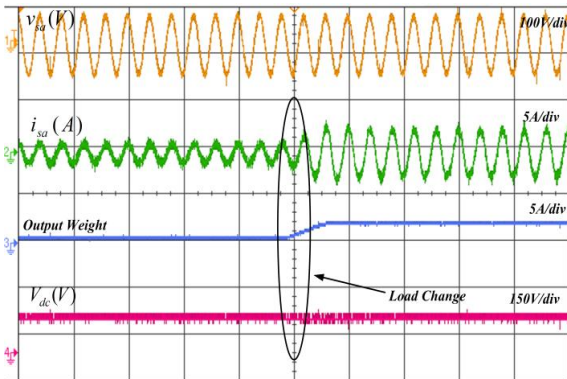
(b)



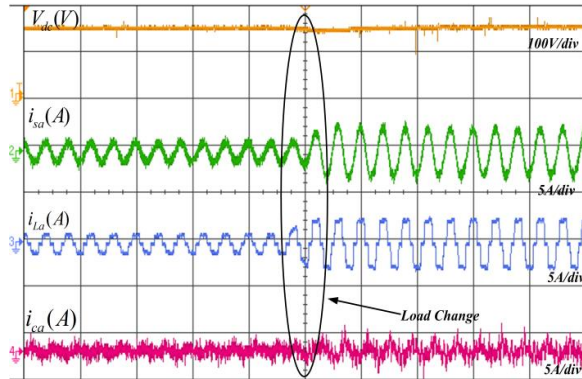
(d)

Fig.4.59 Steady state waveforms of three phase system showing (c) THD of v_{Sabc} (2.11%) and i_{Labc} (22.78%)(d) THD of v_{Sabc} (1.19%) and i_{Sabc} (6.59%)

The dynamic performance of the three-phase system without PV is shown in Fig.4.60 (a-d) in which source voltage of phase a (V_{sa}), source current of all three phases (I_{Sabc}), load current of all three phases (I_{Labc}), converter current of phase a (i_{Ca}), DC link voltage (V_{DC}), and output fundamental weight are shown. From Fig.4.60(a-b) it is observed that during the change in load, the DC link voltage is stable and the grid current is sinusoidal. The harmonic content in grid current is also maintained as per IEEE 519 standard.



(a)



(b)

Fig.4.60 Dynamic performance of SRFT without PV for three phase system showing (a) (v_{sa} , i_{sa} , output weight, V_{dc}) (b) (V_{dc} , i_{sa} , i_{La} , i_{Ca})

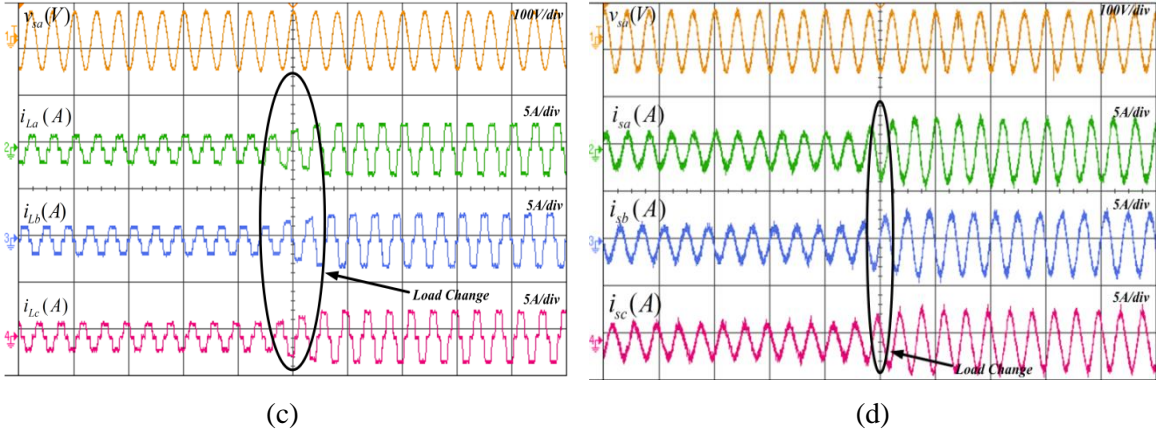


Fig.4.60 Dynamic performance of SRFT without PV for three phase system showing (c) $(v_{sa}, i_{La}, i_{Lb}, i_{Lc})$ (d) $(v_{sa}, i_{sa}, i_{sb}, i_{sc})$

The output weight shows fast convergence and reference current changes as per load changes. This indicates a satisfactory operation of SRF based control technique under different loading condition. The steady state of the system is achieved within one to two cycle of operation. Fig.4.61 (a-b) shows dynamic performance of SRF for three phase system with PV integrated at the DC link of the inverter. Fig.4.61 (a) shows $(v_{sa}, i_{sa}, i_{La}, i_{ca})$ and clearly an out of phase relationship between the source voltage and source current are visible due to PV integration.

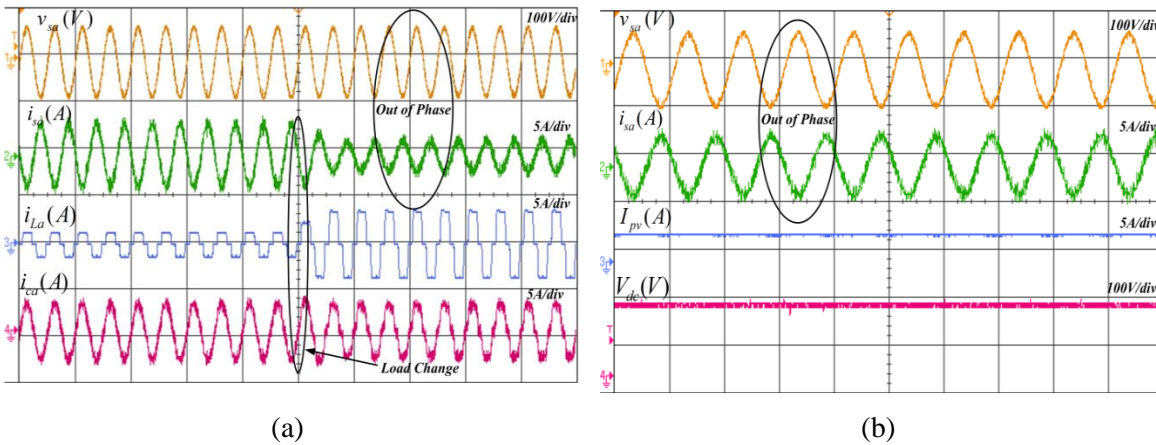


Fig.4.61 Dynamic performance of SRFT with PV for three phase system showing (a) $(v_{sa}, i_{sa}, i_{La}, i_{ca})$ (b) $(v_{sa}, i_{sa}, I_{pv}, V_{dc})$

Figure 4.61(a) shows that the source current is sinusoidal and the source current decreases as the load increased. Grid current harmonic content is also maintained in

accordance with IEEE 1547 standard. Fig.4.61(b) shows $(v_{sa}, i_{sa}, I_{pv}, V_{dc})$. The reference current is computed using the SRFT controller. It is observed that during the operation of PV integrated VSC, PV supplies power to both load and grid. The operation is stable and irrespective of highly non-linear load current, the grid current is sinusoidal and meets IEEE 1547 standard for single and three phase system.

4.11.2.2. Experimental Performance with SOGI Controller for Three-Phase System:

The experimental performance of SOGI controller in a three-phase system is explored, and the steady-state and dynamic response under various loading situations is analyzed for both with and without a PV integrated system. The steady state performance of the three-phase system is shown in Fig.4.62. Fig.4.62(a) shows waveform of three phase source voltage(v_{Sabc}) and three phase load current(i_{Labc}). Fig.4.62(b) shows the waveform of three phase source voltage (v_{Sabc}) and three phase source current(i_{Sabc}). The THD in load current is 24.03% as shown in Fig.4.62(c).The THD in source voltage is 1.41% and THD in source current 3.25% shown in Fig.4.62(d) as per IEEE 519 standard. Harmonic reduction for supply currents in three phase systems is carried out using the single phase SAPF based on the SOGI filter. Furthermore, the supply voltage and current operate with nearly unity power factor due to their in-phase relationship.

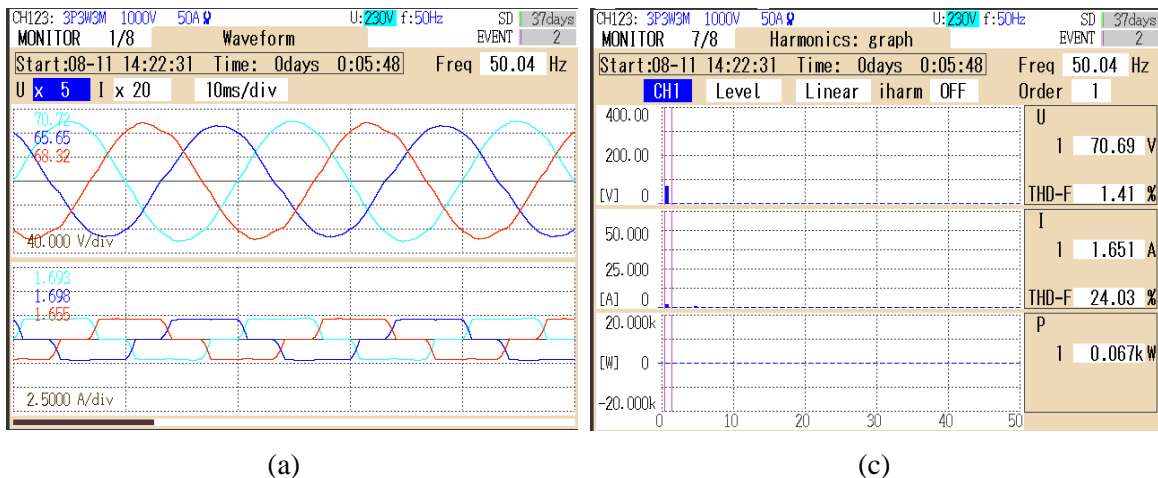
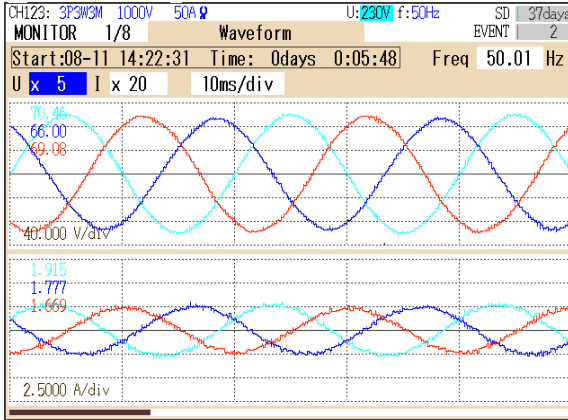
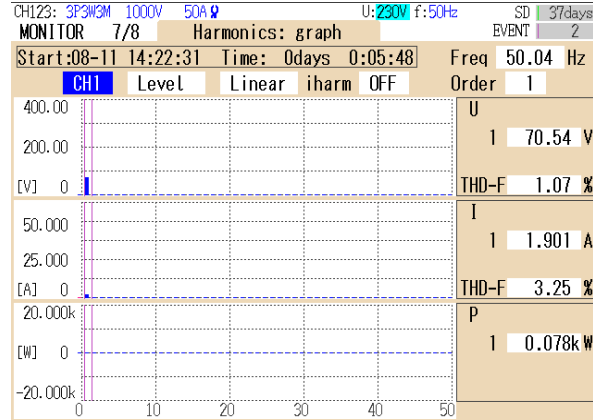


Fig.4.62 Steady state waveforms of three phase system showing (a) source voltage (v_{Sabc}) and load current (i_{Labc}) (b) source voltage (v_{Sabc}) and source current (i_{Sabc})

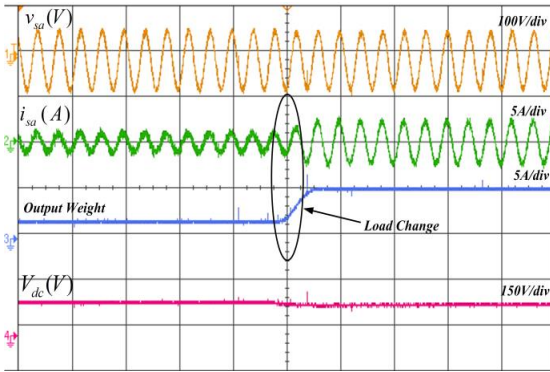


(b)

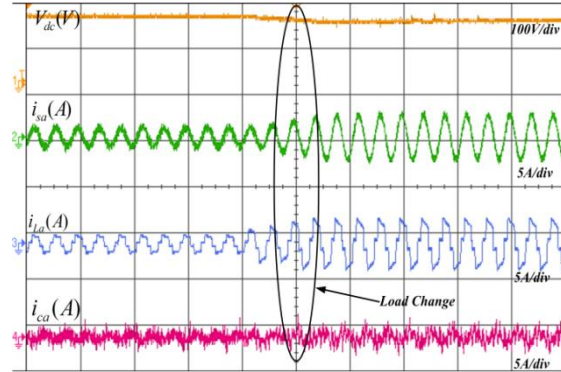


(d)

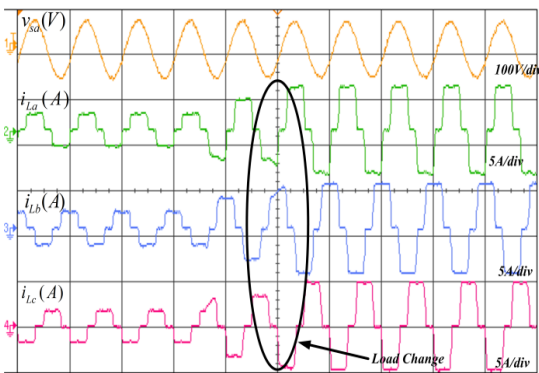
Fig.4.62 Steady state waveforms of three phase system showing (c) THD of v_{Sabc} (1.41%) and i_{Labc} (24.03%)(d) THD of v_{Sabc} (1.07%) and i_{Sabc} (3.25%)



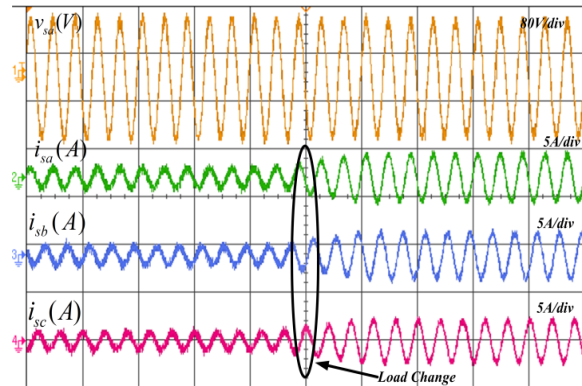
(a)



(b)



(c)



(d)

Fig.4.63 Dynamic performance of SOGI controller without PV for three phase system showing (a) (v_{sa} , i_{sa} , output weight, V_{dc}) (b) (V_{dc} , i_{sa} , i_{La} , i_{Ca}) (c) (v_{sa} , i_{La} , i_{Lb} , i_{Lc}) (d) (v_{sa} , i_{sa} , i_{Sb} , i_{Sc})

The dynamic performance of the three phase system without PV is shown in Fig.4.63 (a-d) in which source voltage of phase-a (v_{sa}), source current of all three phases (i_{sabc}), load current of all three phases (i_{Labc}), converter current of phase a (i_{ca}), DC link voltage (V_{DC}), and output fundamental weight are shown. From Fig.4.63 (a-b) it is observed that during the change in load, the DC link voltage is stable and the grid current is sinusoidal. The harmonic content in grid current is also maintained as per IEEE 519 standard. The output weight exhibits quick convergence and reference current variations with changing loads. This shows that the SOGI filter-based control approach has performed satisfactorily under various loading conditions. The steady state of the system is achieved within two cycles of operation.

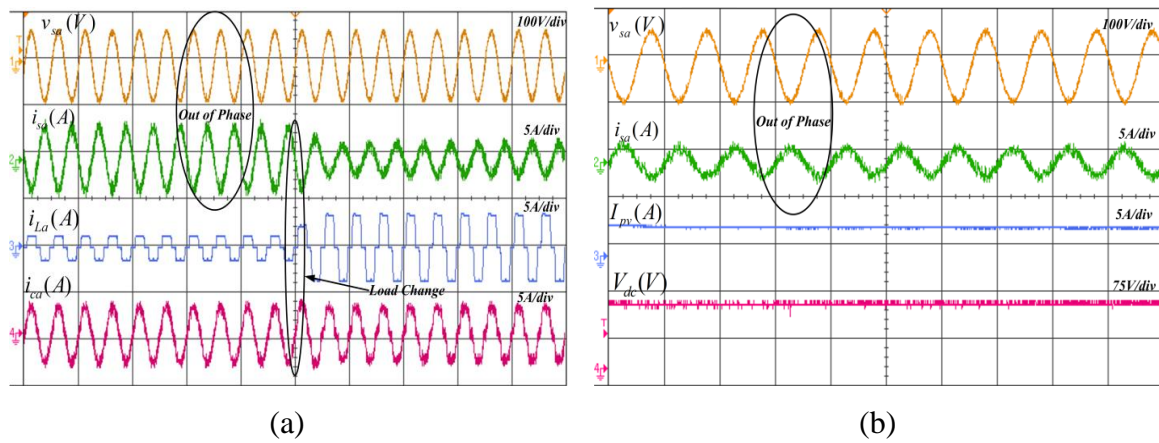


Fig.4.64 Dynamic performance of SOGI controller with PV for three-phase system showing (a) ($v_{sa}, i_{sa}, i_{La}, i_{ca}$) showing (b) ($v_{sa}, i_{sa}, I_{pv}, V_{dc}$)

Fig.4.64 Dynamic performance of SOGI controller with PV for three phase system Fig.4.64 (a-b) shows dynamic performance of SOGI for three phase system with PV integrated at the DC link of the inverter. Fig.4.64 (a) shows ($v_{sa}, i_{sa}, i_{La}, i_{ca}$) and clearly an out of phase relationship between the source voltage and source current are visible due to PV integration. The source current is sinusoidal and decreases as the load increases, as shown in Figure 4.64 (a). Moreover, IEEE 1547 standard compliance is maintained for the harmonic content of the grid. Fig.4.64 (b) shows ($v_{sa}, i_{sa}, I_{pv}, V_{dc}$). It is observed that during the operation of PV integrated SAPF, PV supplies power to both load and grid.

Regardless of the extremely nonlinear load current, the operation is steady, and the source current is sinusoidal and fulfills IEEE 1547 standard for three phase systems.

4.11.2.3. Experimental Performance with Adaptive BP Controller for Three-Phase System:

The steady state performance of BP controller for the three-phase system is shown in Fig.4.65. Fig.4.65(a) shows waveform of three phase source voltage(v_{Sabc}) and three phase load current(i_{Labc}). Fig.4.65(b) shows the waveform of three phase source voltage (v_{Sabc}) and three phase source current(i_{Sabc}). The THD in load current is 22.40% as shown in Fig.4.65(c).The THD in source voltage is 1.31% and THD in source current 3.87% shown in Fig.4.65(d) which is close to IEEE 519 standard.

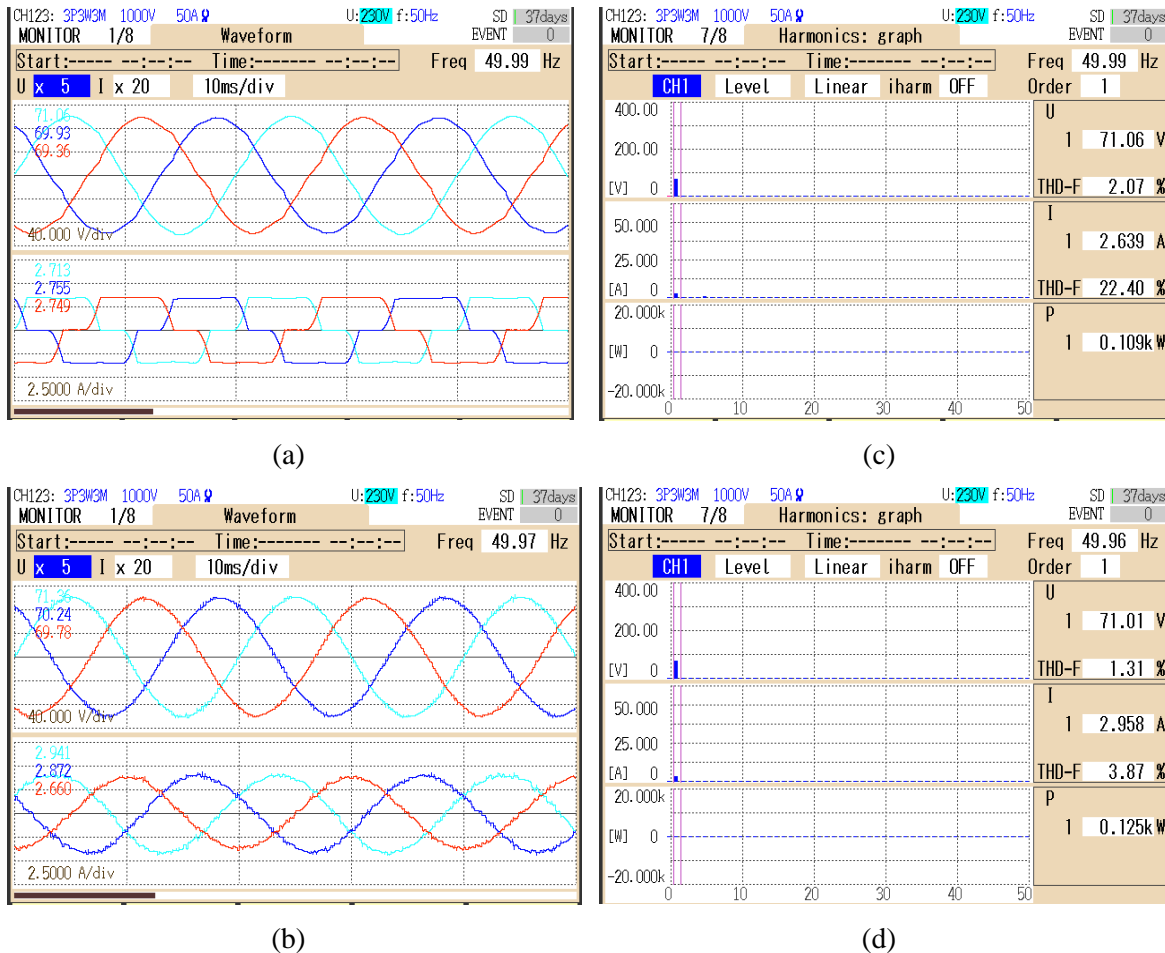


Fig.4.65 Steady state waveforms of three phase system showing (a) source voltage (v_{Sabc}) and load current (i_{Labc}) (b) source voltage (v_S) and source current (i_{Sabc}) (c) THD of v_{Sabc} (2.07%) and i_{Labc} (22.40%)(d) THD of v_{Sabc} (1.31%) and i_{Labc} (3.87%)

The dynamic performance of the three-phase system without PV is shown in Fig.4.66 (a-d) in which source voltage of phase a (v_{sa}), source current of all three phases (i_{sabc}), load current of all three phases (i_{Labc}), converter current of phase a (i_{ca}), DC link voltage (V_{DC}), and output fundamental weight are shown. From Fig.4.66(a-b) it is observed that during the change in load, the DC link voltage is stable and the grid current is sinusoidal. The harmonic content in grid current is also maintained as per IEEE 519 standard.

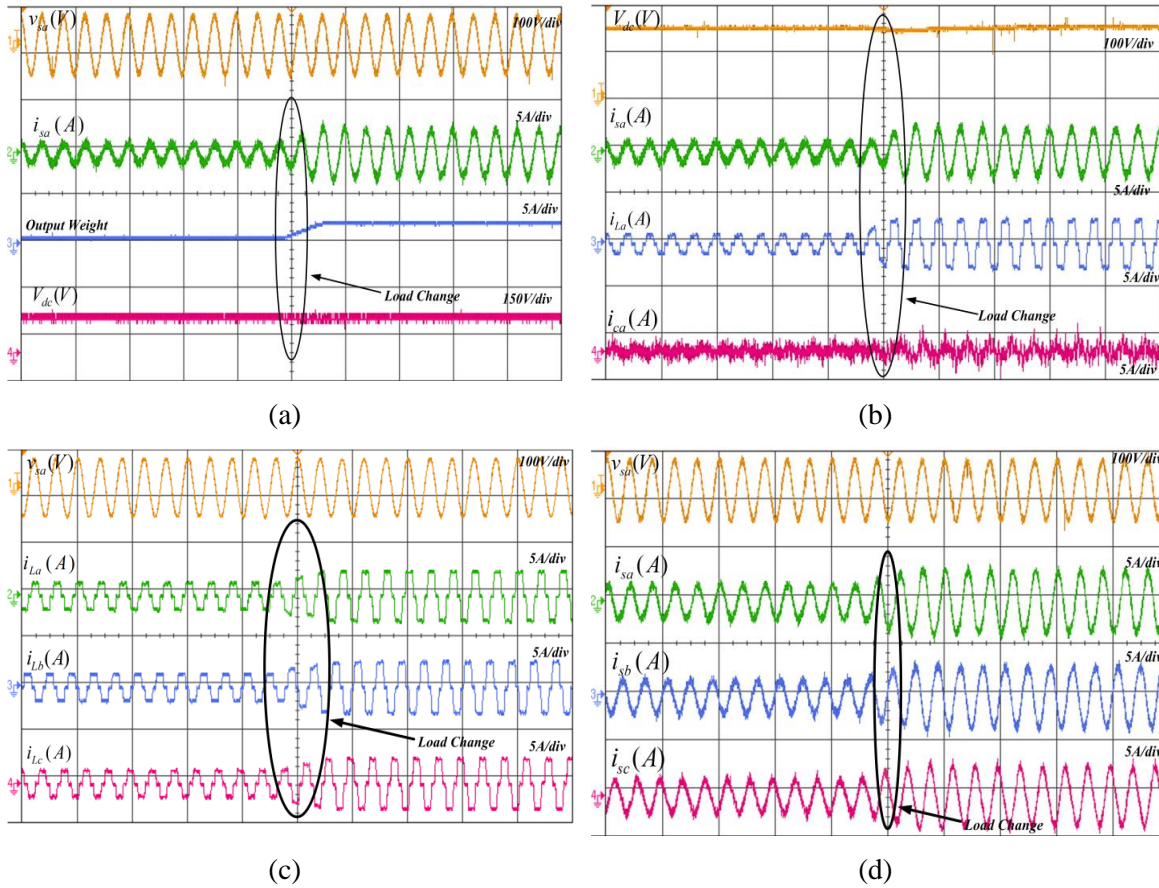


Fig.4.66 Dynamic performance of SRFT without PV for three phase system showing (a) ($v_{sa}, i_{sa}, output\ weight, V_{dc}$) (b) ($V_{dc}, i_{sa}, i_{La}, i_{ca}$) (c) ($v_{sa}, i_{La}, i_{Lb}, i_{Lc}$) (d) ($v_{sa}, i_{sa}, i_{sb}, i_{sc}$)

The output weight shows fast convergence and reference current changes as per load changes. The steady state of the system is achieved within one to two cycle of operation. Fig.4.67 (a-b) shows dynamic performance of three phase system with PV integrated at

the DC link of the inverter. Fig.4.67 (a) shows $(v_{sa}, i_{sa}, i_{La}, i_{ca})$ and clearly an out of phase relationship between the source voltage and source current are visible due to PV integration.

Figure 4.67(a) shows that the source current is sinusoidal and the source current decreases as the load increased. Grid current harmonic content is also maintained in accordance with IEEE 1547 standard. Fig.4.67(b) shows $(v_{sa}, i_{sa}, I_{pv}, V_{dc})$. The reference current is computed using the BP controller. The operation is stable and irrespective of highly non-linear load current, the grid current is sinusoidal and meets IEEE 1547 standard for single and three phase system.

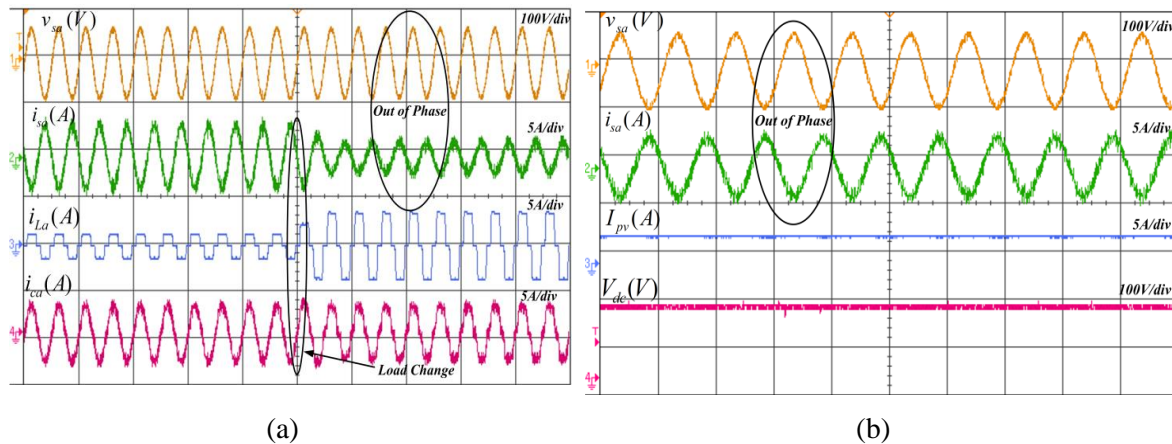
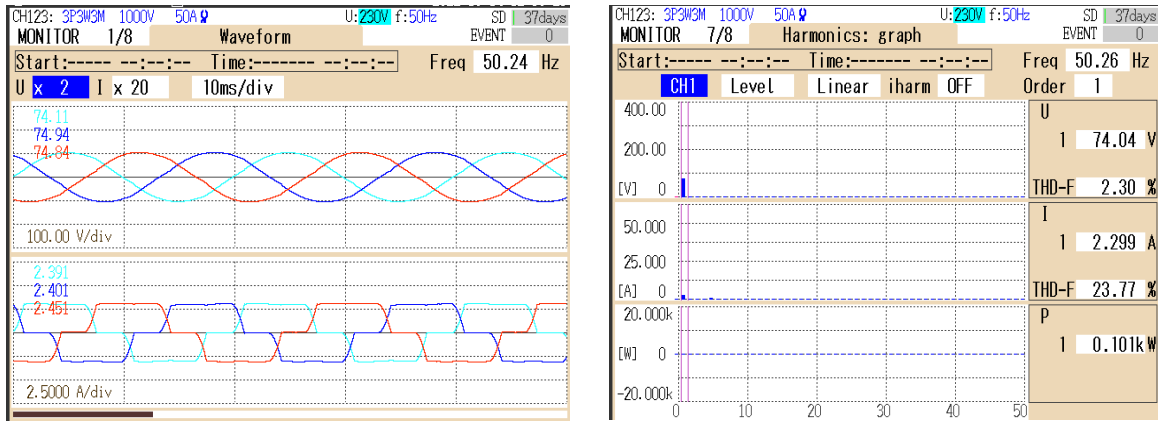


Fig.4.67 Dynamic performance of SRFT with PV for three phase system showing (a) $(v_{sa}, i_{sa}, i_{La}, i_{ca})$ (b) $(v_{sa}, i_{sa}, I_{pv}, V_{dc})$

4.11.2.4. Experimental Performance with Adaptive RBFNN Controller for Three-Phase System:

The steady state performance of the three-phase system is shown in Fig.4.68. Fig.4.68(a) shows waveform of three phase source voltage (v_{sabc}) and three phase load current (i_{Labc}) . Fig.4.68(b) shows the waveform of three phase source voltage (v_{sabc}) and three phase source current (i_{sabc}) . The THD in load current is 23.77% as shown in Fig.4.68(c). The THD in source voltage is 2.30% and THD in source current 2.98% shown in Fig.4.68(d) as per IEEE 519 standard. Harmonic reduction for supply currents in single and three phase systems is carried out using the single phase SAPF based on the

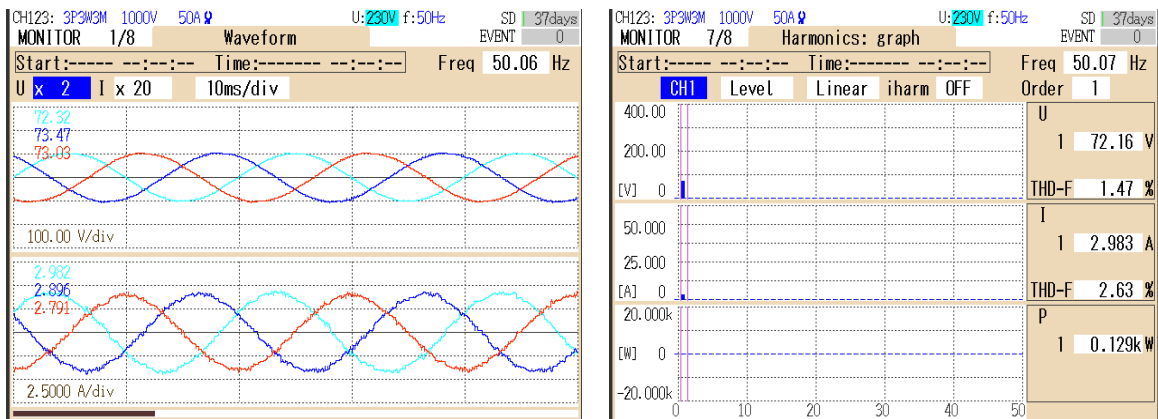
proposed RBFNN controller. Furthermore, the supply voltage and current operate with nearly unity power factor due to their in-phase relationship



(a)

(c)

Fig.4.68 Steady state waveforms of three phase system showing (a) source voltage (v_{Sabc}) and load current (i_{Labc}) (b) source voltage (v_{Sabc}) and source current (i_{Sabc})



(b)

(d)

Fig.4.68 Steady state waveforms of three phase system showing (c) THD of v_{Sabc} (2.30%) and i_{Labc} (23.77%)(d) THD of v_{Sabc} (1.47%) and i_{Sabc} (2.63%)

The dynamic performance of the three phase system without PV is shown in Fig.4.69 (a-d) in which source voltage of phase-a (v_{sa}), source current of all three phases (i_{Sabc}), load current of all three phases (i_{Labc}), converter current of phase a (i_{ca}), DC link voltage (V_{DC}), and output fundamental weight are shown. From Fig.4.69(a-b) it is observed that during the change in load, the DC link voltage is stable and the grid current is sinusoidal. The harmonic content in grid current is also maintained as per IEEE 519 standard. The

harmonic content in grid current is also maintained as per IEEE 519 standard. The fundamental gain FW shows fast convergence and reference current changes as per load changes. This indicates a satisfactory operation of RBFNN based control technique under different loading condition. The steady state of the system is achieved within one cycle of operation.

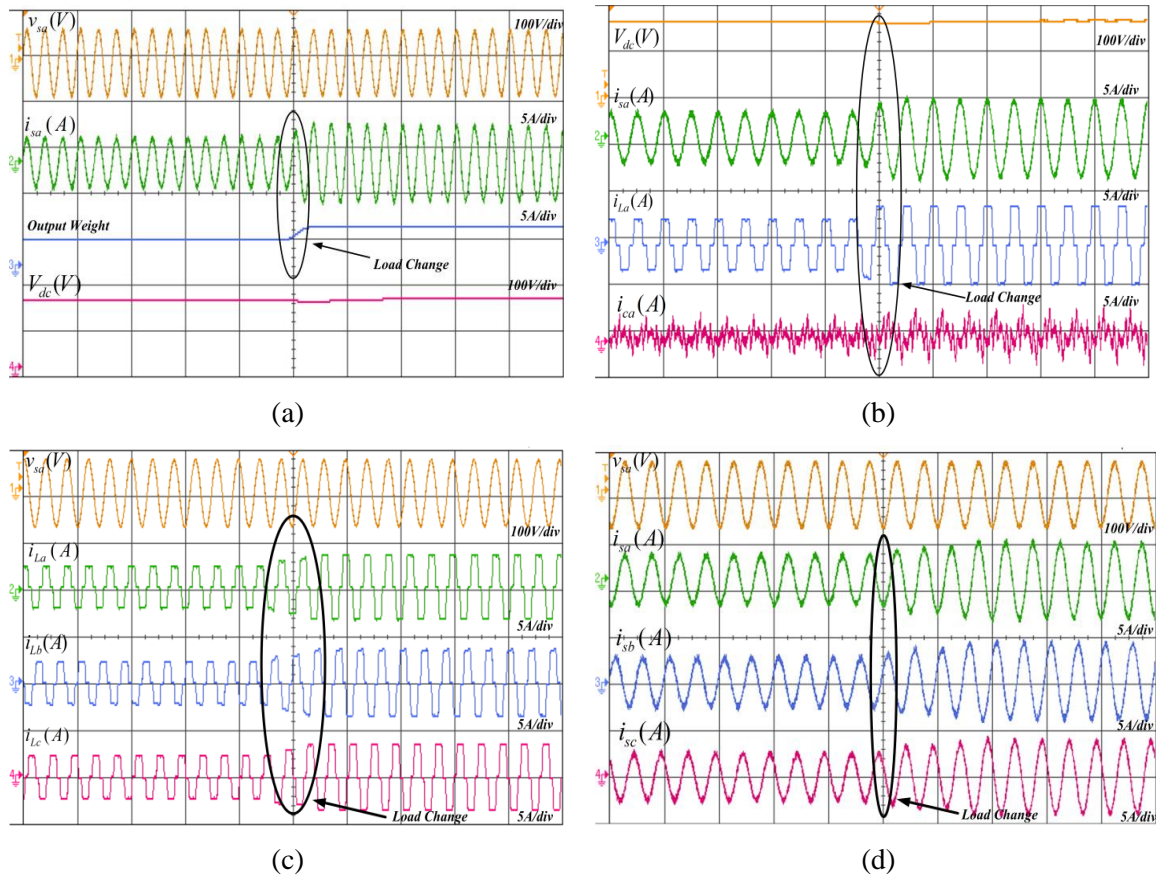


Fig.4.69 Dynamic performance of proposed RBFNN controller without PV for three phase system showing (a) ($v_{sa}, i_{sa}, output\ weight, V_{dc}$) (b) ($V_{dc}, i_{sa}, i_{La}, i_{Ca}$) (c) ($v_{sa}, i_{La}, i_{Lb}, i_{Lc}$) (d) ($v_{sa}, i_{sa}, i_{Sb}, i_{Sc}$)

Fig.4.70 (a-b) shows dynamic performance of proposed RBFNN controller for three phase system with PV integrated at the DC link of the inverter. Fig.4.70(a) shows ($v_{sa}, i_{sa}, i_{La}, i_{Ca}$) and clearly an out of phase relationship between the source voltage and source current are visible due to PV integration. The source current is sinusoidal and decreases as the load increases, as shown in Fig.4.69(a). Moreover, IEEE 1547 standard

compliance is maintained for the harmonic content of the grid. Fig.4.70(b) shows $(v_{sa}, i_{sa}, I_{pv}, V_{dc})$.

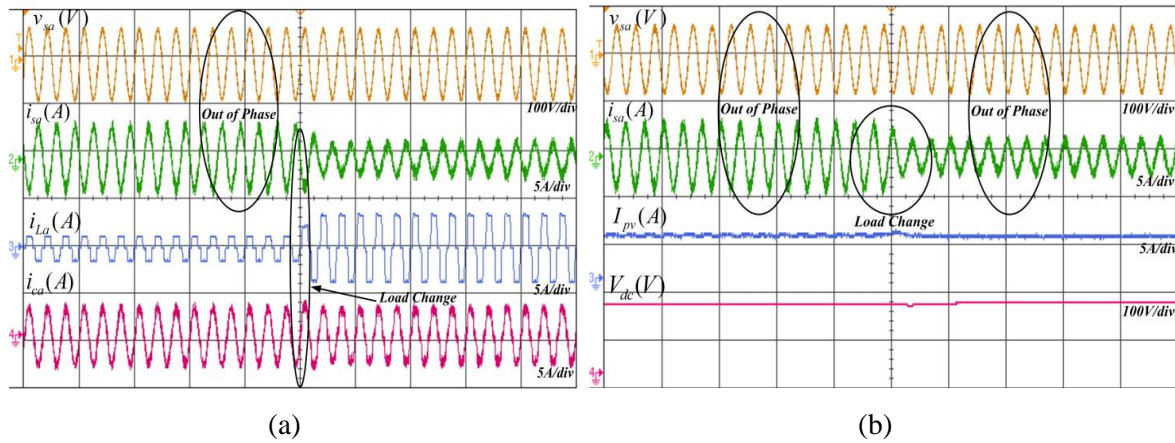


Fig.4.70 Dynamic performance of proposed RBFNN controller with PV for three phase system showing (a) $(v_{sa}, i_{sa}, i_{La}, i_{ca})$ (b) $(v_{sa}, i_{sa}, I_{pv}, V_{dc})$

Table 4.2 shows experimental performances of the conventional and proposed controllers. It is observed that during the operation of PV integrated SAPF, PV supplies power to both load and grid. Regardless of the extremely nonlinear load current, the operation is steady, and the source current is sinusoidal and fulfills IEEE 1547 standard for single and three phase systems.

Table 4.2 Experimental Performances

Experimental Performances of Single phase system					
S.No	Parameter	SRF technique	SOGI	BP	RBFNN
10.	% THD of v_s	2.04%	1.81%	2.50%	1.97%
11.	% THD of i_L	33.61%	33.64%	29.08%	33.54%
12.	% THD of i_s	4.99%	4.71%	4.65%	4.58%
Experimental Performances of Three Phase System					
13.	% THD of v_{sabc}	1.63%	1.41%	2.07%	2.30%
14.	% THD of i_{Labc}	22.78%	24.03%	22.40%	23.77%
15.	% THD of i_{sabc}	6.59%	3.25%	3.87%	2.63%

4.12. Conclusion:

This chapter's major contributions include design of SRFT and SOGI conventional control algorithm and the design and development of self-adaptive BP and RBFNN applied in single phase and three-phase single stage grid connected PV system for active power injection and reactive power compensation. The H-bridge inverters are employed as a SAPF to mitigate many power quality issues. These proposed structures are important for accomplishing load compensation in single-phase and three-phase systems feeding a range of linear and non-linear loads. The use of SRFT, SOGI, adaptive BP and RBFNN-based controllers are broad in scope, and it may be utilized for grid connected systems with or without a PV source interfaced to it. The system performance aspects are demonstrated when taking into account the influence of PV as well as at during night. The control algorithms have been designed to fulfill the entire reactive power needs of the load while also providing power quality enhancement features. The performance of SRFT and SOGI control is not up to standard, extra LPF is required to increase the performance of the SRFT and SOGI control algorithms. Adaptive BP and RBFNN consistently perform better in single-stage grid connected with and without PV condition. This chapter also includes experimental results for all control strategies for single-phase and three-phase grid-connected PV systems. The result clearly validates the efficient injection of active and reactive power to the grid based on load demand and PV power output. Power quality has improved under both linear and non-linear load conditions.

Chapter-5: Control of Three-Phases VSC as a SAPF under Polluted Grid Conditions

5.1 Introduction

Electrical systems must operate effectively and with a reliable power source. However, electrical grids can encounter problems with the quality of the power, resulting in what is known as a "polluted grid." Numerous disturbances, including sag/swell, harmonics, voltage fluctuation, unbalances, and other issues with power quality, are indicative of a polluted grid. These problems may negatively affect the functionality and dependability of connected equipment, resulting in decreased efficiency, equipment damage, and higher operating costs.

By resolving power quality issues, it is feasible to improve the stability, efficiency, and lifespan of electrical systems while reducing the risks associated with grid pollution.

This chapter discusses some established and new control methods for three-phase system to estimate the synchronizing signals under distorted grid voltage scenarios, as well as SAPF operation of a three-phase system under normal grid and polluted grid conditions for reactive power compensation and power quality improvement.

5.2. Unit Template Generation from Polluted Grid in Three Phase System

This chapter deals with three-phase VSC operation under polluted grid condition. The performance of VSC depends on the reference current estimation that depends on unit template of the system. Thus in this section unit template estimation in three phase system is discussed during polluted grid condition.

5.2.1. Unit Template for Three-Phase System:

The voltage signal of each phase can be estimated using the simplest approach is possible using unit templates. For grid synchronization, researchers frequently adopt this approach under conditions of standard grid voltage [168-170]. At PCC, three-phase voltages are monitored and represented as v_a , v_b , and v_c . The conventional unit template method fails to obtain synchronization templates properly under distorted grid condition and it will

impact the performance of VSC. Thus, the individual in-phase component (v_{aabc}) of each phases are obtained from SOGI filter shown in Fig.5.1.

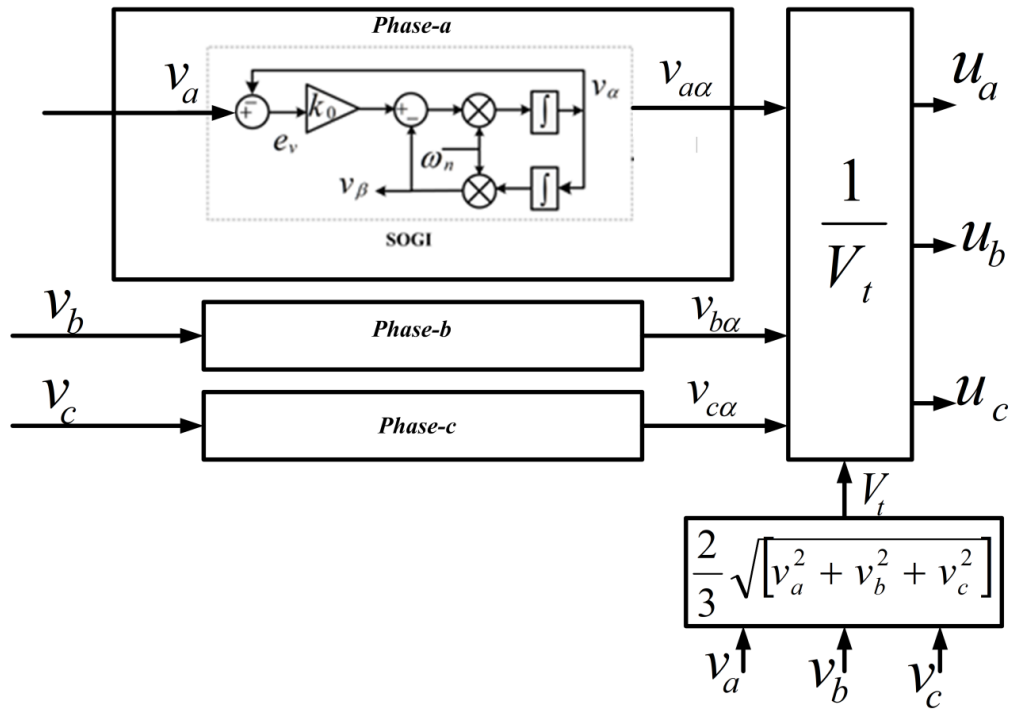


Fig.5.1(a) Structure of SOGI based unit template technique for three-phase system

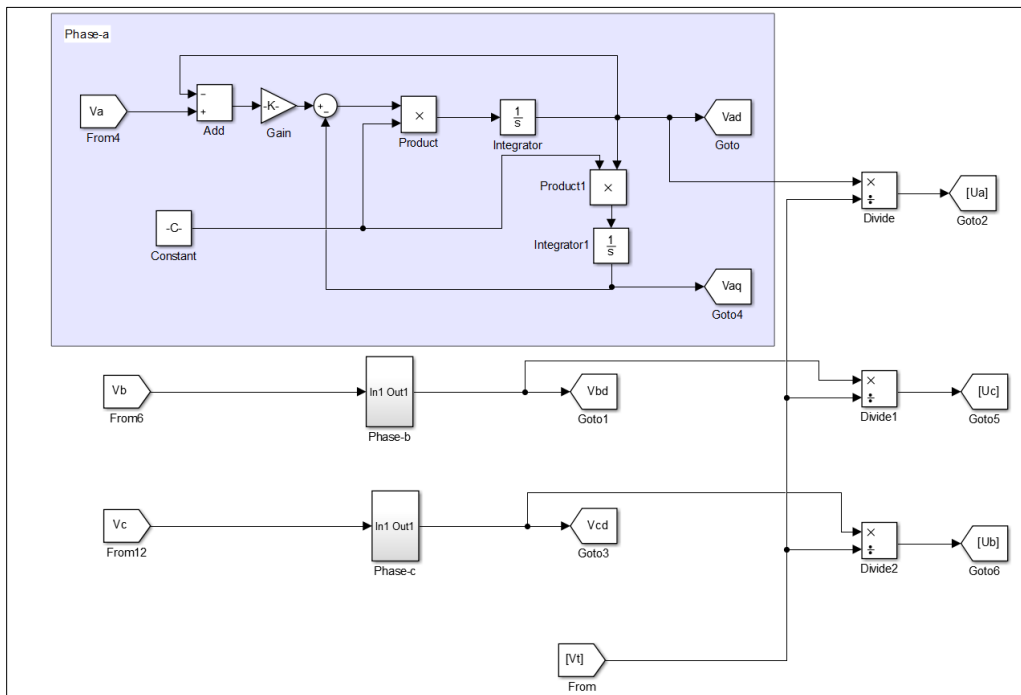


Fig.5.1(b) Simulation model of SOGI based unit template technique for three-phase system

The unit template ($u_{\alpha abc}$) of each phase voltage is determined by dividing in phase component of respective phase by the magnitude of the three-phase grid voltage at PCC (v_t). Eq.(5.1) provides the in-phase unit templates for each phase. The in-phase unit templates for each phase are calculated as

$$u_a = \frac{v_{a\alpha}}{V_t}; u_b = \frac{v_{b\alpha}}{V_t}; u_c = \frac{v_{c\alpha}}{V_t} \quad (5.1)$$

where $v_{a\alpha}$, $v_{b\alpha}$ and $v_{c\alpha}$ are in-phase component of phase-a, phase-b and phase-c respectively. V_t is maximum amplitude of voltage signals is calculated by

$$V_t = \frac{2}{3} \sqrt{v_a^2 + v_b^2 + v_c^2} \quad (5.2)$$

5.2.1.1 Simulation Performance of Unit Template Method:

Fig.5.2 shows simulation performance of three phase system, shows source voltage $v_{Sabc}(V)$, in-phase component of source voltage $v_{S\alpha abc}(V)$, V_t and unit template of each phase u_{abc} . It is the simplest and most efficient method for extracting unit templates. When the source voltage changes in Fig. 5.2 at time $t=0.5s$, the conventional unit template approach performs smoothly during normal grid condition but during distorted grid condition the templates are also distorted shown in Fig.5.2(a) where as in case of SOGI based unit templates method the transition between normal to distorted grid is smooth and unit template maintain sinusoidal and balanced during this transition shown in Fig.5.2(b).

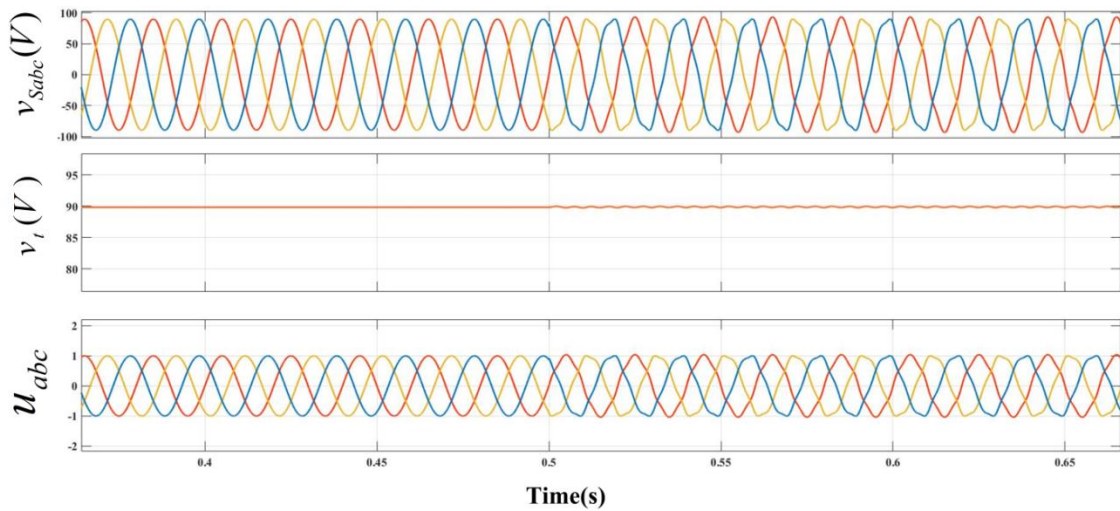


Fig.5.2(a) Simulation performance of conventional unit template method for three phase system

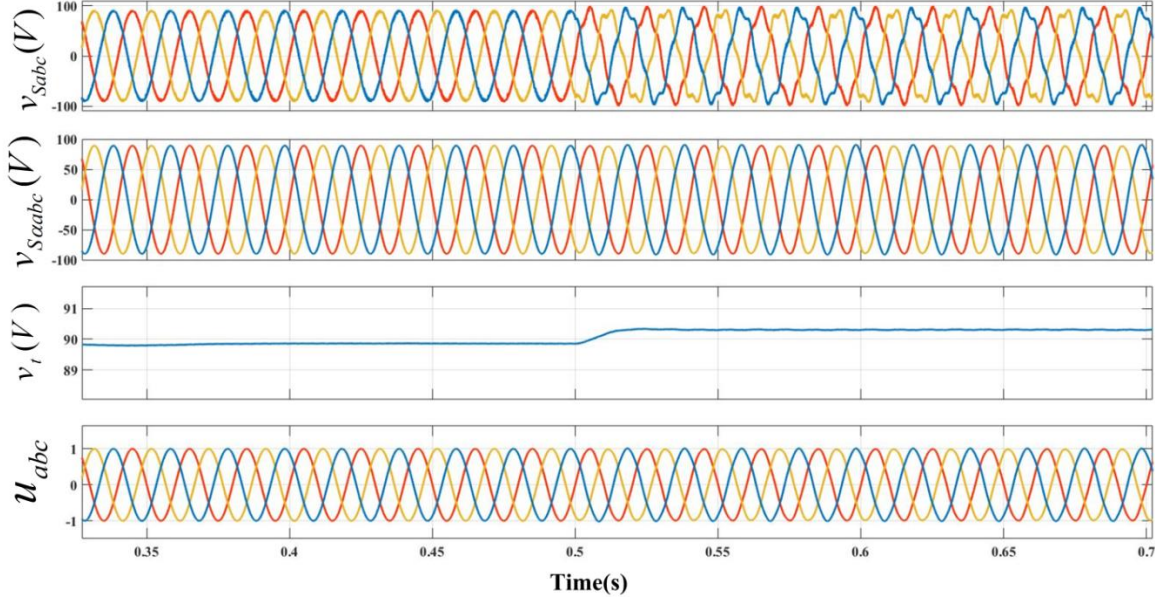


Fig.5.2(b) Simulation performance of SOGI based unit template method for three phase system

5.2.2. D-SOGI for Three-Phase System:

The double second-order generalized integrator (D-SOGI) structure is shown in Fig.5.3 and it is described below. The D-SOGI extracts the instantaneous symmetrical components of voltage based on Second-Order Generalized Integrator [76,171].

In this chapter, an unbalanced and distorted three phase supply is input to the D-SOGI block which extracts the positive and negative sequence. With the help of this method, a voltage vector ($v_{abc} = v_{abc}^+ + v_{abc}^- + v_{abc}^0$) of the supply (which may be unbalanced or distorted) can be split into its sequence component by using following equations [172-173].

$$\begin{bmatrix} v_a^+ \\ v_b^+ \\ v_c^+ \end{bmatrix} = \frac{1}{3} \begin{bmatrix} 1 & \alpha & \alpha^2 \\ \alpha^2 & 1 & \alpha \\ \alpha & \alpha^2 & 1 \end{bmatrix} \begin{bmatrix} v_a \\ v_b \\ v_c \end{bmatrix} \quad (5.3)$$

$$\begin{bmatrix} v_a^- \\ v_b^- \\ v_c^- \end{bmatrix} = \frac{1}{3} \begin{bmatrix} 1 & \alpha^2 & \alpha \\ \alpha & 1 & \alpha^2 \\ \alpha^2 & \alpha & 1 \end{bmatrix} \begin{bmatrix} v_a \\ v_b \\ v_c \end{bmatrix} \quad (5.4)$$

$$\begin{bmatrix} v_a^0 \\ v_b^0 \\ v_c^0 \end{bmatrix} = \frac{1}{3} \begin{bmatrix} 1 & 1 & 1 \\ 1 & 1 & 1 \\ 1 & 1 & 1 \end{bmatrix} \begin{bmatrix} v_a \\ v_b \\ v_c \end{bmatrix} \quad (5.5)$$

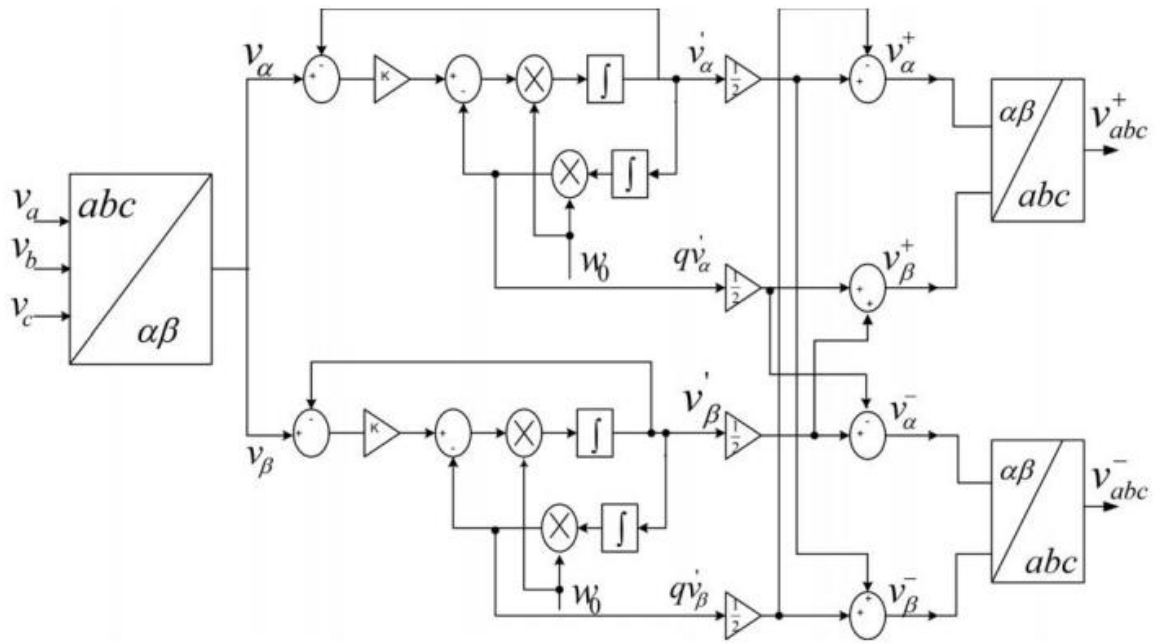


Fig.5.3(a) D-SOGI structure for three-phase system to extract positive and negative voltage components

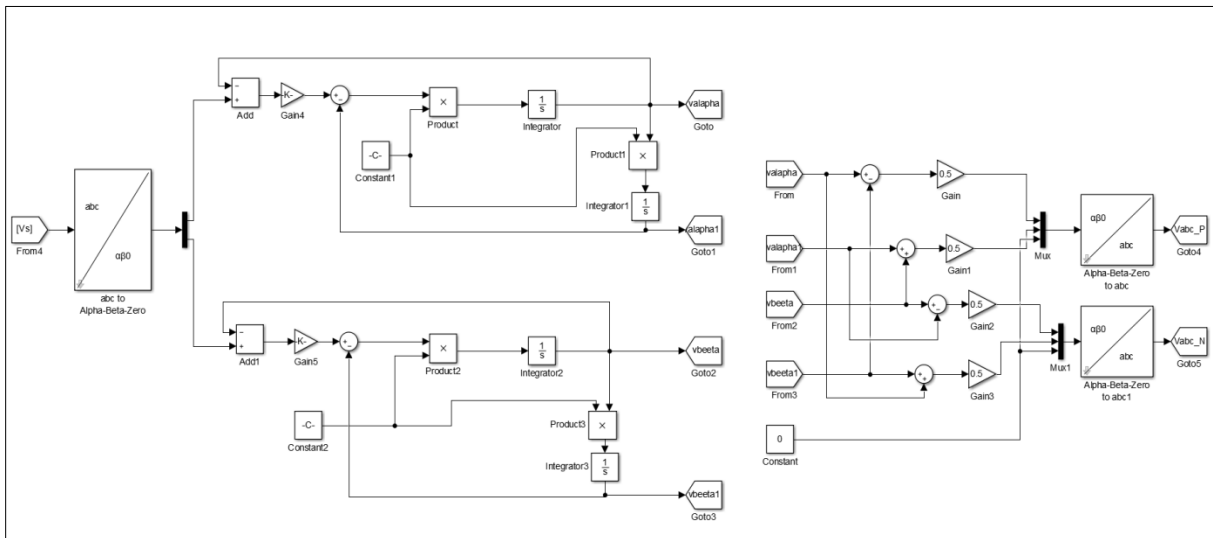


Fig.5.3(b) Simulation model of D-SOGI structure for three-phase system to extract positive and negative voltage components

where α denotes the time shifting operator at fundamental frequency which is equivalent to phase shift ($\alpha = 1 \angle 120^\circ$).

The structure of D-SOGI is shown in Fig.5.3 and it is evident from the figure that it is equivalent to two SOGI filters. Input three phase voltages are converted to direct and in-quadrature signals, α and β components. These signals are further used for calculation of positive sequence component v_{abc}^+ and negative sequence component v_{abc}^- [174]. Thus, D-SOGI filter effectively extracts sequence components, and further used for reference current generation. The in-phase unit templates for each phase:

$$u_a = \frac{v_a^+}{V_t}; u_b = \frac{v_b^+}{V_t}; u_c = \frac{v_c^+}{V_t} \quad (5.6)$$

where u_{abc} is unit template of respective phase-a, phase-b and phase-c, v_{abc}^+ is positive sequence component of respective phase-a, phase-b and phase-c and V_t is maximum amplitude of voltage signals is calculated by

$$V_t = \frac{2}{3} \sqrt{v_a^2 + v_b^2 + v_c^2} \quad (5.7)$$

where v_a is phase-a voltage, v_b is phase-b voltage and v_c is phase-c voltage.

5.2.2.1 Simulation Performance of D-SOGI Filter:

Fig.5.4 shows the simulation performance of D-SOGI filter. Fig.5.4 shows distorted three phase source voltage $v_{Sabc}(V)$, positive sequence component of source voltage (v_{Sabc}^+), V_t and unit template of each phase u_{abc} .

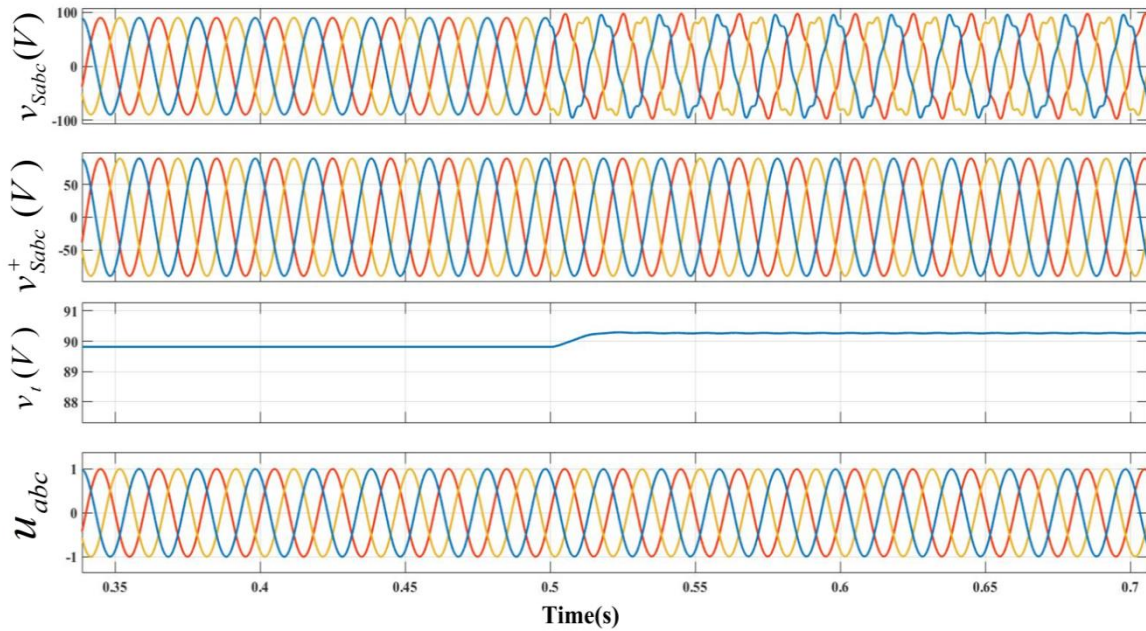


Fig.5.4 Simulation performance of D-SOGI for three phase system

Regardless of the grid status, reference current must be sinusoidal and in phase with source voltage in order for VSC to operate without interruption in a polluted grid condition. D-SOGI is employed in this chapter's three phase VSC to extract the reference current with the help of the positive sequence components.

5.3. VSC Operation of Three-Phase System Under Polluted Grid Condition:

Operating a three-phase system, such as a voltage source converter (VSC) under polluted grid condition can result into a number of difficulties. Pollution in the grid refers to the existence of harmonics, voltage sags, swells, transients, and other disturbances that depart from the ideal sinusoidal waveform. Three-phase systems use three-phase AC power circuits, each of which is 120° apart. Various types of loads, including linear, non-linear, and mixed loads, are connected to three-phase supply systems. The function of the proposed VSC controller design involves compensation of reactive power for power factor correction, harmonic elimination, load balancing, and voltage regulation under non-linear load condition. In this chapter, effective approaches for load compensation are discussed which ensure smooth operation under normal and distorted grid condition. By correcting for the reactive power required by the load, the quality of the power may be enhanced, and this calls for a proper controller design for control of three-phase VSC.

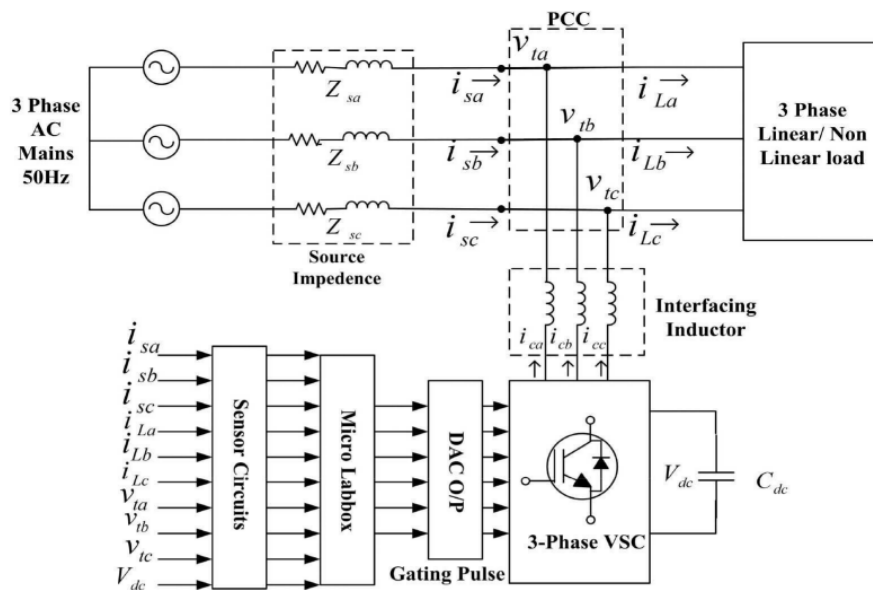


Fig.5.5 Three phase system representation

The system configuration for the compensation of harmonic current of three-phase three-wire distribution system using VSC is shown in Fig.5.5. The system is supplied by three-phase 110 V (L-L), 50 Hz AC supply connected to a non-linear load. The non-linear load is represented by a resistive and inductive load connected at the end of three-phase diode rectifier. The active filter is realized in the form of VSC which is connected at the Point of Common Coupling (PCC) through interface inductors L_c as shown in Fig.5.5. All system parameters are mentioned in the Appendix. The experimental setup is developed using LEM sensors which are used to detect the relevant load and source voltages and currents. Micro LAB box is used for implementing the designed circuits. The Micro LAB box generates the required gating pulses for VSC, which controls the VSC and compensates for the different problems of power quality.

5.3.1. Three-Phase Levenberg Marquardt (LM) Trained SOGI Filter:

This is an adaptive control scheme trained by LM technique applied on SOGI filter as illustrated in Fig.5.6.

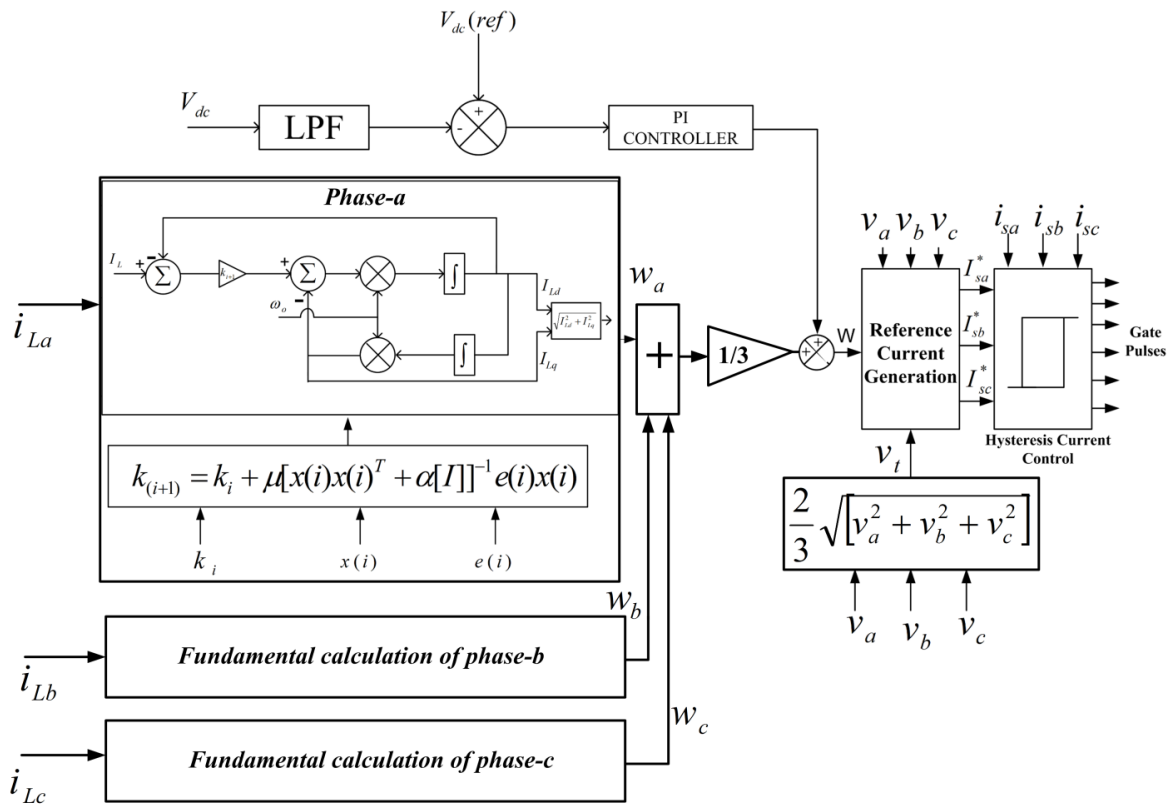


Fig.5.6(a) Proposed LM trained SOGI control scheme

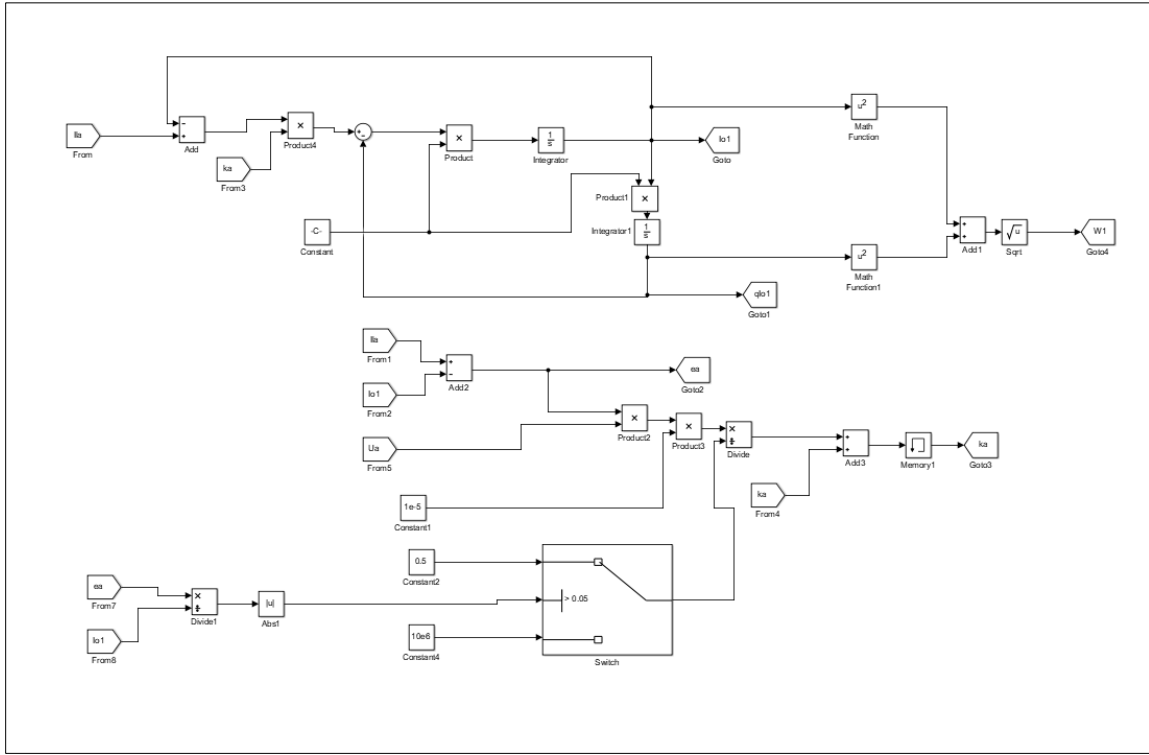


Fig.5.6(b) Simulation model of LM trained SOGI control scheme for phase-‘a’

The gain of SOGI filter used in this proposed control scheme under distorted grid condition is trained by LM control method. SOGI’s DC gain affects the performance of the filter, thus for better performance LM method is used for training and it is an efficient method for obtaining weights automatically. LM algorithm for weight update is based on effective combination of Steepest Descent Method and Newton method[175] . The Steepest Descent method works best when the design vector is away from the optimum value and effectively reduces the value of function. On the other hand, the most important consideration of the Newton method is that it converges fast when design vector is near optimum value. LM method combines the advantages of both Steepest Descent and Newton method [175].

The objective function is defined according to mean square error minimization

$$o(w) = \frac{1}{2} (y - \sum_{i=1}^n w_i x_i)^2 = \frac{1}{2} e^2 = e^T e \quad (5.8)$$

where y denotes the output of the system, w_i weight of i th input, x_i , i^{th} input of network and e is the error of the system. For minimizing the objective function

$$g = \frac{\partial o(w)}{\partial w} = (y - w^T x)(-x) = -ex \quad (5.9)$$

LM method modifies the diagonal element of the Hessian matrix (H_i)

$$H_i = \frac{\partial^2 o(w)}{\partial w^2} = \frac{\partial}{\partial x} \left(\frac{\partial o(w)}{\partial x} \right) = \frac{\partial}{\partial w} (y - w^T x)(-x) = xx^T \quad (5.10)$$

Modified Hessian matrix is expressed as

$$[\tilde{H}_i] = [H_i] + \alpha[I] \quad (5.11)$$

where $[I]$ is identity matrix and α is a positive constant, where value is large initially (around 10^4) and then reduced to zero gradually. The inverse of Hessian matrix $[\tilde{H}_i]^{-1}$ is expressed as

$$[\tilde{H}_i]^{-1} = [[H_i] + \alpha[I]]^{-1} \cong [\alpha[I]]^{-1} \cong \frac{1}{\alpha}[I] \quad (5.12)$$

Thus, LM method is designed to have a large value of α initially which is decreased finally to a low value. Thus, the search method works as Steepest Descent method for high value of α and for low value of α it works as Newton method.

Weight update equation using LM method is depicted as

$$w(i+1) = w(i) - \mu [[H_i] + \alpha_i[I]]^{-1} g(i) \quad (5.13)$$

From Eq.(5.9), Eq.(5.10) and Eq. (5.13)

$$w(i+1) = w(i) + \mu [xx(i)^T + \alpha[I]]^{-1} e(i)x(i) \quad (5.14)$$

where $w(i+1)$ is the updated weight and $w(i)$ is the old weight, μ is the step size of the system. In proposed control system $w(i+1)$ is represented by $k(i+1)$ (updated DC gain of SOGI filter), $w(i)$ is old weight is represented by k_i (old DC gain of SOGI filter), $x(i)$ is unit vector of respective phase voltage of input represented as

$$x(i) = [u_{d_i} \quad u_{q_i}] \quad (5.15)$$

where u_{d_i} is in phase unit template of i th phase and u_{q_i} is quadrature phase unit template of i th phase. Now

$$x(i)x(i)^T = [u_{d_i}^2 \quad u_{q_i}^2] \quad (5.16)$$

From Eq.(5.14) and Eq.(5.16)

$$k(i+1) = k(i) + \mu [[u_{d_i}^2 \quad u_{q_i}^2] + \alpha[I]]^{-1} e(i)x(i) \quad (5.17)$$

Further solving gives the basic weight updating equation which is expressed as

$$k(i+1) = k(i) + \frac{\mu u_{d_i} e}{\alpha+1} \quad (5.18)$$

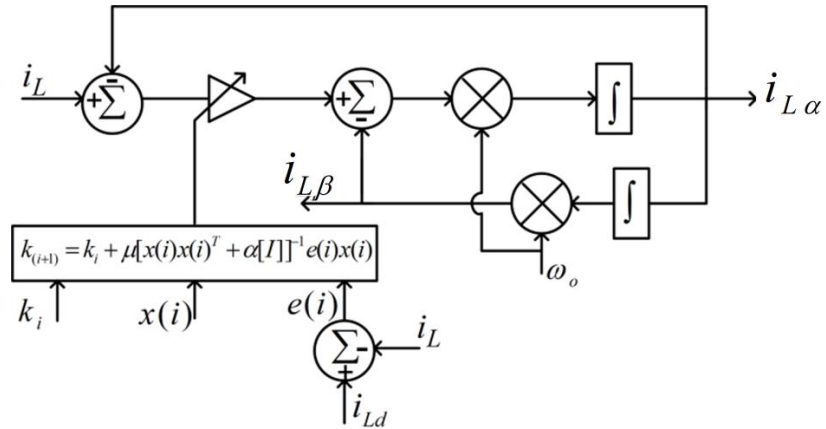


Fig.5.7 Design of LM trained adaptive SOGI for phase-‘a’

The value of α depends on the load current as the variation in load current from fundamental load current is more than 10% the α will switch to high value and when it is less than 10% it will switch to lower value and $e(i)$ is error which is expressed by Eq.(5.19) and shown in Fig.5.7.

$$e = i_{Ld} - i_L \quad (5.19)$$

Thus, in case of any disturbance in system the value of ‘ k ’ gets adjusted automatically and the response of system will settle as per desired condition. The performance of the proposed method using LM technique is investigated.

Now for the reference current generation unit template method is used as discussed in Section 5.2.1 and the reference current of respective phase can be written as

$$i_a^* = W \times u_a; i_b^* = W \times u_b; i_c^* = W \times u_c \quad (5.20)$$

where W is fundamental Weight of three phase system, i_a^* is reference current of phase a, i_b^* is reference current of phase b and i_c^* is reference current of phase c. These reference currents are compared with source current of their respective phase for the generation of gate pulses by using HCC block.

5.3.2. Conductance based Control Algorithm:

The block diagram of the suggested control system is shown in Fig.5.8 which consists of a D-SOGI filter for sequence extraction from unbalanced and distorted grid voltage and SAPF reference current calculation.

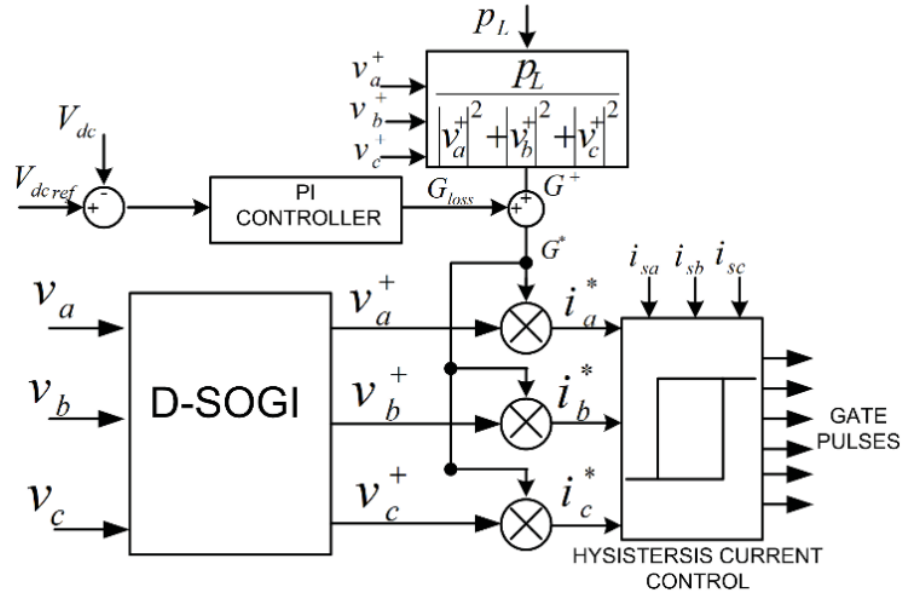


Fig.5.8(a) Conductance Based Control Algorithm with DSOGI block for distorted grid condition

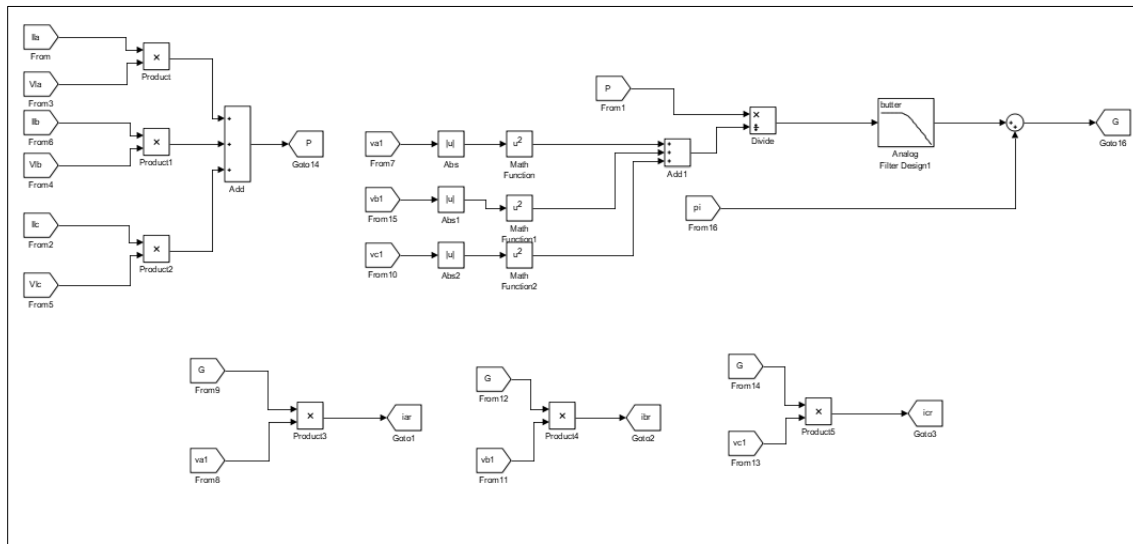


Fig.5.8(b) Simulation model of conductance based control algorithm with DSOGI block for distorted grid condition

The proposed controller consists D-SOGI filter discussed in Section 5.2.2 and reference current generation block, which is based on instantaneous active power supplied to the load determined by the dot output of the PCC voltage and load current.

$$p_L = v \cdot i_L \quad (5.21)$$

where $v = [v_a \ v_b \ v_c]$ denotes the voltage at PCC and $i_L = [i_{La} \ i_{Lb} \ i_{Lc}]^T$ denotes current demanded by load connected to the system at PCC[176].

Now the reference current calculation is based on active power delivered to load, which is determined using the conductance approach as given below:

$$i_p^* = G^* v^+ \quad (5.22)$$

where G^* is total conductance of the system calculated by

$$G^* = G_{loss} + G^+ \quad (5.23)$$

where G_{loss} is output of PI controller which is used to regulate DC link voltage of VSC to set at $V_{dc_{ref}}$ and G^+ is conductance of the system calculated by

$$G^+ = \frac{p_L}{[|v_a^+|^2 + |v_b^+|^2 + |v_c^+|^2]} \quad (5.24)$$

where v_a^+ , v_b^+ and v_c^+ are positive sequence voltages of the respective phases[177].

These reference currents are sinusoidal and balanced irrespective of the unbalancing in load and grid supply. The simplified but effective technique is now tested

5.4. Performance Analysis of Three Phase System under Normal and Distorted Grid Condition:

In this section, the adaptive SOGI tuned using LM technique and conductance based controller are now tested for its performance under distorted and undistorted grid condition. In this case, a three-phase three-wire SAPF is used for supplying compensation currents to the system at PCC. The system feeds three-phase non-linear RL load. The non-linear load is modeled by using R-L connected to diode rectifier end. The reference voltage for SAPF DC link is fixed at 200 V. A PI controller regulates the DC-link voltage by comparing the real-time DC-link capacitor voltage V_{dc} and comparing it with respect to reference DC-link voltage V_{dc}^* . An unbalancing in the load current is introduced, and the performance of the system is analyzed in the following subsections.

5.4.1. Simulation Performance:

The simulation performance of proposed system is analyzed during undistorted and distorted grid supply condition and load variation is also introduced during the operation for both the cases. Two test conditions viz. load decrement and load increment for a short

span of time are considered. The operation and performance of the system is analysed with the help of Simulink results for corresponding cases.

5.4.1.1. Simulation Performance of LM Trained SOGI:

Fig.5.9 shows the intermediate performance of proposed LM trained SOGI. Fig.5.9 shows load current of phase a (i_{La}), filtered in phase component of load current ($i_{La\alpha}$), error ($e(t)$) and output weight, the intermediate performance of proposed system found satisfactory during the load changes.

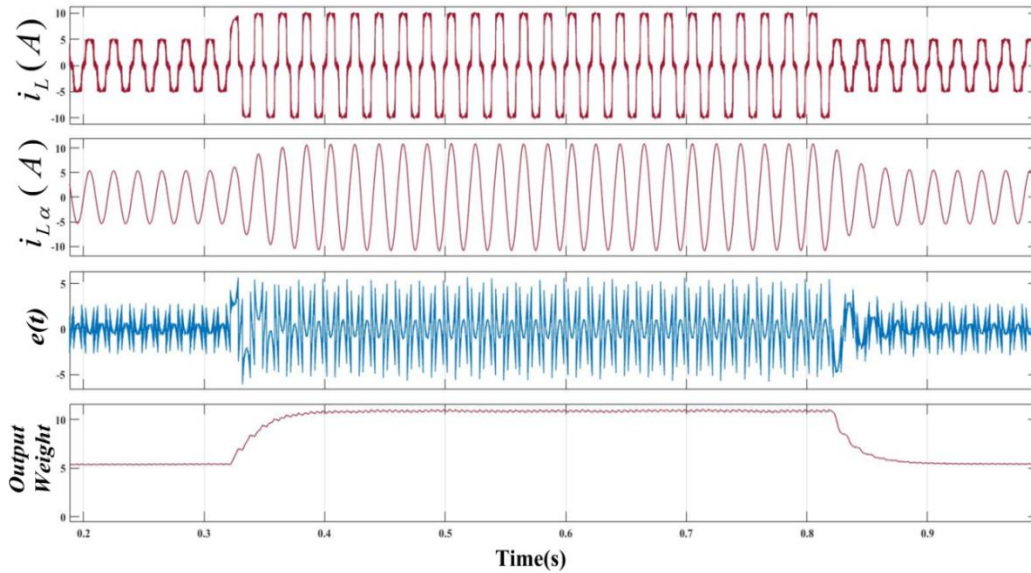


Fig.5.9 Intermediate performance of LM SOGI

The performance of adaptive SOGI is shown in Fig.5.10 in which source voltage (v_{sa}, v_{sb}, v_{sc}), reference current (i_{Ra}, i_{Rb}, i_{Rc}), source current (i_{sa}, i_{sb}, i_{sc}), load current (i_{La}, i_{Lb}, i_{Lc}), compensator current (i_{ca}, i_{cb}, i_{cc}), output weight of three phase and dc link voltage (V_{dc}) are shown.

The THD distortion of 10% in source voltage from 1s is added and load is increased at 1.7s. During normal grid, distorted grid condition and during load changes, the source current i_{Sabc} is sinusoidal and balanced as IEEE519 shown in Fig.5.11(b). Fig.5.11 shows the total harmonic distortion (THD) in source voltage, load current and source current to be 10%, 26.69% and 2.63% respectively during closed loop operation of VSC. The proposed controller is able maintain THD level of source current as per IEEE 519 standard.

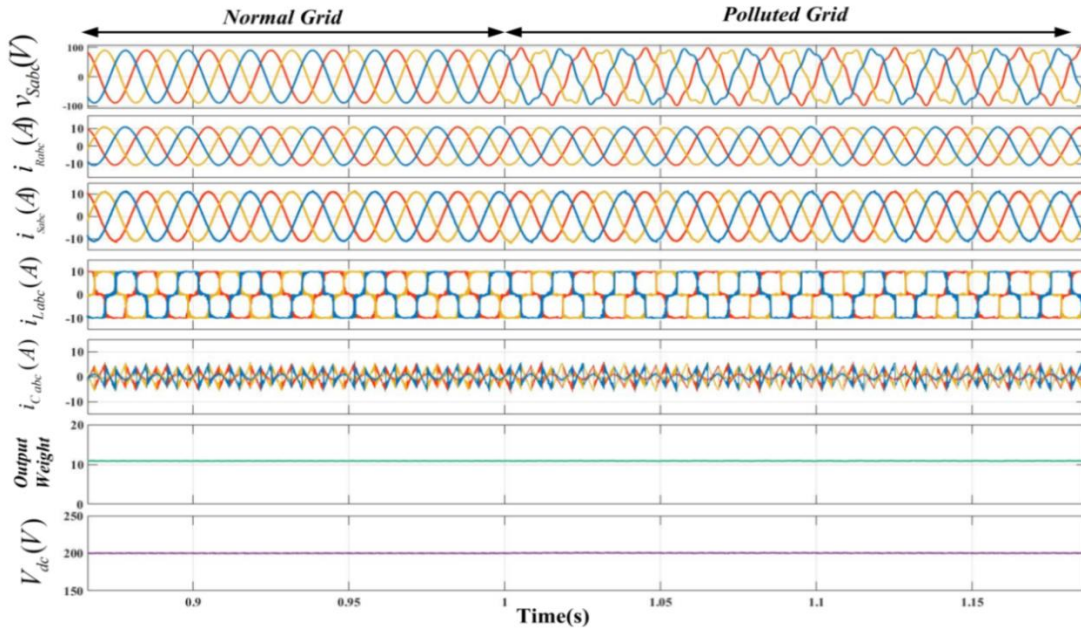


Fig.5.10(a) Simulation performance of LM SOGI showing (a) source voltage, v_{Sabc} (b) reference current, i_{Rabc} (c) source current, i_{Sabc} (d) load current, I_{Labc} (e) converter current, i_{Cabc} (f) output weight (g) DC link voltage, V_{DC}

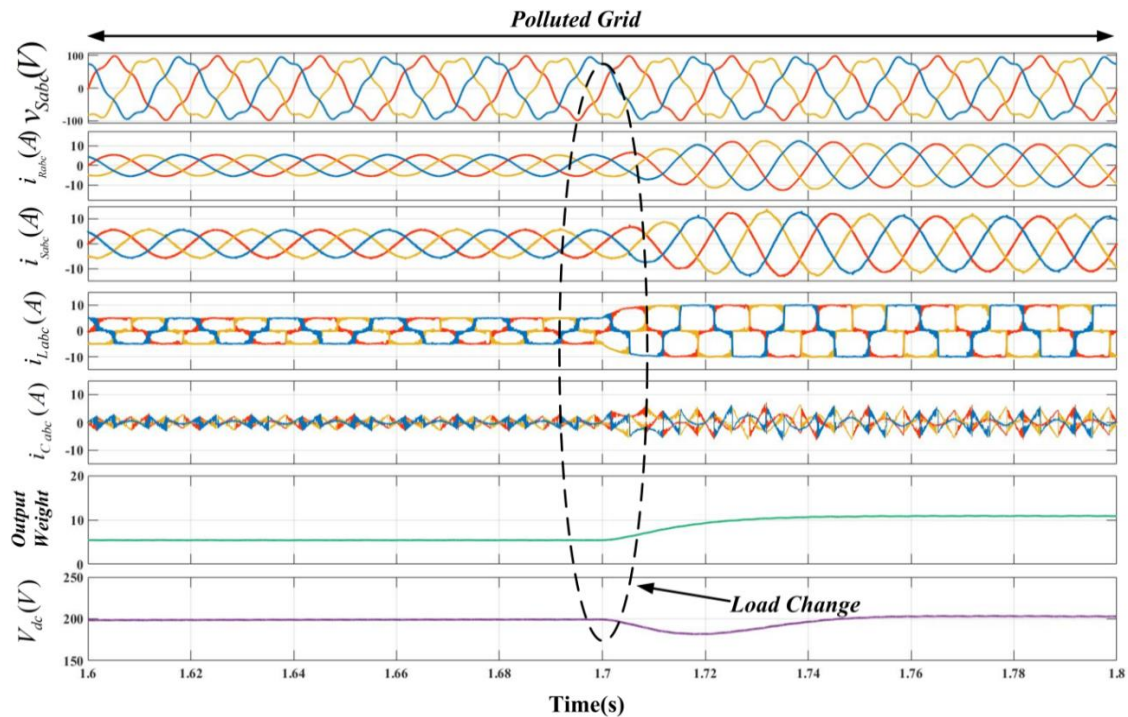


Fig.5.10(b) Simulation performance of LM SOGI showing (a) source voltage, v_{Sabc} (b) reference current, i_{Rabc} (c) source current, i_{Sabc} (d) load current, I_{Labc} (e) converter current, i_{Cabc} (f) output weight (g) DC link voltage, V_{DC}

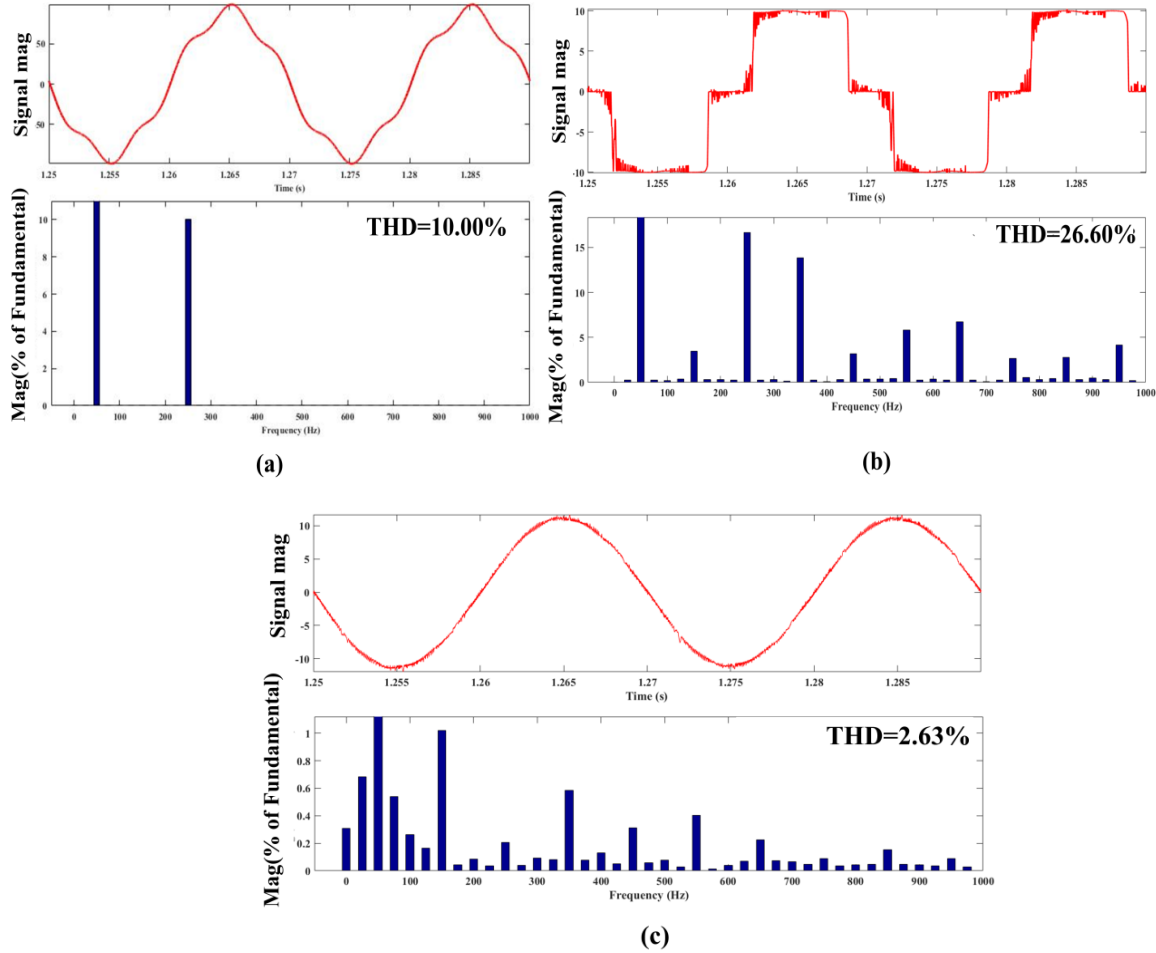


Fig.5.11 THD performance of LM based SOGI (a) source voltage v_s (b) load current i_L (c) source current i_s

5.4.1.2. Simulation Performance of Conductance based Algorithm:

The proposed conductance based controller reference current calculation is based on positive sequence component of source voltage calculated by using D-SOGI filter discussed in Section 5.2.2. The performance of conductance based controller is shown in Fig.5.12 in which source voltage (v_{sa}, v_{sb}, v_{sc}), reference current (i_{Ra}, i_{Rb}, i_{Rc}), source current (i_{sa}, i_{sb}, i_{sc}), load current (i_{La}, i_{Lb}, i_{Lc}), compensator current (i_{Ca}, i_{Cb}, i_{Cc}), load conductance of three phase and dc link voltage (V_{dc}) are shown. The THD distortion of 10% in source voltage from 1.0s is added in Fig5.12(a) and load is increased at 1.7s in Fig.5.12(b). During normal grid, distorted grid condition and during load changes, the source current i_{sabc} is sinusoidal and balanced as IEEE519 shown in Fig.5.12.

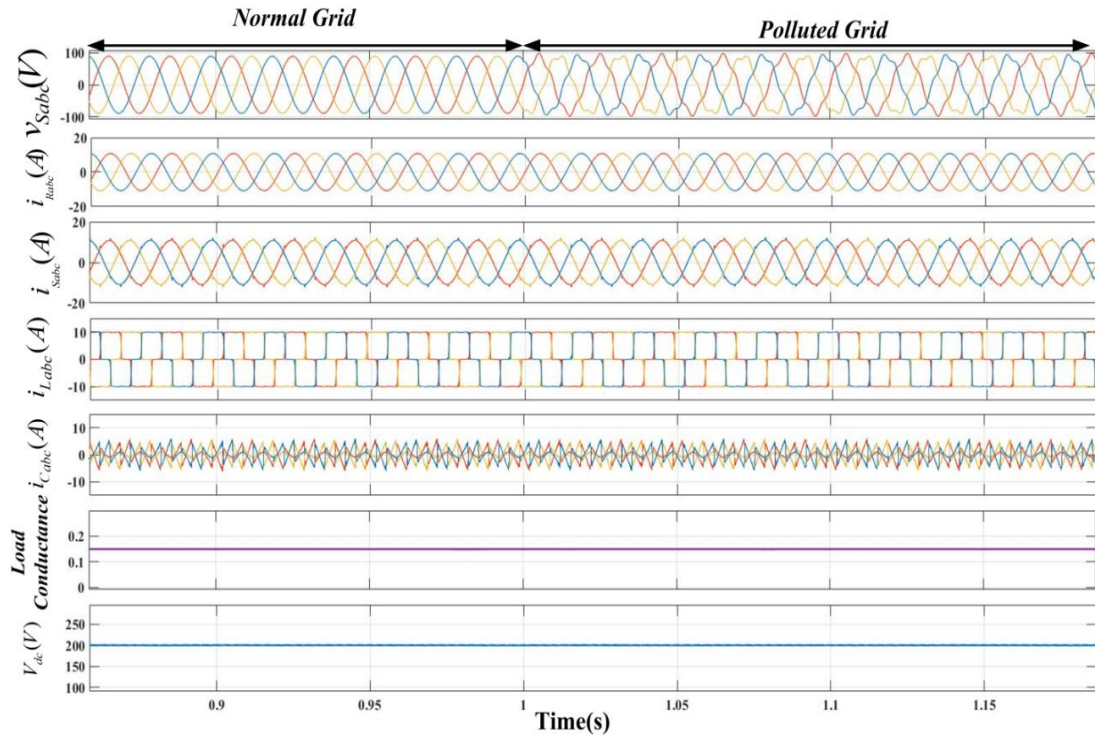


Fig.5.12(a) Simulation performance of conductance based controller showing (a) source voltage, v_{Sabc} (b) reference current, i_{Rabc} (c) source current, i_{Sabc} (d) load current, i_{Labc} (e) converter current, i_{Cabc} (f) load conductance (g) DC link voltage, V_{DC}

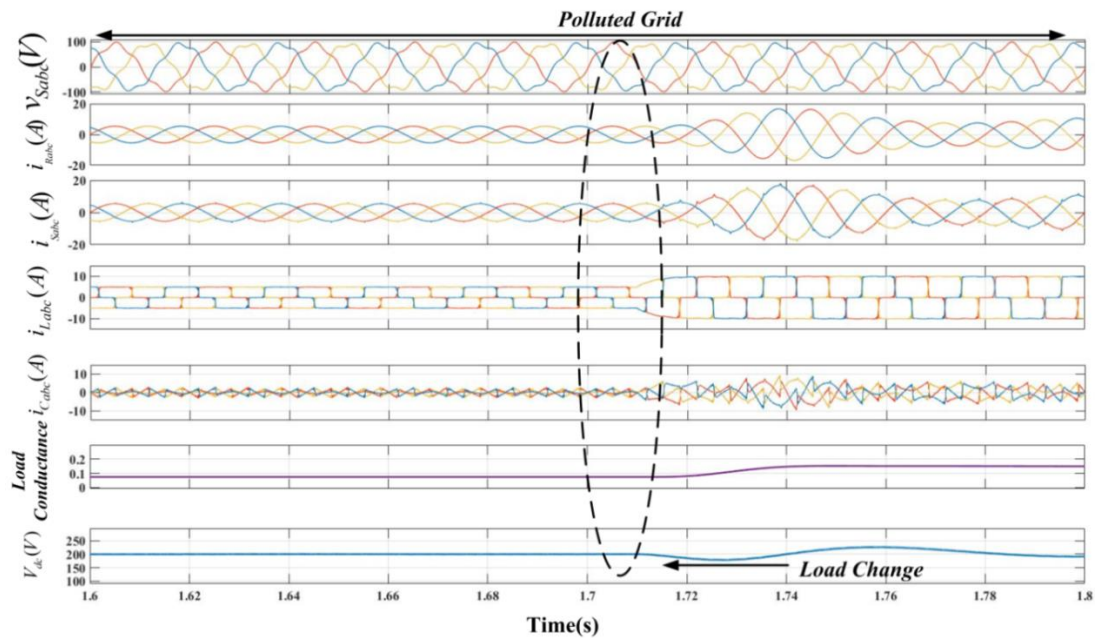


Fig.5.12(b) Simulation performance of conductance based controller showing (a) source voltage, v_{Sabc} (b) reference current, i_{Rabc} (c) source current, i_{Sabc} (d) load current, i_{Labc} (e) converter current, i_{Cabc} (f) load conductance (g) DC link voltage, V_{DC}

Fig.5.13 shows the total harmonic distortion (THD) in source voltage, load current and source current to be 10%, 26.33% and 4.43% respectively during closed loop operation of SAPF. The proposed conductance based controller is able maintain THD level of source current as per IEEE 519 standard under normal and polluted grid condition.

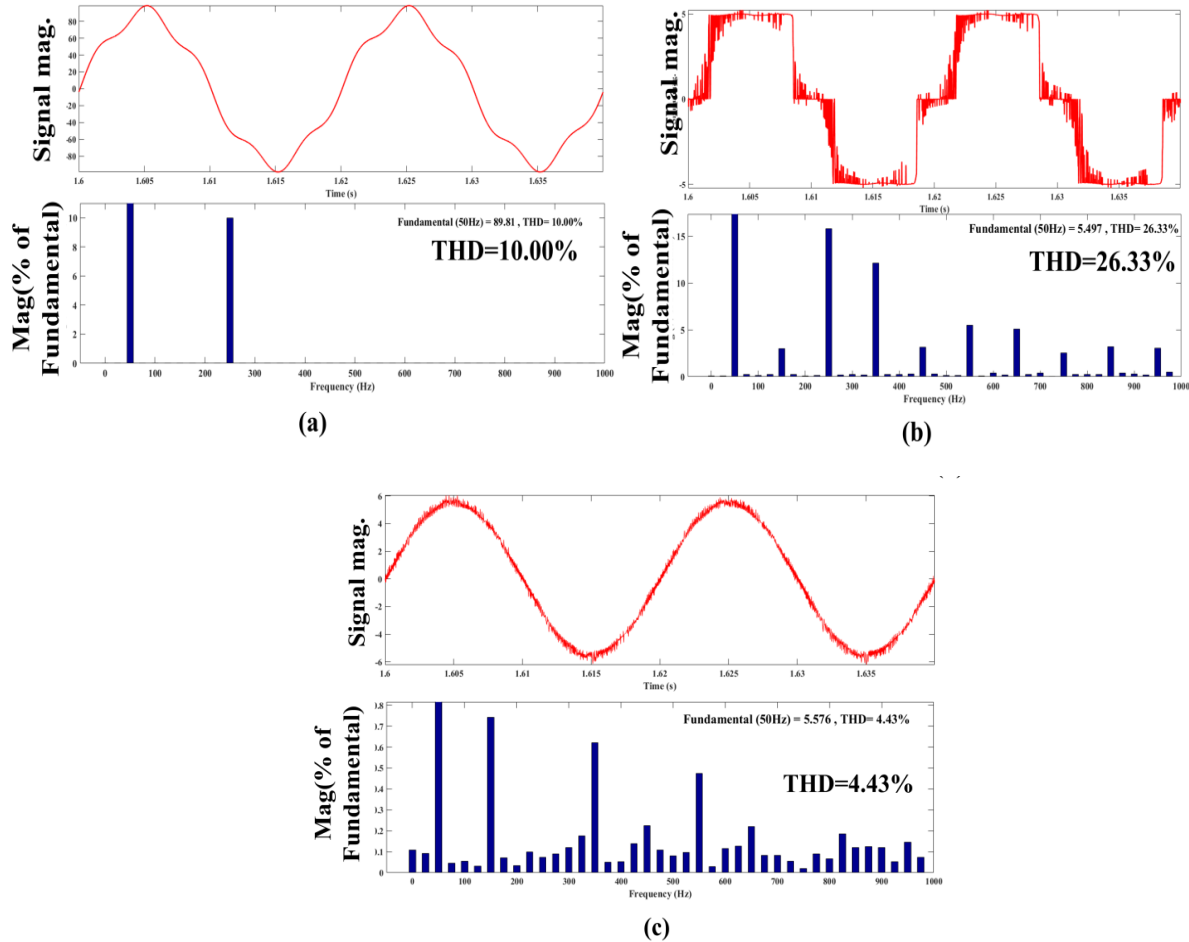


Fig.5.13 THD performance of conductance based controller (a) source voltage v_s (b) load current i_L (c) source current i_s

5.4.2. Experimental Performance:

An experimental setup of three-phase system has been developed to validate the simulation results of the proposed system. The proposed control techniques used for both distorted and undistorted grid supply conditions and used to examine the steady state and dynamic performance under different conditions. The Experimental parameters are mentioned in the Appendix.

5.4.2.1. Experimental Performance of LM trained SOGI:

Fig.5.14 Shows intermediate performance of LM trained SOGI filter, which shows load current (i_L), filtered in phase component of load current ($i_{L\alpha}$), error ($e(t)$) and output weight of the system. The system performance is observed during load increment and decrement and it found satisfactory during these disturbances. Fig.5.15 shows the steady state performance of proposed LM based SOGI filter for normal grid condition. Fig 5.15(a) shows waveforms of source voltage (v_{Sabc}) and load current (i_{Labc}). Fig5.15(b) shows THD of source voltage (v_{Sabc}) and load current (i_{Labc}). Fig 5.15(c) shows waveforms of source voltage (v_{Sabc}) and source current (i_{Sabc}). Fig5.15 (d) shows THD of source voltage (v_{Sabc}) and source current (i_{Sabc}). The values of THD in the load current and source voltage are observed to be 23.77% and 2.30% as shown in Figs.5.15 (b). The THD of source current is 2.88% as shown in Fig.5.15 (d). The VSC is controlled as SAPF and performs harmonic reduction satisfactorily for supply currents. In addition, the supply voltage and current have an in-phase relationship showing almost unity power factor operation

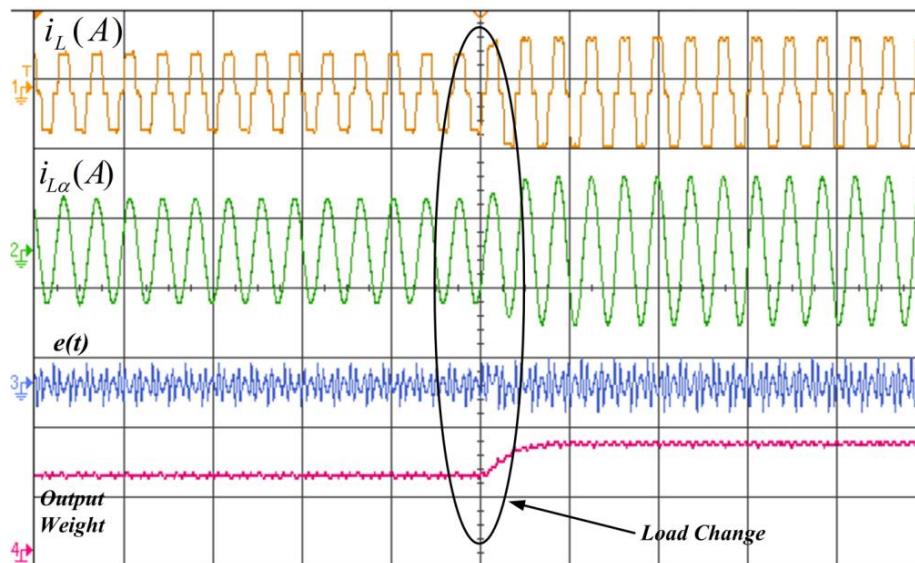
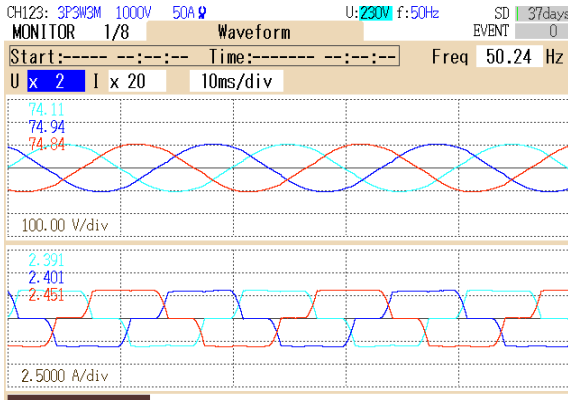
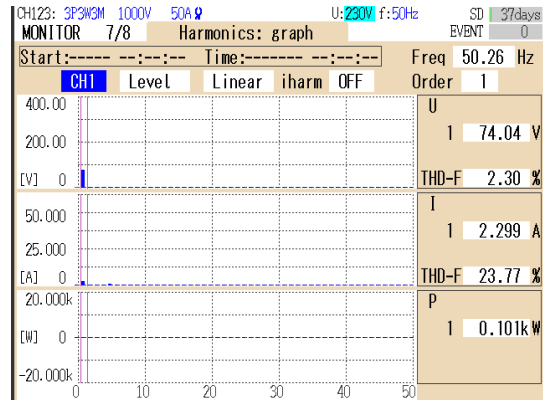


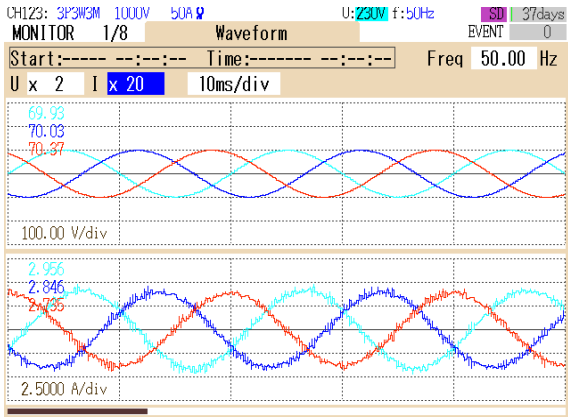
Fig.5.14 Experimental intermediate performance of LM SOGI showing (a) load current (i_L), (b) in-phase component of load current ($i_{L\alpha}$), (c) error ($e(t)$) and (d) output weight



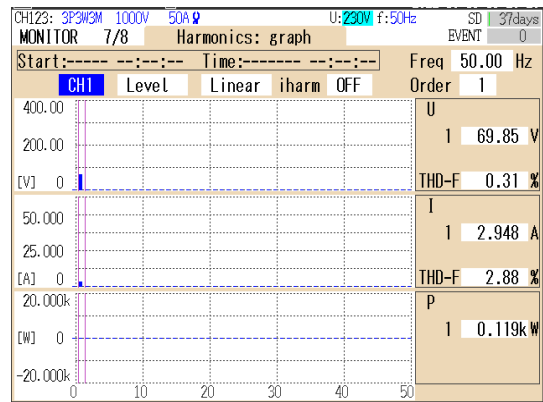
(a)



(b)



(c)

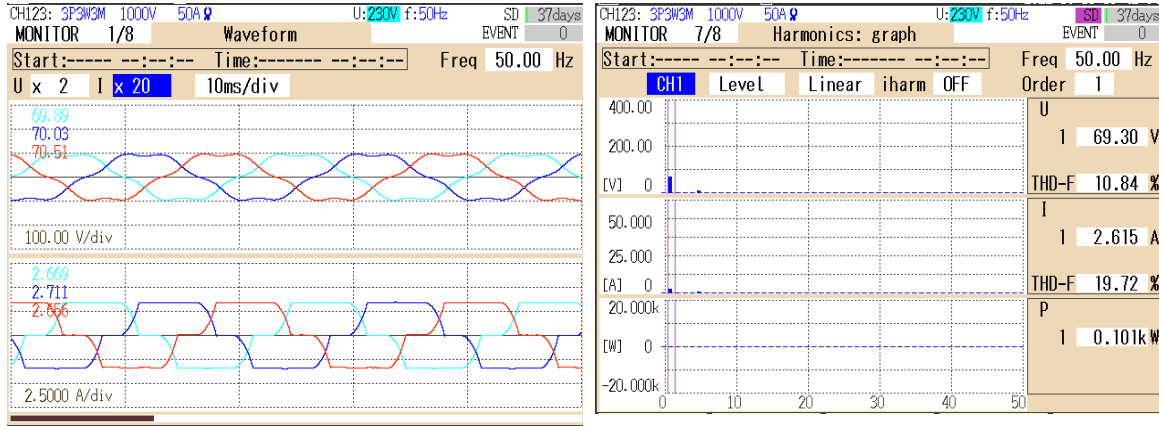


(d)

Fig.5.15 Steady state waveforms under normal grid system showing (a) source voltage (v_{Sabc}) and load current (i_{Labc}) (b) THD of v_{Sabc} and i_{Labc} (c) source voltage (v_{Sabc}) and source current (i_{Sabc}) (d) THD of v_{Sabc} and i_{Sabc}

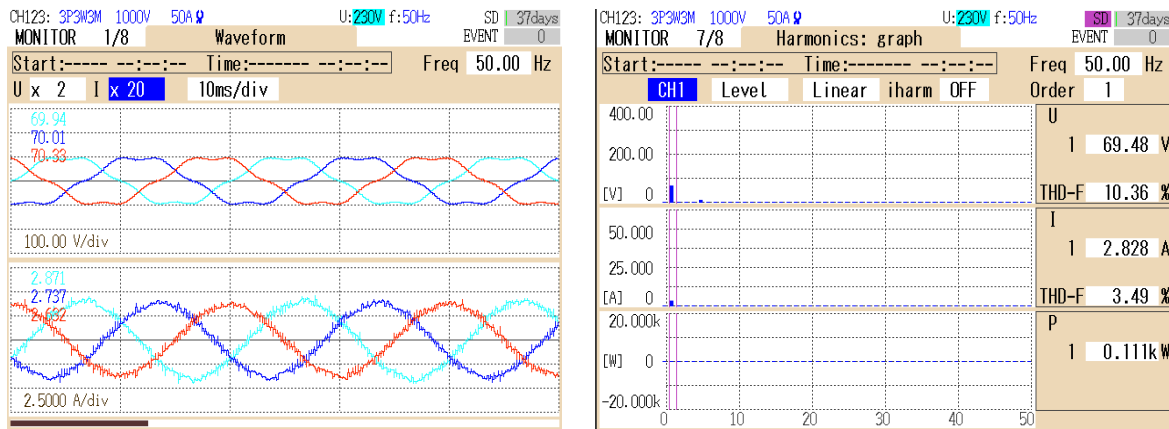
Fig.5.16 show the steady state performance of proposed LM based SOGI filter for distorted grid condition with 10% THD in source voltage. Fig 5.16(a) shows waveforms of source voltage (v_{Sabc}) and load current (i_{Labc}). Fig5.16(b) shows THD of source voltage (v_{Sabc}) and load current (i_{Labc}). Fig 5.16(c) shows waveforms of source voltage (v_{Sabc}) and source current (i_{Sabc}). Fig5.16(d) shows THD of source voltage (v_{Sabc}) and source current (i_{Sabc}). The values of THD in the load current and source voltage is observed to be 19.72% and 10.84% as shown in Figs.5.16(b). The THD of source current is 3.49% as shown in Fig.5.16(d). The proposed VSC also performs load balancing and satisfactorily harmonics compensation in supply current under distorted grid condition.

Under this condition the supply voltage and current are in phase and unity power factor operation.



(a)

(b)



(c)

(d)

Fig.5.16 Steady state waveforms under distorted grid system showing (a) source voltage (v_{Sabc}) and load current (i_{Labc}) (b) THD of v_{Sabc} and I_L (c) source voltage (v_{Sabc}) and source current (i_{sabc}) (d) THD of v_{Sabc} and i_{sabc}

Fig.5.17 presents the dynamic response due to introduction of sudden disturbances in the system under distorted grid condition. The responses are captured with the help of storage oscilloscope for distorted grid supply condition. Fig.5.17(a) shows results under distorted grid supply condition and the plots show supply voltage (v_{Sa}), reference current (i_{Ra}), source current (i_{Sa}) and load current (i_{La}). Fig.5.17(b) results have been captured for distorted grid supply condition and these show supply voltage (v_{Sa}), source current (i_{sabc}). Fig.5.17(c) shows supply voltage (v_{Sa}), source current (i_{Sa}), output weight and

DC-link voltage (V_{dc}). From Figs. 5.17(a-c) it is observed that on increasing the load, the fundamental weight changes fast and reference current is increased due to increase in load. This indicates fast and satisfactory response of LM trained SOGI technique for both distorted and undistorted grid condition. The steady state is achieved well within one cycle with the proposed strategy.

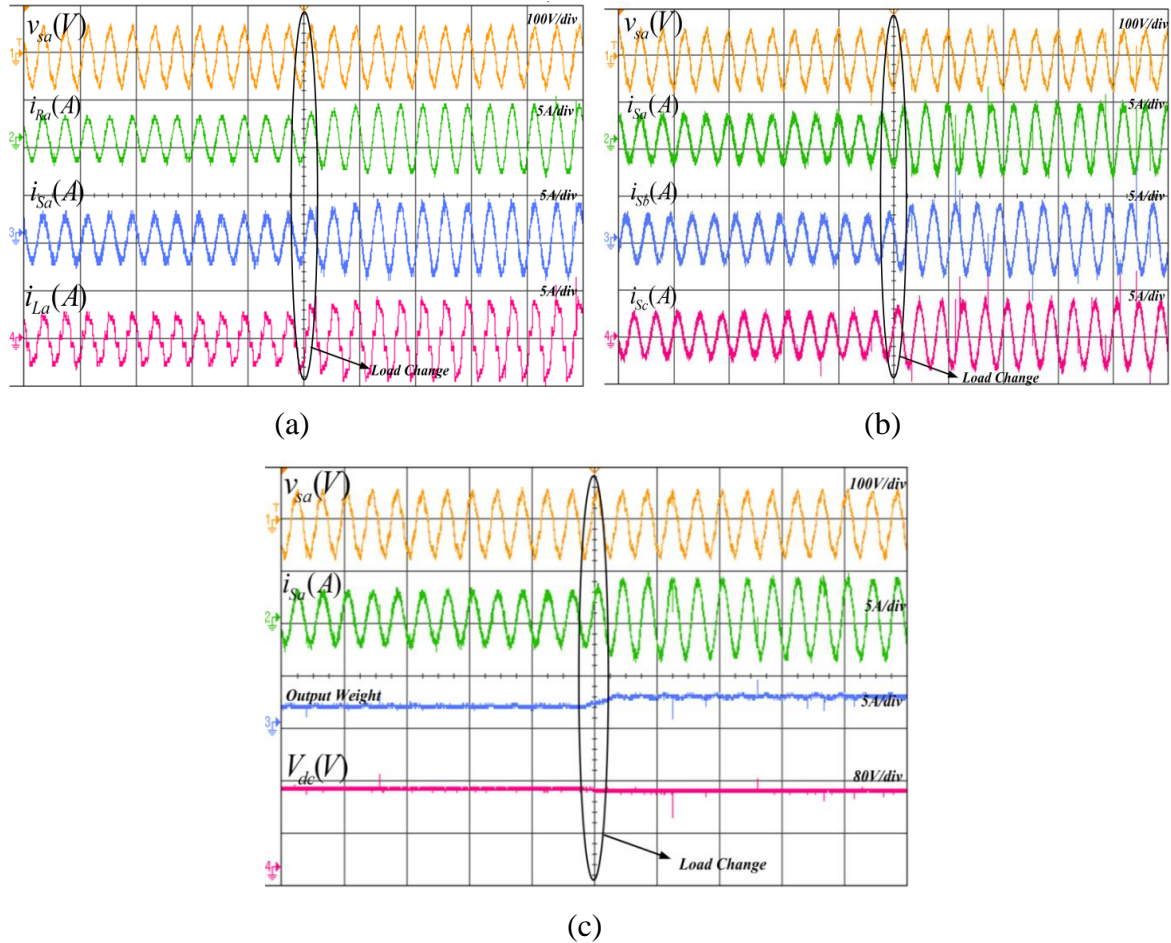


Fig.5.17 Dynamic performance of LM trained SOGI for three phase system showing (a) (v_{sa} , i_{Ra} , i_{sa} , i_{La} , output weight, V_{dc}) (b) (v_{sa} , i_{sa} , i_{sb} , i_{sc}) (c) plot of (v_{sa} , i_{sa} , output weight, V_{dc})

5.4.2.2. Experimental Performance of Conductance Based Algorithm:

Fig.5.18 Shows intermediate performance of conductance based controller, which shows distorted source voltage (v_{sa}), load current (i_L), load conductance and total load power of the system. The system performance is observed during load increment and it found satisfactory during disturbances.

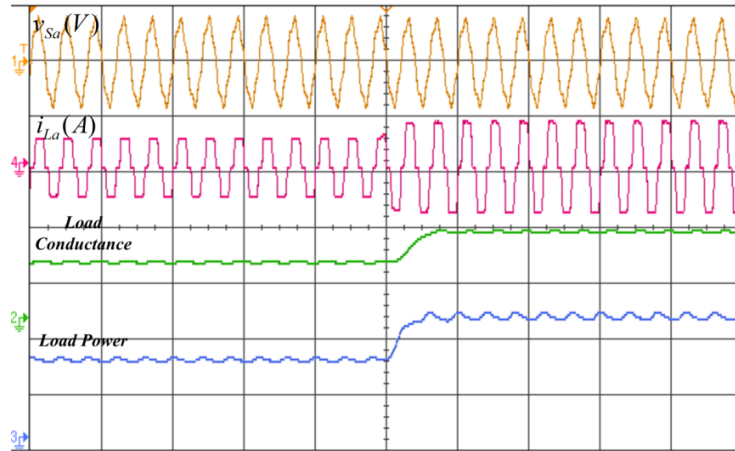


Fig.5.18 Intermediate performance conductance based controller showing (a) distorted source voltage (v_{Sa}), (b) load current (i_{La}), (c) load conductance and (d) total load power

Fig.5.19 show the steady state performance of proposed conductance based controller for normal grid condition. Fig 5.19(a) shows waveforms of source voltage (v_{Sabc}) and load current (i_{Labc}). Fig5.19(b) shows THD of source voltage (v_{Sabc}) and load current (i_{Labc}). Fig 5.19(c) shows waveforms of source voltage (v_{Sabc}) and source current (i_{Sabc}). Fig5.19(d) shows THD of source voltage (v_{Sabc}) and source current (i_{Sabc}). The values of THD in the load current and source voltage is observed to be 23.40% and 1.95% as shown in Figs.5.19(b). The THD of source current is 3.25% as shown in Fig.5.19(d) for supply currents and the VSC controller successfully reduces harmonics.

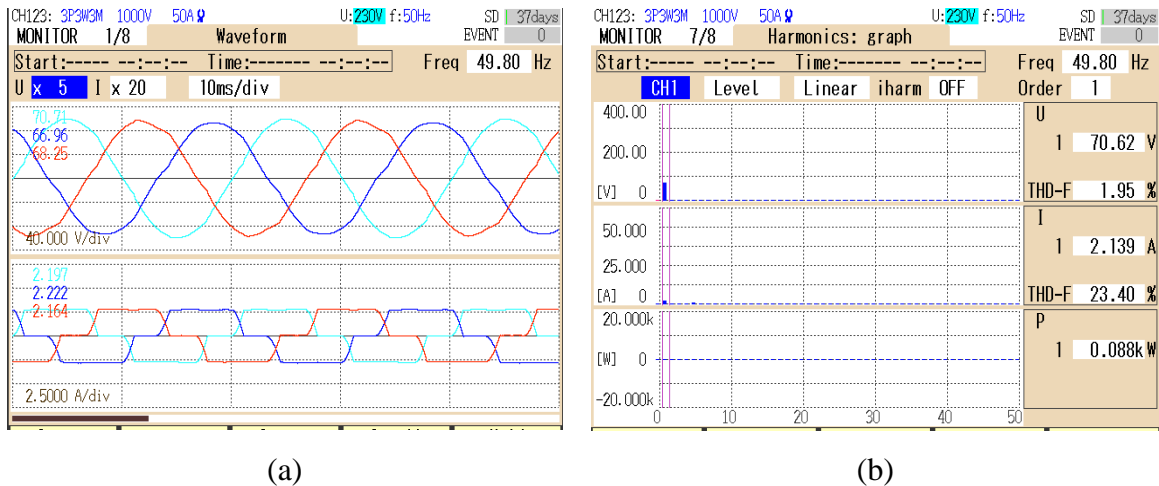
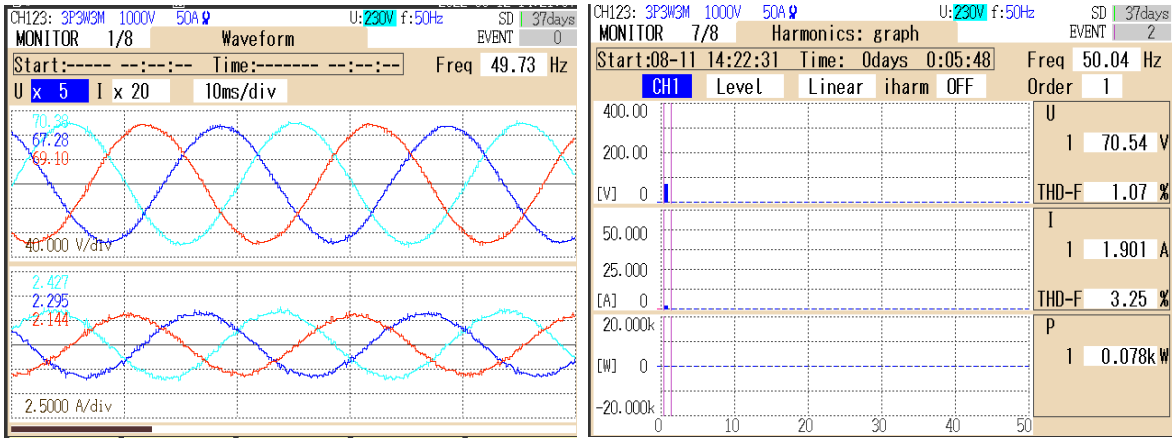


Fig.5.19 Steady state waveforms under normal grid system showing (a) source voltage (v_{Sabc}) and load current (i_{Labc}) (b) THD of v_{Sabc} and i_{Labc}

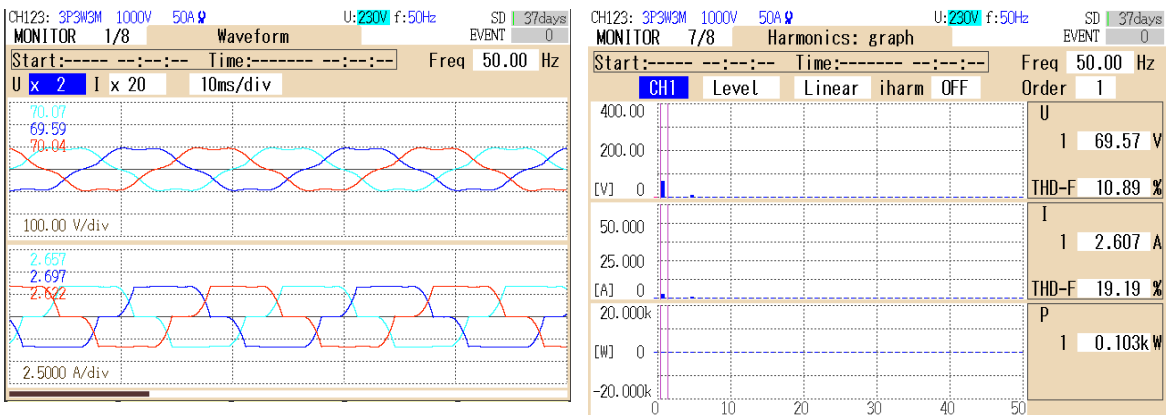


(c)

(d)

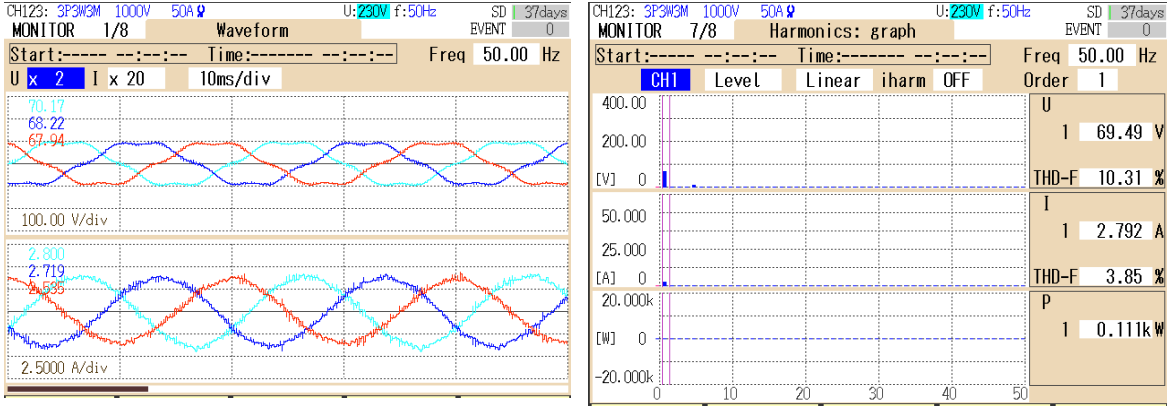
Fig.5.19 Steady state waveforms under normal grid system showing (c) source voltage (v_{Sabc}) and source current (i_{Sabc}) (d) THD of v_{Sabc} and i_{Sabc}

Fig.5.20 shows the steady state performance of proposed conductance based controller for distorted grid condition with 10% THD in source voltage. Fig 5.20(a) shows waveforms of source voltage (v_{Sabc}) and load current (i_{Labc}). Fig5.20(b) shows THD of source voltage (v_{Sabc}) and load current (i_{Labc}). Fig 5.20(c) shows waveforms of source voltage (v_{Sabc}) and source current (i_{Sabc}). Fig5.20(d) shows THD of source voltage (v_{Sabc}) and source current (i_{Sabc}).The values of THD in the load current and source voltage is observed to be 19.72% and 10.84% as shown in Figs.5.20(b). As per Fig. 5.20(d), the source current's THD is 3.85%. Moreover, the conductance based controller successfully balances loads and corrects harmonics in supply current under distorted grid conditions. The supply voltage and current operate with a unity power factor under these circumstances.



(a)

(b)

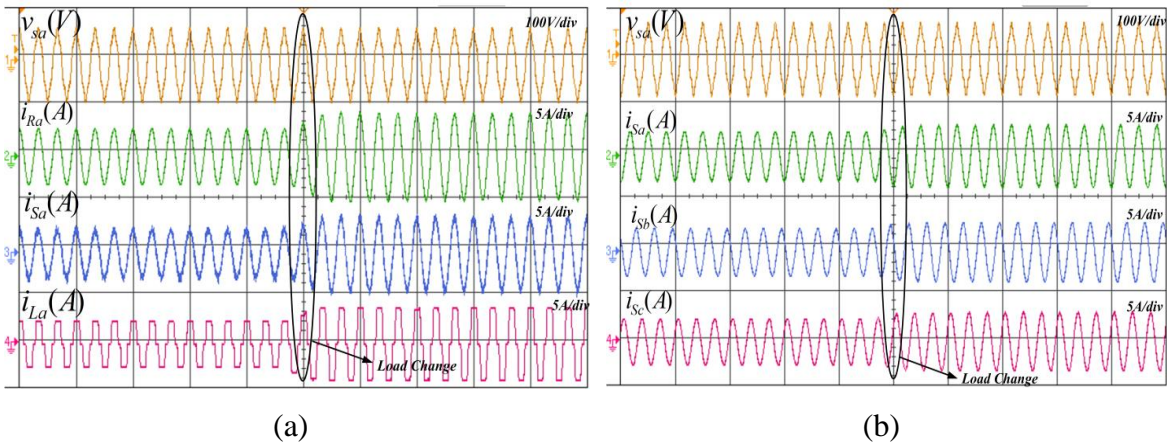


(c)

(d)

Fig.5.20 Steady state waveforms under distorted grid system showing (a) source voltage (v_{Sabc}) and load current (i_{Labc}) (b) THD of v_{Sabc} and i_{Labc} (c) source voltage (v_{Sabc}) and source current (i_{Sabc}) (d) THD of v_{Sabc} and i_{Sabc}

The dynamic response under distorted grid conditions is shown in Fig.5.21. Digital storage oscilloscope is used to record the responses for the distorted grid supply condition. Fig.5.21(a) shows results under distorted grid supply condition and the plots show supply voltage (v_{Sa}), reference current (i_{Ra}), source current (i_{Sa}) and load current (i_{La}). Fig.5.21(b) results have been captured for distorted grid supply condition and these show supply voltage (v_{Sa}), source current (i_{Sabc}). Fig5.21(c) shows supply voltage (v_{Sa}), source current (i_{Sa}), output weight and DC-link voltage (V_{dc}).



(a)

(b)

Fig.5.21 Dynamic performance of conductance based controller for three phase system showing (a) ($v_{sa}, i_{Ra}, i_{Sa}, i_{La}$) (b) ($v_{sa}, i_{Sa}, i_{Sb}, i_{Sc}$)

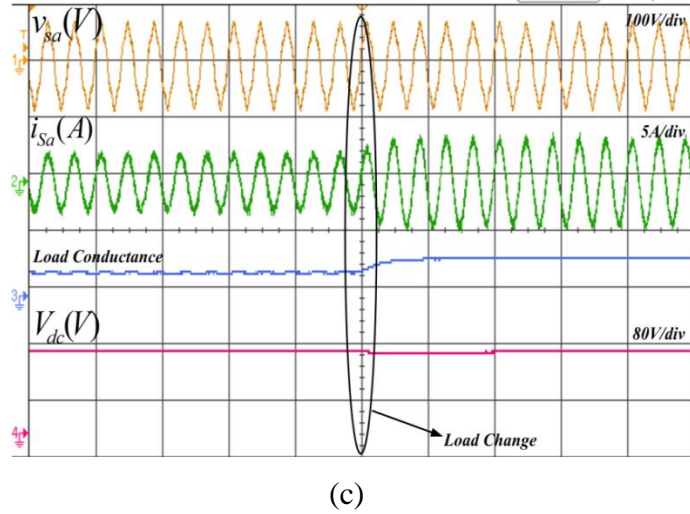


Fig.5.21 Dynamic performance of conductance based controller for three phase system showing (c) (v_{sa} , i_{sa} , load conductance, V_{dc})

As the load increases, the calculated load conductance changes and reference current increases as a result, as seen in Figs. 5.21(a)–(c). This shows that the conductance based controller approach responds quickly and satisfactorily to both distorted and undistorted grid conditions. The suggested technique successfully reaches the steady state in just two cycles.

5.5. Comparison:

Table 5.1 summarizes the results of a detailed investigation of the simulation and experimental performance of LM trained based SOGI with unit template control technique and Conductance based algorithm with D-SOGI technique for three-phase system under normal and polluted grid conditions and compared with standard SOGI based controller. According to IEEE 519 standards, the suggested adaptive LM SOGI and conductance-based controller is simple and produces outstanding results under load changes in polluted and normal grid conditions.

Table 5.1: Comparative Performance of different techniques				
S.No.	Parameter	LM SOGI	Conductance based controller	Standard SOGI
1.	PLL (requirement)	No	No	No
2.	Technique	Self- adaptive	Non-adaptive	Non-adaptive
3.	Tracking performance	Very good	Good	Moderate
4.	Weight Convergence	Fast (< 2 cycles)	Moderate(2-3cycle)	Moderate
6.	Dependency on control parameters	No, self-adaptive	Dependent	Dependent
7.	Meets International standards	Yes	Yes	Yes
Performance under normal grid condition				
8.	% THD of v_{sabc}	0.31%	1.07%	0.23%
9.	% THD of i_{Labc}	23.77%	23.40%	27.19%
10.	% THD of i_{sabc}	2.29%	3.25%	3.93%
Performance under distorted grid condition				
11.	% THD of v_{sabc}	10.84%	10.89%	10.80%
12.	% THD of i_{Labc}	19.72%	19.19%	20.14%
13.	% THD of i_{sabc}	3.94%	3.85%	4.2%

5.6. Conclusion:

Techniques for improving power quality are discussed in this chapter for grid conditions that are distorted or contaminated. In this chapter, a variety of unit template extraction methods, such as D-SOGI and the unit template approach for three phase systems are discussed. For SAPF operation in a polluted grid situation in a three phase system, two control strategies are explored and compared with standard SOGI controller. The first of these techniques is the LM trained SOGI filter; in this approach, the unit template method is employed for unit template computation. In the second controller technique, a conductance-based approach is employed, in this approach, a D-SOGI filter is used for positive sequence extraction, and the extracted sequence is then used for reference current calculation based on the load power demand. In simulation and experimental performances of both controllers were found satisfactory under polluted and normal grid

condition. Both active and reactive power compensation, as well as power quality improvement has been achieved.

Chapter-6: LVRT Operation of Single-Phase System

6.1 Introduction

A voltage sag is a short dip in voltage that may occur in grid-connected systems as a result of a number of different types of incidents (e.g., lightning strikes, switching, short circuit in power lines, power outage etc.). A sag in the grid voltage amplitude may be enough to surpass the usual voltage threshold, which will then cause the islanding protection [178] to be triggered, and lead to the disconnection of the power supply. For a PV connected grid system these kinds of disturbances may threaten grid stability of the system.

This chapter concentrates on the advanced control mechanisms that are used in single-phase grid-connected photovoltaic systems ensure stable and reliable operation under abnormal condition such as voltage sags.

6.2. Grid Codes for Single Phase System for Low Voltage Ride Through Operation (LVRT):

There are various difficulties with low voltage ride through (LVRT) operation in renewable energy systems. These include accurately detecting voltage drops, ensuring grid code compliance, managing implementation costs, minimizing the impact on energy production, and maintaining grid stability. Key concerns include interoperability with LVRT systems, technical issues, and communication. In addition, choosing the right LVRT parameters and performing frequent testing and maintenance are critical. LVRT systems must adjust to new requirements and obstacles as power grids develop. To address these difficulties, a combination of technical solutions, regulatory measures, and collaboration between renewable energy system operators and grid management bodies is required.

Grid codes are normally set and enforced by regulatory agencies or standards organizations in charge of the operation and stability of the electrical grid. Depending on the nation or location, different grid codes have been applied to single-phase LVRT systems.

Here a few grid codes for different countries are specified for single phase system [138,139]

1. Germany: The German grid code, also known as "VDE-AR-N 4105," addresses the technical criteria for grid connection of decentralized energy generation systems, including single-phase systems. The ranges of voltage and frequency, response periods, and other pertinent factors are specified in the regulations for LVRT functioning [139].

2. Spain: The "RD 1699/2011" grid code specifies the technical requirements for connecting low voltage, single-phase generation units to the grid. The specifications cover the necessary LVRT capabilities, voltage and frequency ranges, reaction times, and safety precautions and are listed in [139].

3. UK: The National Grid Electricity System Operator (ESO), which is in charge of managing the UK grid code, lays out the technical specifications for integrating and running generation systems, including single-phase systems. In accordance with the grid code, LVRT operation, voltage and frequency restrictions, and other relevant parameters have been detailed in [139].

Fig.6.1(a) depicts multiple LVRT curves for specific countries. The German grid code requires generating systems to be capable of riding through a 0.15s voltage failure when the grid voltage amplitude drops to 0 V and inject some reactive current I_q into the grid, as shown in Fig.6.1(a). On the same lines, other countries have set their benchmarks for reactive power injection.

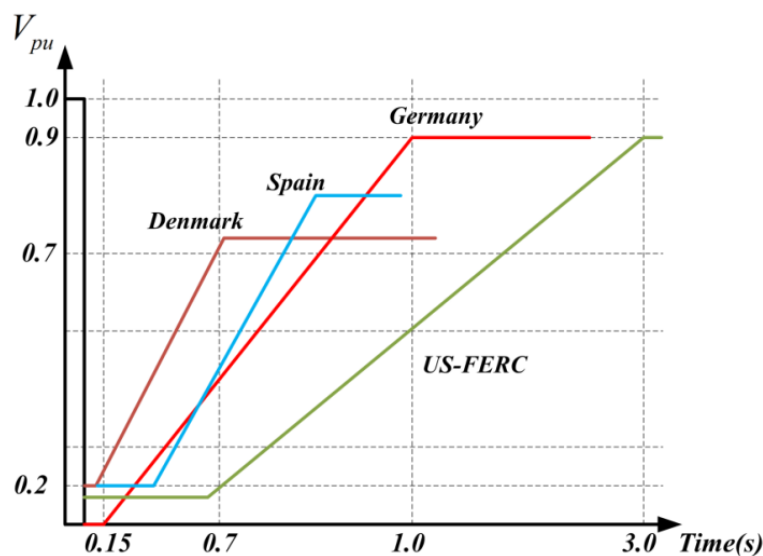


Fig.6.1(a) LVRT Curves as per grid codes of different countries

The functioning of a single phase system under normal and abnormal grid conditions is set in accordance with the grid codes that are specified by standard bodies in the following parts.

6.3. Low Voltage Ride Through Operation in Single-Phase System:

In single phase grid connected PV system, the LVRT operation is more challenging as compared to three phase grid connected PV system. This chapter delves with a detailed discussion of LVRT and UPF mode of operation for single phase grid connected PV system.

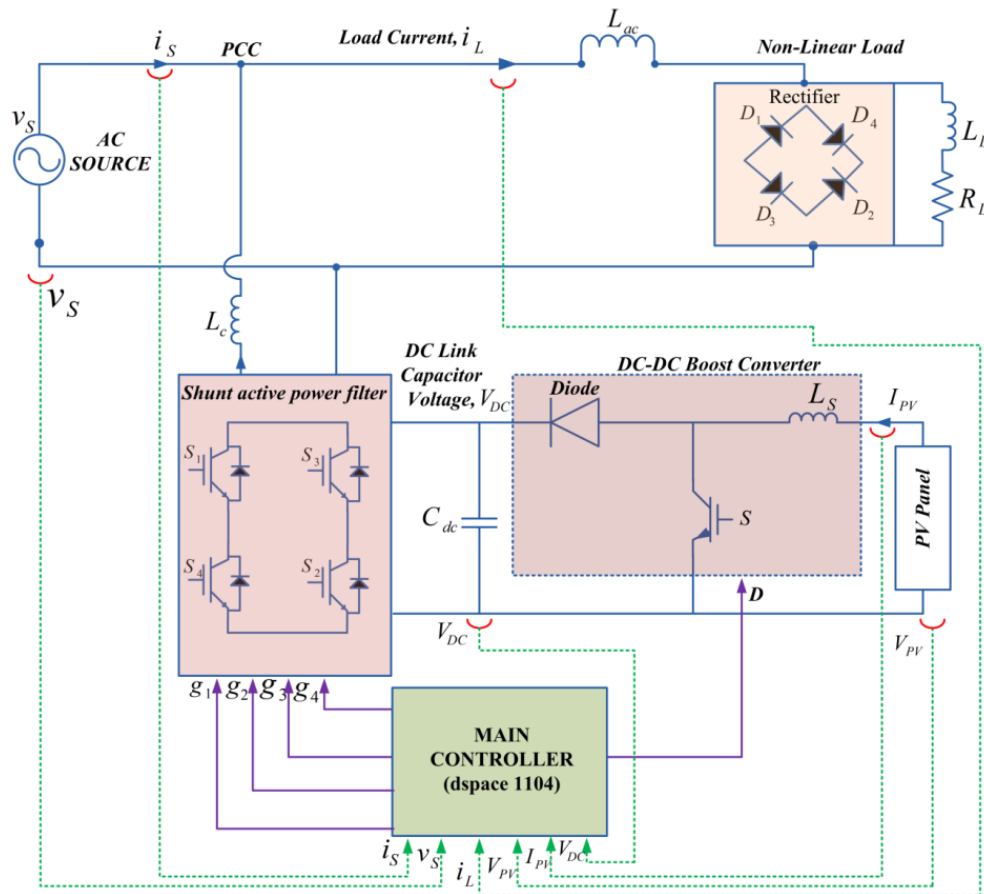


Fig.6.1(b) Proposed single phase system description

The proposed system has the conventional H bridge topology of the single phase VSC as shown in Fig.6.1(b). It comprises a single phase full bridge inverter having four Insulated gate bipolar transistors (IGBT) switches and a DC bus. A 1.3 kW PV array is connected

at the DC link. An interfacing inductor L_C is used to connect the inverter at the point of common coupling (PCC). This ensures control of power through the active filter and secondly, the inductor acts as a first order passive filter and helps in harmonic attenuation.

The system is supplied by single phase 110V, 50Hz ac supply and the non-linear load is modeled as a combination of resistive-inductive (RL) load connected at the terminals of full wave bridge rectifier. The controller is equipped to handle abnormal operating condition. The complete system description is mentioned in Appendix.

6.4. Reference Current Generation Control Techniques:

In this section two different control techniques have been discussed for extracting the required reference current and tested for working in two modes namely LVRT and UPF. LVRT controllers are built specifically to solve the unique issues associated with grid voltage disruptions. They must be capable of quick and dynamic control, grid code compliance, safety, and adaptability. These characteristics set them apart from standard controllers used in renewable energy systems, which are typically incapable of handling the complex and critical tasks required during LVRT events. The required reference current for both modes of operation consists of two components: an active component that is responsible for of UPF mode of operation and a reactive component that is responsible for the LVRT mode of operation. Three different control techniques viz. Laguerre polynomial based controller, Sliding window recursive discrete Fourier transform (SWRDFT) based controller and SOGI based controller are discussed below for VSC controlled as active filter under normal and LVRT condition.

6.4.1. Laguerre Polynomial based Controller:

Fig.6.2 shows the proposed Laguerre polynomial based controller which is utilized for the control of single-phase PV system to generate switching pulses for the single phase VSC. The required inputs for the control are grid current (i_g), load current (i_L), DC link voltage (V_{DC}), PCC voltage (v_{pcc}), PV current (I_{PV}) and PV voltage (V_{PV}).

All the grid and load parameters are sensed instantaneously and depending on the prevailing conditions, either MPPT mode or LVRT mode is implemented. The control

scheme has been formulated to compute the required active and reactive power references and discussed in detail for both the operation modes.

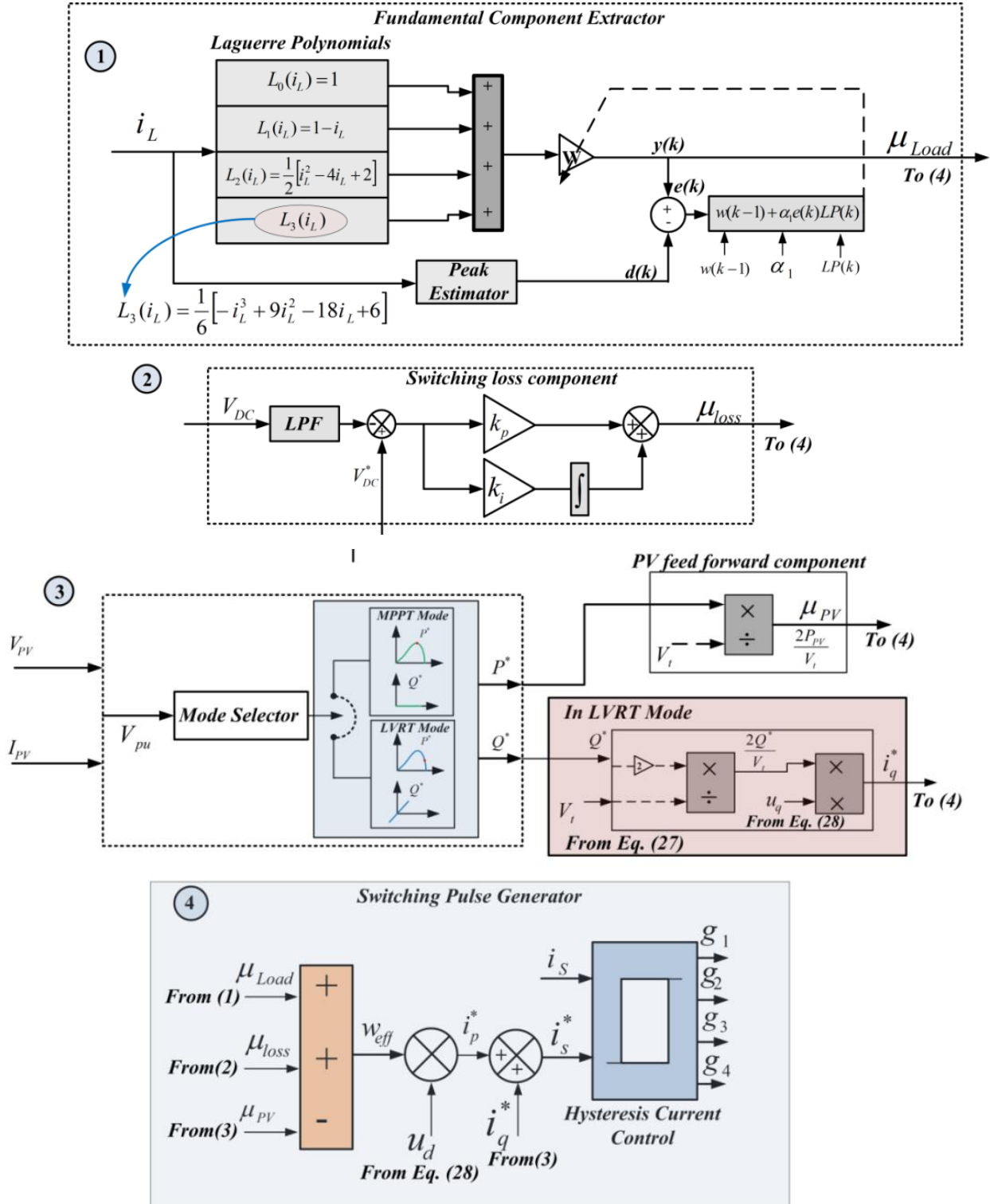


Fig.6.2(a) Block diagram representation of the proposed LP controller

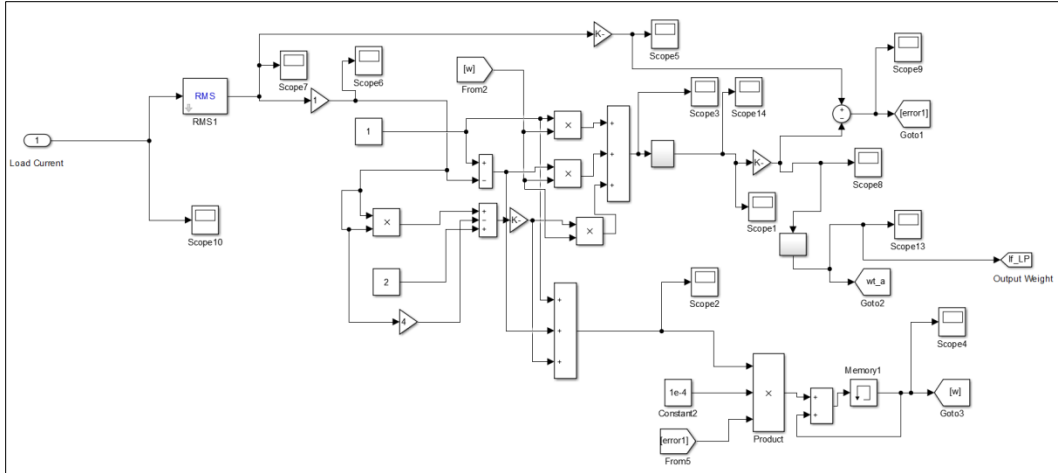


Fig.6.2(b) Simulation model of LP controller

The proposed control scheme is divided into several sub-parts as shown in Fig.6.2.

1. Fundamental current extraction using Laguerre polynomials
2. Calculation of unit templates required for synchronization
3. Calculation of reference current in normal mode of operation
4. Calculation of reference current under LVRT operation mode
5. Generation of switching pulses

These processes are discussed in detail as follows:

6.4.1.1. Mathematical Formulation of LP Control Technique:

Laguerre polynomial (LP) was proposed by Edmond Laguerre[179]. These polynomials have remarkable properties that include a guarantee of convergence for polynomial and orthogonal properties[179]. These polynomials find applications in the areas of uniform approximation, numerical analysis and solution of ordinary and partial differential equations.

The proposed controller realizes adaptive Laguerre polynomial (LP) control as shown in Fig.6.2. It uses one input (load current) and a single output $y(k)$ which corresponds to the fundamental weight extracted. This network is trained online using the Least Mean Square (LMS) approach. Only one parameter weight (w) is required to be trained for obtaining the fundamental component of load current. The output of this network is utilized for PQ improvement. The mathematical formulation of the proposed control technique and stability analysis is also discussed in this Section.

The sensed load current is processed through Laguerre polynomial function and it is controlled to estimate the fundamental component of load current. The standard Laguerre polynomial based differential equation is given by[180]

$$x \frac{d^2y}{dx^2} + (1-x) \frac{dy}{dx} + ny = 0 \quad (6.1)$$

for $x < |1|$ Laguerre differential equation has regular singular points at -1,1 and ∞ . Thus by using series solution method, the solution of Laguerre differential equation (y) can be evaluated as follows

$$\text{Let } y = \sum_{j=0}^{\infty} c_j x^{(m+j)} \quad (6.2)$$

Substituting the derivatives suitably in Eq.(6.1) gives

$$y' = \frac{dy}{dx} = \sum_{j=0}^{\infty} c_j (m+j) x^{(m+j-1)} \quad (6.3)$$

$$y'' = \frac{d^2y}{dx^2} = \sum_{j=0}^{\infty} c_j (m+j)(m+j-1) x^{(m+j-2)} \quad (6.4)$$

substituting Eq. (6.2,6.3) and Eq.(6.4) in Eq.(6.1) and arranging in increasing order of x gives

$$\begin{aligned} x \sum_{j=0}^{\infty} c_j (m+j)(m+j-1) x^{(m+j-2)} + (1-x) \sum_{j=0}^{\infty} c_j (m+j) x^{(m+j-1)} + n \sum_{j=0}^{\infty} c_j x^{(m+j)} \\ = 0 \end{aligned} \quad (6.5)$$

$$\sum_{j=0}^{\infty} c_j [(m+j)(m+j-1) + (m+j)] x^{(m+j-1)} - \sum_{j=0}^{\infty} c_j (m+j-n) x^{(m+j)} = 0 \quad (6.6)$$

From Eq.(6.6) coefficient of $x^{(m-1)}$ (i.e. $j=0$)

$$c_0 [m(m-1) + m] = 0$$

$$c_0 m^2 = 0 \quad (6.7)$$

from Eq.(6.7) $c_0 \neq 0$ and $m = 0$

coefficient of $x^{(m+j-1)}$ is

$$c_j (m+j)^2 - c_{j-1} (m+j-1-n) = 0$$

$$c_j = \frac{(m+j-1-n)}{(m+j)^2} c_{j-1} \quad (6.8)$$

In Eq.(6.8) substituting $m=0$ gives

$$c_j = \frac{-(n+1-j)}{j^2} c_{j-1} \quad (6.9)$$

where $j = 1, 2, 3 \dots$ so on

This recursive relation can be computed for any value of j , in particular for $j = 1$

$$c_1 = \frac{-n}{1^2} c_0 \quad (6.10)$$

$$\text{when } j=2, c_2 = \frac{-(n-1)}{2^2} c_1 = \frac{n(n-1)}{1^2 \cdot 2^2} c_0 \quad (6.11)$$

In Eq.(6.2) putting $m=0$ gives

$$y = \sum_{j=0}^{\infty} c_j x^j \quad (6.12)$$

This is expanded and written as

$$y = [c_0 + c_1 x + c_2 x^2 + \dots] \quad (6.13)$$

Now substituting the coefficients from Eq.(6.10) and (6.11) in Eq. (6.13)

$$y = c_0 \left[1 - \frac{n}{1} x + \frac{n(n-1)}{1^2 \cdot 2^2} x^2 - \dots \right] \quad (6.14)$$

If we put $c_0 = 0$, the value of y is known as LP, denoted by $L_n(x)$

$$L_n(x) = 1 - \frac{n}{(1!)^2} x + \frac{n(n-1)}{(2!)^2} x^2 - \dots \quad (6.15)$$

which can be written in short form as

$$L_n(x) = \sum_{j=0}^n \frac{(-1)^j n!}{(j!)^2 (n-j)!} x^j \quad (6.16)$$

Now, using Eq.(6.16) $L_n(x)$ can be written as

where $L_0(x) = 1$, $L_1(x) = 1 - x$

$$L_2(x) = \frac{1}{2}(x^2 - 4x + 2), L_3(x) = \frac{1}{6}(-x^3 + 9x^2 + 18x + 6)$$

Thus, the recursive relation of LP is

$$(n+1)L_{(n+1)}(x) = (2n+1-x)L_n(x) - nL_{(n-1)}(x) \quad (6.17)$$

Generally, $L_n(x)$ is used to approximate any given function and in this chapter it is used to estimate the load fundamental current from the load current input. This polynomial function can be easily used in place of hidden layer in ANN network. This helps to make the overall algorithm using LP more efficient and less time consuming as compared to multi-layer perceptron network.

6.4.1.2. Unit Template Calculation:

The unit template of the system voltage is required for grid synchronization and it is calculated by using grid voltage. The unit vector template (u_p) is generated by using Second order Generalized Integrator (SOGI) filter as shown in Fig.6.2.

$$V_t = \sqrt{v_{sp}^2 + v_{sq}^2} \quad (6.18)$$

$$u_p = \frac{v_{sp}}{V_t} \text{ and } u_q = \frac{v_{sq}}{V_t} \quad (6.19)$$

where V_t is the maximum amplitude of voltage, v_{sp} is the in-phase component and v_{sq} is the quadrature component.

6.4.1.3. Estimation of Reference Currents in Normal Mode:

Two modes of operation are defined for the system viz. normal mode and the LVRT mode. The normal mode of operation works in the maximum power point tracking (MPPT) while the LVRT mode working is based on the regulations specified by the grid codes.

In case of normal mode of operation, the controller is designed such that system works in unity power factor mode. The reference grid current is estimated based on the active power injection. The fundamental component of load current (μ_p) is estimated by using Laguerre polynomial function. Secondly, to enhance dynamic response and incorporate the contribution of solar PV, the feed forward term (μ_{pv}) is evaluated as

$$\mu_{pv} = \frac{2P_{PV}}{V_t} \quad (6.20)$$

where P_{PV} is the power fed by PV module and V_t is the maximum amplitude of voltage. Third, the DC link voltage regulation is also considered and the output of the PI controller is regarded as switching loss in voltage source converter (VSC). Monitoring and regulating the DC link voltage (V_{DC}) is crucial for efficient VSC operation. A conventional proportional-integral (PI) feedback controller is required to reduce the error in DC link voltage (V_{DC}) and may be easily constructed. The error can be expressed as follows:

$$e_{DC} = V_{DCref} - V_{DC} \quad (6.21)$$

For switching losses requirement, the reference value of DC link (V_{DCref}) is subtracted from real time DC link voltage (V_{DC}), and thus switching loss is estimated as w_{loss}

$$w_{loss} = k_p e_{DC} + k_i \int e_{DC} dt \quad (6.22)$$

where k_p and k_i are the PI controller's proportional and integral gains. The overall active power demand of the load is computed by estimating the basic active power component of load current and the loss component determined from dc link voltages (V_{DC}).

$$w_{eff} = w_{loss} + \mu_p - \mu_{pv} \quad (6.23)$$

Furthermore, the required fundamental reference current (i_p^*) is calculated by multiplying the predicted fundamental active component of the load (w_{eff}) by the unit in-phase component (u_p).

$$i_p^* = w_{eff} \times u_p \quad (6.24)$$

6.4.1.4. Estimation of Reference Currents in LVRT Mode:

The VSC supplies reactive power during two conditions i.e. high reactive loading or during fault condition. The system shown in Fig.6.2 depicts a sag detection unit. Fig.6.3 shows a mode selector switch for choosing between MPPT and LVRT modes and controller details in both the modes for generating switching logic are discussed.

In case of normal mode of operation, the PV unit injects power to grid through MPPT mode at unity power factor by ensuring maximum power injection from PV panels. The mode selection unit will change operation from MPPT to LVRT and vice versa according to per unit value of the grid voltage (V_{pu}) as shown in Fig.6.3. This V_{pu} is computed from the instantaneous value of terminal voltage and the maximum value.

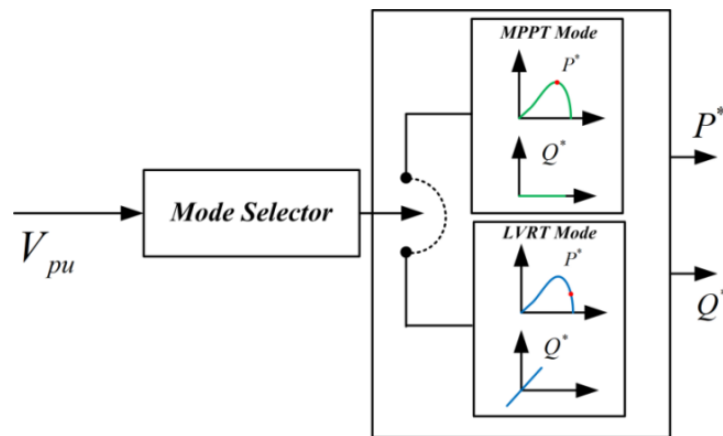


Fig.6.3 Diagram indicating switchover between two modes of operation

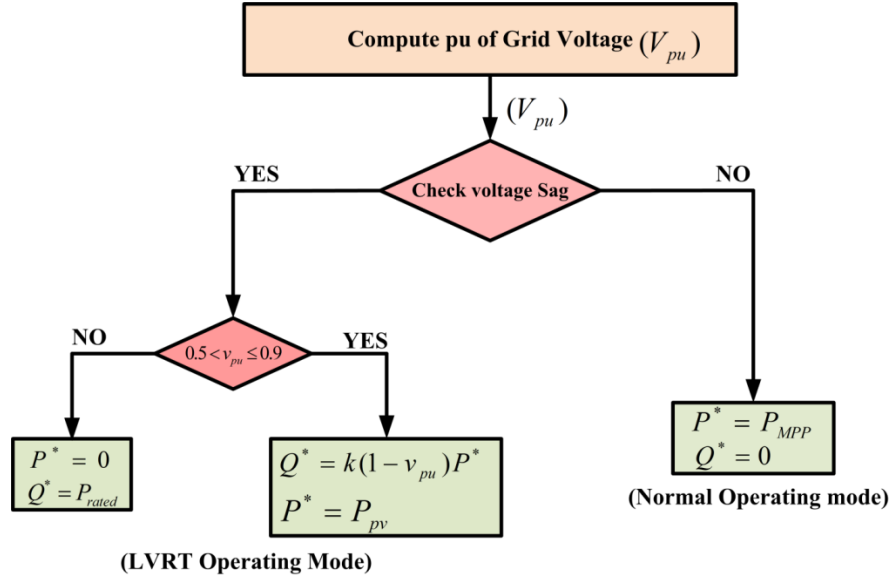


Fig.6.4 Flowchart showing the selection of reference powers for designed controller

Fig.6.4 shows the flowchart of operation of proposed system in abnormal grid condition that in normal mode of operation, active power reference is determined by MPPT operation i.e $P^* = P_{MPP}$, while reference reactive power will be zero i.e $Q^* = 0$ var for unity power factor operation. In case of fault, the power reference will change according to amount of sag in voltage and grid codes shall be followed. The active power reference will be the output power of PV panels in non-MPPT mode operation. The reactive power injection during fault is decided by requirement of IEEE Std. 1547-2018 [181] and is specified in grid codes as

$$Q^* = \begin{cases} 0 & 0.9pu \leq V_{pu} \leq 1.1pu \\ k(1 - v_t)P^* & 0.5pu \leq V_{pu} < 0.9pu \\ P^* & 0.5pu < v_{pu} \end{cases} \quad (6.25)$$

where k is the adjustment factor and taken as a constant.

Once the reference powers have been computed in both the modes, the next step involves computing the reference currents.

$$i_q^* = \left(\frac{2 \times Q^*}{v_t} \right) \times u_q \quad (6.26)$$

6.4.1.5. Switching Pulse Generation:

The total reference current of the grid will be

$$i_{ref}^* = i_p^* + i_q^* \quad (6.27)$$

The hysteresis current controller (HCC) block is used to compare i_{ref}^* current with the sensed grid current (i_s) and generate the required pulses for single phase VSC as shown in Fig.6.2. The next technique discussed is Sliding window recursive discrete Fourier transform (SWRDFT) based controller and SOGI based controller in the following Sections.

6.4.2. SWRDFT Control Technique:

A novel SWRDFT based control technique is proposed and developed as shown in Fig.6.5 which controls the single-phase double-stage PV system to generate switching pulses for single phase VSC. The required control variables are grid voltage (v_g), grid current (i_g), load current (i_L), DC link voltage (V_{DC}), PV voltage (V_{PV}) and PV current (I_{PV}). The controller monitors the instantaneous values of these parameters of the system and computes the active and reactive powers. Current reference signals are generated and compared using hysteresis current control (HCC) to generate the requisite control action. The proposed controller is divided into the following sub-parts for analysis viz. unit template calculation, switching loss calculation, switching pulse generation, V_{pu} calculation, current reference generation in normal and LVRT mode and SWRDFT controller. This is represented in Fig.6.5(a) and the details of the controller are discussed in the following Sections.

6.4.2.1. Mathematical Design of SWRDFT Controller:

A discrete Fourier transform (DFT) based SWRDFT control is mathematically designed for the extraction of fundamental component of load current. It is based on signal decomposition technique which is a special case of short-time Fourier transform (STFT) [182-184]. In this technique, a signal $x[n]$ is multiplied by window $g[n]$ having finite length in time and the output signal $x_o[n]$ can be represented as $x_o[n] = x[n].g[n]$.

The window duration governs the analysis of time localization, whereas bandwidth of window governs frequency resolution. If δ is the center of window, the frequency

representation is given by $x[e^{j\omega}]_\delta$ where ω is digital frequency in range of $-\pi \leq \omega < \pi$.

Mathematically, the STFT can be defined as

$$x[e^{j\omega}]_\delta = \sum_{p=-\infty}^{\infty} x[p]g[p - \delta] \quad (6.28)$$

where p is a constant shift imposed on the window. Eq.(6.28) can be rewritten for a frequency ω_o

$$x[e^{j\omega_o}]_\delta = e^{-j\omega_o\delta} \sum_{p=-\infty}^{\infty} x[p]g[p - \delta]e^{-j\omega_o(p-\delta)} \quad (6.29)$$

$$y[\delta] = \sum_{p=-\infty}^{\infty} x[p]h[\delta - p] \quad (6.30)$$

$$h[\delta] = g[-\delta]e^{j\omega_o\delta} \quad (6.31)$$

The filter interpretation of STFT is as shown in Fig.6.6(a)

In this case $g[n]$ is low-pass filter and its discrete time fourier transform (DTFT) is $g[e^{j\omega}]$. The DTFT time reversal property involves

$$g[-n] \leftrightarrow g[e^{-j\omega}] \quad (6.32)$$

The frequency shifting property involves

$$g[-n]e^{j\omega_o n} \leftrightarrow g[e^{-j(\omega-\omega_o)}] = H_o(e^{j\omega}) \quad (6.33)$$

Thus for a particular frequency ω_p

$$g[-n]e^{j\omega_p n} \leftrightarrow g[e^{-j(\omega-\omega_p)}] = H_p(e^{j\omega}) \quad (6.34)$$

For sliding window recursive DFT, rectangular window is used

$$g[n] = \begin{cases} 1 & -(N-1) \leq n \leq 0 \\ 0 & \text{otherwise} \end{cases} \quad (6.35)$$

The z-transform of Eq.(6.35) is given by

$$G(Z) = \frac{Z^{N-1} - Z^{-1}}{1 - Z^{-1}} \quad (6.36)$$

Representing Eq.(6.34) in z-domain

$$g[-n]e^{j\omega_p n} \leftrightarrow g[z^{-1}e^{j(\omega_p)}] = H_p(z) \quad (6.37)$$

From Eq.(6.36) and Eq.(6.37)

$$H_p(z) = \frac{1 - \mu_p^N z^{-N}}{1 - \mu_p z^{-1}} \quad (6.38)$$

where

$$\mu_p = e^{j\omega_p}$$

If $\omega_p = \frac{j2\pi}{N} p$ in DFT, then

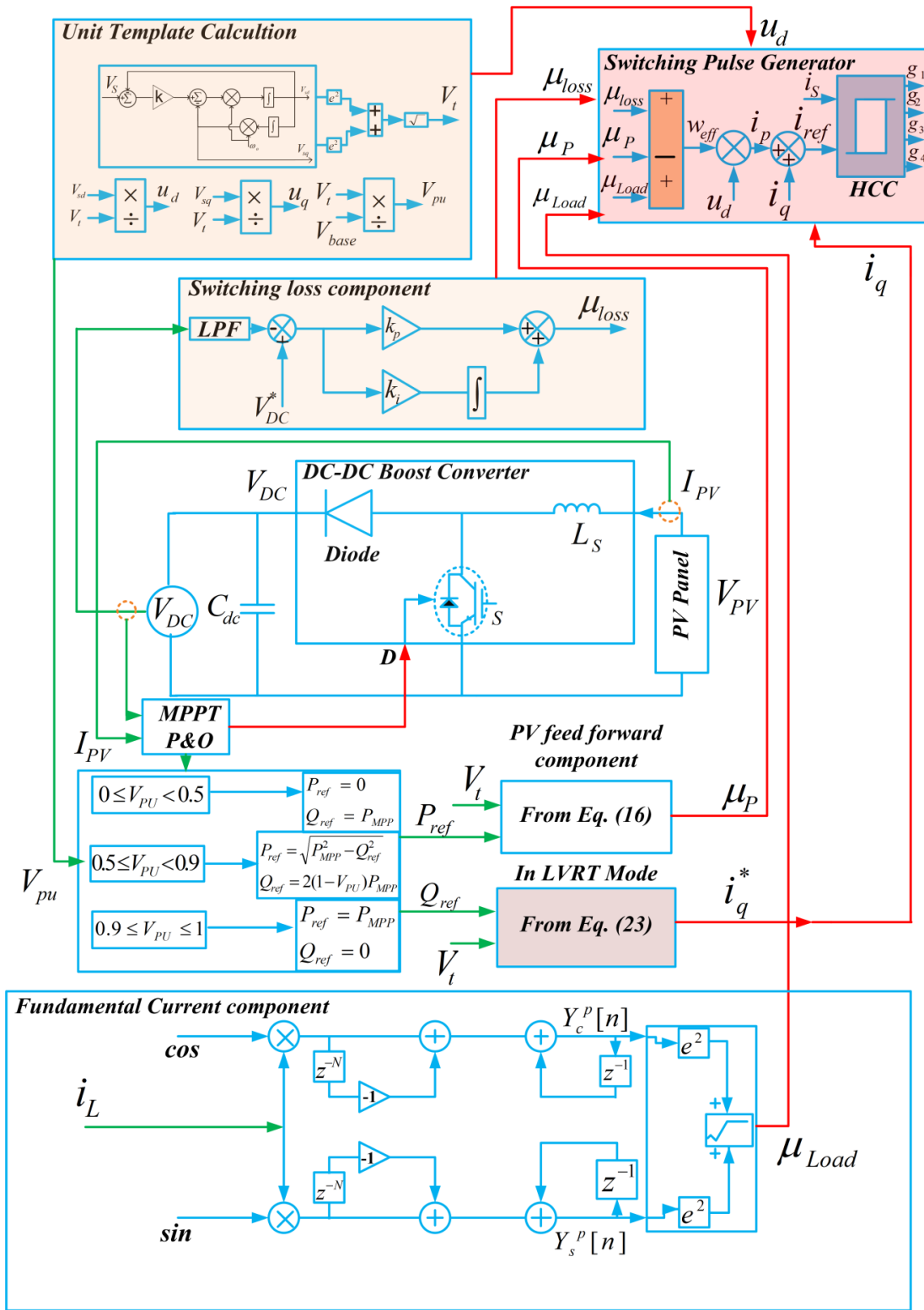


Fig.6.5(a) Control layout based on SWRDFT controller.

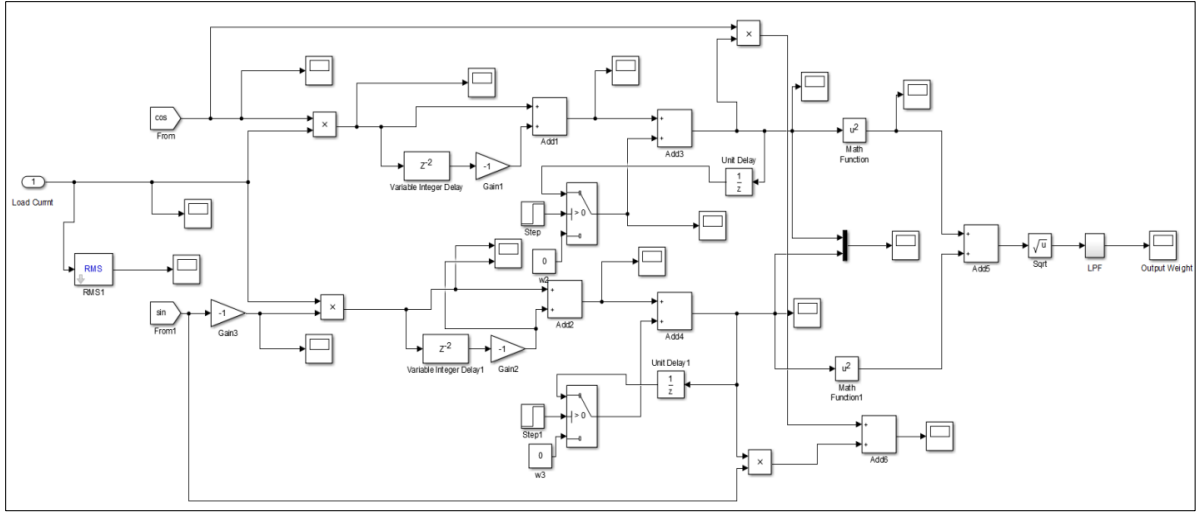


Fig.6.5(b) Simulation Model of SWRDFT controller

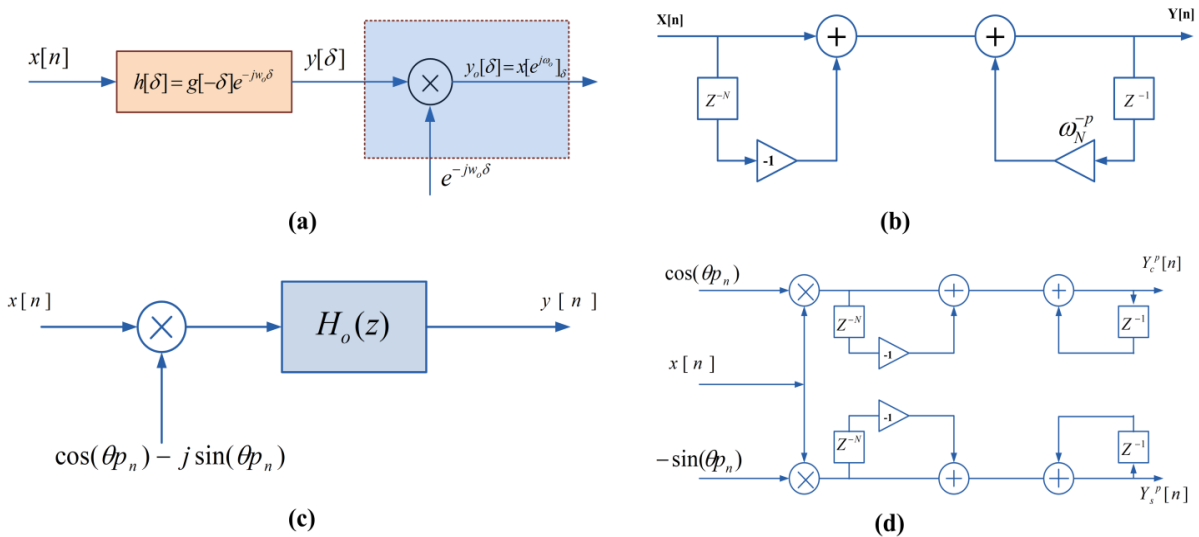


Fig.6.6 SWRDFT controller showing (a) filter interpretation of STFT (b) block diagram of SWRDFT technique (c) equivalent structure of SWRDFT (d) block diagram of SWRDFT based technique

$$\mu_p = e^{j\frac{2\pi}{N}p} = W_N^{-p}$$

where W_N^{-p} is delay element. From Eq.(6.38) the block diagram of SWRDFT can be drawn which is shown in Fig.6.6(b). The SWRDFT block diagram shown in Fig.6.6(b) is a digital filter with complex coefficient. Fig.6.6(c) is the equivalent structure of Fig.6.6(b) where $\theta = 2\pi/N$ and $H_o(z)$ is obtained from Eq.(6.38)

Now by taking the real and imaginary portion of STFT from Fig.6.6(c) gives

$$Y_c^p[n] = Y_c^p[n-1] + [x[n] - x[n-N]]\cos(\theta p_n) \quad (6.39)$$

$$Y_s^p[n] = Y_s^p[n-1] - [x[n] - x[n-N]]\sin(\theta p_n) \quad (6.40)$$

Fig.6.6(d) is the equivalent time-varying filter structure obtained using Eq. (6.39) and Eq.(6.40).

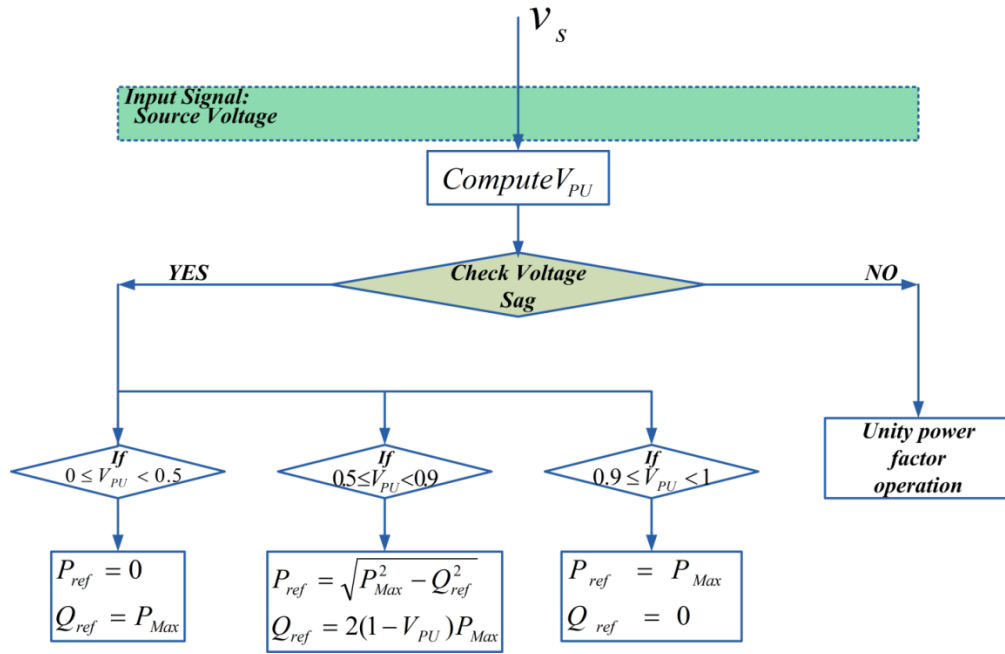


Fig.6.7 Flowchart showing the selection for reference powers for the designed controller

6.4.2.2. Estimation of Reference Current:

The proposed controller has the capability to operate in unity power factor mode and in LVRT mode based on the prevailing grid conditions. The per unit grid voltage V_{pu} is first calculated to ascertain the amount of sag. Using the grid code specification in Eq.(6.41) the reference power components for both active power and reactive power in normal and LVRT condition are specified as Eq.(6.41).

The flowchart of proposed control action is next formulated which detects the case of normal or faulty grid condition and it is shown in Fig.6.7.

$$\left\{ \begin{array}{l} 0 \leq V_{PU} < 0.5 \\ 0.5 \leq V_{PU} < 0.9 \\ 0.9 \leq V_{PU} < 1 \end{array} \right. \left\{ \begin{array}{l} P_{ref} = 0 \\ Q_{ref} = P_{ref} \\ P_{ref} = \sqrt{P_{MPP}^2 - Q_{ref}^2} \\ Q_{ref} = 2(1 - V_{PU})P_{MPP} \\ P_{ref} = P_{MPP} \\ Q_{ref} = 0 \end{array} \right. \quad (6.41)$$

The reference current generation is carried out next on the basis of active power component (i_p) and the reactive power component (i_q). The detailed formulation of reference current generation is divided in following two sections

6.4.2.3. Active Power Component (i_p)

In case of normal mode of operation, the controller is designed such that system works in unity power factor mode. The reference grid current is estimated based on the active power injection. The fundamental component of load current (μ_p) is estimated by using SWRDFT.

$$\mu_p = \sqrt{[Y_c^p[n]]^2 + [Y_s^p[n]]^2} \quad (6.42)$$

Further, to enhance the dynamic response and incorporate the contribution of solar PV, the feed forward term is evaluated. This term is evaluated based on the P_{ref} computed according to the amount of sag present in the grid voltage as shown in Fig.6.7

$$\mu_{PV} = \frac{2P_{ref}}{V_t} \quad (6.43)$$

Third, DC link voltage regulation of the VSC is also considered and the output of the PI controller is regarded as switching loss in voltage source converter (VSC). Monitoring and regulating the DC link voltage (V_{DC}) is crucial for efficient SAPF compensation operation. A conventional proportional-integral (PI) feedback controller is required to reduce the error in DC link voltage (V_{DC}) and may be easily constructed. The error can be expressed as follows:

$$e_{DC} = V_{DCref} - V_{DC} \quad (6.44)$$

For switching loss estimation, the reference value of DC link (V_{DCref}) is subtracted from the actual DC link voltage (V_{DC}) and thus switching loss is estimated as μ_{loss}

$$\mu_{loss} = k_p e_{DC} + k_i \int e_{DC} dt \quad (6.45)$$

where k_p and k_i are the proportional and integral gains of PI controller. The overall active power demand of the load is computed by estimating the basic active power component of load current and the loss component determined from dc link voltages (V_{DC}).

$$w_{eff} = \mu_{loss} + \mu_p - \mu_{pv} \quad (6.46)$$

Furthermore, the required fundamental reference current (i_p) is calculated by multiplying the predicted fundamental active component of the load (w_{eff}) by the unit in-phase component (u_p).

$$i_p = w_{eff} \times u_p \quad (6.47)$$

where u_p is unit template of the system.

6.4.2.4. Reactive Power Component (i_q):

Once voltage sag fault is detected, the controller is designed to work in LVRT mode. The reference grid current is estimated based on the reactive power injection. In Fig.6.7 the reference reactive power demand under different conditions is illustrated as per grid code requirement. It is observed that both reference active and reactive power reference are varied as per the severity of the fault. Eq.(6.41) shows that under severe sag condition when V_{pu} is less than 0.5pu, the reference reactive power is equal to maximum PV power P_{MPP} , i.e. during this case reactive power injection given priority over active power injection. Once the reference powers have been computed according to the level of voltage sag, the next step involves computing the reference currents.

$$i_q = \left(\frac{2 \times Q_{ref}}{v_t} \right) \times u_q \quad (6.48)$$

The total reference current of the grid is computed as

$$i_{ref} = i_p + i_q \quad (6.49)$$

The hysteresis current controller (HCC) block compares i_{ref} current with the sensed source current (i_s) and generates four pulses for the proper operation of single phase VSC as shown in Fig.6.5.

6.4.3. SOGI based Controller:

It is a second order generalized integrator which acts like BPF and LPF. The block diagram of SOGI is shown in Fig.6.8(a) and Fig.6.8(b) shows simulation model of SOGI

based controller. SOGI controller produces two orthogonal outputs namely direct axis and quadrature axis at same frequency ω_o and having same amplitude. The direct axis output ($i_{L\alpha}$) is in phase with input and quadrature axis output ($i_{L\beta}$) lags input by 90° . The transfer function shown in Eq.(6.50) and Eq.(6.51) acts like BPF and LPF respectively and gain (k) of SOGI filter decides the bandwidth of filter. The fixed gain SOGI controller works best under narrow range of operating conditions. Moreover, once tuned it is not possible to vary these gains.

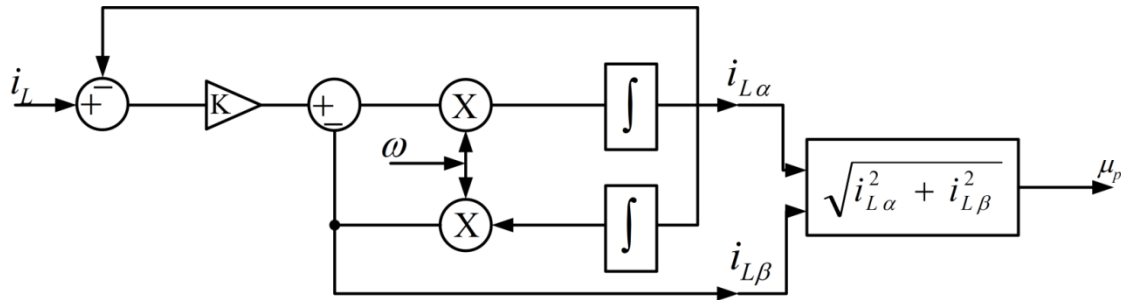


Fig.6.8(a) Design of Adaptive SOGI filter

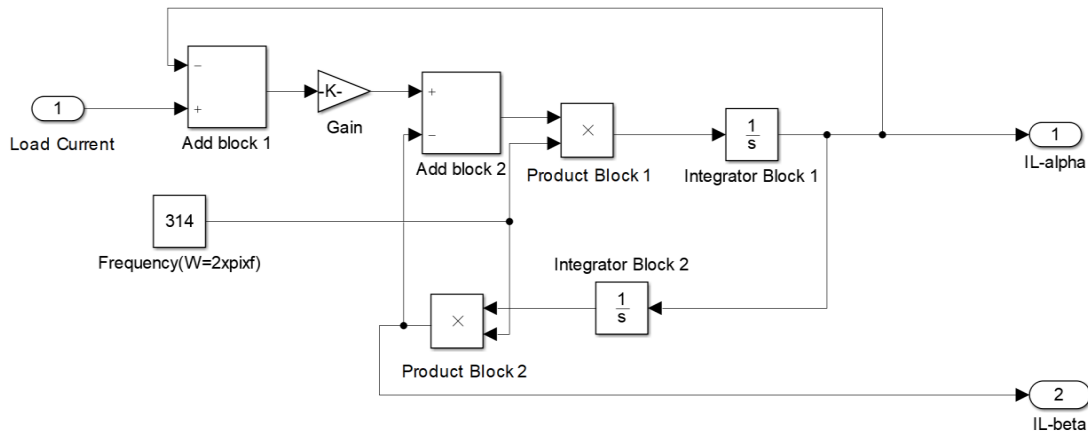


Fig.6.8(b) Simulation Model of SOGI based Controller

$$\frac{I_{L\alpha}}{i_L} = \frac{K\omega_o S}{S^2 + K\omega_o S + \omega_o^2} \quad (6.50)$$

$$\frac{i_{L\beta}}{i_L} = \frac{K\omega_o^2}{S^2 + K\omega_o S + \omega_o^2} \quad (6.51)$$

6.4.3.1. Reference Current Generation:

In case of normal mode of operation, the controller is designed such that system works in unity power factor mode. The reference grid current is estimated based on the active

power injection. The fundamental component of load current (μ_p) is estimated by using SOGI.

$$\mu_p = \sqrt{i_{L\alpha}^2 + i_{L\beta}^2} \quad (6.52)$$

For switching loss estimation, the reference value of DC link (V_{DCref}) is subtracted from the actual DC link voltage (V_{DC}) and thus switching loss is estimated as μ_{loss} in Eq.(6.45). The overall active power demand of the load is computed by estimating the basic active power component of load current and the loss component determined from dc link voltages (V_{DC}) in Eq.(6.46), furthermore the active power reference current is given by Eq.(6.47)

$$i_p = w_{eff} \times u_p$$

In LVRT mode of operation, the reference current estimation depends on the amount of reactive power injection based on magnitude of voltage sag shown in Eq.(6.41). Once the reference powers have been computed according to the level of voltage sag, the next step involves computing the reference currents as per Eq.(6.48).

$$i_q = \left(\frac{2 \times Q_{ref}}{v_t} \right) \times u_q$$

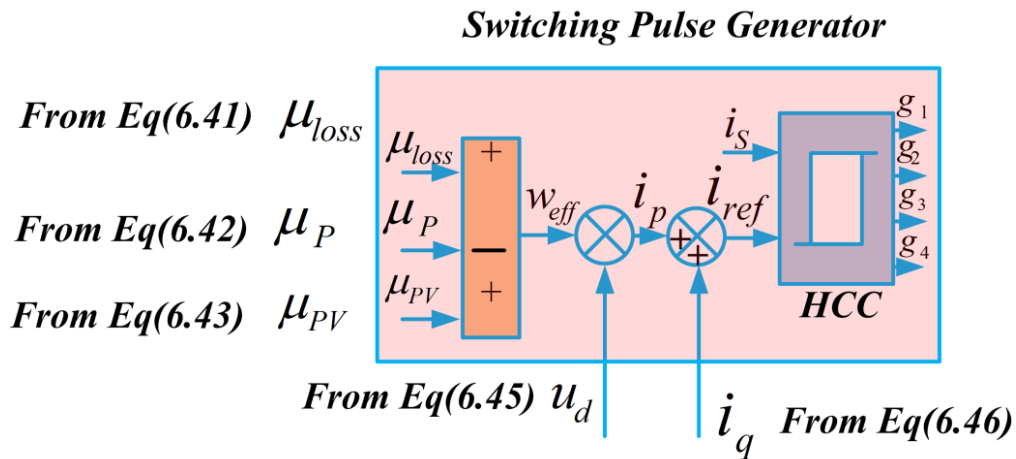


Fig.6.8(c) Switching Pulse generator Based on SOGI Controller

Thus, the total reference current (i_{ref}) is given by

$$i_{ref} = i_p + i_q \quad (6.53)$$

The required gate pulses to control of single phase VSC operation is generated with HCC block by comparing the source current (i_s) and reference current (i_{ref}) for the proper operation shown in Fig.6.8(c).

6.5.Simulation Performance Analysis:

This section presents the simulation performances with the developed Laguerre and SWRDFT technique for a single-phase grid-connected PV distribution system feeds nonlinear loads and linear loads. The simulation performance is analyzed into two modes, namely, normal mode of operation and abnormal mode of operation using Simulink/MATLAB. Appendix highlights the design value of parameters of the proposed system for simulation as well as experimental studies.

6.5.1. Simulation Performance of Laugerre Polynomial Based Control Technique:

Fig.6.9 depicts MATLAB/Simulink performance of proposed LP based controller with added LVRT capability. The intermediate performance of LP is shown in Fig.6.9(a), which shows load current (i_L), desired fundamental Weight, output weight and error of desired weight and output weight.

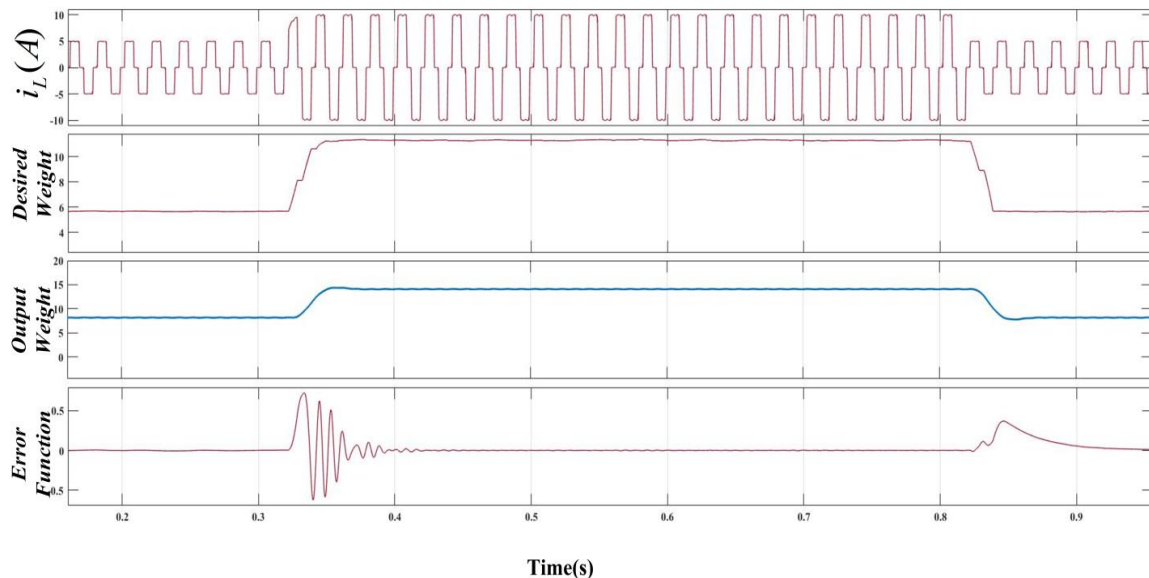


Fig.6.9(a) Intermediate Performance of LP based controller

Fig.6.9(b) and Fig.6.9(c) depicts MATLAB/Simulink performance of proposed LP based controller with added LVRT capability. Fig.6.9(b) shows the plots of source voltage (v_s), source current (i_s), source reactive power (Q_s) and the generated PV power P_{PV} . Fig.6.9(b) shows the performance of proposed system during transition from night-time to day-time. During daytime, PV array of 1.3kW with irradiance of 1000 W/m^2 is simulated at $t=3\text{s}$. Before $t=3\text{s}$ PV array irradiance is 0W/m^2 which is considered as night time. Thus, the results in Fig.6.9(b) highlight the effect of PV integration at $t=3\text{s}$. The night time operation (till $t=3\text{s}$) corresponds to SAPF operation without renewable energy integration ($P_{PV} = 0\text{W}$). During the normal mode of operation, reactive power requirement of grid is zero ($Q_s = 0\text{Var}$) and Power delivered by PV to the grid and load is 1.2kW as shown in Fig.6.9 (b). Further, the source voltage and current are in phase relationship demonstrating UPF operation during night-time. The phase relationship changes from in-phase to out of phase during PV integration after $t=3\text{s}$.

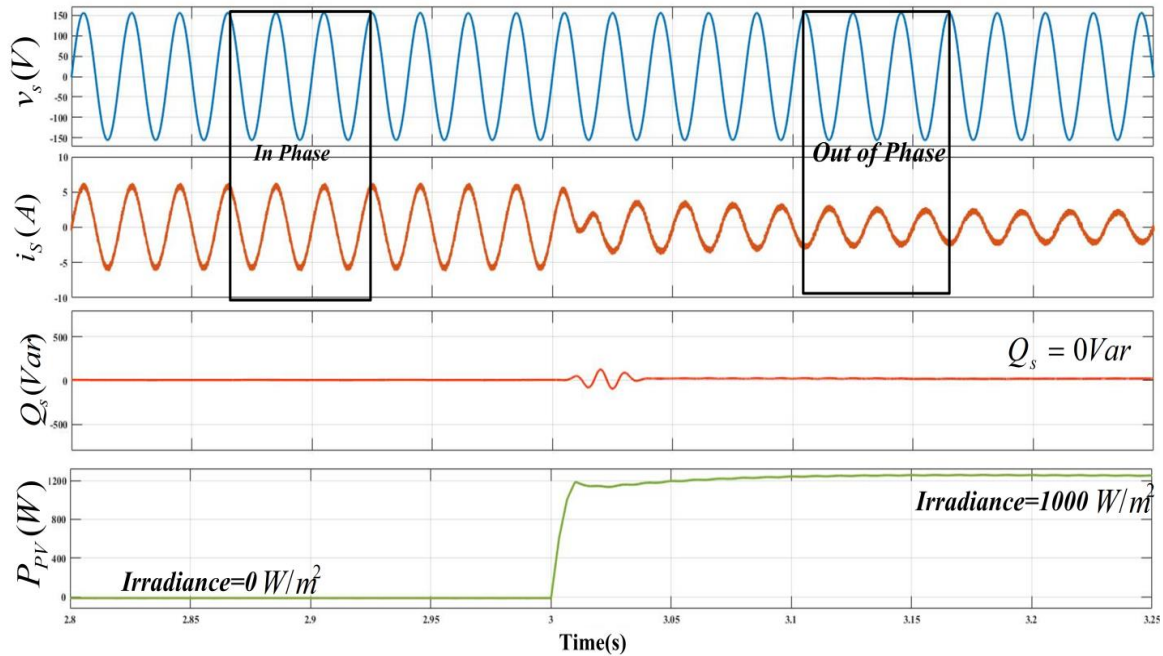


Fig.6.9(b) Simulation performance of LP controller during normal mode operation showing (a) source voltage (v_s), (b) source current (i_s), (c) source reactive power (Q_s) (d) generated PV power P_{PV}

Fig.6.9(c) shows the performance under transition between UPF-operation to LVRT operation. Fig6.9(c) shows source voltage v_s , source current i_s , per unit voltage V_{PU} , inverter active power P_{inv} , inverter reactive power Q_{inv} and DC link voltage V_{DC} .

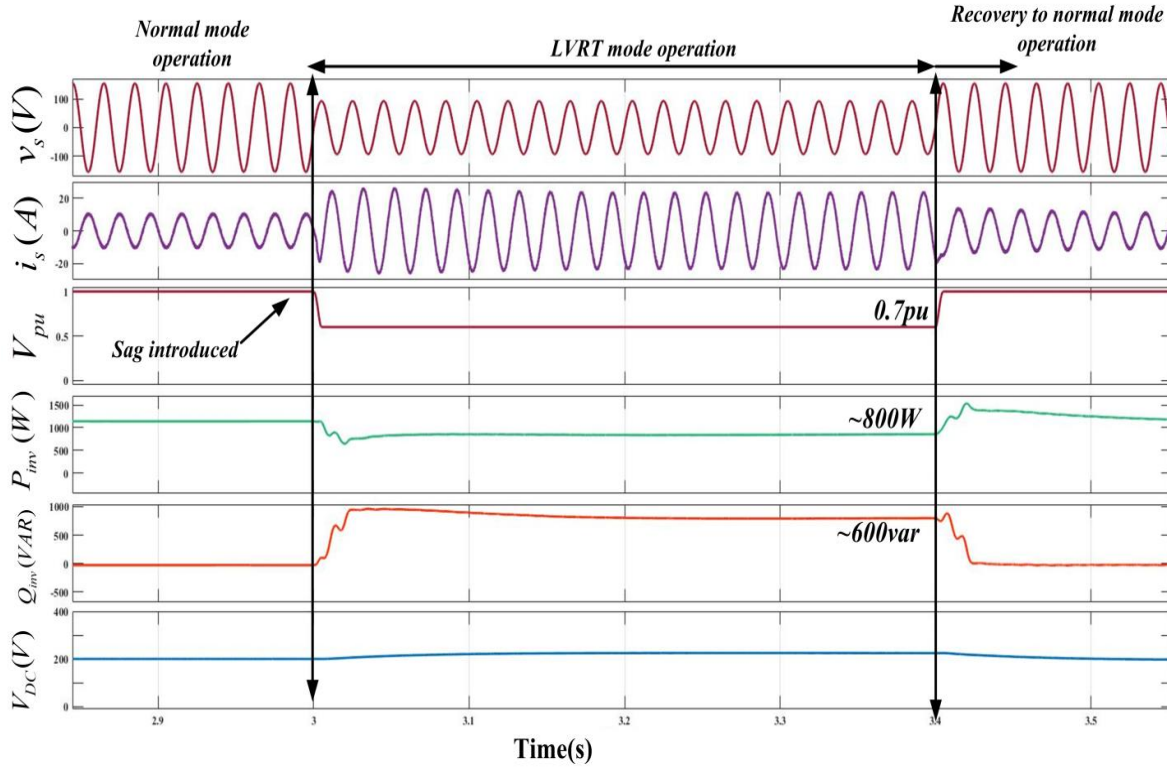


Fig.6.9(c) Simulation performance of LP controller during LVRT operation showing (a) source voltage v_s , (b) source current i_s , (c) per unit voltage V_{PU} , (d) inverter active power P_{inv} , (e) inverter reactive power Q_{inv} (f) DC link voltage V_{DC}

In Fig.6.8(c) from $t=3s$ to $3.4s$ a voltage sag of $0.7pu$ is introduced. According to the established grid codes, the reactive and active power inverter references get modified as per Eq.(6.25) to $600Var$ and $800W$ respectively. Now from Eq.(6.25) for a voltage sag of $0.7pu$ the power output of the VSC is computed to be

$$Q_{ref} = 2(1 - 0.7)1000$$

$$Q_{ref} \cong 600Var$$

$$P_{ref} = \sqrt{1000^2 - Q_{ref}^2}$$

$$P_{ref} \cong 800W$$

The magnitude of voltage sag also influences the reactive power demand of the grid. Thus, for 0.7pu voltage during sag conditions, the power injection from the inverter i.e. Q_{inv} and P_{inv} change from 0var to 600var and 1000W to 800W respectively. Severe sag requires higher reactive power support along with a corresponding lower value of active power injection from the inverter when the kVA rating of VSC is considered constant. Further, the DC link voltage exhibits a little perturbation during the onset of sag but stabilizes due to PI controller action at reference dc link voltage value of 200V.

6.5.2. Simulation Performance of SWRDFT Control Technique:

Fig.6.10 depicts MATLAB/Simulink performance of proposed SWRDFT based controller with added LVRT capability. The intermediate performance of SWRDFT is shown in Fig.6.10(a), which shows load current (i_L), real part of SWRDFT ($Y_c^p(n)$) from Eq.(6.39), imaginary part of SWRDFT ($Y_s^p(n)$) from Eq.(6.40) and fundamental weight of load current from Eq.(6.42).

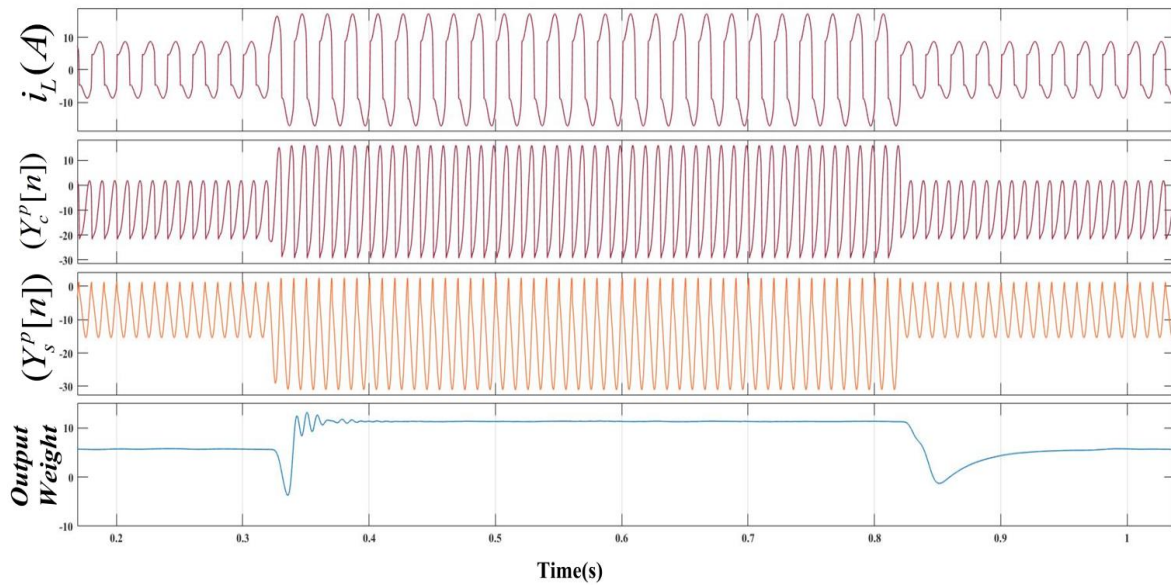


Fig.6.10(a) Intermediate performance of SWRDFT based controller

Fig.6.10(b) and Fig.6.10(c) depicts MATLAB/Simulink performance of proposed SWRDFT based controller with added LVRT capability. Fig.6.10(b) shows the plots of source voltage (v_s), source current (i_s), source reactive power (Q_s) and the generated

PV power P_{PV} . Fig.6.10(b) shows the performance of proposed system during transition from night-time to day-time. During daytime, PV array with irradiance of 1000 W/m^2 is simulated at $t=3\text{s}$. Before $t=3\text{s}$ PV array irradiance is 0W/m^2 which is considered as night time. Thus, the results in Fig.6.10(b) highlight the effect of PV integration at $t=3\text{s}$. The night time operation (till $t=3\text{s}$) corresponds to SAPF operation without renewable energy integration. During the normal mode of operation, reactive power requirement of grid is zero as shown in Fig.6.10(b). Further, the source voltage and current are in phase relationship demonstrating UPF operation during night-time. The phase relationship changes from in-phase to out of phase during PV integration after $t=3\text{s}$.

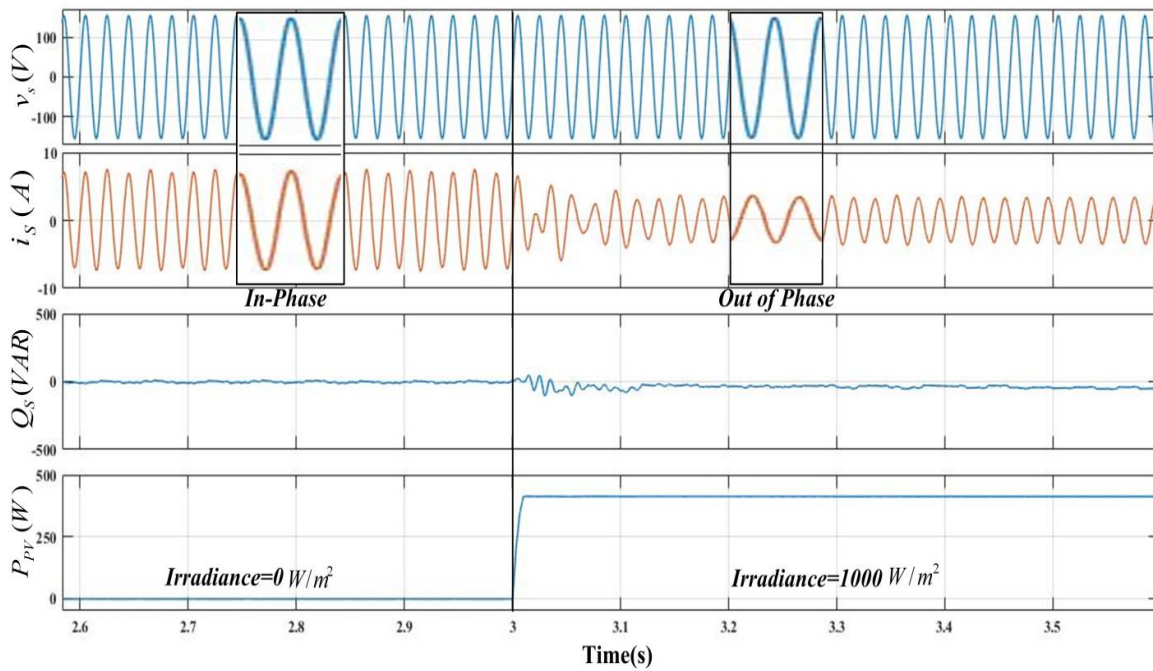


Fig.6.10(b) Simulation performance of system using SWRDFT control during normal operation showing (a) source voltage (v_s), (b) source current (i_s), (c) source reactive power (Q_s) (d) generated PV power P_{PV}

Fig.6.10(c) shows the performance under transition between UPF operation to LVRT operation. Fig.6.10(c) shows source voltage v_s , source current i_s , per unit voltage V_{PU} , inverter active power P_{inv} , inverter reactive power Q_{inv} and DC link voltage V_{DC} . In Fig.6.10(c) from $t=3\text{s}$ to 3.4s a voltage sag of 0.7pu is introduced. According to the established grid codes, the reactive and active power inverter references get modified as

per Eq.(6.41). The magnitude of voltage sag also influences the reactive power demand of the grid. Thus, for 0.7pu voltage during sag conditions, the power injection from the inverter i.e. Q_{inv} and P_{inv} change from 0var to 600var and 1000W to 800W respectively. Severe sag ($V_{pu} < 0.5pu$) requires higher reactive power ($Q_{ref} = P_{MPP}$) support along with a corresponding lower value of active power injection ($P_{ref} = 0$) from the inverter when the kVA rating of VSC is considered constant. Further, the DC link voltage exhibits a little perturbation during the onset of sag but stabilizes due to PI controller action at reference dc link voltage value of 200V.

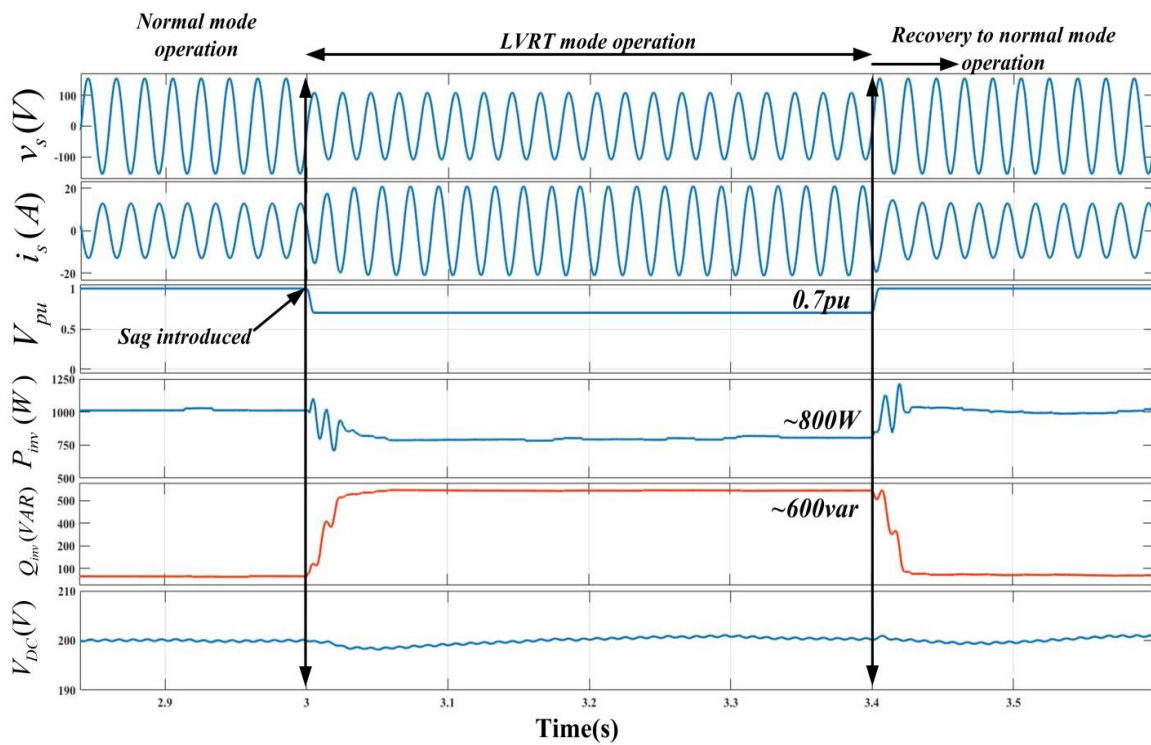


Fig.6.10(c) Simulation performance of SWRDFT during LVRT operation showing (a) source voltage v_s , (b) source current i_s , (c) per unit voltage V_{PU} , (d) inverter active power P_{inv} , (e) inverter reactive power Q_{inv} (f) DC link voltage V_{DC}

6.5.3. Simulation Performance of SOGI Based Control Technique:

Fig.6.11 depicts MATLAB/Simulink performance of proposed SOGI based controller with LVRT capability. The intermediate performance of SOGI is shown in Fig.6.11(a), which shows load current (i_L), in-phase part of SOGI ($i_{L\alpha}$) from Eq.(6.50), quadrature

phase part of SOGI ($i_{L\beta}$) from Eq.(6.51) and fundamental weight of load current from Eq.(6.53).

Fig.6.11(b) and Fig.6.11(c) depict MATLAB/Simulink performance of proposed SOGI based controller with added LVRT capability. Fig.6.11(b) shows the plots of source voltage (v_s), source current (i_s), source reactive power (Q_s) and the generated PV power P_{PV} . Fig.6.11(b) shows the performance of proposed system during transition from night-time to day-time. During daytime, PV array with irradiance of 1000 W/m^2 is simulated at $t=3\text{s}$. Before $t=3\text{s}$ PV array irradiance is 0W/m^2 which is considered as night time. Thus, the results in Fig.6.9(b) highlight the effect of PV integration at $t=3\text{s}$. The night time operation (till $t=3\text{s}$) corresponds to SAPF operation without renewable energy integration. During the normal mode of operation, reactive power requirement of grid is zero as shown in Fig.6.11(b). Further, the source voltage and current are in phase relationship demonstrating UPF operation during night-time. The phase relationship changes from in-phase to out of phase during PV integration after $t=3\text{s}$.

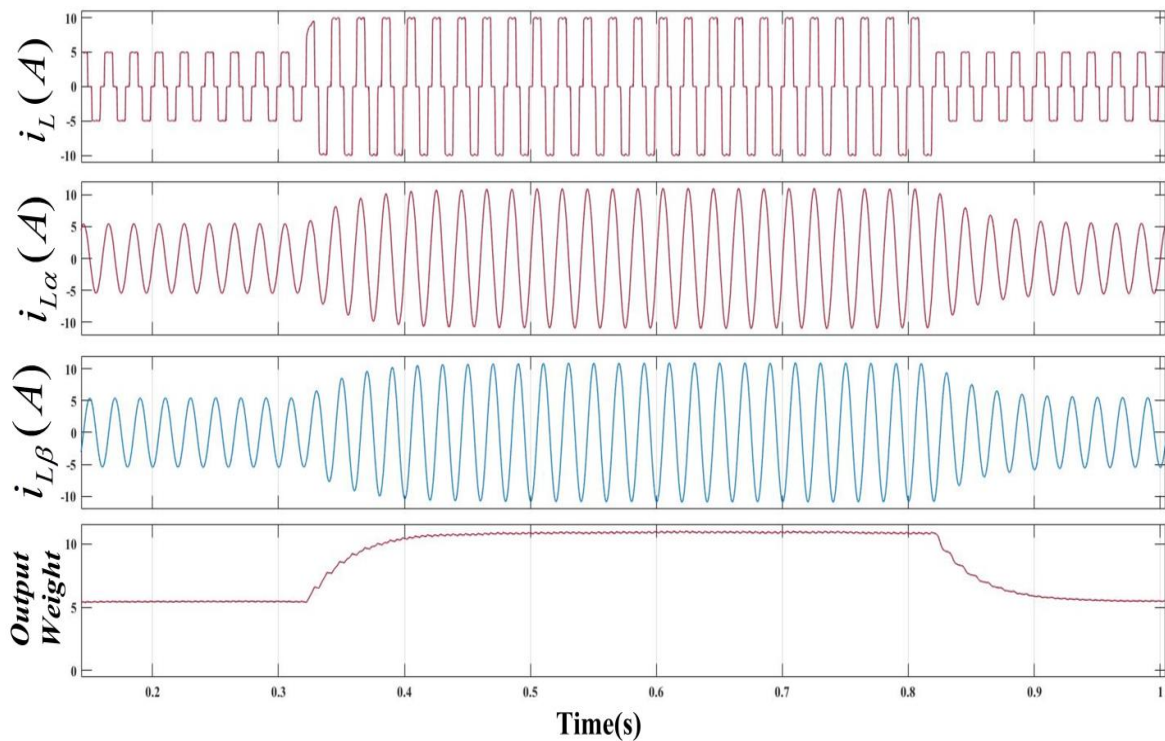


Fig.6.11(a) Intermediate performance of SOGI based controller

Fig.6.11(c) shows the performance under transition between UPF operation to LVRT operation. Fig.6.11(c) shows source voltage v_s , source current i_s , per unit voltage V_{pu} , inverter active power P_{inv} , inverter reactive power Q_{inv} and DC link voltage V_{DC} . In Fig.6.11(c) from $t=3s$ to $3.4s$ a voltage sag of $0.7pu$ is introduced. According to the established grid codes, the reactive and active power inverter references get modified as per Eq.(6.41). The magnitude of voltage sag also influences the reactive power demand of the grid. Thus, for $0.7pu$ voltage during sag conditions, the power injection from the inverter i.e. Q_{inv} and P_{inv} change from $0var$ to $600var$ and $1000W$ to $800W$ respectively. Severe sag ($V_{pu} < 0.5pu$) requires higher reactive power ($Q_{ref} = P_{MPP}$) support along with a corresponding lower value of active power injection ($P_{ref} = 0$) from the inverter when the kVA rating of VSC is considered constant. Further, the DC link voltage exhibits a little perturbation during the onset of sag but stabilizes due to PI controller action at reference dc link voltage value of $200V$.

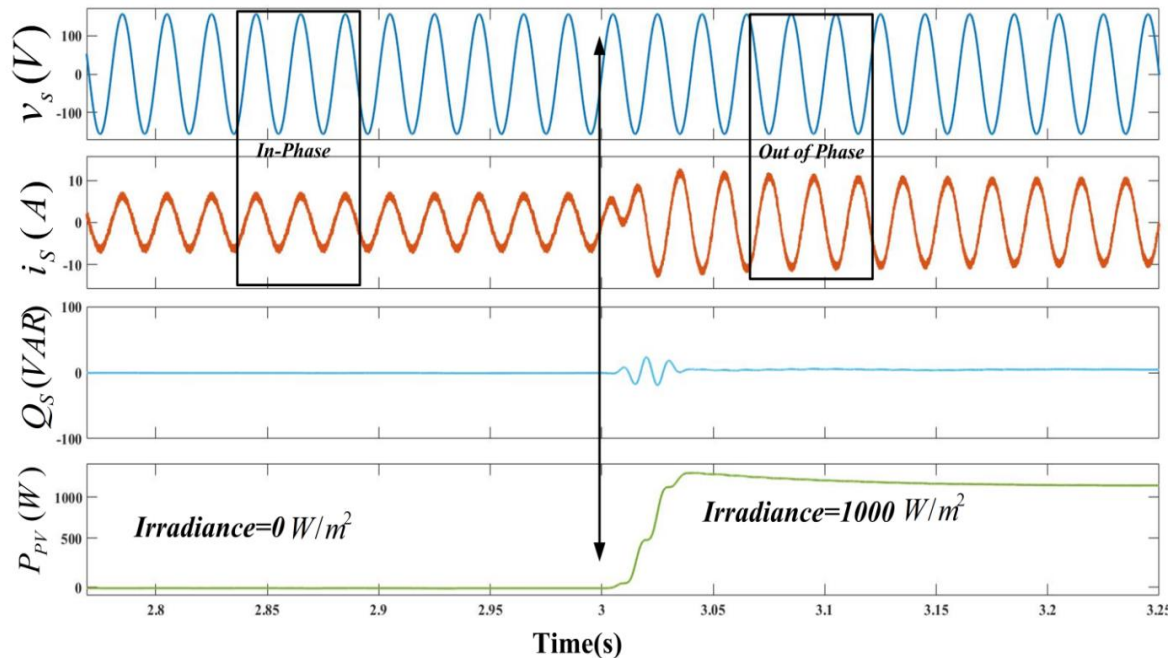


Fig.6.11(b) Simulation performance of system using SOGI control during normal operation showing (a) source voltage (v_s), (b) source current (i_s), (c) source reactive power (Q_s) (d) generated PV power P_{PV}

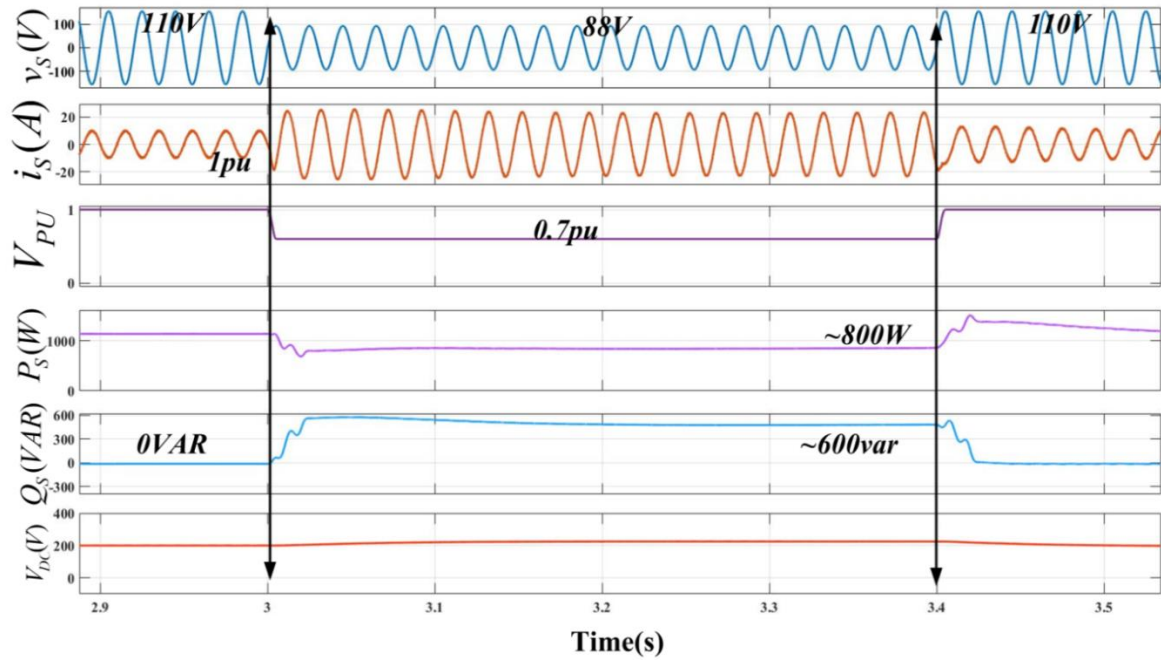


Fig.6.11(c) Simulation performance of SWRDFT during LVRT operation showing (a) source voltage v_s , (b) source current i_s , (c) per unit voltage V_{PU} , (d) inverter active power P_{inv} , (e) inverter reactive power Q_{inv} (f) DC link voltage V_{DC}

6.6.Comparison:

The controllers are based on Laguerre polynomials, SWRDFT and SOGI to extract the fundamental component of load current and use it for control algorithm design. As a result, the suggested LP control, SWRDFT and SOGI performances and responsiveness are compared as shown in Fig.6.12. The fundamental weights obtained from load current (i_L) utilizing the proposed LP, SWRDFT and SOGI controller are shown in Fig.6.12. The detailed simulation performances of LP, SWRDFT and SOGI controller have been discussed during UPF and LVRT mode of operation. The LP controller shows better performance than SWRDFT and SOGI controller in terms of fast settling time, less oscillations, lower peak overshoot and peak undershoot. Table-6.1 shows the results of a comparison using LP, SWRDFT and SOGI controllers. It may also be demonstrated that the SWRDFT and SOGI controllers are non-adaptive in nature and SWRDFT is complex

in nature. Table 6.1 and Fig.6.12 shows LP based controller shows better performance than other two controller viz SWRDFT and SOGI based controller.

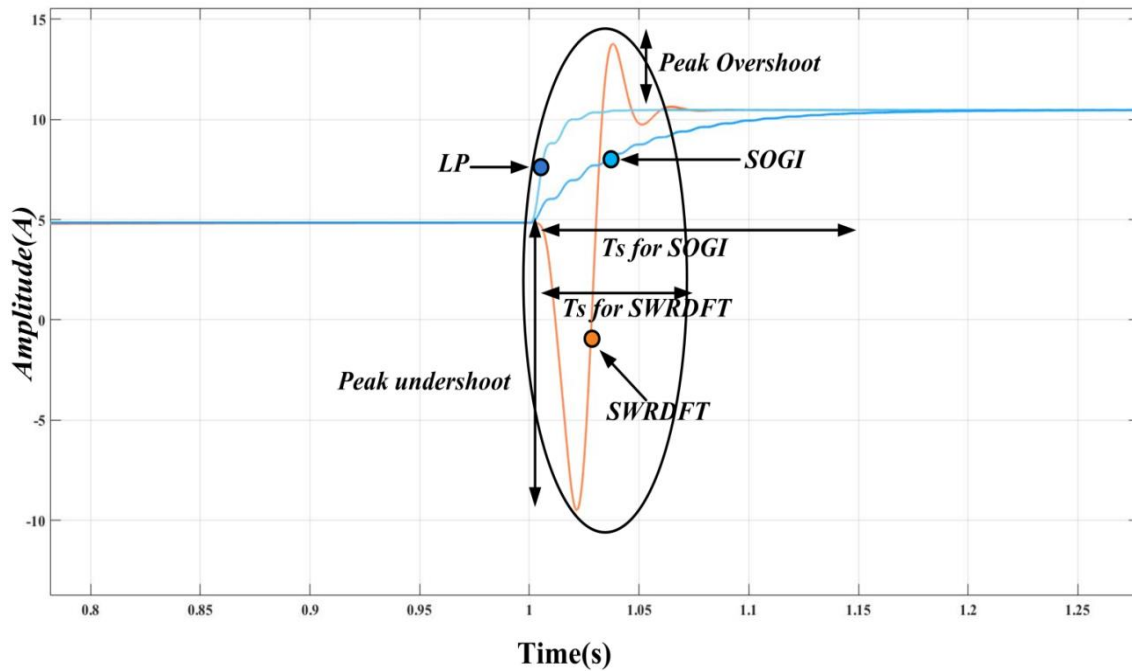


Fig.6.12 Comparison of Fundamental Weight with different controllers

Table 6.1: Comparative performance of different techniques				
S.No.	Parameter	Proposed SWRDFT	Proposed LP	SOGI
1.	PLL (requirement)	No	No	No
2.	Technique	Non-adaptive	Adaptive	Non-adaptive
3.	Settling Time	(~0.08sec)	(~0.03sec)	(~0.10sec)
4.	Weight Convergence	Fast(<2.5 cycles)	Fast(<2 cycles)	Slow
5.	Oscillation	Less(< $\pm 2\%$)	Less(< $\pm 2\%$)	Less(< $\pm 2\%$)
6.	Dependency on control parameters	Yes	No, self-adaptive	Yes
7.	Complexity	High	Lower	Least
8.	% Peak overshoot	50%	NA	NA
9.	% Peak undershoot	>100%	NA	NA
10.	Sampling Time	50 μ s	50 μ s	50 μ s

6.7. Experimental Performance:

An experimental setup of a single phase system has been developed to validate the simulation results of the proposed LP based controller. The performance of Laguerre Polynomial control technique is investigated in steady state and dynamic changes under various loading scenarios for both the cases viz. SAPF operation is shown without and with PV integrated system and under normal and abnormal grid conditions. The experimental setup shown in chapter 3 and to replicate the solar PV curve, a PV array simulator (Chroma) is used. Voltage and current measurements are performed using Hall Effect sensors for current (LA55-P) and voltage (LA55-V). A digital signal processor dSpace-1104 is employed to execute the control approach. A power quality analyzer (HIOKI make) is used to evaluate the harmonic spectra of various parameters and various signals are recorded on a four channel oscilloscope (Aglient make).

6.7.1. Operation in Normal Mode Without PV Integration:

The intermediate performance of proposed LP control technique for SAPF control is shown in Fig.6.13 for a load change. Fig.6.13 shows load current, desired weight, output weight and error function of the system.

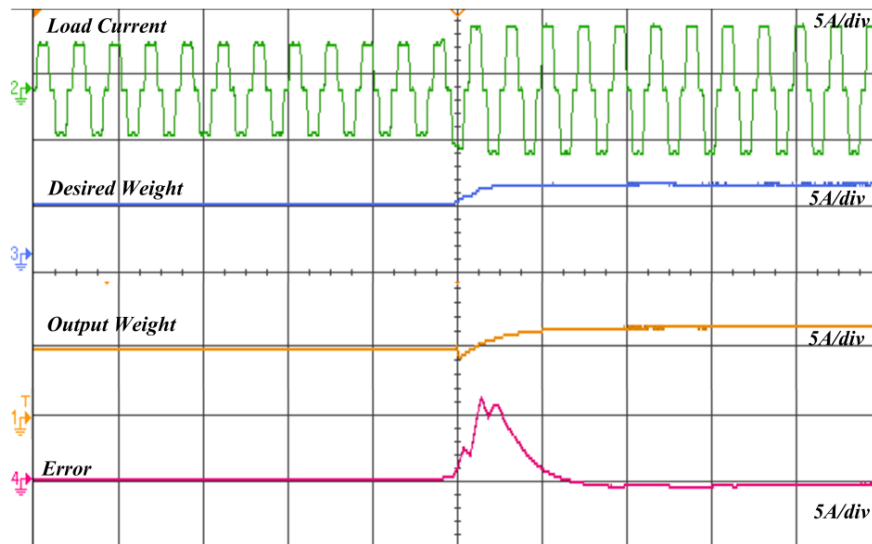


Fig.6.13 Intermediate performance of LP controller

The steady state performance of the system for non-linear RL load is shown in Fig.6.14. Fig.6.14(a) shows waveform of source voltage (V_s) and source current (I_s). Fig.6.14(b)

shows the waveform of source voltage (V_S) and load current (I_L). The THD in load current is 27.54% as shown in Fig.6.14(c). The THD in source voltage is 1.87% and THD in source current is 3.94% as shown in Fig.6.14(d) which as per IEEE 519 standard. The proposed single phase SAPF performs harmonic reduction satisfactorily for supply currents. In addition, the supply voltage and current have an in-phase relationship showing almost unity power factor operation.

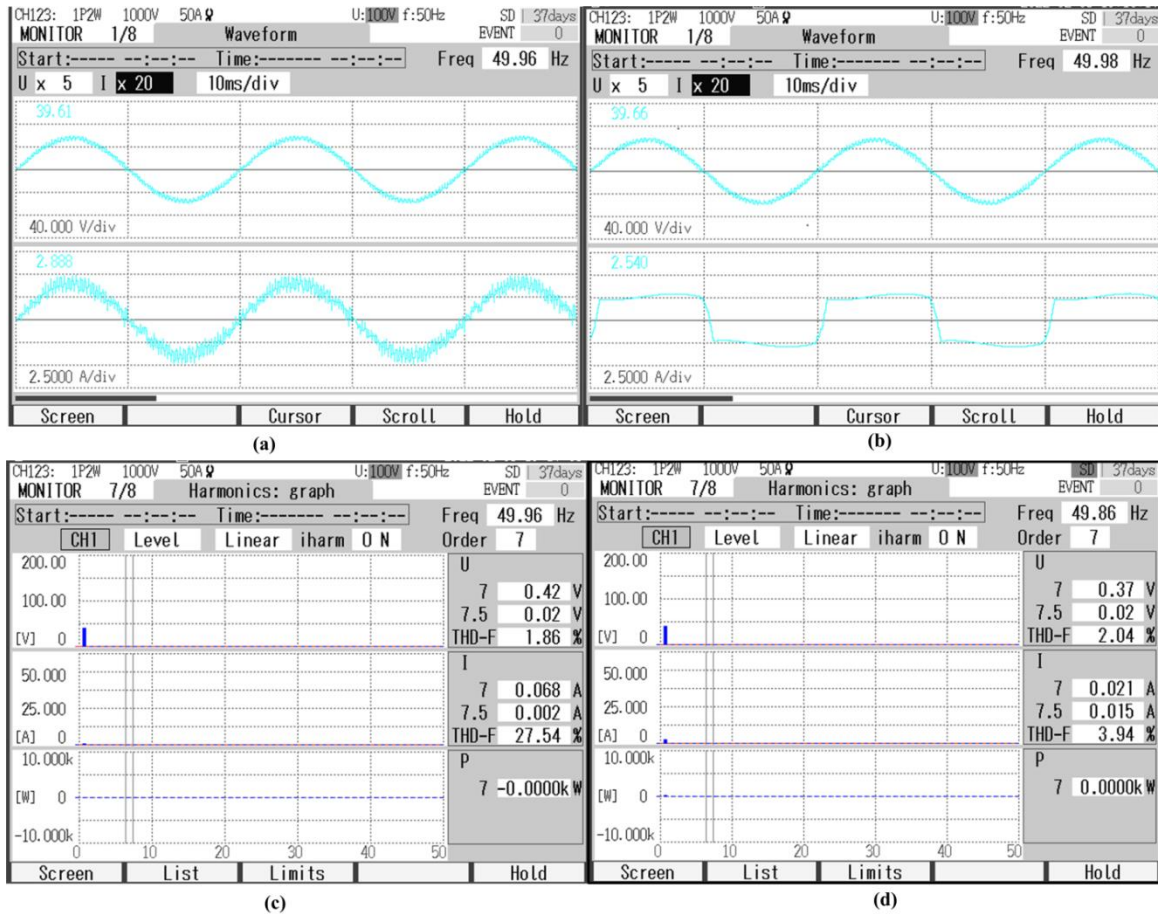


Fig.6.14 Waveforms showing (a) source voltage (v_s) and grid current (i_s) (b) source voltage (v_s) and load current (i_L) (c) THD of v_s (1.87%) and i_L (27.54%) (d) THD of v_s (1.87%) and i_s (3.94%) for harmonic reduction

The dynamic performance of the system is shown in Fig.6.15 in which source voltage (v_s), source current (i_s), load current (i_L), DC link voltage (V_{DC}), reference current (i_{Ref}), load RMS current ($i_{L(rms)}$) and output fundamental weight of load current are shown. From Fig.6.15 it is observed that during the change in load, the DC link voltage is stable

and the grid current is sinusoidal. The harmonic content in grid current is also maintained as per IEEE 519 standard. The load fundamental gain μ_{Load} shows fast convergence and reference current changes as per load changes. The steady state of the system is achieved within 2-3 cycles of operation using Laguerre Polynomial control approach.

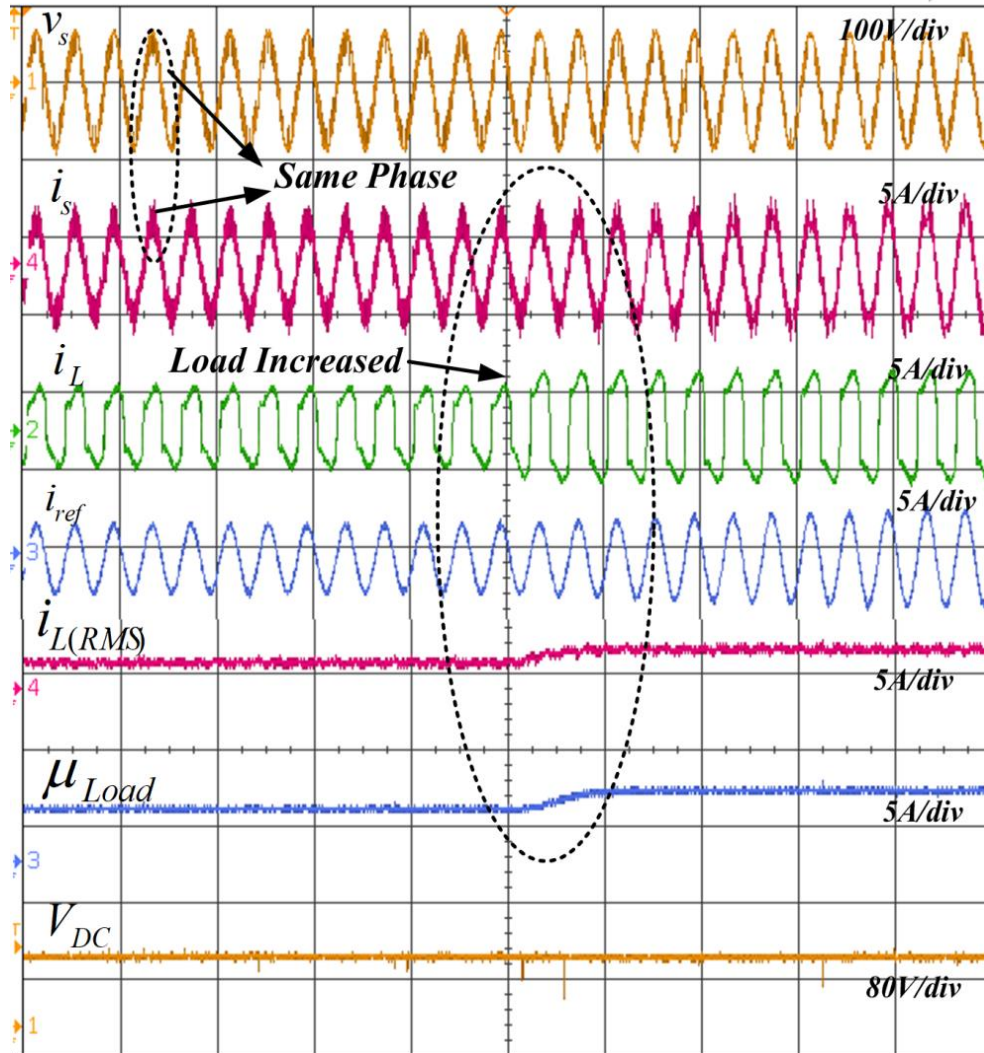


Fig.6.15 Dynamic response during load increase using LP controlled VSC showing $v_s, i_s, i_L, i_{ref}, i_{L(rms)}, \mu_{Load}, V_{DC}$

6.7.2. Operation in Normal condition with Integrated PV

Fig.6.16 depicts the steady-state performance of the proposed system integrated with PV. The single phase system operates in the MPPT mode. This set of results is obtained using the PV array simulator. Fig.6.16(a) depicts the waveform of (v_s, i_L) , and Fig.6.16(b)

depicts the power demand of the load is 75.9W Fig.6.16(c) depicts the waveforms of (v_s, i_s) and Fig.6.16(d) depicts the power delivered to the grid by PV is 317.6W. In this study, PV meets the load power demand and also simultaneously exports the net surplus power to the grid.

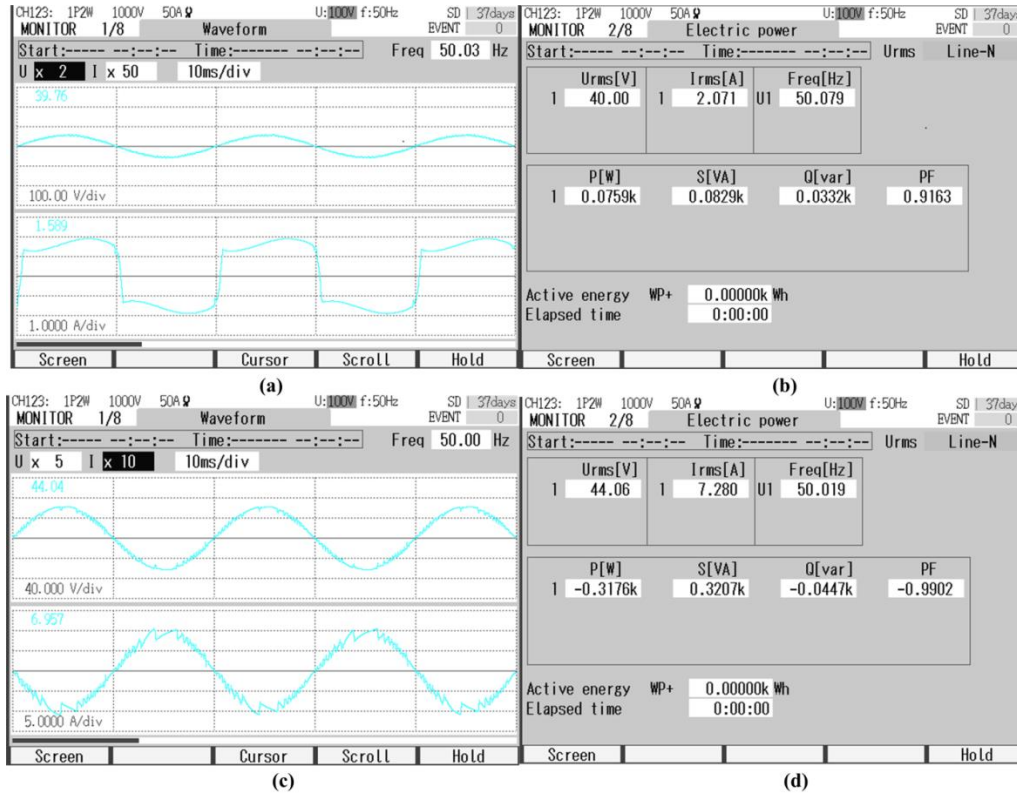


Fig.6.16 Waveforms showing (a) source voltage (v_s) and load current (i_L) (b) load power demand (P_L, Q_L) (c) Source Voltage (v_s) and grid current (i_s) (d) power supplied to the grid

Fig.6.17(a) shows the dynamic performance of proposed system with PV integrated at the DC link of the inverter. Fig.6.17(a) shows $v_s, i_s, i_L, i_{ref}, V_{DC}$ plots and clearly an out of phase relationship between the source voltage and source current is visible due to PV integration. It is observed that during the operation of PV integrated SAPF, PV supplies power to both load and grid. Fig.6.17(b) shows PV and IV curves of the system during PV integration and the maximum power is drawn from PV using MPPT at the provided DC link voltage. The operation is stable and irrespective of highly non-linear load

current, the grid current is sinusoidal and meets IEEE 1547 standard. Thus, PQ improvement is obtained with the designed controller.

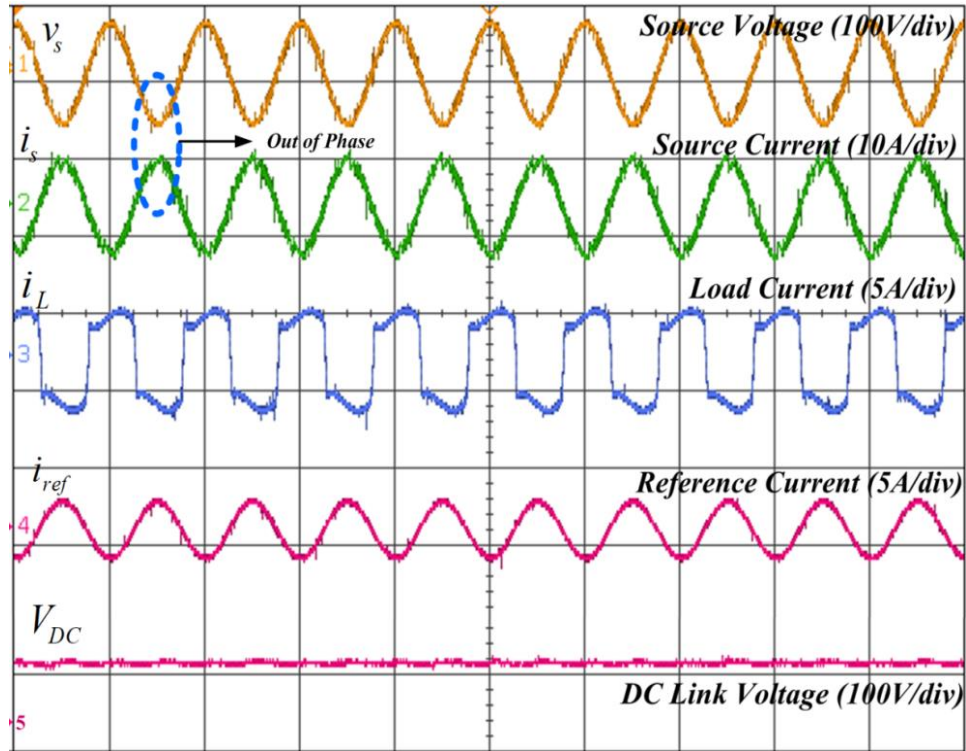


Fig.6.17(a) Response of LP controlled SAPF integrated with PV

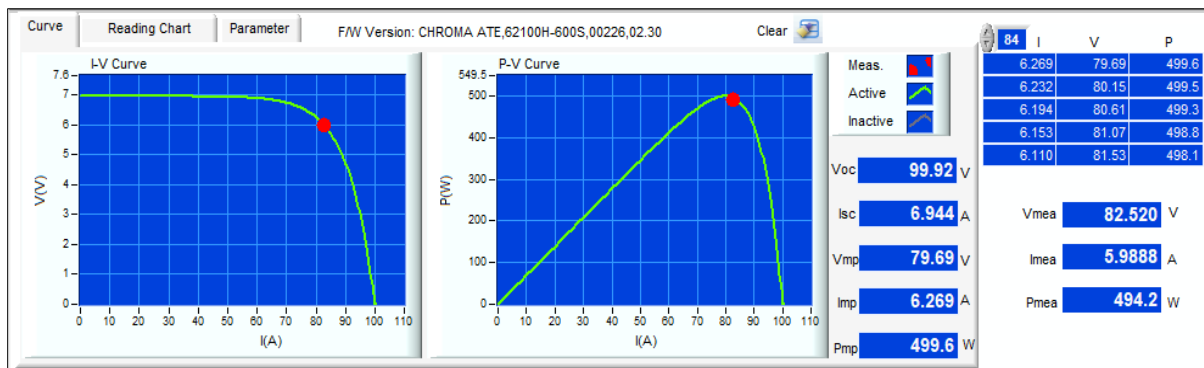
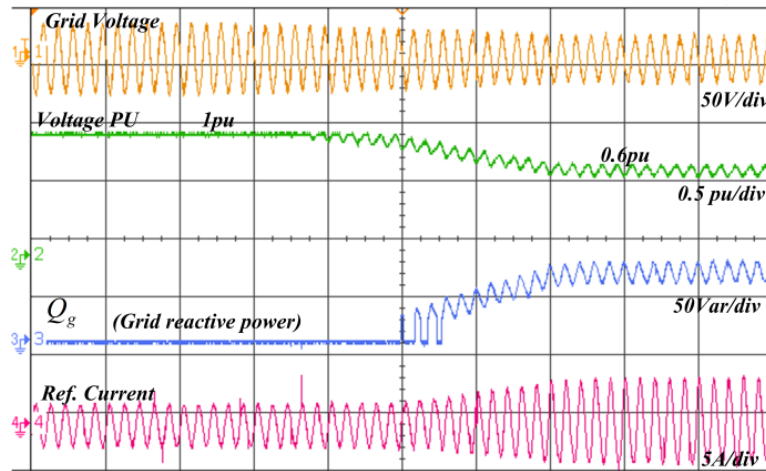


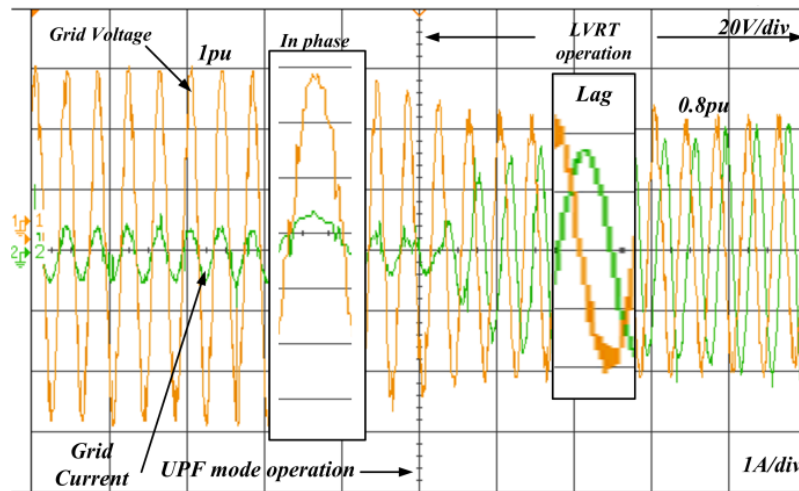
Fig.6.17(b) IV and PV curves for PV module indicating MPPT operation point in normal mode of operation

6.7.3. Operation Under Abnormal Grid Condition

Fig.6.18(a-b) show the performance of proposed system in LVRT mode. Fig.6.18(a) shows the grid voltage (v_g), voltage pu (v_{pu}), grid reactive power (Q_g) and reference current (i_{ref}). As voltage sag is detected by sag detector, the operation shifts from UPF mode of operation to LVRT mode of operation. Fig.6.18(a) and Fig.6.18(b) capture the transition period. In Fig.6.18(a), the voltage (input) is reduced from 1.0 to 0.6 pu and it can be observed that the reactive power demand has increased from an initial value of zero. Moreover, the reference current increases during LVRT period as an additional reactive current component needs to be injected as per grid code standards.



(a)



(b)

Fig.6.18 Response of LP controlled VSC in LVRT mode

Fig.6.18(b) shows the grid voltage (v_g) and grid current(i_g) for both the modes. In UPF mode of operation, both grid voltage and grid current are in same phase and in LVRT mode of operation the grid current start lagging behind grid voltage because the grid reactive demand increases during sag.

6.8. Conclusion:

This chapter discusses the operation and grid requirement of single phase system during LVRT mode of operation. The designs of proposed controllers adaptive LP and SWRDFT based controller are one of the primary accomplishments of this study. All controllers are able to track the fundamental component of load current faithfully. Under normal condition and voltage sag condition the simulation performance of LP, SWRDFT and SOGI controllers are discussed in detail. LP, SWRDFT and SOGI controllers have been designed to work effectively in normal and LVRT modes. Even under normal mode of operation, both daytime and nighttime operations have been depicted. The grid code standards have been referred to while designing the LVRT control operation. Based on the level of voltage sag, the reference reactive power and active power are computed, and accordingly fed to the grid during LVRT mode of operation. The transition from one mode to another is also depicted and shows the grid voltage and grid current relationship. The experimental performance of LP controller during normal and LVRT mode of operation is discussed in detail. The designed LP controller effectively meets the criteria of enhanced power quality in the form of reduced harmonic distortion in grid current and shows better performance as compared to other two controllers.

Chapter: 7 LVRT Operation in Three-Phase System

7.1 Introduction

Three-phase Low Voltage Ride-Through (LVRT) is the ability of a three-phase power generation system to continue operating and ride through voltage dips or grid disturbances without disconnecting the network. LVRT is especially significant for renewable energy sources including wind turbines and solar photovoltaic systems, which are gradually being incorporated into the power grid.

The power generated by renewable sources is supplied to the grid during normal operation, contributing to the overall power supply. However, voltage disruptions such as grid faults or rapid changes in load demand can occur on the grid. These disruptions can induce a drop in voltage, which can lead to power generation system instability or disconnection.

LVRT capacity plays an essential role in maintaining the stability of renewable energy systems during voltage drops. It allows the system to ride through the disruptions while remaining connected to the grid. Thus power generation system contributes to grid stability and reliability.

LVRT requirements and standards vary from one country to another and regions. In order to guarantee grid stability, grid regulations typically state the minimal LVRT capabilities that power generation systems must achieve. Three-phase power generation systems employ control algorithms and protection devices to accomplish LVRT. These solutions often include monitoring grid voltage and responding to voltage drops by altering system operational settings. To ride through a voltage disturbance, the control system may regulate power output and alter reactive power production.

This chapter focuses on the advanced control techniques used in three-phase grid-connected solar systems to provide reliable and stable operation under abnormal conditions such as voltage sag.

7.2. System Description of Three-Phase System:

This chapter deals with LVRT and UPF mode of operation for three phase grid connected PV system. The proposed system has the conventional three phase three leg topology of converter. It comprises a three phase full bridge inverter having six IGBT switches and

DC bus. A 2.7kW PV array is connected at the DC link. The VSC connected at PCC through interfacing inductor shown in Fig.7.1. This figure also displays the system setup for reactive power and harmonic current correction in an unbalanced and distorted three-phase, three-wire PV-connected distribution system. For simulation investigations, a three-phase programmable supply is utilized while a CHROMA make PV array simulator is utilized for experimental verification. A three-phase diode rectifier feeding resistive–inductive load represents a nonlinear load at the rectifier end. A shunt compensator is depicted in Fig.7.1 by a VSC that is coupled to the Common Coupling Point (PCC) via interface inductors. Using LEM sensors, the load and supply voltages and currents are measured for the hardware setup. The controller based on the Micro LAB box 1202 is utilized to generate the gating pulse logic required by the VSC.

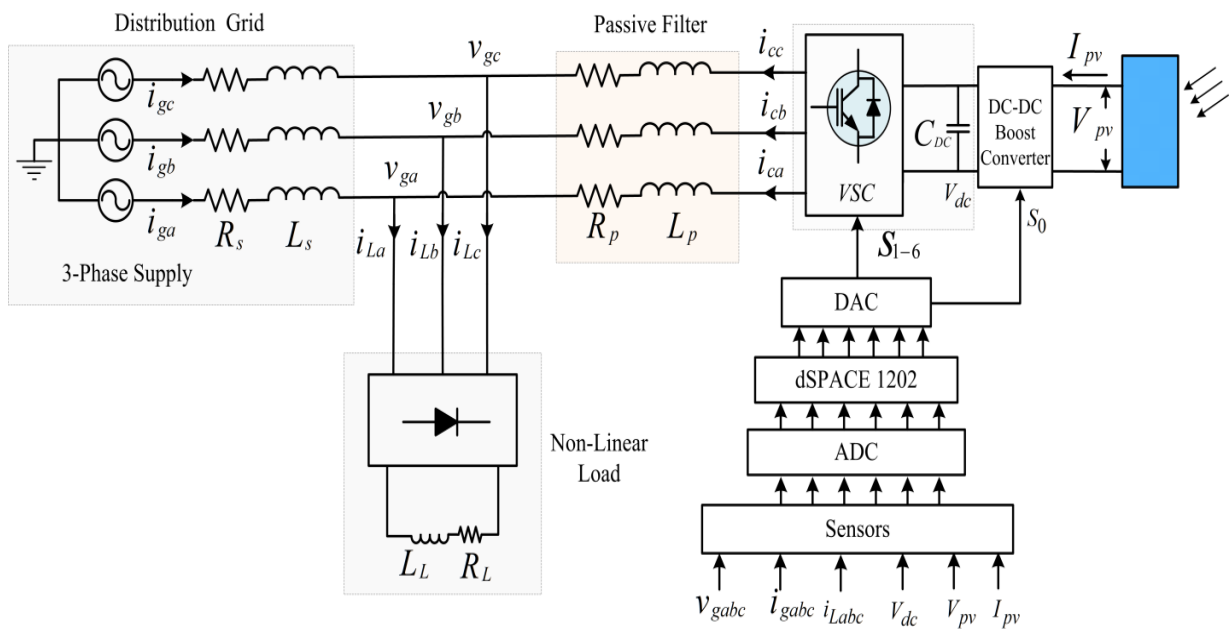


Fig.7.1 System Description of Three Phase System

7.3. Reference Current Generation Control Techniques

In this section, three different control strategies for extracting the required reference current have been presented and tested for operation in two modes, namely LVRT and UPF. The required reference currents for both modes of operation are made up of two parts: an active component for the UPF mode of operation and a reactive component for

the LVRT mode of operation. For three-phase VSC controlled as active filter under normal and LVRT conditions, three alternative control strategies are discussed below: Gegenbaur polynomial based controller, load power based controller and SOGI based controller. These controllers are designed and utilized to regulate a three-phase PV system connected to the grid.

7.3.1 Gegenbaur Polynomial based Controller:

Fig.7.2 shows the proposed Gegenbaur polynomial (GP) based controller which is made to control three-phase PV system to provide six switching pulses for three-phase VSC and simulation model of GP based controller. The required inputs for the control are source current ($i_{S(abc)}$), load current ($i_{L(abc)}$) DC-link voltage (V_{DC}), PV current (I_{PV}) and PV power (P_{PV}). Depending on the current state of the system, the controller takes action after sensing all the source and load parameters. An additional part of the control algorithm involves computing the requisite amount of active and reactive power into the grid based on the presence/absence of voltage sag.

Gegenbaur polynomial (GP) was proposed by Leopold Gegenbaur [185]. This GP polynomial shows orthogonal properties in interval [-1 to1]. The GP's $G_n^{(\sigma)}(x)$ is a generalized case of Legendre polynomial [186] and Chebyshev polynomials [187]. The proposed GPs $G_n^{(\sigma)}(x)$ are solutions of Gegenbauer differential equation for integer values of 'n'

$$(1 - x^2) \frac{d^2y}{dx^2} - (2\sigma + 1)x \frac{dy}{dx} + n(n + 2\sigma)y = 0 \quad (7.1)$$

where n is integer and σ is a constant, for $\sigma = 1/2$ the above equation reduces to Legendre and for $\sigma = 1$, the same equation reduces to Chebyshev differential equation. By using series solution method, the solution of Gegenbauer differential equation is obtained and the GPs $G_n^{(\sigma)}(x)$ are

$$G_0^\sigma(x) = 1 \quad (7.2)$$

$$G_1^\sigma(x) = 2\sigma x \quad (7.3)$$

$$G_2^\sigma(x) = \sigma[2x^2(1 + \sigma) - 1] \quad (7.4)$$

Thus the recursive relation of GPs is

$$G_n^\sigma(x) = \frac{1}{n} [2x(n + \sigma - 1)G_{n-1}^\sigma(x) - (n + 2\sigma - 2)G_{n-2}^\sigma(x)] \quad (7.5)$$

The fundamental current of a load is estimated in this study using the approximation function $G_n^\sigma(x)$, which is applicable to any function. In an ANN network, this polynomial function may simply replace the hidden layer. This means that GP-based algorithms can be designed to be faster and less resource-intensive than those based on multi-layer perceptron networks.

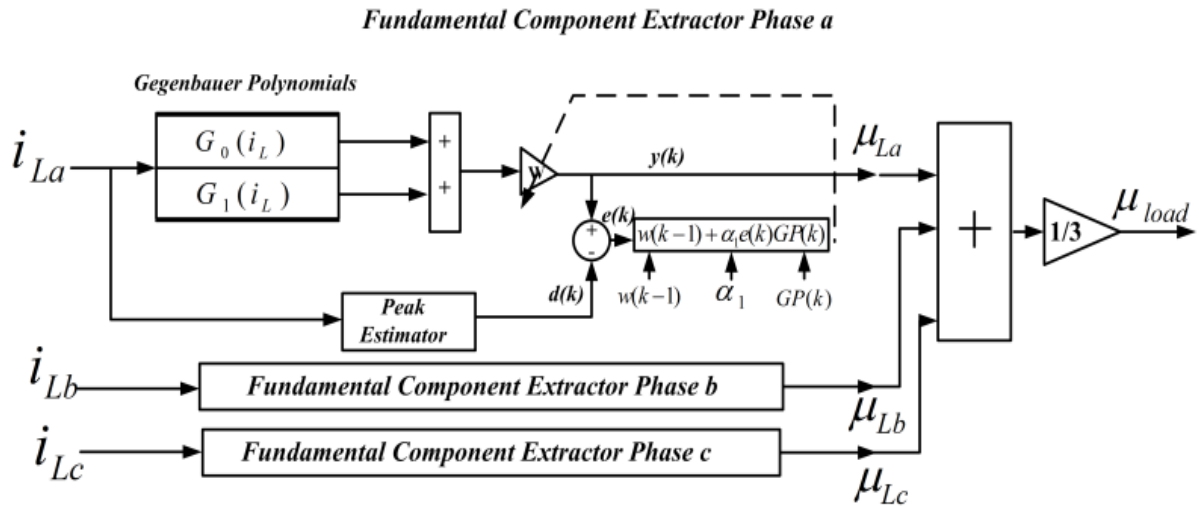


Fig.7.2(a) Proposed GP polynomial based adaptive control system

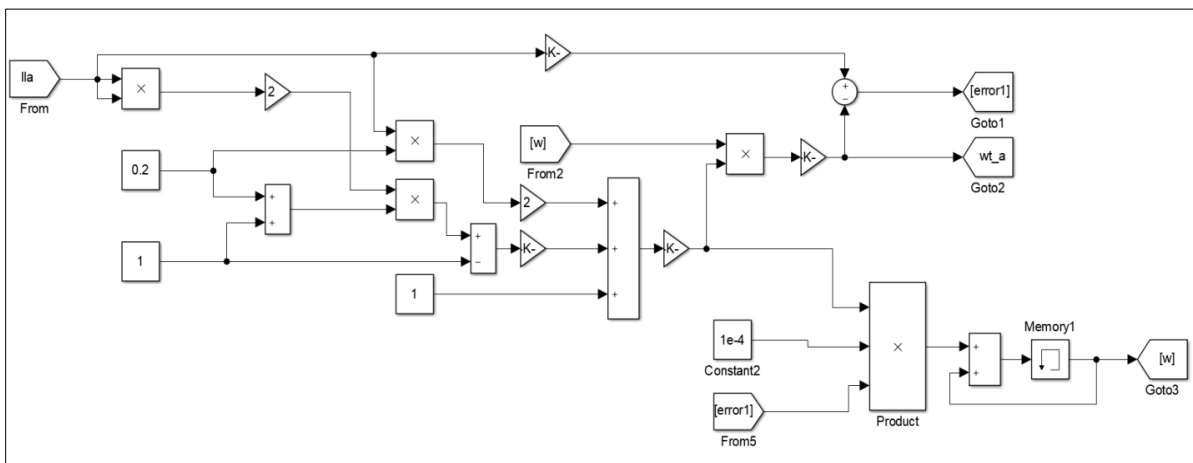


Fig.7.2(b) Simulation model of GP polynomial based adaptive controller

It can be observed in Fig.7.2, a new controller implementation is based on adaptive Gegenbauer polynomials. The input is the three-phase load currents (i_{Labc}), and the output is the extracted fundamental weight of the load (μ_{load}). The Least Mean Square (LMS) method is used to train this network remotely. The basic component of load

current may be obtained by training with just one parameter weight (w). This network's output is put to use in the order to enhance PQ of the three-phase system.

The formula for weight updation of the given GP based controller using the LMS training approach is

$$w(k) = w(k - 1) + \alpha_1 e(k) G_n^\sigma(k) \sin\theta \quad (7.6)$$

where α is the learning rate, $w(k)$ is the updated fundamental weight of respective phase and $\sin\theta$ is the in-phase component of the respective phase. Now μ_{La} for phase-a

$$\mu_{La} = w_a(k) [\sum_{k=0}^n G_k(i_{La})] \quad (7.7)$$

where $w_a(k)$ is weight of phase-a trained by LMS. Similarly for phase-b and phase-c

$$\mu_{Lb} = w_b(k) [\sum_{k=0}^n G_k(i_{Lb})] \quad (7.8)$$

$$\mu_{Lc} = w_c(k) [\sum_{k=0}^n G_k(i_{Lc})] \quad (7.9)$$

where $w_b(k)$ and $w_c(k)$ are the respective weights of phase-‘b’ and phase- ‘c’ trained by LMS and μ_{Lb} and μ_{Lc} are fundamental weights extracted for phase-b and phase-c.

7.3.2. Load Power based Adaptive Controller:

Load power control algorithm is developed based on the calculation of load current, compute the fundamental load requirement and train the load fundamental with LMS technique and this control algorithm is designed to operate in LVRT and UPF mode of operation. Fig.7.3 (a) shows the load power requirements of the three phase system.

For phase-a load power can be written as,

$$P_{La} = v_a \times i_{La} \quad (7.10)$$

Similarly for phase-b and for phase-c

$$P_{Lb} = v_b \times i_{Lb} \quad (7.11)$$

$$P_{Lc} = v_c \times i_{Lc} \quad (7.12)$$

Now from Eq. (7.10), (7.11) and (7.12) the total load power is

$$P_T = v_a \times i_{La} + v_b \times i_{Lb} + v_c \times i_{Lc} \quad (7.13)$$

Now for fundamental component of the load current

$$I_{FL} = \frac{P_T}{v_t} \quad (7.14)$$

where v_t equivalent voltage of three phase system is can be written as

$$V_t = \frac{2}{3} \sqrt{v_a^2 + v_b^2 + v_c^2} \quad (7.15)$$

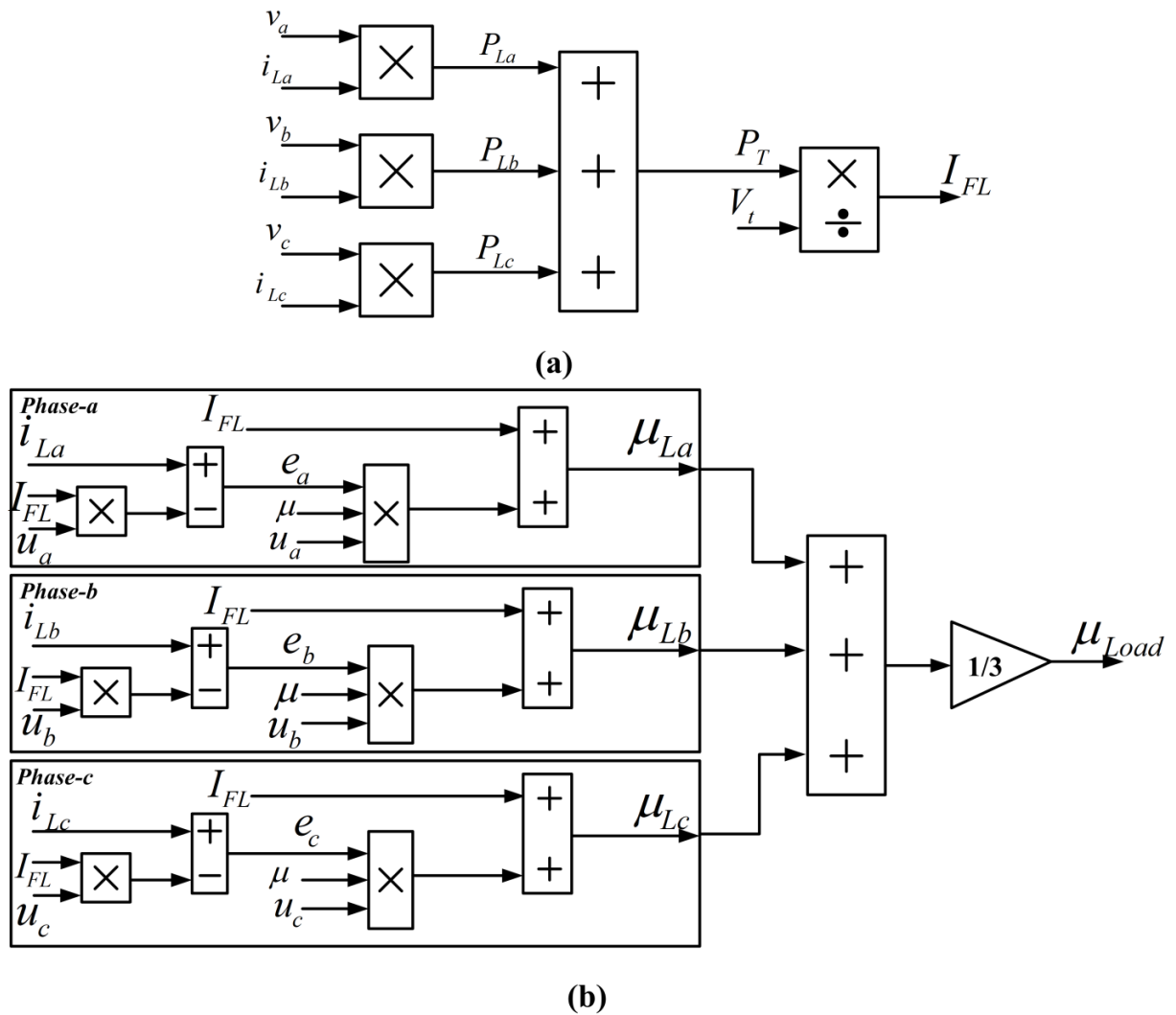


Fig.7.3 Proposed load power based controller

Now the weight extraction from load power based control technique is trained by LMS algorithm, the updated fundamental weight for phase-a, phase-b and phase-c load current shown in Fig.7.3(b) can be written as

For phase-a

$$\mu_{La} = I_{FL}(n) = I_{FL}(n-1) + e_{La} \times \rho \times u_a \quad (7.16)$$

where ρ is step size, e_{La} is error function of phase-a and μ_{La} is active load power requirement of phase-a

$$e_{La} = i_{La} - I_{FL} \times u_a \quad (7.17)$$

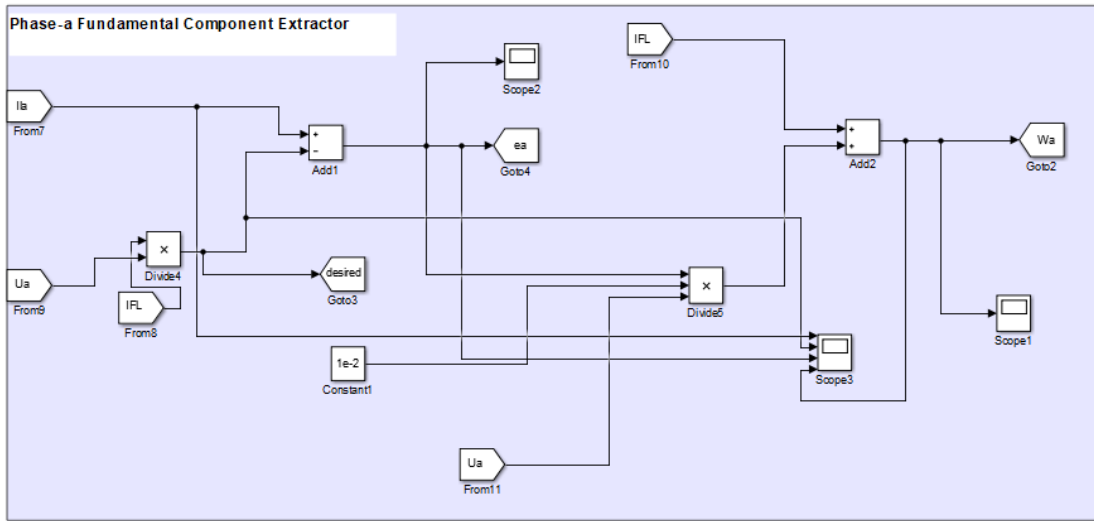
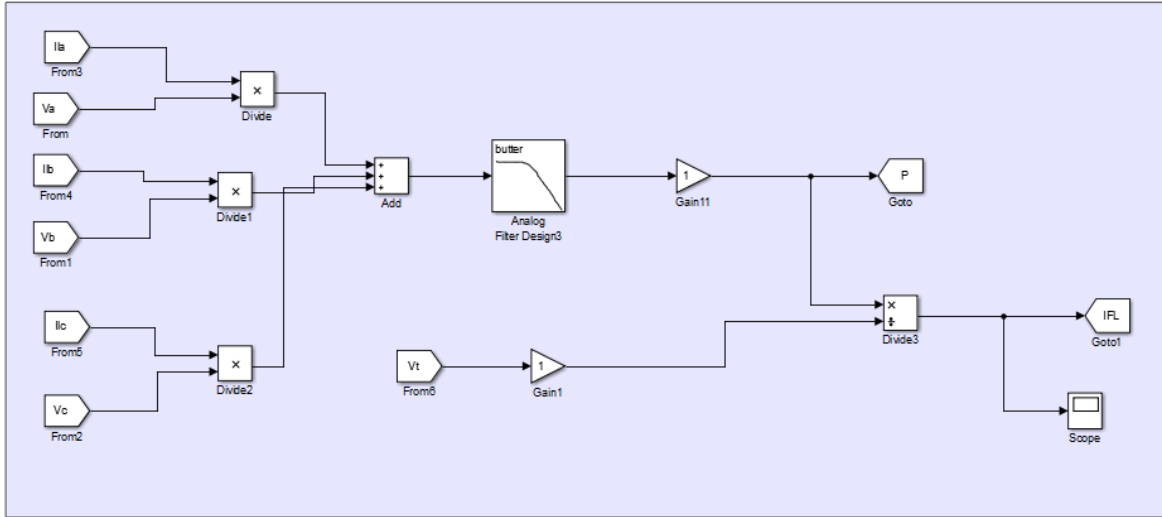


Fig.7.4 Matlab model of Load power based controller

where u_a is unit template of phase-a

$$u_a = \frac{v_a}{v_t} \quad (7.18)$$

where v_a is phase-a voltage. Similarly for phase-b

$$\mu_{Lb} = I_{FL}(n) = I_{FL}(n-1) + e_{Lb} \times \rho \times u_b \quad (7.19)$$

$$e_{Lb} = i_{Lb} - I_{FL} \times u_b \quad (7.20)$$

$$u_b = \frac{v_b}{v_t} \quad (7.21)$$

For phase-c

$$\mu_{Lc} = I_{FL}(n) = I_{FL}(n-1) + e_{Lc} \times \rho \times u_c \quad (7.22)$$

$$e_{Lc} = i_{Lc} - I_{FL} \times u_c \quad (7.23)$$

$$u_c = \frac{v_c}{v_t} \quad (7.24)$$

where μ_{Lb} and μ_{Lc} are the fundamental weights extracted by phase-‘b’ and phase-‘c’.

7.3.3 SOGI based Controller:

It is a second order generalized integrator which acts like BPF and LPF. The block diagram of SOGI is shown in Fig.7.5(a) and Fig.7.5(b) shows simulation model of SOGI based controller. SOGI controller produces two orthogonal outputs namely direct axis and quadrature axis at same frequency ω_o and having same amplitude. The direct axis output ($i_{La\alpha}$) is in phase with input and quadrature axis output ($i_{La\beta}$) lags input by 90° . The transfer function shown in Eq.(7.25) and Eq.(7.26) acts like BPF and LPF respectively and gain (K) of SOGI filter decides the bandwidth of filter. The fixed gain SOGI controller is works best under narrow range of operating conditions. Moreover, once tuned it is not possible to vary these gains.

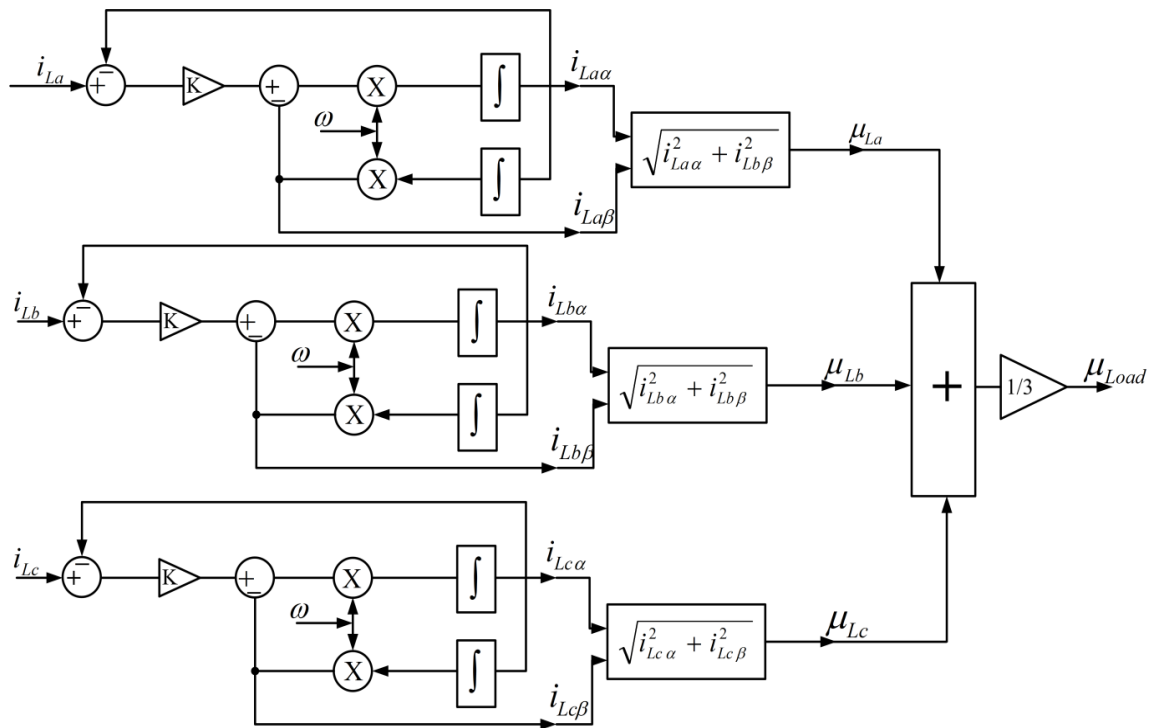


Fig.7.5(a) Design of SOGI based controller for three phase system

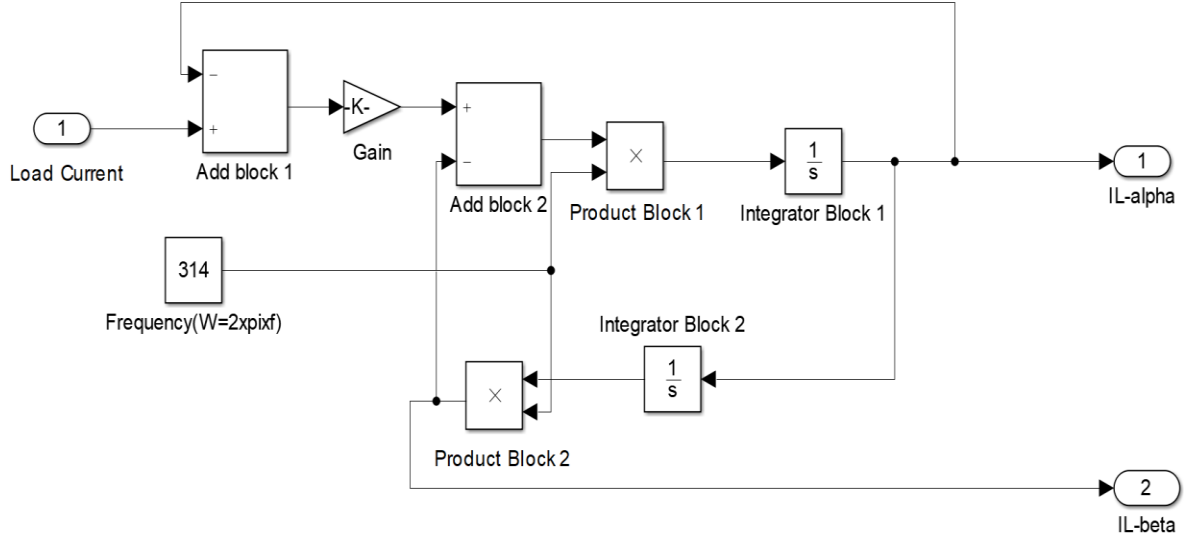


Fig.7.5(b) Simulation model of SOGI based controller

$$\frac{I_{L\alpha}}{i_L} = \frac{K\omega_o S}{S^2 + K\omega_o S + \omega_o^2} \quad (7.25)$$

$$\frac{i_{L\beta}}{i_L} = \frac{K\omega_o^2}{S^2 + K\omega_o S + \omega_o^2} \quad (7.26)$$

The fundamental component of load current of phase a (μ_{La}) is estimated by using SOGI.

$$\mu_{La} = \sqrt{i_{L\alpha a}^2 + i_{L\beta a}^2} \quad (7.27)$$

where $i_{L\alpha a}$ is phase a in phase component, $i_{L\beta a}$ is phase a quadrature axis output which lags input by 90° . Similarly, for phase b fundamental component of load current

$$\mu_{Lb} = \sqrt{i_{L\alpha b}^2 + i_{L\beta b}^2} \quad (7.28)$$

where μ_{Lb} is fundamental weight of load current for phase b. For phase c fundamental component of load current

$$\mu_{Lc} = \sqrt{i_{L\alpha c}^2 + i_{L\beta c}^2} \quad (7.29)$$

where μ_{Lc} is fundamental weight of load current for phase c.

7.3.4 Switching Loss Component Extraction:

The switching loss in VSC is considered based on the output of the PI controller and the DC link voltage regulation. The proper operation of shunt compensator depends on the monitoring and regulation of the DC link voltage (V_{DC}). The active power switching loss of the power electronics converter is taken as the PI controller's output in Fig.7.6 and can be represented as

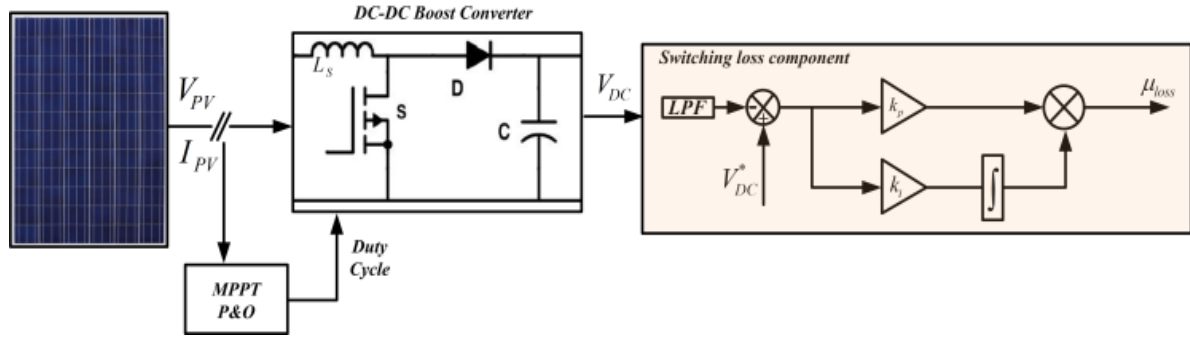


Fig.7.6 Switching loss component

$$\mu_{loss} = k_p e_{DC} + k_i \int e_{DC} dt \quad (7.30)$$

where k_i and k_p are integral and proportional gains of PI controller respectively and e_{DC} is the error in dc link voltage which can be written as follows:

$$e_{DC} = V_{DCref} - V_{DC} \quad (7.31)$$

where V_{DCref} is the DC link reference voltage.

7.3.5. Operation during Voltage Sag:

As shown in Fig. 7.7, the newly built controller provides more ability to operate in the LVRT mode based on the current grid situation. The magnitude of sag is initially established by computing the grid voltage per unit.

$$V_t = \frac{2}{3} \sqrt{v_a^2 + v_b^2 + v_c^2} \quad (7.32)$$

$$V_{pu} = \frac{v_t}{base\ value} \quad (7.33)$$

The reference power components for active power and reactive power in both normal and LVRT conditions are then calculated using the grid code standards in Eq.(7.34)

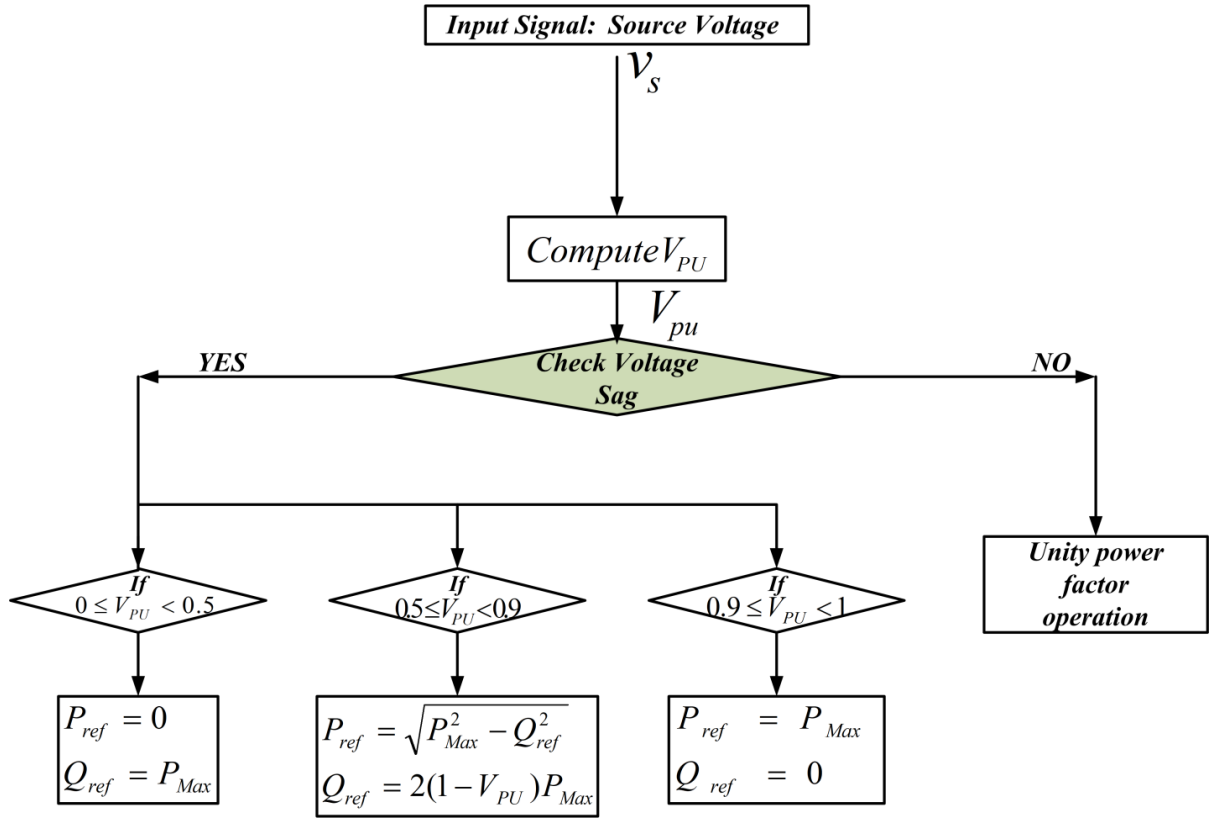


Fig.7.7 Flowchart for control action under voltage sag conditions

$$\left\{ \begin{array}{l} 0 \leq V_{PU} < 0.5 \\ 0.5 \leq V_{PU} < 0.9 \\ 0.9 \leq V_{PU} < 1 \end{array} \right. \left\{ \begin{array}{l} P_{ref} = 0 \\ Q_{ref} = P_{ref} \\ P_{ref} = \sqrt{P_{MPP}^2 - Q_{ref}^2} \\ Q_{ref} = 2(1 - V_{PU})P_{MPP} \\ P_{ref} = P_{MPP} \\ Q_{ref} = 0 \end{array} \right. \quad (7.34)$$

7.3.6. Reference Current Generation:

The active component and reactive component are used to generate the reference currents which are discussed below.

7.3.6.1. Active Power Component:

Normal mode of operation is controlled by the active power component of the system. In this case, the system work is controlled to unity power factor (UPF) mode when the pu

voltage is close to unity. Grid current and supply voltage are in phase with one another after compensation. The load current fundamental (μ_{load}), switching loss component (μ_{loss}), and PV feed forward component (μ_{PV}), the active power component of the load determined. Using the GP function, Load power based controller and SOGI based controller, the fundamental of load current is calculated as illustrated in Fig.7.2, Fig.7.3 and Fig.7.5 respectively

$$\mu_{load} = \frac{1}{3}[\mu_{La} + \mu_{Lb} + \mu_{Lc}] \quad (7.35)$$

where μ_{La} , μ_{Lb} and μ_{Lc} are load current fundamental weight components for phase-a, phase-b and phase-c respectively.

Also, to include the contribution of solar PV, the feed-forward term is calculated based on the sag in the system shown in Fig.7.5.

$$\mu_{PV} = \frac{2P_{ref}}{3v_t} \quad (7.36)$$

where P_{ref} denotes the active power of solar PV array.

Now, from Eq.(7.30), Eq.(7.35) and Eq.(7.36)

$$\mu_p = \mu_{load} + \mu_{loss} - \mu_{PV} \quad (7.37)$$

The required active fundamental reference currents (i_{pabc}) are computed as:

$$i_{pabc} = \mu_p \times u_{d(abc)} \quad (7.38)$$

where $u_{d(abc)}$ represent the three in-phase voltage templates of three phase system.

7.3.5.2 Reactive Power Component

The system is regulated to operate in LVRT mode in the event of voltage sag in the system. This mode is distinct from the default operating mode and has been added in accordance with grid code specifications. The grid reference currents are calculated during LVRT mode of operation based on reactive power injection, as illustrated in Fig.7.7. Voltage sag calculation is the first step, and thereafter from Eq.(7.34) the appropriate reference power (Q_{ref}) to be injected is determined. The reference three-phase currents are calculated after the reference powers have been calculated based on the degree of voltage sag.

$$i_q = \left(\frac{2 \times Q_{ref}}{3v_t} \right) \times u_q \quad (7.39)$$

The three-phase grid reference currents are calculated as

$$i_{ref} = i_p + i_q \quad (7.40)$$

According to Fig.7.8, the hysteresis current controller (HCC) block creates six pulses by comparing the measured source current (i_s) with the reference current (i_{ref}).

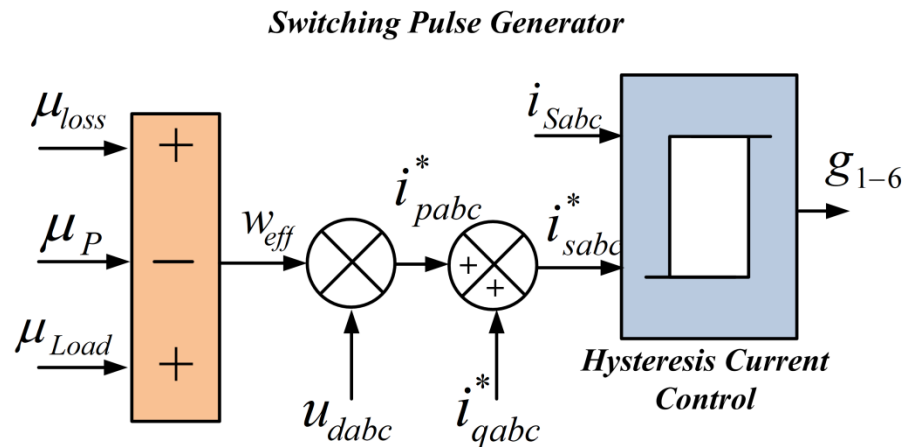


Fig.7.8 Layout of reference current and gating pulse generation

7.4. Simulation Result and Discussion:

This section covers the simulation performance of the Gegenbuer polynomial based controller, Load power based control technique and SOGI based control approaches for three-phase grid-connected and PV-integrated power distribution system in the presence of normal and abnormal grid conditions. The system's performance is analyzed in several ways: before the sag, during the sag, and after the sag. Simulink / MATLAB software is used to simulate the system and analyze its operation under various situations. The design value of the proposed system's parameters for simulation studies are mentioned in Appendix.

7.4.1 Simulation Performance with GP Controller:

Fig.7.9 shows simulation performance of proposed GP function trained by LMS. Fig.7.9(a) shows intermediate performance of proposed GP controller. Fig7.9(a) shows load current of phase-a (i_{La}), desired fundamental weight, output fundamental weight and error of phase-a. The proposed GP controller output is trained by LMS algorithm, in

Fig.7.9(a) it is observed that the output weight is tracking the fundamental component of load current. The error is almost close to zero except during the disturbance. the load changes the intermediate performance of the proposed system is tracking the desired condition.

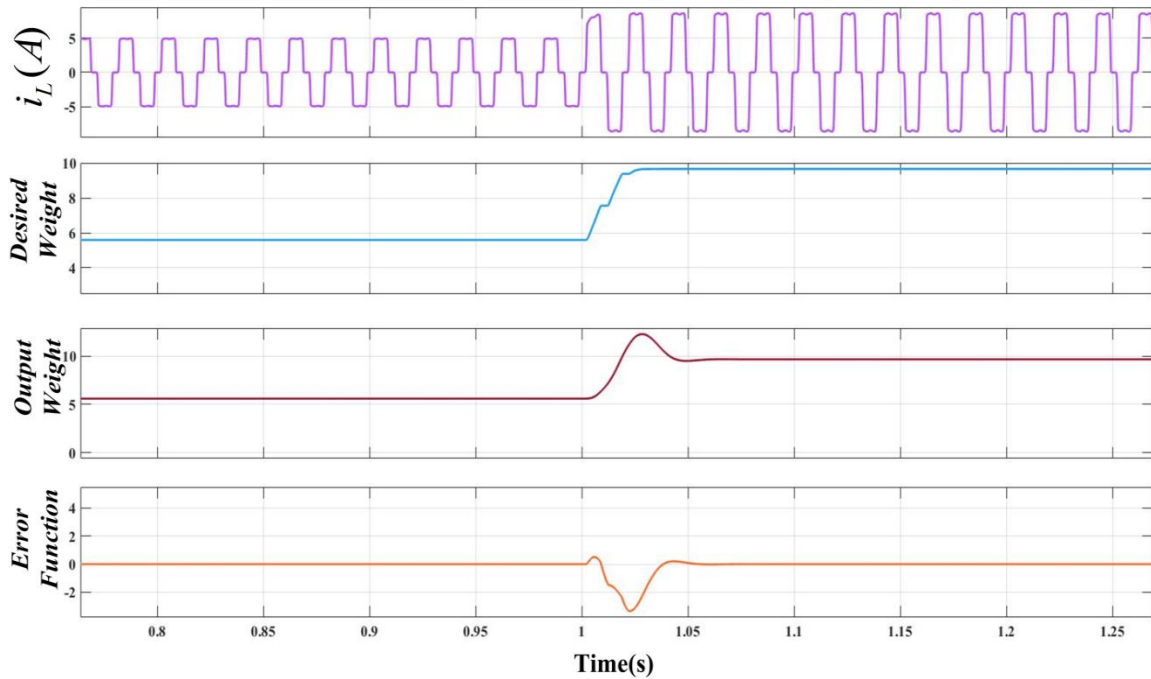


Fig.7.9(a) Intermediate performance of GP controller

Fig.7.9(b) shows simulation performance of GP control algorithm during the variation from day time to night time and non-linear load variation for three phase grid connected PV system of 2.7kW. Fig.7.9(b) shows the plots for supply voltage (v_{Sabc}), supply currents (i_{sabc}), load currents (i_{Labc}), compensator currents (i_{Cabc}), DC link voltage (V_{dc}) and irradiance (I_{rr} (W/m^2)). At starting time day mode is present and the irradiance is considered as $1000W/m^2$. At $t=1.0s$ load is increased. At $t=1.3s$ night time is simulated and irradiance level is decreased to $0W/m^2$ and PV output power becomes zero during this period. As a result, the source voltage and current are out of phase when the grid is operating during the day. Similarly, when the grid is operating at night, when PV power is zero and the load is provided by the source, the source voltage and current are in phase.

The supply current maintains sinusoidal behavior throughout load change and irradiance change, even in the presence of distorted load currents.

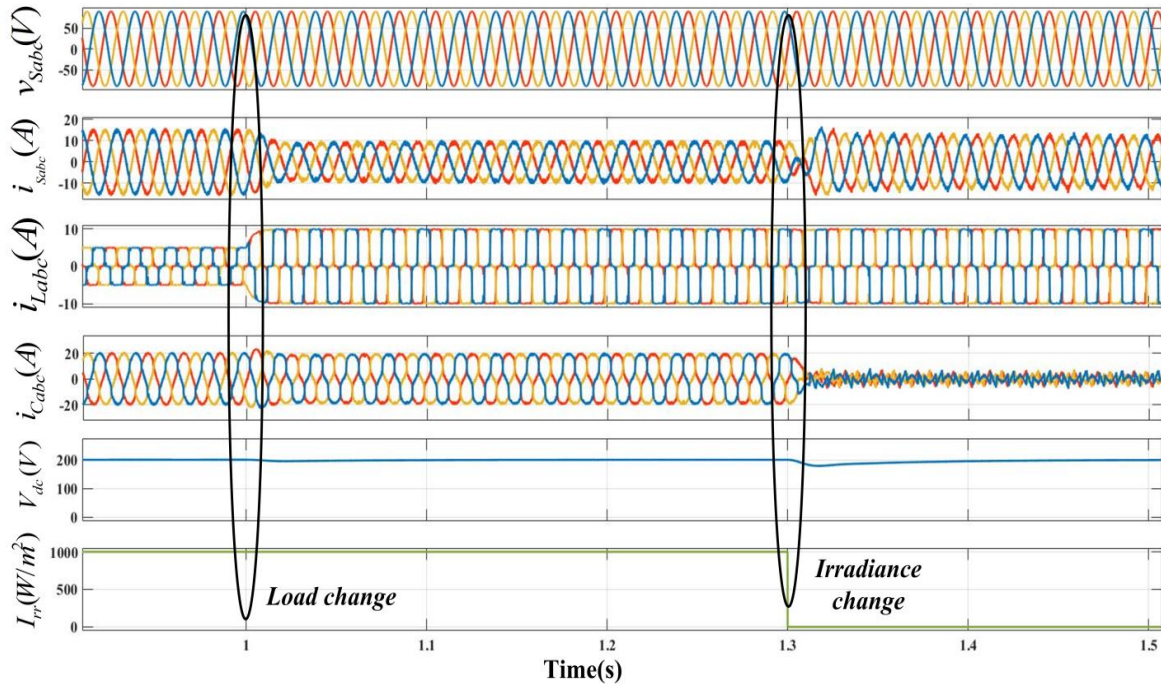


Fig.7.9(b) Simulation performance of GP controller under UPF mode

Fig.7.9(c) shows the performance of the system during a transient between UPF mode to LVRT mode and back again to UPF mode of operation. Fig.7.9(c) shows the source voltage (v_{Sabc}), source currents (i_{Sabc}), inverter active power ($P_{inv}(W)$) and inverter reactive power ($Q_{inv}(Var)$). The proposed system is integrated with 2.7kW PV array. Fig.7.9(c) demonstrates that before sag grid current is out of phase with grid voltage, which shows PV power is feeding to the grid, when a sag of 0.55pu is introduced at $t=0.6s$, the system responds by changing its active and reactive power shown in Fig.7.9(c). The active power supplied by VSC of the system is lowered by 200W, but the VSC reactive power is raised by 700var. At $t=2.5s$ sag is cleared and it is observed that the system transitions from faulty to normal mode smoothly during the pre-sag, sag and post sag conditions as illustrated in Fig.7.9(c).

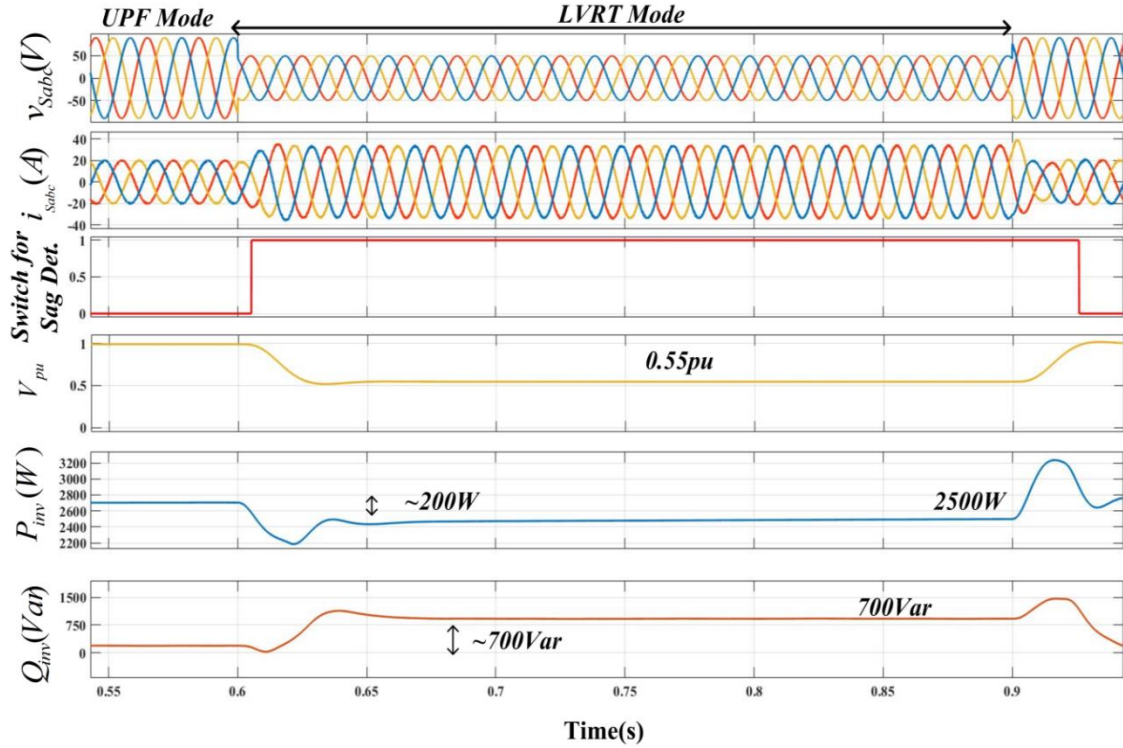


Fig.7.9(c) Simulation performance of GP controller during LVRT mode

7.4.2 Simulation Performance of Load Power based Controller:

Fig.7.10 shows simulation performance of proposed load power based function trained by LMS. Fig.7.10(a) shows intermediate performance of proposed load power based controller. Fig.7.10(a) shows load current of phase-a (i_{La}), desired load current of phase-a, error of phase-a and fundamental weight of phase-a. The proposed load power based controller output is trained by LMS algorithm, as per Fig.7.10(a) as the load changes the intermediate performance of the proposed system is tracking and the fundamental weight also increases.

Fig.7.10(b) shows simulation performance of load power based control algorithm during the variation from day time to night time and non-linear load variation for three phase grid connected PV system of 2.7kW. Fig.7.10(b) shows the plots for supply voltage(v_{Sabc}), supply currents (i_{Sabc}), load currents (i_{Labc}), compensator currents (i_{Cabc}), DC link voltage (v_{dc}) and irradiance(I_{rr} (W/m^2)). At starting time day mode is present, the irradiance is $1000W/m^2$. At $t=1.0s$ load is increased of the system. At $t=1.3s$ night time started and irradiance level decreased till $0W/m^2$ and PV output power become

zero during this period. As a result, the source voltage and current are out of phase during the day. However, at night, PV power is zero and the load is supplied by the source, the source voltage and current are in phase. To satisfy the increased load need, the supply current increases. Even in the case of distorted load currents, the supply current retains sinusoidal behavior during load and irradiance changes.

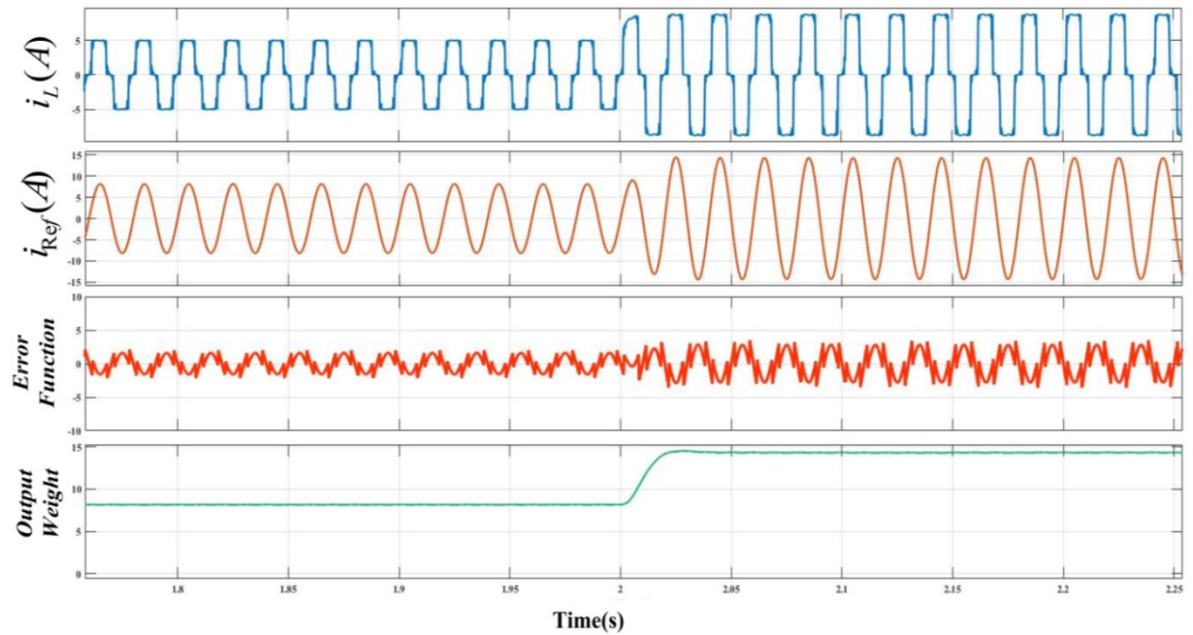


Fig.7.10(a) Intermediate performance of Load Power based controller

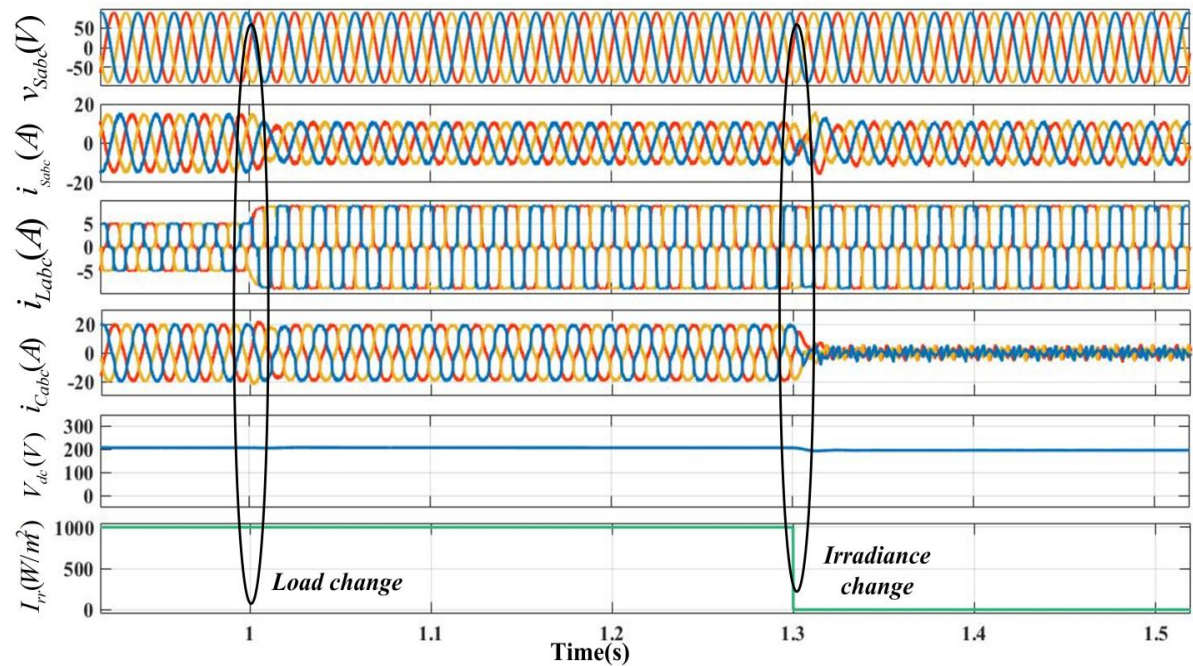


Fig.7.10(b) Simulation performance of Load Power based controller under UPF mode

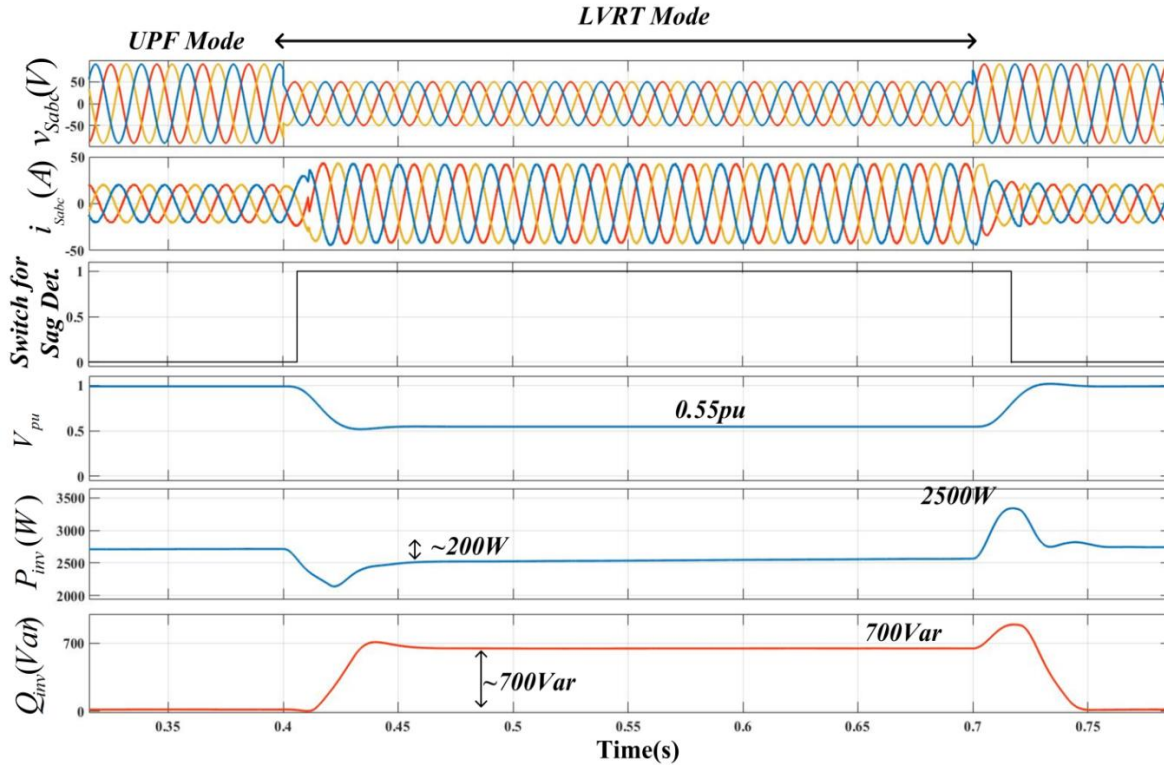


Fig.7.10(c) Active power and reactive power demand during LVRT mode

Fig.7.10(c) shows the performance of the system during a transition between UPF mode to LVRT mode and back again to UPF mode of operation. Fig.7.10(c) shows the source voltage (v_{Sabc}), source currents (i_{Sabc}), inverter active power ($P_{inv}(W)$) and inverter reactive power ($Q_{inv}(Var)$). The proposed system is integrated with 2.7kW PV power. Fig.7.10(c) demonstrates that before sag system works in UPF mode of operation in which grid current is out of phase with grid voltage, which shows PV power is feeding to the grid, when a sag of 0.55pu is introduced at $t=0.4s$, the VSC responds by changing its active and reactive power shown in Fig.7.10(c). The active power of the system is lowered by 200W, but the reactive power is raised by 700var. Similarly, at $t=0.7s$ sag is cleared and it has been observed that the system transitions from faulty to normal mode smoothly during the pre-sag, sag and post sag conditions as illustrated in Fig.7.10(c).

7.4.3 Simulation Performance of SOGI based Controller:

Fig.7.11 shows simulation performance of SOGI based controller. Fig.7.11(a) shows intermediate performance of SOGI based controller, which shows load current (i_L), in-

phase part of SOGI ($i_{L\alpha}$) from Eq.(7.25), quadrature phase part of SOGI ($i_{L\beta}$) from Eq.(7.26) and fundamental weight of load current from Eq.(7.27), Eq.(7.28) and Eq.(7.29) of their respective phases. Fig.7.11(a) shows as the load changes, the fundamental weight also increases.

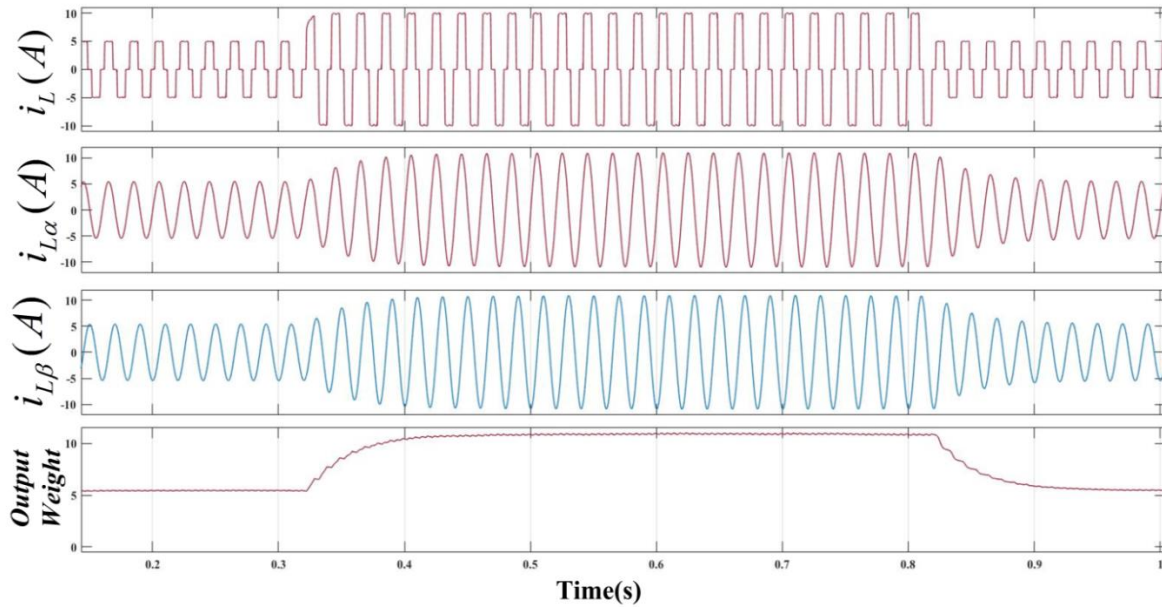


Fig.7.11(a) Intermediate performance of SOGI based controller

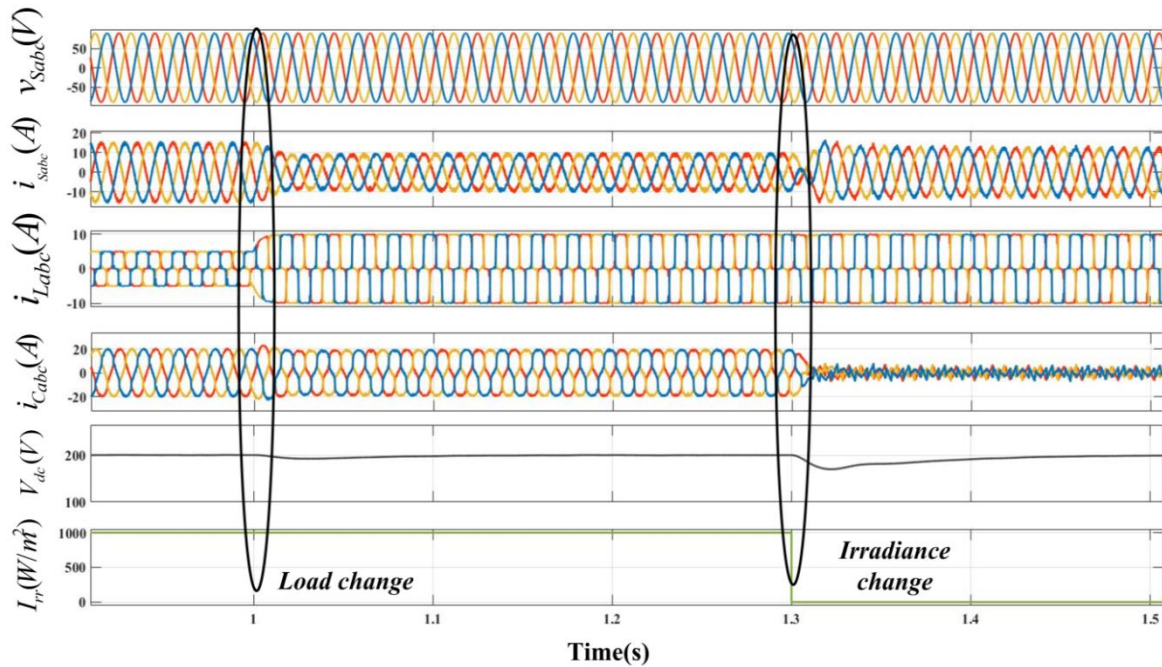


Fig.7.11(b) Simulation performance of SOGI based controller under UPF mode

Fig.7.11(b) shows simulation performance of SOGI based control algorithm during the variation from day time to night time and non-linear load variation for three phase grid connected PV system of 2.7kW. Fig.7.11(b) shows the plots for supply voltage (V_{Sabc}), supply currents (i_{Sabc}), load currents (i_{Labc}), compensator currents (i_{Cabc}), DC link voltage (V_{dc}) and irradiance (I_{rr} (W/m^2)). At starting time day mode is present, the irradiance is $1000W/m^2$. At $t=1.0s$ load is increased. At $t=1.3s$ night time simulated and irradiance level decreased till $0W/m^2$ and PV output power become zero during this period. As a result, the source voltage and current are out of phase when the grid is operating during the day. At night, when PV power is zero and the load is supplied by the source, the source voltage and current are in phase. To satisfy the increased load need, the supply current increases. Even in the case of distorted load currents, the supply current retains sinusoidal behavior during load and irradiance changes.

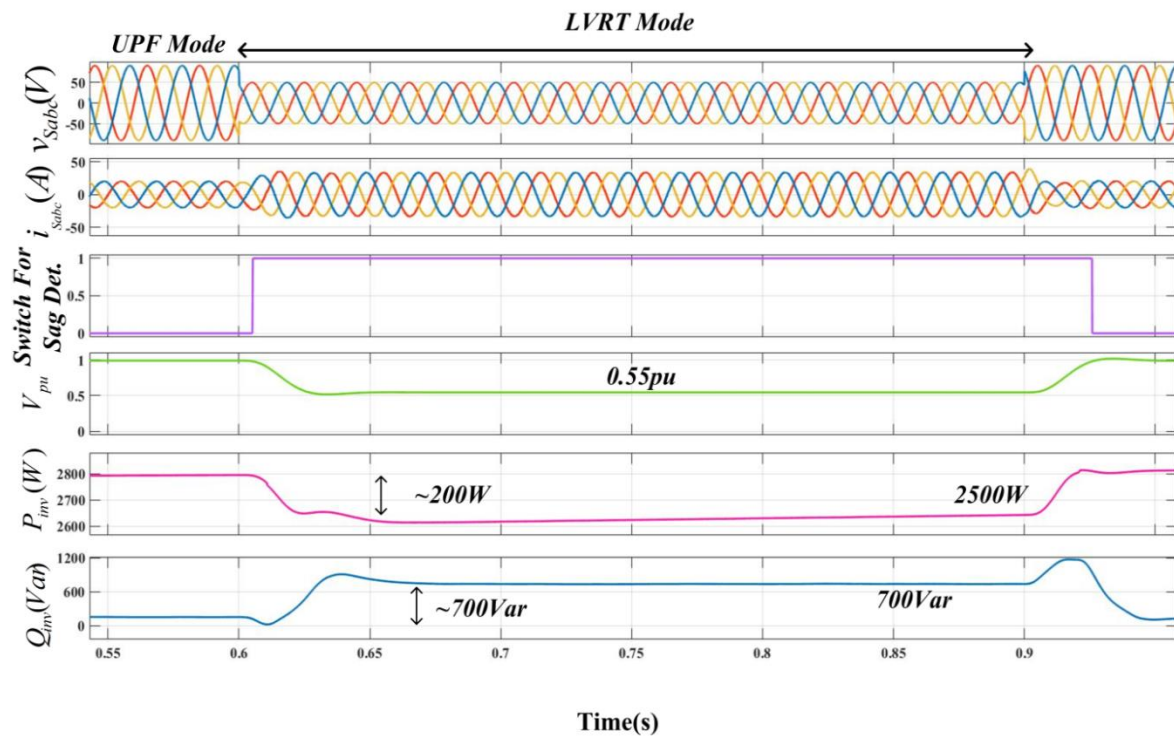


Fig.7.11(c) Active power and reactive power demand during LVRT mode

Fig.7.11(c) shows the performance of the system during a transient between UPF mode to LVRT mode and back again to UPF mode of operation. Fig.7.11(c) shows the source voltage (v_{Sabc}), source currents (i_{Sabc}), inverter active power ($P_{inv}(W)$) and inverter

reactive power ($Q_{inv}(Var)$). The proposed system is integrated with 2.7kW PV power. Fig.7.11(c) demonstrates that before sag system works in UPF mode of operation in which grid current is out of phase with grid voltage, which shows PV power is feeding to the grid, when a sag of 0.55pu is introduced at $t=0.4s$, the VSC responds by changing its active and reactive power shown in Fig.7.11(c). The active power of the system is lowered by 200W, but the reactive power is raised by 700var. Similarly, at $t=0.7s$ sag is cleared and it has been observed that the system transitions from faulty to normal mode smoothly during the pre-sag, sag and post sag conditions as illustrated in Fig.7.11(c).

7.4.4 Comparison of Proposed GP and Load power based Control Technique-

These proposed controllers based on GP, load power and SOGI based controller are used to extract the fundamental component of load current and use it for control algorithm design. As a result, the proposed GP, load power and SOGI based controller performances and responsiveness are compared, as shown in Fig.7.12. The fundamental weights obtained from load current (i_L) utilizing the GP based controller, load power based controller and SOGI based controller are shown in Fig.7.12. The GP based controller outperforms load power controller and SOGI based controller in terms of fast settling time, less oscillation and less peak overshoot. Table-7.1 shows the results of a comparison using GP controller, Load power based controller and SOGI based controller. The fundamental weights of Load power based controller is fast to converge but it has steady state error in response with some oscillation. In addition, the suggested approach has a substantially lower total harmonic distortion (THD) of supply currents than the other control technique. The suggested GP and load power based controller are straightforward and produce great performance under varying loads and during normal and abnormal grid conditions.

Table 7.1: Comparative performance of different techniques				
S.No.	Parameter	Proposed GP	Proposed Load Power	SOGI
1.	PLL (requirement)	No	No	No
2.	Technique	Adaptive	Adaptive	Non-

				Adaptive
3.	Settling Time	<4cycles (~0.08sec)	<5cycles (~0.10sec)	(0.15sec)
4.	Weight Convergence	Fast(<3 cycles)	Fast(<2 cycles)	Moderate
5.	Oscillation	Less(< $\pm 2\%$)	Less(< $\pm 2\%$)	Less(< $\pm 2\%$)
6.	Load Current(I_L), % THD of I_L	2.5A,27%	2.5A,27%	2.5A,27%
7.	Source Current(I_S), % THD of I_s	2.8A,(~4.2%)	2.8A,(~3.94%)	2.8A(~4.8%)
8.	Dependency on control parameters	No, self-adaptive	No, self-adaptive	Dependent
9.	Complexity	Lower	Lower	Lower
10.	Sampling Time	50 μs	50 μs	50 μs

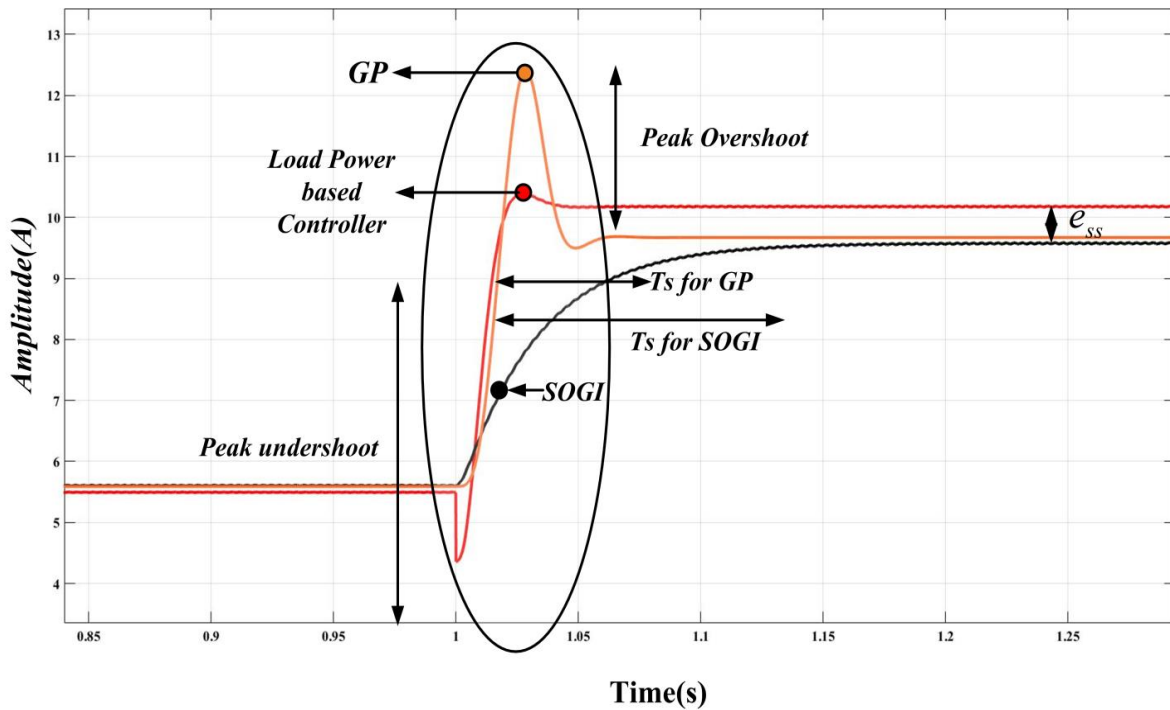


Fig.7.12 Comparison of Output Fundamental Weight

7.5. Experimental Performance

The experimental setup of three-phase compensator has been developed in the laboratory and proposed GP polynomial function based control technique is validated under various conditions. A programmable PV array simulator (Chroma) is used to recreate PV curves. For measurement and control of the system LEM make Hall Effect sensors are used and both voltage (LV25-P) and current (LA25-P) sensors are used. MicroLAB Box 1202 is used to control VSC digital signal processing. The measurements are taken using an HIOKI power analyzer, and the dynamic responses of the system are collected with a four channel oscilloscope.

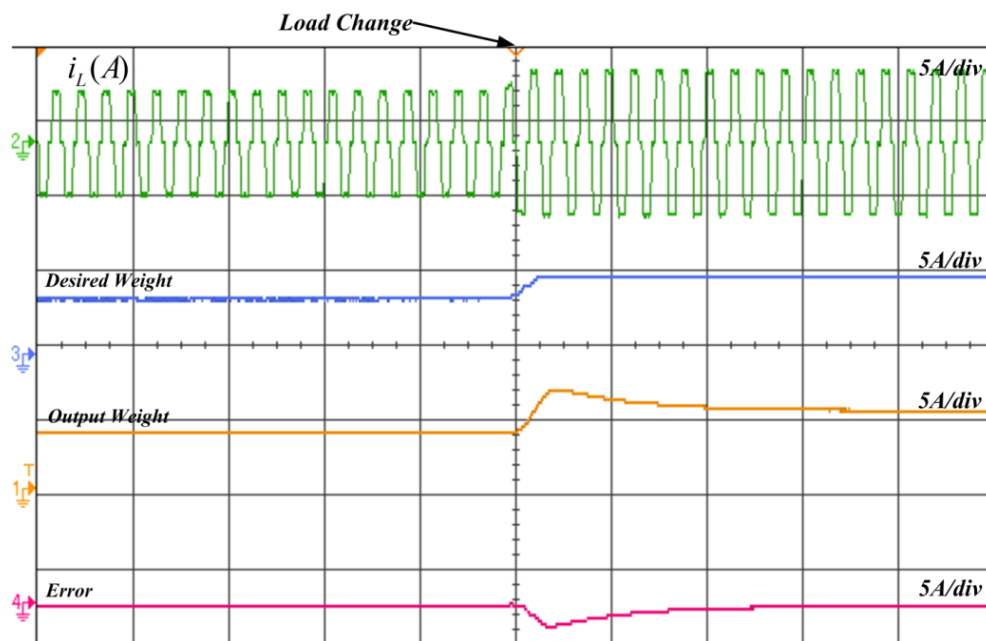


Fig.7.13 Intermediate Performance of GP Controller showing (a) load current of phase-a (i_{La}), (b) desired fundamental weight, (c) output fundamental weight (d) error of phase-a

Fig.7.13 shows intermediate performance of GP controller. Fig.7.13 shows load current of phase-a (i_{La}), desired fundamental weight, output fundamental weight and error of phase-a. The GP controller output is trained by LMS algorithm. Fig.7.14 shows the performance of GP function based control technique for three phase system. Fig.7.14 shows the response of phase-a showing source current of phase-a (i_{sa}), load current of phase-a (i_{La}), load RMS current of phase-a and fundamental weight of phase-a (μ_{La}) extracted by using GP function based control technique. It is clear that the source current is sinusoidal even

though load current is distorted. Further, GP polynomial technique shows fast convergence and fundamental extraction of load varies in accordance with the load changes.

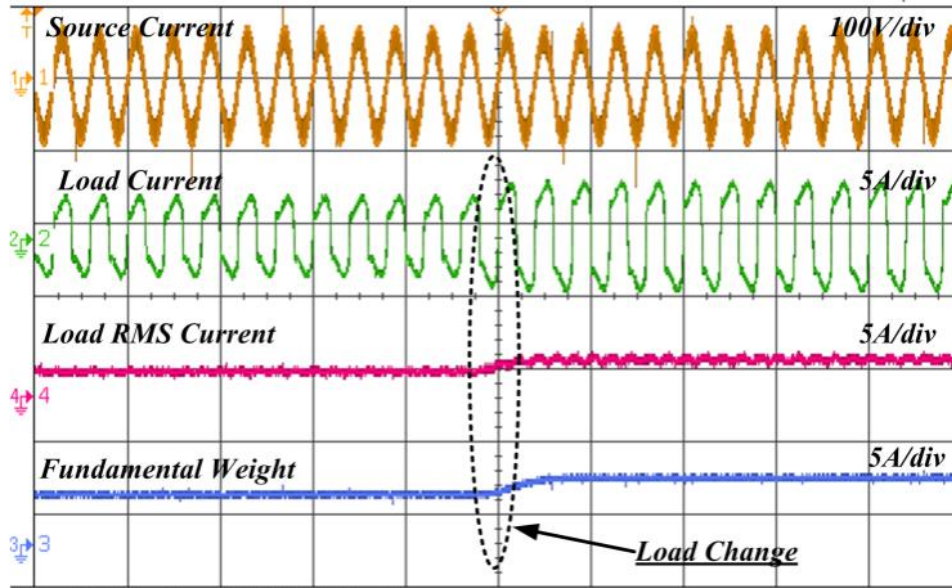


Fig.7.14 Dynamics performance of phase-a during load increase (i_{Sa} , i_{La} , $I_{La(rms)}$, μ_{La})

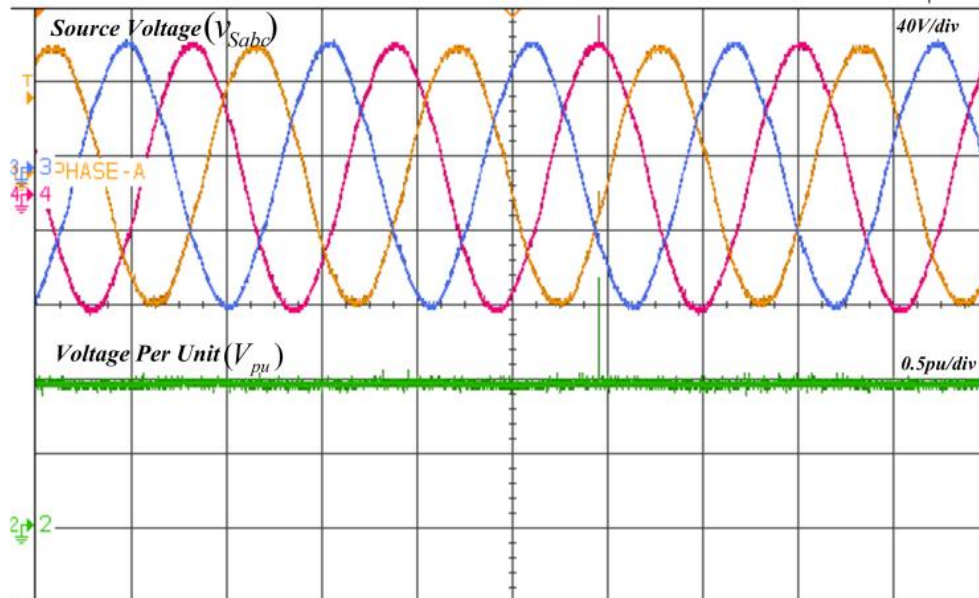


Fig.7.15(a) Waveforms of source voltage (v_{Sabc}) and voltage in per unit (V_{pu})

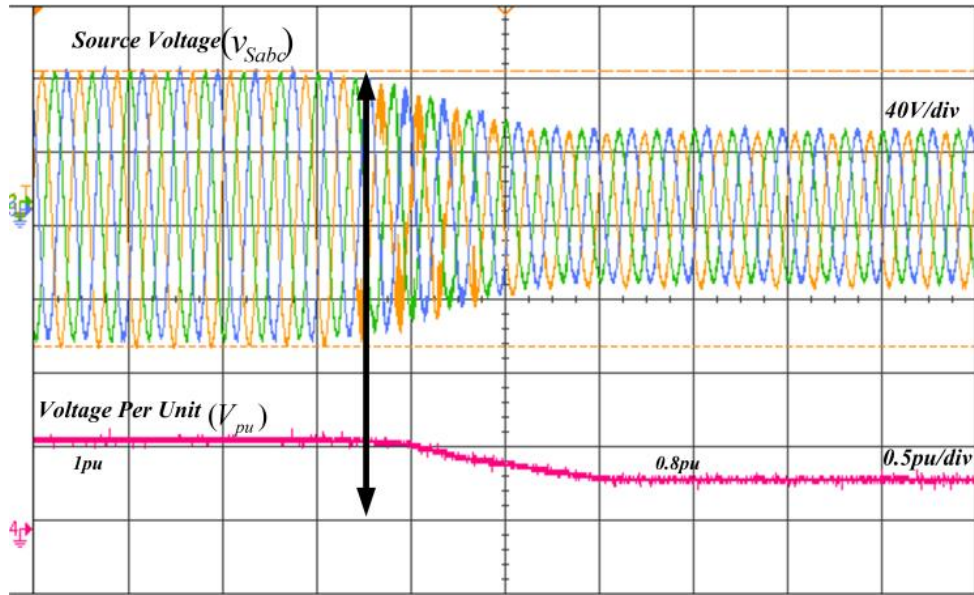


Fig.7.15(b) Estimation of pu voltage (V_{pu}) from three-phase source voltages (v_{Sabc}) under different sag conditions.

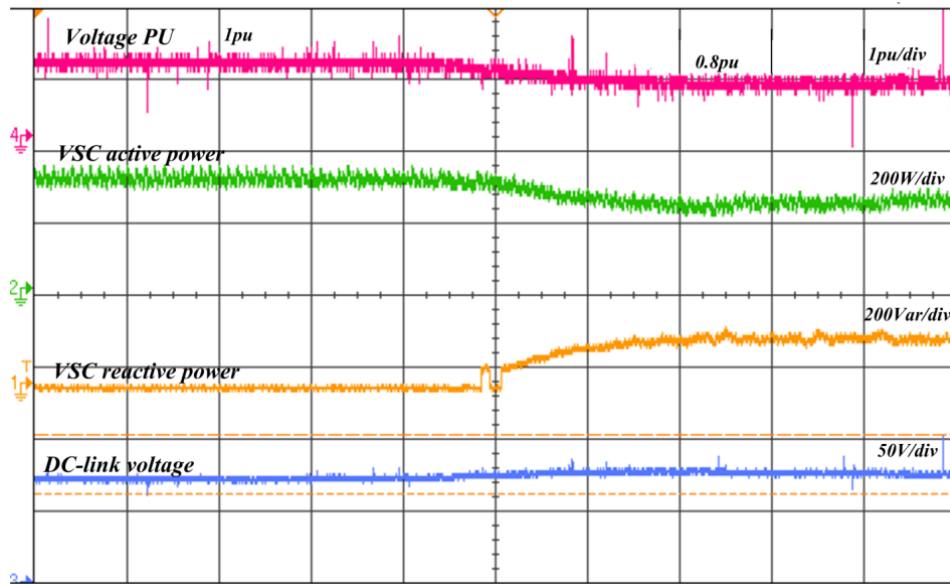


Fig.7.16(a) Dynamic performance during sag (V_{pu} , P_S , Q_S , V_{DC})

The source voltage (v_{Sabc}) and estimated voltage in per unit (V_{pu}) are shown in Fig.7.15(a). According to Fig.7.15(b), a voltage sag conditions is shown when voltage dips from 1pu to 0.8pu. It is clear that the calculated per unit value of voltage varies appropriately when the amount of sag in the grid voltage is introduced. The performance

of GP function based control technique is demonstrated experimentally under abnormal grid condition. Fig.7.16(a) and Fig.7.16(b) show the experimental results with LVRT capability of the controller in the presence of voltage sag.

Fig.7.16(a) shows the voltage pu (V_{pu}), VSC active power (P_{VSC}) in W, source reactive power (Q_{VSC}) in Var and dc-link voltage (V_{DC}). It is noted that in accordance with the established grid regulations [138,139], the active power decreases and the reactive power increases when the grid voltage decreases from 1pu to 0.8pu. The DC link voltage of the system is well regulated.

Source voltage of phase-a (v_{Sa}), source current of phase-a (i_{Sa}) and reactive power (Q_{VSC}) during UPF and LVRT operation are shown in Fig.7.16(b). This figure also depicts the change from UPF to LVRT mode when sag occurs. According to the observed results, both the source voltage and source current are in phase in the UPF mode of operation under the pre-sag mode of operation. However, during sag conditions, LVRT mode is activated and the source current begins to lag behind the source voltage as the grid reactive demand rises during this mode of operation. Thus, the performance of the GP polynomial controller is observed to be satisfactory under different operating modes.

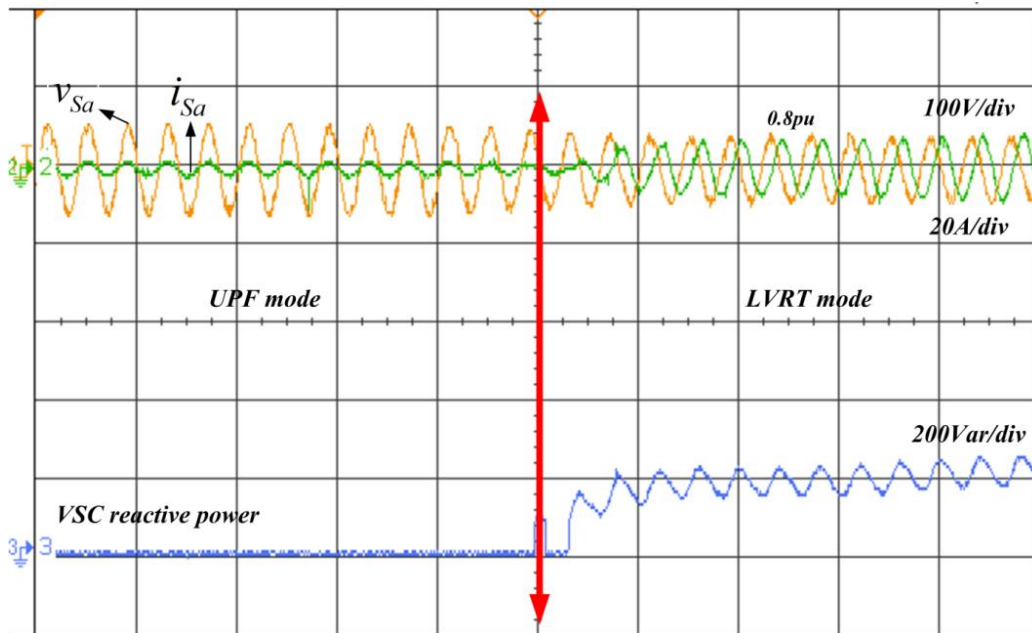


Fig.7.16(b) Performance of phase-a during transition from no-sag to sag introduction (v_{Sa} , i_{Sa} , Q_S)

The findings also show that when a voltage sag in the supply voltage is detected, the reactive power demand of the system rises while the active power demand falls accordingly. This is in line with the stringent grid codes which necessitate grid support during low voltage conditions. Further, the power rating (kVA) of VSC is constant and the system has to be safeguarded, this is also necessary to protect the system. Thus, the controller is designed to contribute to Q and reduce P during adverse grid conditions. Additionally, the dc link voltage is properly stabilized to its reference value both before and after the introduction of sag. So, the results show that a three-phase PV integrated system can be used to provide grid support when needed and in accordance with grid standards. A perfect conformity between the simulation results and the experimental findings is observed. The established power control method based on GP is effective, efficient, and quick to react as desired.

7.5 Conclusion:

This chapter discusses the operation of PV-grid interface three-phase systems and discusses their augmented control operation during LVRT mode. The chapter includes the design and development of a GP function-based, Load power based controller and standard SOGI based controller for LVRT and normal mode of operation. These two new controllers have been designed and developed to track the fundamental component of load current effectively in both normal and LVRT modes and compared with conventional standard SOGI controller, as per the grid code standards. The controllers have been designed in such a way based on the magnitude of voltage sag, the needed reactive power is estimated first and then injected into the system and the active power is correspondingly reduced during this operation. The simulation findings of GP and Load power based controller are satisfactory and are demonstrated for normal and abnormal grid conditions. The transition from one mode to another is also depicted as well as the phase relationship between grid voltage and grid current in both the modes. The designed controllers operate as a shunt active filter during the normal operation and ensure good power quality by lowering harmonic distortion in grid current. Moreover, the GP based controller performs adequately under normal grid voltage setting, voltage sag conditions

and during the post-sag phase. Thus, the experimental performance of GP controller during normal and LVRT mode of operation is discussed which shows better results under simulation studies. The developed GP controller has been equipped with enhanced LVRT capabilities and responds quickly and correctly to changing system conditions and shows better performances as compared to other two controllers.

Chapter:8 Conclusion and Future Scope

The objective of this thesis is to develop and design techniques for improving the quality of power supplied to non-linear loads by single-phase and three-phase systems during normal and abnormal grid conditions including low voltage ride through operation. To achieve these objectives, several control algorithms have been developed for improving power quality and LVRT operation. The control methods require the feed forward term, DC-link voltage controllers, synchronization techniques, estimation of the basic component of load current and reference active and reactive power based on magnitude of voltage sag during LVRT operation. Extensive simulation and experimental investigations have been conducted to assess the effectiveness of the system and the control algorithms. The following part discusses the thesis's concluding remarks.

8.1. Conclusion

Chapter 1 provides an introduction and the background for the various power challenges, harmonic sources, and mitigation techniques and in Chapter 2, a comprehensive literature review was conducted on single-phase and three-phase PV systems that are grid-connected. This chapter focuses on PV modeling, MPPT approaches, control algorithms, installation, and power management. Based on the literature review and the justifications for employing PV, research gaps have been identified and lists of objectives have been decided.

Chapter 3 provides a detailed discussion of the design and development of single-phase and three-phase grid-connected PV systems. Moreover, experimental prototype setup figures, system configuration, and design equations have been developed. PV arrays can be connected in single-stage and double-stage configurations. To enhance the quality of the power, offer reactive power compensation, inject active power into the grid, and inject reactive power into the grid, this system single phase and three phase configurations have been developed and tested both simulation as well as in experimental prototype studies have been carried out and investigated.

Chapter 4 major contributions include design and development of SRFT and SOGI conventional control algorithm and the design and development of self-adaptive BP and RBFNN algorithm applied as single phase and three-phase single stage grid connected

PV system for active power injection and reactive power compensation. The H-bridge inverters are employed as a SAPF to mitigate many power quality issues and achieve load compensation in single-phase and three-phase systems feeding a range of linear and non-linear loads. The SRFT, SOGI, adaptive BP and RBFNN-based controllers may be utilized for control of grid connected systems with or without a PV source interfaced to it. The system performance aspects are demonstrated when taking into account the influence of PV as well as at during night. The control algorithm has been designed to fulfill the entire reactive power needs of the load while also providing power quality enhancement features. The performance of SRFT and SOGI control requires extra LPF to improve the performance of the SRFT and SOGI control algorithms. Adaptive BP and RBFNN consistently perform better in single-stage grid connected with and without PV condition. This chapter also includes experimental results for all control strategies for single-phase and three-phase grid-connected PV systems. The result clearly validates the efficient injection of active and reactive power to the grid based on load demand and PV power output. Power quality improvement is depicted under both linear and non-linear load conditions.

Chapter 5 presents different control techniques for improving power quality for performance under distorted grid. In this chapter, a variety of unit template extraction methods, such as D-SOGI and the unit template approach for three phase systems are discussed. For SAPF operation in a polluted grid situation in a three phase system, two control strategies are explored. The first of these control techniques is the LM trained SOGI filter; in this approach, the unit template method is employed for synchronization. In the second controller technique, a conductance-based approach is employed, in this approach, a D-SOGI filter is used for positive sequence extraction, and the extracted sequence is then used for reference current calculation based on the load power demand. Simulation and experimental performances of both controllers were found good under polluted and normal grid condition. Both active and reactive power compensation, as well as power quality improvement has been achieved under distorted grid condition.

Chapter 6 discusses the operation and grid requirement of single phase system during LVRT mode of operation. The designed controllers include adaptive LP and SWRDFT and this happen to be one of the primary accomplishments of this study. The results show

that controllers are able to track the fundamental component of load current faithfully; the simulation performance of LP, SWRDFT and conventional SOGI based controller are discussed in detail. The controllers have been designed to work effectively in normal and LVRT modes. Even under normal mode of operation, both daytime and nighttime operations have been depicted. The grid code standards have been referred to while designing the controller in LVRT control operation. Based on the level of voltage sag, the reference reactive power and active mode, and accordingly reactive power support is provided during LVRT mode of operation. The transition from one mode to another is also depicted and shows the grid voltage and grid current relationship. The experimental performance of LP controller during normal and LVRT mode of operation is discussed. The designed controller effectively meets the criteria of enhanced power quality in the form of reduced harmonic distortions in grid current and reactive power support under LVRT condition.

Chapter 7 discusses the operation and grid requirement of three-phase system during LVRT mode of operation. This chapter includes the design and development of a GP function-based and Load power based controller for LVRT and UPF mode of operation. This proposed controller has been designed to track the fundamental component of load current effectively in both normal and LVRT modes, as per the grid code standards. The controllers have been designed in such a way that based on the magnitude of voltage sag, the needed reactive power is estimated first and then injected into the system and the active power is correspondingly reduced during this operation. The simulation findings of GP function based, Load power based controller and SOGI based controller are satisfactory and are demonstrated for normal and abnormal grid conditions. The transition from one mode to another is also depicted as well as the phase relationship between grid voltage and grid current in both the modes. The designed controller operates as a shunt active filter during the normal operation and ensures good power quality by lowering harmonic distortion in grid current. The designed controller performs adequately under normal grid voltage setting, voltage sag conditions and during the post-sag phase. The experimental performance of GP function based controller during normal and LVRT mode of operation is also discussed. The developed controllers have been equipped with enhanced LVRT capabilities and respond quickly and correctly to changing system

conditions. The performance of the GP function based controller has been found better in terms of fast settling time, oscillation convergence, no steady state error as compared to other two controllers.

8.2. Future Scope

Design, control, and analysis of single-phase as well as three-phase grid-connected with and without PV systems have been demonstrated in this thesis work. Various synchronization algorithms, both old and modern, have been developed to perform under undesirable grid-voltage conditions. The development of new synchronization methods, particularly for DC-offset situation, still need more research work and investigation. The stable operation of the synchronization algorithms under varied grid voltage conditions could also be examined mathematically.

In this work various conventional and advanced adaptive signal processing algorithms have been demonstrated to estimate the fundamental component of load current. Nowadays, researchers are focusing on adaptive digital filters. These filters reduce the system complexity and require less computation time to implement in digital signal processors. In addition, the proposed controllers have to be designed to operate under have low voltage ride through capability during abnormal grid condition. The future scope of this research could concentrate on new control approaches with reduced complexity with an integrated PV system, as well as new PLL techniques for grid synchronization for operation under polluted grid conditions. The broad scope of this study includes PV integration with a new design of DC-DC converter that minimizes converter switch count, power management in hybrid system by integrating fuel cell, wind power and PV arrays, and EV integration with the grid.

References

- [1]. R. Belaidi, M. Hatti, A. Haddouche and M. M. Larafi, "Shunt active power filter connected to a photovoltaic array for compensating harmonics and reactive power simultaneously," 4th International Conference on Power Engineering, Energy and Electrical Drives, 2013, pp. 1482-1486, doi: 10.1109/PowerEng.2013.6635834.
- [2]. A. Haque and Zaheeruddin, "Research on Solar Photovoltaic (PV) energy conversion system: An overview," Third International Conference on Computational Intelligence and Information Technology (CIIT 2013), 2013, pp. 605-611, doi: 10.1049/cp.2013.2653.
- [3]. "Solar-10 Predictions for 2022". BNEF – Bloomberg New Energy Finance. 1 February 2022. Retrieved 1 February 2022
- [4]. IRENA (2023), Renewable energy statistics 2023, International Renewable Energy Agency, Abu Dhabi.
- [5]. P. T. Szemes and M. Melhem, "Analyzing and modeling PV with "P&O" MPPT Algorithm by MATLAB/SIMULINK," 2020 3rd International Symposium on Small-scale Intelligent Manufacturing Systems (SIMS), 2020, pp. 1-6, doi: 10.1109/SIMS49386.2020.9121579.
- [6]. Juamperez, M., Yang, G. & Kjær, S.B., "Voltage regulation in LV grids by coordinated volt-var control strategies", J. Mod. Power Syst. Clean Energy **2**, 319328(2014),<https://doi.org/10.1007/s40565-014-0072-0>
- [7]. B. Singh, A. Chandra, and K. Al-Haddad, "Power quality: problems and mitigation techniques", John Wiley & Sons Ltd., U.K, 2015.
- [8]. A. Ghosh and G. Ledwich, "Power quality enhancement using custom power devices", Springer International Edition, Delhi, 2009.
- [9]. P. Chittora, A. Singh and M. Singh, "Chebyshev Functional Expansion Based Artificial Neural Network Controller for Shunt Compensation," in IEEE Transactions on Industrial Informatics, vol. 14, no. 9, pp. 3792-3800, Sept. 2018
- [10]. S.S.Reddy and P.R.Bijwe, "Real time economic dispatch considering renewable energy resources," Renew Energy, vol.83,pp.1215-1226, Nov.2015
- [11]. M. Badoni, A. Singh and B. Singh, "Comparative Performance of Wiener Filter and Adaptive Least Mean Square-Based Control for Power Quality Improvement," in IEEE Transactions on Industrial Electronics, vol. 63, no. 5, pp. 3028-3037, May 2016, doi: 10.1109/TIE.2016.2515558.
- [12]. D. V. Roopashree and N. Venugopal, "A Low-Voltage Ride-Through strategy using fuzzy based controller for 3phase grid connected PV system," 2021 International Conference on Recent Trends on Electronics, Information, Communication & Technology (RTEICT), 2021, pp. 34-37, doi: 10.1109/RTEICT52294.2021.9573643.
- [13]. Y. Yang, H. Wang, and F. Blaabjerg, "Reactive Power Injection Strategies for Single-Phase Photovoltaic Systems Considering Grid Requirements," IEEE Transactions on Industry Applications, vol. 50, no. 6, pp. 4065- 4076, 2014.
- [14]. R..A. de Oliveira, B. P. Ferraz, R. Agustini, R. Ferraz, R. Chouhy Leborgne,"Chapter 8 - Voltage dips caused by faults in a transmission system: a monitoring case study of a sensitive industrial consumer", Power Quality in Modern PowerSystems,AcademiPress,2021,Pages219244,ISBN9780128233467.
- [15]. Mojtaba Nasiri, Ali Arzani, Sarah J. McCormack,"A simple and effective grid-supporting low voltage ride-through scheme for single-stage photovoltaic power plants,Solar Energy",Volume 232,2022,Pages 248-262,ISSN 0038-092X,<https://doi.org/10.1016/j.solener.2021.11.052>
- [16]. M. H. Bollen, "What is power quality ?," Electric power systems research, vol. 66, no. 1, pp. 5–14, 2003.
- [17]. C. Sankaran, "Power quality" CRC Press, 2017.
- [18]. M. B. Latran, T. Ahmet, and Y. Yolda,s, "Mitigation of power quality problems using distribution static synchronous compensator: a comprehensive review," IET power electronics, vol. 8, no. 7, pp. 1312–1328, 2015.

- [19]. S. Devassy and B. Singh, "Design and performance analysis of three-phase solar pv integrated UPQC," *IEEE Transactions on Industry Applications*, vol. 54, no. 1, pp. 73–81, 2017.
- [20]. Ewald F. Fuchs and Mohammad A. S. Mausoum, "Power Quality in Power Systems and Electrical Machines", Elsevier Academic Press, London, UK, 2008.
- [21]. Antonio Moreno-Munoz, "Power Quality: Mitigation Technologies in a Distributed Environment", Springer-Verlag London limited, London, 2007.
- [22]. V. Kavitha and K. Subramanian, "Investigation of power quality issues and its solution for distributed power system", in 2017 International Conference on Circuit ,Power and Computing Technologies (ICCPCT), pp. 1–6, 2017.
- [23]. S. Kaur and B. Dwivedi, "Power quality issues and their mitigation techniques in microgrid system-a review", in 2016 7th India International Conference on Power Electronics (IICPE), pp. 1–4, 2016.
- [24]. S. Elphick, P. Ciufo, V. Smith, and S. Perera, "Summary of the economic impacts of power quality on consumers", in 2015 Australasian Universities Power Engineering Conference (AUPEC), pp. 1–6, 2015.
- [25]. P. P. Barker, T. A. Short, C. a Warren, J. J. Burke, R. T. Mancao, and J. J. Siewierski, "Power quality monitoring of a distribution system", in *IEEE Transactions on Power Delivery*, vol. 9, no. 2, pp. 1136-1142, Apr 1994. doi: 10.1109/61.296300
- [26]. A. K. Karmaker, S. Roy, and M. R. Ahmed, "Analysis of the impact of electric vehicle charging station on power quality issues", in 2019 International Conference on Electrical, Computer and Communication Engineering (ECCE), pp. 1–6, 2019
- [27]. M. H. Bollen, "Understanding power quality problems", in *Voltage sags and Interruptions*, IEEE press, 2000
- [28]. "IEEE recommended practice for monitoring electric power quality", *IEEE Std 1159-1995*, pp. 1–80, 1995.
- [29]. "IEEE recommended practice for monitoring electric power quality," *IEEE Std 1159-2009 (Revision of IEEE Std 1159-1995)*, pp. 1–94, 2009.
- [30]. "IEEE recommended practice and requirements for harmonic control in electric power systems," *IEEE Std 519-2014 (Revision of IEEE Std 519-1992)*, pp. 1–29, 2014.
- [31]. "IEEE standard for interconnection and interoperability of distributed energy resources with associated electric power systems interfaces," *IEEE Std 1547- 2018 (Revision of IEEE Std 1547-2003)*, pp. 1–138, 2018.
- [32]. "IEEE standard for interconnecting distributed resources with electric power systems," *IEEE Std 1547-2003*, pp. 1–28, 2003
- [33]. B. Singh, K. Al-Haddad, and A. Chandra, "A review of active power filters for power quality improvements," *IEEE Trans. Ind. Electron.*, vol. 46, no. 5, pp. 960–971, Oct. 1999.
- [34]. S. Bhattacharya, T. M. Frank, D. M. Divan, and B. Banerjee, "Active filter system implementation," *IEEE Ind. Appl. Mag.*, vol. 4, no. 5, pp. 47–63, Sep./Oct. 1998.
- [35]. H. Akagi, Y. Kanazawa, and A. Nabae, "Instantaneous reactive power compensators comprising switching devices without energy storage components," *IEEE Trans. Ind. Appl.*, vol. IA-20, no. 3, pp. 625–630, May 1984
- [36]. F. Z. Peng, G. W. Ott, Jr., and D. J. Adams, "Harmonic and reactive power compensation based on the generalized instantaneous reactive power theory for three phase four wire system," *IEEE Trans. Power Electron.*, vol. 13, no. 6, pp. 1174–1181, Nov. 1998.
- [37]. R. S. Herrera and P. Salmeron, "Instantaneous reactive power theory: A reference in the nonlinear loads compensation," *IEEE Trans. Ind. Electron.*, vol. 56, no. 6, pp. 2015–2022, Jun. 2009

- [38]. H. Karimi, M. Karimi-Ghartemani, and M. R. Iravani, "An adaptive filter for synchronous extraction of harmonics and distortions," *IEEE Trans. Power Del.*, vol. 18, no. 4, pp. 1350–1356, Oct. 2003.
- [39]. M. Forghani and S. Afsharnia, "Online wavelet transform-based control strategy for UPQC control system," *IEEE Trans. Power Del.*, vol. 22, no. 1, pp. 481–491, Jan. 2007.
- [40]. J. Liu, S. Choi, and S. Chen, "Design of step dynamic voltage regulator for power quality enhancement," *IEEE Transactions on Power Delivery*, vol. 18, no. 4, pp. 1403–1409, 2003.
- [41]. M. Badoni, "Analysis, Design and Control of DSTATCOM and its Applications", PhD dissertation, Delhi Technological University, 2015.
- [42]. "Analysis and Control of Shunt Compensator in Distribution System", PhD dissertation, Delhi Technological University, 2018.
- [43]. Wamare Madhukar Maruti, "Multilevel Inverter Based Active Filter", PhD dissertation, IIT – Roorkee, 2011.
- [44]. P. Chittora, "Analysis and Control of Shunt Compensator in Distribution System", PhD dissertation, Delhi Technological University, 2018.
- [45]. S. R. Arya, B. Singh, R. Niwas, C. Ambrish, and K. Al-Haddad, "Power quality enhancement using dstatcom in distributed power generation system," *IEEE Transactions on Industry Applications*, vol. 52, no. 6, pp. 5203–5212, 2016
- [46]. V. Khadkikar, "Enhancing electric power quality using UPQC: A comprehensive overview," *IEEE transactions on Power Electronics*, vol. 27, no. 5, pp. 2284– 2297, 2011
- [47]. A. Ghosh and G. Ledwich, "A unified power quality conditioner (UPQC) for simultaneous voltage and current compensation," *Electric power systems research*, vol. 59, no. 1, pp. 55–63, 2001
- [48]. M. Kesler and E. Ozdemir, "Synchronous-reference-frame-based control method for UPQC under unbalanced and distorted load conditions," *IEEE transactions on industrial electronics*, vol. 58, no. 9, pp. 3967–3975, 2010.
- [49]. Gonzalez-Espin, F., Figueres, E., Garcera, G.: "An adaptive synchronous reference-frame phase-locked loop for power quality improvement in a polluted utility grid", *IEEE Trans. Ind. Electron.*, 2012, 59, (6), pp. 2718–2731
- [50]. Herrera, R.S., Salmerón, P., Kim, H.: "Instantaneous reactive power theory applied to active power filter compensation: different approaches, assessment, and experimental results", *IEEE Trans. Ind. Electron.*, 2008, 55, (1), pp. 184–196
- [51]. Kumar, S., Singh, B.: "Control of 4-Leg VSC based DSTATCOM using modified instantaneous symmetrical component theory". 2009 Int. Conf. Power Systems, Kharagpur, 2009, pp. 1–6
- [52]. Pouresmaeil E, Montesinos-Miracle D, Gomis-Bellmunt O, Sudrià-Andreu A "Instantaneous active and reactive current control technique of shunt active power filter based on the three-level NPC inverter". *European Transactions Electrical Power* Oct. 2011; 21(7):2007–2022
- [53]. Singh B, Arya S, Verma P. "An implementation of double-frequency oscillation cancellation technique in control of DSTATCOM", *International Transactions on Electrical Energy System* 2014; 24:796–807
- [54]. Singh B, Arya S. "Composite observer-based control algorithm for distribution static compensator in four-wire supply system", *IET Power Electronics* 2013; 6(2):251–260
- [55]. Valdez-Fernandez A, Martinez P, Escobar G, Limones-Pozos C, Sosa J. "A model-based controller for the cascade H-bridge multilevel converter used as a shunt active filter", *IEEE Transactions on Industrial Electronics* Nov. 2013; 60(11):5019–5028
- [56]. Arya S, Singh B. "Implementation of kernel incremental learning algorithm in distribution static compensator", *IEEE Transactions on Power Electronics* Mar 2015; 30(3):1157–1169

- [57]. P. Chittora, A. Singh and M. Singh, "Performance evaluation of a new Kalman filter based least mean square algorithm for power quality improvement," in Int. Conf. on Power Electronics, Intelligent Control and Energy Systems (ICPEICES), Delhi, India, 2016, pp. 1-5
- [58]. S. Haykin, "Adaptive Filter Theory", 4th ed. Prentice-Hall, Upper Saddle River, NJ, 2001
- [59]. D.T.M. Solck, "On the convergence behavior of the LMS and NLMS algorithms", IEEE Trans. Signal Process. 41 (1993) 2811–2825
- [60]. R.H. Kwong, E.W. Johnston, "A variable step size LMS algorithm", IEEE Trans. Signal Process. 40 (7) (1992) 1633–1642
- [61]. E. Walach, B. Widrow, "The least mean fourth (LMF) adaptive algorithm and its family", IEEE Trans. Inf. Theory 30 (1984) 275–283
- [62]. Haiquan Zhao, Yi Yu, Shibin Gao, Xiangping Zeng, ZhengyouHe, "A new normalized LMAT algorithm and its performance analysis", Signal Processing, Volume 105,2014,Pages 399-409,ISSN 0165-1684
- [63]. M. Qasim, P. Kanjiya and V. Khadkikar, "Optimal Current Harmonic Extractor Based on Unified ADALINEs for Shunt Active Power Filters," in IEEE Transactions on Power Electronics, vol. 29, no. 12, pp. 6383-6393, Dec. 2014, doi: 10.1109/TPEL.2014.2302539
- [64]. R. Chilipi, N. Al Sayari and J. Y. Alsawalhi, "Control of Single-Phase Solar Power Generation System With Universal Active Power Filter Capabilities Using Least Mean Mixed-Norm (LMMN)-Based Adaptive Filtering Method", in IEEE Transactions on Sustainable Energy, vol. 11, no. 2, pp. 879-893, April 2020, doi: 10.1109/TSTE.2019.2911852
- [65]. M. Badoni, A. Singh and B. Singh, "Comparative Performance of Wiener Filter and Adaptive Least Mean Square-Based Control for Power Quality Improvement," in IEEE Transactions on Industrial Electronics, vol. 63, no. 5, pp. 3028-3037, May 2016, doi: 10.1109/TIE.2016.2515558
- [66]. R. Panigrahi and B. Subudhi, "Performance Enhancement of Shunt Active Power Filter Using a Kalman Filter-Based H_∞ Control Strategy," in IEEE Transactions on Power Electronics, vol. 32, no. 4, pp. 2622-2630, April 2017, doi: 10.1109/TPEL.2016.2572142
- [67]. M. Singh, and A. Chandra, "Real-Time Implementation of ANFIS Control for Renewable Interfacing Inverter in 3P4W Distribution Network," IEEE Trans. Ind. Electron., vol.60, no.1, pp.121,128, Jan. 2013
- [68]. G. W. Chang, C-I. Chen, and Y-F. Teng, "Radial-Basis-Function-Based Neural Network for Harmonic Detection," IEEE Trans. Ind. Electron., vol.57, no.6, pp.2171,2179, June 2010
- [69]. M. Qasim and V. Khadkikar, "Application of Artificial Neural Networks for Shunt Active Power Filter Control," in IEEE Transactions on Industrial Informatics, vol. 10, no. 3, pp. 1765-1774, Aug. 2014
- [70]. Badoni, Manoj & Singh, Alka & Singh, Bhim, "Design and Implementation of Adaptive Neuro-Fuzzy Inference System Based Control Algorithm for Distribution Static Compensator". Electric Power "Components and Systems
- [71]. P. Chittora, A. Singh, and M. Singh, "Simple and efficient control of DSTATCOM in three phase four wire polluted grid system using MCCF-SOGI based controller," In IET Generation, Trans. Distrib., vol. 12, no. 5. pp. 1–10, doi:10.1049/ietgtd.2017.0901.
- [72]. Badoni, M., Singh, A., and Singh, B. "An implementation of variable step-size least-mean-square based control algorithm for DSTATCOM". Int. Trans. Electr. Energ. Syst., 26: 1540– 1554. doi: 10.1002/etep.2163.
- [73]. B. Singh and J. Solanki, "An Implementation of an Adaptive Control Algorithm for a Three-Phase Shunt Active Filter," in IEEE Transactions on Industrial Electronics, vol. 56, no. 8, pp. 2811-2820, Aug. 2009.

- [74]. Badoni, M., Singh, A., Singh, B.: “Comparative performance of wiener filter and adaptive least mean square-based control for power quality improvement”, *IEEE Trans. Ind. Electron.*, 2016, 63, (5), pp. 3028–3037
- [75]. Chittora, Prakash; Singh, Alka; Singh, Madhusudan: “Gauss–Newton-based fast and simple recursive algorithm for compensation using shunt active power filter”, *IET Generation, Transmission & Distribution*, 2017, 11, (6), p. 1521-1530, DOI: 10.1049/iet-gtd.2016.1222
- [76]. Badoni, Manoj; Singh, Alka; Singh, Bhim: “Power quality improvement using DSTATCOM with affine projection algorithm”, *IET Generation, Transmission & Distribution*, 2018, 12, (13), p. 3261-3269, DOI: 10.1049/iet-gtd.2017.0841
- [77]. F.S. Cattivelli , A.H. Sayed , “Diffusion LMS strategies for distributed estimation”, *IEEE Trans. Signal Process.* 58 (3) (2010) 1035–1048 .
- [78]. S. Lee H. , H. Yim S. , J. Song W. , “ z^2 -proportionate diffusion LMS algorithm with mean square performance analysis”, *Signal Process* 131 (2016) 154–160
- [79]. Alhaj Hussam, M.M., Nor, N.M., AsirvadamVijanth, S., et al.: “Power system harmonics estimation using LMS, LMF and LMS/LMF”. *Proc. ICIAS*, 2014
- [80]. G. Modi, S. Kumar and B. Singh, "Improved Widrow–Hoff Based Adaptive Control of Multiobjective PV-DSTATCOM System," in *IEEE Transactions on Industry Applications*, vol. 56, no. 2, pp. 1930-1939, March-April 2020, doi: 10.1109/TIA.2019.2960732.
- [81]. B. Singh, M. Kandpal and I. Hussain, "Control of Grid Tied Smart PV-DSTATCOM System Using an Adaptive Technique," in *IEEE Transactions on Smart Grid*, vol. 9, no. 5, pp. 3986-3993, Sept. 2018, doi: 10.1109/TSG.2016.2645600.
- [82]. P. Shukl and B. Singh, "Grid Integration of Three-Phase Single-Stage PV System Using Adaptive Laguerre Filter Based Control Algorithm Under Non ideal Distribution System," in *IEEE Transactions on Industry Applications*, vol. 55, no. 6, pp. 6193-6202, Nov.-Dec. 2019, doi: 10.1109/TIA.2019.2931504.
- [83]. P. Mitra and G. K. Venayagamoorthy, "An Adaptive Control Strategy for DSTATCOM Applications in an Electric Ship Power System," in *IEEE Transactions on Power Electronics*, vol. 25, no. 1, pp. 95-104, Jan. 2010, doi: 10.1109/TPEL.2009.2024152.
- [84]. M. Qasim and V. Khadkikar, “Application of artificial neural networks for shunt active power filter control,” *IEEE Trans. Ind. Inform.*, vol. 10, no. 3, pp. 1765-1774 , Aug. 2014.
- [85]. S. Arya and B. Singh, “Neural network based conductance estimation control algorithm for shunt compensator,” *IEEE Trans. Ind. Inform.*, vol. 10, no. 1, pp. 569–577, Feb. 2014.
- [86]. A. Bhattacharya and C. Chakraborty, "A Shunt Active Power Filter With Enhanced Performance Using ANN-Based Predictive and Adaptive Controllers," in *IEEE Transactions on Industrial Electronics*, vol. 58, no. 2, pp. 421-428, Feb. 2011, doi: 10.1109/TIE.2010.2070770.
- [87]. Meyer R, Zlotnik A, Mertens A. “Fault Ride-Through Control of Medium-Voltage Converters With LCL Filter in Distributed Generation Systems”, *IEEE Trans Ind Appl* 2014;50:3448–56. <https://doi.org/10.1109/TIA.2014.2304589>.
- [88]. Habib A, Sou C, Hafeez HM, Arshad A. “Evaluation of the effect of high penetration of renewable energy sources (RES) on system frequency regulation using stochastic risk assessment technique (an approach based on improved cumulant)”, *Renew Energy* 2018;127:204–12. <https://doi.org/10.1016/J.RENENE.2018.04.063>.
- [89]. Al-Shetwi AQ, Sujod MZ. “Modeling and Control of Grid-Connected Photovoltaic Power Plant With Fault Ride-Through Capability”, *J Sol Energy Eng* 2017;140:021001 <https://doi.org/10.1115/1.4038591>.

- [90]. Etxegarai A, Eguia P, Torres E, Buigues G, Iturregi A. “Current procedures and practices on grid code compliance verification of renewable power generation”, *Renew Sustain Energy Rev* 2017;71:191–202. <https://doi.org/10.1016/j.rser.2016.12.051>.
- [91]. Luo X, Wang J, Wojcik JD, Wang J, Li D, Draganescu M, et al. “Review of voltage and frequency grid code specifications for electrical energy storage applications”. *Energies* 2018;11:1070. <https://doi.org/10.3390/en11051070>.
- [92]. Robles E, Haro-Larrode M, Santos-Mugica M, Etxegarai A, Tedeschi E. “Comparative analysis of European grid codes relevant to offshore renewable energy installations”, *Renew Sustain Energy Rev* 2019;102:171–85. <https://doi.org/10.1016/j.rser.2018.12.002>.
- [93]. Hanzaei SH, Gorji SA, Ektesabi M. “A scheme-based review of MPPT techniques with respect to input variables including solar irradiance and PV Arrays temperature”, *IEEE Access* 2020;8:18229–39.
- [94]. Nofuentes G, Gueymard C, Aguilera J, P´erez-Godoy M, Charte F. “Is the average photon energy a unique characteristic of the spectral distribution of global irradiance?”, *Sol Energy* 2017;149:32–43.
- [95]. Gunasekaran M, Krishnasamy V, Selvam S, Almakhles DJ, Anglani N. “An Adaptive Resistance perturbation based MPPT algorithm for photovoltaic applications”, *IEEE Access* 2020; 8:196890–901.
- [96]. Hirata Y, Aihara K. “Improving time series prediction of solar irradiance after sunrise: comparison among three methods for time series prediction”, *Sol Energy* 2017;149:294–301
- [97]. Huynh DC, Dunnigan MW. “Development and comparison of an improved incremental conductance algorithm for tracking the MPP of a solar PV panel”, *IEEE Trans Sustain Energy* 2016;7:1421–9.
- [98]. Ishaque K, Salam Z. “A review of maximum power point tracking techniques of PV system for uniform insolation and partial shading condition”, *Renew Sustain Energy Rev* 2013;19:475–88.
- [99]. Eltawil MA, Zhao Z. “MPPT techniques for photovoltaic applications”, *Renew Sustain Energy Rev* 2013;25:793–813.
- [100]. Ali AI, Sayed MA, Mohamed EE. “Maximum Power Point Tracking technique applied on partial shaded grid connected PV system”, *Eighteenth international middle east power systems conference (MEPCON)*; 2016. p. 656–63.
- [101]. Ali AIM, Sayed MA, Takeshita T. “Isolated single-phase single-stage DC-AC cascaded transformer-based multilevel inverter for stand-alone and grid-tied applications”, *Int J Electr Power Energy Syst* 2021;125:106534.
- [102]. Ali AIM, Sayed MA, Takeshita T. “Analysis and design of high-power single-stage three-phase differential-based flyback inverter for photovoltaic applications”, *22nd European conference on power electronics and applications (EPE’20 ECCE Europe)*; 2020. p. 1–8
- [103]. Ahmed J, Salam Z. “An improved perturb and observe (P&O) maximum power point tracking (MPPT) algorithm for higher efficiency”, *Appl Energy* 2015;150:97–108.
- [104]. Aisyah, N., Yusof, M., Ali, Z. “Review of active synchronization for renewable powered microgrid”, *Int. J. Eng. Technol.* 8 (1), 14–21, www.sciencepubco.com/index.php/IJET.
- [105]. Murillo-Yarce, D., Alarcón-Alarcón, J., Rivera, 2.M., Restrepo, C., Muñoz, J., Baier, C., Wheeler, P. “A review of control techniques in photovoltaic systems”, *Sustainability (Switzerland)* 12 (24), 1–22. <http://dx.doi.org/10.3390/su122410598>.
- [106]. R. Majumder, “Reactive power compensation in single-phase operation of microgrid,” *IEEE Transactions on Industrial Electronics*, vol. 60, no. 4, pp. 1403– 1416, 2013.
- [107]. J. Rocabert, A. Luna, F. Blaabjerg, and P. Rodr´ıguez, “Control of power converters in ac microgrids,” *IEEE Transactions on Power Electronics*, vol. 27, no. 11, pp. 4734–4749, 2012.

- [108]. Y. Yang, K. Zhou, and F. Blaabjerg, "Current harmonics from single-phase grid-connected inverters—examination and suppression," *IEEE Journal of Emerging and Selected Topics in Power Electronics*, vol. 4, no. 1, pp. 221–233, 2016.
- [109]. F. Blaabjerg, R. Teodorescu, M. Liserre, and A. Timbus, "Overview of control and grid synchronization for distributed power generation systems," *IEEE Transactions on Industrial Electronics*, vol. 53, no. 5, pp. 1398–1409, 2006. 243
- [110]. J. Selvaraj and N. A. Rahim, "Multilevel inverter for grid-connected pv system employing digital pi controller," *IEEE Transactions on Industrial Electronics*, vol. 56, no. 1, pp. 149–158, 2009.
- [111]. A. Kumar and V. Verma, "Performance enhancement of single-phase gridconnected pv system under partial shading using cascaded multilevel converter," *IEEE Transactions on Industry Applications*, vol. 54, no. 3, pp. 2665–2676, 2018.
- [112]. W. Libo, Z. Zhengming, and L. Jianzheng, "A single-stage three-phase gridconnected photovoltaic system with modified mppt method and reactive power compensation," *IEEE Transactions on Energy Conversion*, vol. 22, no. 4, pp. 881–886, 2007.
- [113]. H. Patel and V. Agarwal, "MPPT scheme for a PV-fed single-phase single-stage grid-connected inverter operating in ccm with only one current sensor," *IEEE Transactions on Energy Conversion*, vol. 24, no. 1, pp. 256–263, 2009.
- [114]. E. Sreeraj, K. Chatterjee, and S. Bandyopadhyay, "One-cycle-controlled single-stage single-phase voltage-sensorless grid-connected PV system," *IEEE Transactions on Industrial Electronics*, vol. 60, no. 3, pp. 1216–1224, 2013.
- [115]. A. Datta, R. Sarker, and I. Hazarika, "An efficient technique using modified p–q theory for controlling power flow in a single-stage single-phase gridconnected PV system," *IEEE Transactions on Industrial Informatics*, vol. 15, no. 8, pp. 4635–4645, 2019.
- [116]. B. N. Alajmi, K. H. Ahmed, G. P. Adam, and B. W. Williams, "Single-phase single-stage transformer less grid-connected PV system," *IEEE Transactions on Power Electronics*, vol. 28, no. 6, pp. 2664–2676, 2013.
- [117]. A. Kumar, Seema, B. Singh, and R. Jain, "Double stage grid-tied solar PV system using hc-lms control," 9th Power India International Conference (PIICON), pp. 1–6, 2020. 244
- [118]. H. S. Sahu and S. K. Nayak, "Extraction of maximum power from a PV array under nonuniform irradiation conditions," *IEEE Transactions on Electron Devices*, vol. 63, no. 12, pp. 4825–4831, 2016.
- [119]. M. S. ElNozahy and M. M. A. Salama, "Uncertainty-based design of a bilayer distribution system for improved integration of phevs and PV arrays," *IEEE Transactions on Sustainable Energy*, vol. 6, no. 3, pp. 659–674, 2015.
- [120]. B. Lu and M. Shahidehpour, "Short-term scheduling of battery in a grid connected PV/battery system," *IEEE Transactions on Power Systems*, vol. 20, no. 2, pp. 1053–1061, 2005.
- [121]. V. Rallabandi, O. M. Akeyo, N. Jewell, and D. M. Ionel, "Incorporating battery energy storage systems into multi-mw grid connected PV systems," *IEEE Transactions on Industry Applications*, vol. 55, no. 1, pp. 638–647, 2019.
- [122]. T.-F. Wu, C.-H. Chang, L.-C. Lin, and C.-L. Kuo, "Power loss comparison of single- and two-stage grid-connected photovoltaic systems," *IEEE Transactions on Energy Conversion*, vol. 26, no. 2, pp. 707–715, 2011.
- [123]. S. Jain and V. Agarwal, "A single-stage grid connected inverter topology for solar PV systems with maximum power point tracking," *IEEE Transactions on Power Electronics*, vol. 22, no. 5, pp. 1928–1940, 2007.

- [124]. T. Sreekanth, N. Lakshminarasamma, and M. K. Mishra, "A single-stage gridconnected high gain buck–boost inverter with maximum power point tracking," *IEEE Transactions on Energy Conversion*, vol. 32, no. 1, pp. 330–339, 2017.
- [125]. EPIA, "EPIA-Photovoltaic Market Report, 2011," [http://www .epia.org/](http://www.epia.org/).
- [126]. Rao, PN, Saini, LM. "Power enhancement of single-phase transformer-less grid-connected cascaded half-bridge diode clamped inverter under partial shaded photovoltaic". *Int Trans ElectrEnergy Syst*. 2021; 31(9):e12998. <https://doi.org/10.1002/2050-7038.12998>
- [127]. Yang, Yongheng&Blaabjerg, F. "Low-Voltage Ride-Through Capability of a Single-Stage Single-Phase Photovoltaic System Connected to the Low-Voltage Grid" *International Journal of Photoenergy*. 2013. 10.1155/2013/257487.
- [128]. V. Saxena, N. Kumar, B. Singh and B. K. Panigrahi, "A Voltage Support Control Strategy for Grid Integrated Solar PV System During Abnormal Grid Conditions Utilizing Interweaved GI," in *IEEE Transactions on Industrial Electronics*, vol. 68, no. 9, pp. 8149-8157, Sept. 2021, doi: 10.1109/TIE.2020.3013771.
- [129]. Jami, R, Nakka, J, Pulavarthi, SVK' "Grid integration of three phase solar powered fault-tolerant cascaded H-bridge inverter" *Int J CircTheor Appl*. 2022; 1- 18. doi:10.1002/cta.3272
- [130]. F. Blaabjerg, R. Teodorescu, M. Liserre, and A. V. Timbus, "Overview of control and grid synchronization for distributed power generation systems," *IEEE Transactions on Industrial Electronics*, vol. 53, no. 5, pp. 1398–1409, 2006.
- [131]. M. Rajeev and V. Agarwal, "Low Voltage Ride-Through Capability of a Novel Grid Connected Inverter Suitable for Transformer-Less Solar PV–Grid Interface," in *IEEE Transactions on Industry Applications*, vol. 56, no. 3, pp. 2799-2806, May-June 2020, doi: 10.1109/TIA.2020.2979134.
- [132]. Nwaigwe, Kevin & Mutabilwa, Philemon & Dintwa, Edward, "An overview of Solar Power (PV Systems) Integration into Electricity Grids *Materials Science for Energy Technologies*" 2. 10.1016/j.mset.2019.07.002.
- [133]. Rajiv K. Varma, "Impacts of High Penetration of Solar PV Systems and Smart Inverter Developments," in *Smart Solar PV Inverters with Advanced Grid Support Functionalities* , IEEE, 2022, pp.1-34, doi: 10.1002/9781119214236.ch1.
- [134]. R. Hudson and G. Heilscher, "PV grid integration—System management issues and utility concerns," *Energy Procedia*, vol. 25, pp. 82–92, 2012.
- [135]. G. Hunter, I. Andrade, J. Riedemann, R. Blasco-Gimenez and R. Peña, "Active and reactive power control during unbalanced grid voltage in PV systems," *IECON 2016 - 42nd Annual Conference of the IEEE Industrial Electronics Society*, 2016, pp. 3012-3017, doi: 10.1109/IECON.2016.7793525
- [136]. Divya, K.C. & P S, Nagendra, "Effect of Grid Voltage and Frequency Variations on the Output of Wind Generators" *Electric Power Components And Systems - electr power compon syst*. 36. 602-614. 10.1080/15325000701801595.
- [137]. L. A. C. Lopes and Huili Sun, "Performance assessment of active frequency drifting islanding detection methods," in *IEEE Transactions on Energy Conversion*, vol. 21, no. 1, pp. 171-180, March 2006, doi: 10.1109/TEC.2005.859981.
- [138]. B. -I. Crăciun, T. Kerekes, D. Séra and R. Teodorescu, "Overview of recent Grid Codes for PV power integration," *13th International Conference on Optimization of Electrical and Electronic Equipment (OPTIM)*, 2012, pp. 959-965, doi: 10.1109/OPTIM.2012.6231767.
- [139]. Blaabjerg, F., "Control of Power Electronic Converters and Systems" Elsevier, ISBN-978-0-12-819432-4 Vol 3.

- [140]. Y. Yang, F. Blaabjerg and Z. Zou, "Benchmarking of Grid Fault Modes in Single-Phase Grid-Connected Photovoltaic Systems," in *IEEE Transactions on Industry Applications*, vol. 49, no. 5, pp. 2167-2176, Sept.-Oct. 2013, doi: 10.1109/TIA.2013.2260512.
- [141]. Y. Yang, F. Blaabjerg and H. Wang, "Low voltage ride-through of single-phase transformerless photovoltaic inverters," *IEEE Energy Conversion Congress and Exposition*, 2013, pp. 4762-4769, doi: 10.1109/ECCE.2013.6647340.
- [142]. M. Nasiri, A. Arzani and J. M. Guerrero, "LVRT Operation Enhancement of Single-Stage Photovoltaic Power Plants: An Analytical Approach," in *IEEE Transactions on Smart Grid*, vol. 12, no. 6, pp. 5020-5029, Nov. 2021, doi: 10.1109/TSG.2021.3108391.
- [143]. Sajadian, S. and Ahmadi, R. (2018), "ZSI for PV systems with LVRT capability", *IET Renewable Power Generation*, 12: 1286-1294. <https://doi.org/10.1049/iet-rpg.2018.5104>
- [144]. Elazab, O.S., Debouza, M., Hasanien, H.M., Muyeen, S. and Al-Durra, A. (2020), "Salp swarm algorithm-based optimal control scheme for LVRT capability improvement of grid-connected photovoltaic power plants: design and experimental validation", *IET Renewable Power Generation*, 14: 591-599. <https://doi.org/10.1049/iet-rpg.2019.0726>
- [145]. Ding, F. Gao, H. Tian, C. Ma, M. Chen, G. He, et al., "Adaptive DC Link Voltage Control of Two-Stage Photovoltaic Inverter During Low Voltage Ride-Through Operation," *IEEE Transactions on Power Electronics*, vol. 31, no. 6, pp. 4182-4194, 2016.
- [146]. A. Petucco, P. Mattavelli, A. Zuccato, and A. Abdelhakim, "Low-voltage ride through (LVRT) testing of full power converter for wind turbines using all-electronic equipment," in *8th IET International Conference on Power Electronics, Machines and Drives (PEMD 2016)*, 2016, pp. 1-6
- [147]. E. Afshari, B. Farhangi, Y. Yang and S. Farhangi, "A low-voltage ride-through control strategy for three-phase grid-connected PV systems," *2017 IEEE Power and Energy Conference at Illinois (PECI)*, 2017, pp. 1-6, doi: 10.1109/PECI.2017.7935767.
- [148]. G. Sun, Y. Li, W. Jin, S. Li and Y. Gao, "A Novel Low Voltage Ride-Through Technique of Three-Phase Grid-Connected Inverters Based on a Nonlinear Phase-Locked Loop," in *IEEE Access*, vol. 7, pp. 66609-66622, 2019, doi: 10.1109/ACCESS.2019.2912859.
- [149]. F. Lin, K. Tan, W. Luo and G. Xiao, "Improved LVRT Performance of PV Power Plant Using Recurrent Wavelet Fuzzy Neural Network Control for Weak Grid Conditions," in *IEEE Access*, vol. 8, pp. 69346-69358, 2020, doi: 10.1109/ACCESS.2020.2984803
- [150]. M. I. Hossain and M. A. Abido, "Positive-Negative Sequence Current Controller for LVRT Improvement of Wind Farms Integrated MMC-HVDC Network," in *IEEE Access*, vol. 8, pp. 193314-193339, 2020, doi: 10.1109/ACCESS.2020.3032400.
- [151]. R. Teodorescu and M. Liserre, "Grid converters for photovoltaic and wind power systems" vol. 29: John Wiley & Sons, 2011.
- [152]. P. Rodriguez, A. V. Timbus, R. Teodorescu, M. Liserre, and F. Blaabjerg, "Flexible active power control of distributed power generation systems during grid faults," *IEEE Transactions on Industrial Electronics*, vol. 54, no. 5, pp. 2583-2592, 2007.
- [153]. Vahedi, Hani & Sheikholeslami, Abdolreza & Tavakoli Bina, Mohammad & Vahedi, Mahmood. (2011), "Review and Simulation of Fixed and Adaptive Hysteresis Current Control Considering Switching Losses and High-Frequency Harmonics", *Advances in Power Electronics*. 2011. 10.1155/2011/397872.
- [154]. Vahedi, Hani & Sheikholeslami, Abdolreza. "The source-side inductance based adaptive hysteresis band current control to be employed in active power filters", 2010, 3. 840-845.
- [155]. P. Karuppanan, S. K. Ram, and K. Mahapatra, "Three level hysteresis current controller based active power filter for harmonic compensation," in *2011 International Conference on Emerging Trends in Electrical and Computer Technology*, pp. 407-412, 2011.
- [156]. Venkata Dinavahi; Ning Lin, "DC-DC Converters," in *Real-Time Electromagnetic Transient Simulation of AC-DC Networks*, IEEE, 2021, pp.377-395, doi: 10.1002/9781119819035.ch9

- [157]. B. Singh, S. Dwivedi, I. Hussain, and A. K. Verma, "Grid integration of solar pv power generating system using qpll based control algorithm," in 2014 6th IEEE Power India International Conference (PIICON), pp. 1–6, 2014.
- [158]. Luis Morán, Juan Dixon, Miguel Torres, "Chapter 41 - Active Power Filters" Power Electronics Handbook (Fourth Edition), Butterworth-Heinemann, 2018, pp. 1341-1379, ISBN 9780128114070, <https://doi.org/10.1016/B978-0-12-811407-0.00046-5>.
- [159]. K. Bhattacharjee, "Design and simulation of synchronous reference frame based shunt active power filter using simulink," in National Conference on Challenges in Research Technology in the Coming Decades (CRT 2013), pp. 1– 7, 2013.
- [160]. Saxena, H., Singh.A., Rai, N. "Design and performance analysis of generalized integrator-based controller for grid connected PV system", Int. J. Electron., 2018, 105, (7), pp. 1079–1096, doi: 10.1080/00207217.2018.1426117
- [161]. S. Alam and A. K. Chongdar. "On generating functions of modified Laguerre polynomials", Rev. Real Acad. De Ciencias Zaragoza, 62 (2007), 91-98.
- [162]. M. P. Chen and H.M. Srivastava. "Some extensions of Bateman's product formulas for the Jacobi polynomials". Appl. J. Math. Stochastic Anal, 4(1995), 423-428.
- [163]. K. A. Driver and S. J. Johnston. "An integral representation of some hypergeometric functions". Electronic Trans. Num. Anal, 25(2006), 115- 120.
- [164]. A. Khan and G.M. Habibullah. "Extended Laguerre polynomials". Int. J. Contemp. Math. Sciences, 22(2012), 1089 – 1094.
- [165]. R. B. Paris. "A Kummer type transformation for a ${}_2F_2$ hypergeometric function". J. Comput. Appl. Math., 173(2004), 379-382.
- [166]. M. I. Qureshi and C.W. Muhammad. "Expansions formulae for general tripped hypergeometric series". J. Aust. Math. Soc, 27(1985), 376-385.
- [167]. Elgendy, Mohammed & Zahawi, Bouchaib & Atkinson, D.J.. "Evaluation of perturb and observe MPPT algorithm implementation techniques". 1-6. 10.1049/cp.2012.0156.
- [168]. M. Badoni, A. Singh, and B. Singh, "Adaptive neurofuzzy inference system least-mean-square-based control algorithm for dstatcom," IEEE Transactions on Industrial Informatics, vol. 12, no. 2, pp. 483–492, 2016.
- [169]. S. B. Q. Naqvi, S. Kumar, and B. Singh, "Three-phase four-wire pv system for grid interconnection at weak grid conditions," IEEE Transactions on Industry Applications, vol. 56, no. 6, pp. 7077–7087, 2020.
- [170]. S. K. Pandey, B. Singh, and G. Modi, "Frequency-adaptive complex-coefficient filter-based control for grid-integrated pv system," IET Generation, Transmission Distribution, vol. 14, no. 19, pp. 4141–4151, 2020
- [171]. Chittora, P., Singh, A., Singh, M.: "Performance evaluation of digital filters in distribution static compensator for non-linear loads", IET Power Electron., 2017, 10, (14), pp. 1915–1923, doi: 10.1049/iet-pel.2016.0914
- [172]. Barros, J., Perez, E.: "An adaptive method for determining the reference compensating current in single-phase shunt active power filters", IEEE Trans. Power Deliv., 2003, 18, (4), pp. 1578–1580
- [173]. Wang, L., Lam, C., Wong, M.: "Minimizing inverter capacity design and comparative performance evaluation of SVC-coupling hybrid active power filters", IEEE Trans. Power Electron., 2019, 34, (2), pp. 1227–1242, doi: 10.1109/TPEL.2018.2828159
- [174]. Meloni, L.F.J., Tofoli, F.L., Rezek, J.J., et al.: "Modeling and experimental validation of a single-phase series active power filter for harmonic voltage reduction", IEEE Access, 2019, 7, pp. 151971–151984, doi: 10.1109/ ACCESS.2019.2947917
- [175]. Rao, S.S. "Engineering optimization theory and practices" (Wiley Eastern, New Jersey,USA, 2019, 5th edn.), pp. 316–319

- [176]. Lyon, W.V., "Application of the Method of Symmetrical Components", New York: McGraw-Hill, 1937.
- [177]. R. Teodorescu, M. Liserre and P. Rodriguez, "Grid Converters for Photovoltaic and Wind Power Systems," John Wiley & sons Pub., ISBN 9780470057513, 2011.
- [178]. Lopes LAC, Sun H. "Performance assessment of active frequency drifting islanding detection methods". IEEE Trans Energy Convers. 2006; 21(1):171-180. doi:10.1109/TEC.2005.859981
- [179]. Aizenshtadt VS, Krylov VI, Metel'skii AS. "Tables of Laguerre Polynomials and Functions". Mathematical Tables Series. Vol. 39. Elsevier Science; 2014.
- [180]. Abeyratne, Isuru. "Laguerre Differential Equation and the radial solution of the Hydrogen Atom", (2019).
- [181]. IEEE Standard Committee. IEEE Standard for Interconnection and Interoperability of distributed energy resources with associated electric power system interfaces. April, 2018, pp. 1–138. IEEE std 1547-2018
- [182]. P.M. Silveira, C. Duque, T. Baldwin, P.F. Ribeiro, "Sliding window recursive DFT with dyadic down sampling — A new strategy for time-varying power harmonic decomposition", IEEE Power & Energy Society General Meeting, 2009, pp. 1–6, <https://doi.org/10.1109/PES.2009.5275212>.
- [183]. P.F. Riderio, C.A. Duque, P.M. Silvira, A.S. Cerqueira, "Power system signal processing for smart grid", Wiley, 2014.
- [184]. P.M. Silveira, C. Duque, T. Baldwin, P.F. Ribeiro, "Sliding window recursive DFT with dyadic down sampling — A new strategy for time-varying power harmonic decomposition", in: 2009 IEEE Power & Energy Society General Meeting, 2009, pp. 1–6, <https://doi.org/10.1109/PES.2009.5275212>.
- [185]. V. D. Pavlović, A. D. Ilić and Z. Ž. Cvetković, "3D parametric analysis of the RC active Gegenbauer filters," 2013 21st Telecommunications Forum Telfor (TELFOR), 2013, pp. 455-458, doi: 10.1109/TELFOR.2013.6716266.
- [186]. A.Arora and A.Singh, "Design and Implementation of LegendreBased Neural Network Controller in Grid-Connected PV System," in IET Renewable Power Generation, Vol. 13, Issue 15, pp. 2783-2792,2019
- [187]. P.Chittora, A.Singh and M. Singh, "Chebyshev Function Expression Based Artificial Neural Network Controller for Shunt Compensattion," in IEEE Transactions on Industrial Informatics, vol. 14, no. 9, pp. 3792-3800, Sept. 2018

Appendix

Simulation and Experimental Parameters for considered single phase system:

Parameters	Simulation	Experimental
Grid Voltage	$V_S = 110V$ (without & with PV)	$V_S = 40V$ (without & with PV)
Grid frequency	$\omega_o = 2\pi \times 50 \text{ rad/sec}$	$\omega_o = 2\pi \times 50 \text{ rad/sec}$
Sampling time	$T_S = 50\mu s$	$T_S = 50\mu s$
Interfacing Inductor	$L_S = 3.5mH$	$L_S = 3.5mH$
Irradiance	$I_{rr} = 1000W/m^2$	$I_{rr} = 1000W/m^2$
PV Rating	2.7kW	500W
DC-link Capacitor	$C_{DC} = 4700\mu F$	$C_{DC} = 5600\mu F$
Feeder Parameters	$L_S = 0.5mH, R = 0.02\Omega$	$L_S = 0.5mH, R = 0.02\Omega$
Controller gains	$k_p=1.5$ and $k_i=0.33$	Adjusted and tuned
Non-linear load	Single phase diode rectifier with $R=80\Omega$ and $L=100mH$	Single phase diode rectifier with $R=90\Omega$ and $L=100mH$

Simulation and Experimental Parameters for considered three-phase system:

Parameters	Simulation	Experimental
Grid Voltage	$V_S = 110V$ (without & with PV)	$V_S = 40V$ (without & with PV)
Grid frequency	$\omega_o = 2\pi \times 50 \text{ rad/sec}$	$\omega_o = 2\pi \times 50 \text{ rad/sec}$
Sampling time	$T_S = 50\mu s$	$T_S = 50\mu s$
Interfacing Inductor	$L_S = 3.5mH$	$L_S = 3.5mH$
Irradiance	$I_{rr} = 1000W/m^2$	$I_{rr} = 1000W/m^2$
PV Rating	2.7kW	500W
DC-link Capacitor	$C_{DC} = 4700\mu F$	$C_{DC} = 5600\mu F$
Feeder Parameters	$L_S = 0.5mH, R = 0.02\Omega$	$L_S = 0.5mH, R = 0.02\Omega$
Controller gains	$k_p=0.9$ and $k_i=0.19$	Adjusted and tuned
Non-linear load	Three-Phase diode rectifier with $R=80\Omega$ and $L=100mH$	Three-Phase diode rectifier with $R=90\Omega$ and $L=100mH$